The Ion-implanted Arsenic Tail In Silicon.

INFORMATION TO USERS

The most advanced technology has been used to photograph and reproduce this manuscript from the microfilm master. UMI films the text directly from the original or copy submitted. Thus, some thesis and dissertation copies are in typewriter face, while others may be from any type of computer printer.

The quality of this reproduction is dependent upon the quality of the copy submitted. Broken or indistinct print, colored or poor quality illustrations and photographs, print bleedthrough, substandard margins, and improper alignment can adversely affect reproduction.

In the unlikely event that the author did not send UMI a complete manuscript and there are missing pages, these will be noted. Also, if unauthorized copyright material had to be removed, a note will indicate the deletion.

Oversize materials (e.g., maps, drawings, charts) are reproduced by sectioning the original, beginning at the upper left-hand corner and continuing from left to right in equal sections with small overlaps. Each original is also photographed in one exposure and is included in reduced form at the back of the book.

Photographs included in the original manuscript have been reproduced xerographically in this copy. Higher quality 6" x 9" black and white photographic prints are available for any photographs or illustrations appearing in this copy for an additional charge. Contact UMI directly to order.

U·M·I

University Microfilms International
A Bell & Howell Information Company
300 North Zeeb Road. Ann Arbor. MI 48106-1346 USA
313 761-4700 800 521-0600

Order Number 9030312

The ion-implanted arsenic tail in silicon

Beck, Scott Edward, Ph.D.

Lehigh University, 1990

U·M·I
300 N. Zeeb Rd.
Ann Arbor, MI 48106

THE ION IMPLANTED ARSENIC TAIL IN SILICON

by

Scott Edward Beck

A Dissertation

Presented to the Graduate Committee

of Lehigh University

in Candidacy for the Degree of

Doctor of Philosphy

in

Physics

Lehigh University

1990

Approved and recommended for acceptance as a dissertation in partial fulfillment of the requirements for the degree of Doctor of Philosophy.

May 18, 1990
Date

Professor Ralph J. Jaccodine
(Professor in Charge)

Accepted May 18, 1990
Date

Special Committee directing
the doctoral work of
Scott Edward Beck

W. Beall Fowler
Professor W. Beall Fowler
(Chairman)

Professor Ralph J. Jaccodine

Professor Brent W. Benson

Professor Alvin S. Kanofsky

ACKNOWLEDGEMENTS

Any effort of this magnitude requires contributions from many sources. The author is quite grateful to his dissertation advisor, Professor Ralph J. Jaccodine, and his dissertation committee chairman, Professor W. Beall Fowler, for their support and guidance. Appreciation is sincerely given to committee members, Professors Brent W. Benson and Alvin S. Kanofsky for their many suggestions. Also the late Professor Frank J. Feigl is acknowledged for his guidance and encouragement.

The technical assistance of AT&T Bell Laboratories is greatly appreciated. In particular, the author wishes to thank Drs. Albert J. Filo and Richard B. Irwin for performing RBS measurements, Messrs. Fred A. Stevie and Peter Kahora for performing SIMS measurements, Mr. Conrad Clark for his assistance with DLTS and spreading resistance measurements. Special thanks go to Dr. Leonard C. Feldman for availing his van de Graaff accelerator for angular yield measurements and the assistance of Ms. Bonnie Weir in performing those measurements. The author is indebted to Richard Knoell for supplying the arsenic implanted samples.

The assistance of Lehigh University personnel is also appreciated. In particular, the assistance of Messrs. Richard O. White and Floyd Miller at the Sherman Fairchild Center and Messrs. Robert Wolfinger and Joseph Zelinkski in the Physics Department is gratefully acknowledged. Discussion with Drs. Jenn-Hwa Huang and Jeffrey M. Parks were of great value. The author is greatly appreciative of the conscientious efforts of Mr. Saikumar Vivekanand who performed the XTEM work presented within this dissertation. A special thanks to the other members of Professor Jaccodine's research group F. Patrick McCluskey, Der-Tsyr "Dennis" Fan, Jenn-Gwo Huang,

Unsoon Kim, and Charles L.A. Cerny for their assistance and many enlightening discussions. The author is also grateful for the support by a Physics Department Teaching Assistantship and a Sherman Fairchild Fellowship.

Above all, the author would like to express his deepest thanks to his family. His parents, Marlin and Miriam Beck, and his wife, Brenda Scheirer Beck, are thanked for their constant love, encouragement, and support. Special thanks are given to Brenda for typing this manuscript.

TABLE OF CONTENTS

Certificate of Approval ii
Acknowledgements iii
Table of Contents v
List of Tables ix
List of Figures x
Abstract 1

1. Fundamental Background 1a

1.1 Ion Implantation 2
1.1.1 Ion Implantation of Arsenic into Silicon 4
1.1.2 Ion Implantation Damage 15
1.1.2.1 Kinchin and Pease Calculations of Damage 21
1.1.2.2 Brice Method: Energy Deposition Distribution 23
1.1.2.3 TRIM-89 Simulation: Resultant Profile and Damage 25
1.2 Thermal Treatment of Implanted Silicon 28
1.2.1 Furnace Annealing 28
1.2.2 Rapid Thermal Annealing 29
1.2.3 Annealing of Implanted Silicon 35
1.2.4 Diffusion of Dopants in Silicon 45
1.2.4.1 Point Defects in Silicon 46
1.2.4.2 The Nature of Diffusion 51
1.2.4.3 Fick's Law of Diffusion and the Diffusion Coefficient 57
1.2.4.4 Diffusion of an Ion Implanted Distribution 61
References 64

2. Arsenic in Silicon: Electrical Activation and Diffusion 69

2.1 Arsenic Clustering/Complexing 69

2.2 Metastability 77

2.3 Precipitation 80

2.4 Arsenic Diffusion Simulations 82

2.5 Arsenic Tail Diffusion 84

2.6 Purpose of the Present Investigation 85

References 87

3. Experimental Details and Results 89

3.1 Anodic Oxidation 89

3.1.1 Principles of Anodic Oxidation 90

3.1.2 Oxide Growth Principles 94

3.1.3 Silicon Dioxide Growth by Anodic Oxidation 96

3.1.4 Anodizing Systems Used 97

3.1.5 Experimental Results 98

3.2 Sample Preparation 106

3.3 Electrical Measurements 107

3.3.1 Spreading Resistance Measurements 107

3.3.1.1 Experimental Results 111

3.3.2 Hall Effect Measurements 126

3.3.2.1 The Hall Effect 126

3.3.2.2 The Sheet Hall Coefficient and Resistivity 128

3.3.2.3 Van der Pauw Sample Fabrication 132

3.3.2.4 Experimental Procedures 134

3.3.2.5 Profiling by Layer Removal 138

3.3.2.6 Experimental Results 139

3.3.3 Deep Level Capacitance Transient Spectroscopy 154

3.3.3.1 Sample Fabrication 158

3.3.3.2 Experimental Results 160

3.4 Ion Beam Analysis 165

3.4.1 Secondary Ion Mass Spectrometry 165

3.4.1.1 Experimental Results 168

3.4.2 Rutherford Backscattering Spectrometry 176

3.4.2.1 Experimental Results 178

3.4.3 Angular Yield 188

3.4.3.1 Experimental Results 191

3.5 Structural Characterization 191

3.5.1 Cross-Sectional Transmission Electron Microscopy 195

3.5.1.1 Experimental Results 197

References 203

4. Discussion 206

4.1 Arsenic Tail Diffusion 206

4.2 The Annealing of Above Amorphization Dose Arsenic Implanted into Silicon 221

4.3 The Effects of Implant Damage on Arsenic Diffusion 226

4.4 A Discussion of Arsenic Clustering/Declustering 227

4.5 The Effect of Recoil Implanted Oxygen on Arsenic Diffusion and Electrical Activation 229

4.5.1 Furnace Anneal Study 230

4.5.2 Rapid Thermal Anneal Study 230

4.6 The Role of the Capping Spin-on-Glass 236

References 239

5. Summary and Recommendations 241

5.1 Summary 241

5.2 Recommendations for Further Work 244

References 246

Vita 247

LIST OF TABLES

Table		Page
1-1	Fluence values at room temperature of the common dopants in silicon needed to create a continuous amorphous layer	18
3-1	Implant conditions used in the RTA studies	119
3-2	Plasma etching conditions for forming the mesa van der Pauw pattern for Hall effect measurements. A PlasmaTherm 2400 plasma etching system was used	134
3-3	Results from the DLTS study of 10 second rapid thermal annealed arsenic implanted samples	161
3-4	Fraction of arsenic atoms that are substitutional along different channeling directions for the 1 X 10^{16} cm^{-2}, furnace annealed samples	188
3-5	Angular half-widths for the 1100°C, 1 X 10^{16} cm^{-2} tail sample	192

LIST OF FIGURES

Figure		Page
1- 1.	Fifty ion trajectories for 100 keV arsenic implanted into silicon. These trajectories were simulated by Monte Carlo calculations in the program TRIM-89	5
1- 2.	Energy loss due to nuclear (- - -) and electronic (—) stopping of arsenic in silicon. The maximum energy loss due to nuclear stopping occurs at ion energy E_1 (73 keV). E_2 (800 keV) is the ion energy where nuclear and electronic stopping are equal in value. Data for these curves was calculated by TRIM-89	10
1- 3.	A single ion trajectory showing the range, R, projected range, R_p, straggle ΔR_p, and lateral straggle $\Delta R_\perp$	12
1- 4.	Monte Carlo calculations of the projected range, straggle, and lateral straggle of arsenic in silicon	13
1- 5.	Model of the diamond lattice viewed along the (a) <100> direction and (b) 7° from the <100> direction	16
1- 6.	Schematic representation of how implantation damage builds up as a function of dose for 100 keV arsenic implanted into silicon. (a) Single ion damage, (b) Low dose damage, (c) A buried amorphous layer is formed, (d) Amorphous layer continues to grow until upper boundary reaches the silicon surface. Increasing the amount of arsenic continues the movement of the deeper amorphous/crystalline boundary. Doses were determined by Prussin et al. [15]	19
1- 7.	A comparison of the range distribution (histogram) and the damage distribution (solid line) for 100 keV arsenic in silicon. Note that the damage distribution peak depth is less than the projected range of the arsenic distribution. Five thousand trajectories were used in calculating these profiles by TRIM-89	26
1- 8.	The distribution of energy given up in displacing a silicon atom by a 100 keV arsenic ion. This profile was calculated by TRIM-89 using 5000 trajectories	27
1- 9.	Schematic diagram of the Heatpulse 210M rapid thermal annealer	31
1-10.	A cross sectional view of the SensArray series 1501A-3-0001 instrumental wafer	32

Figure		Page
1-11.	Thermocouple output voltage (temperature) versus time for various 10 second anneals	33
1-12.	Schematics of the relationship between the effective threshold damage density (TDD) and the damage density distribution. The location of each category of defect is also shown	36
1-13.	The model developed by Seshan and Washburn for low temperature anneals of below amorphization dose implants of phosphorous	39
1-14.	A two dimensional schematic representation of various simple point defects in a group IV semiconductor, (a) vacancy, (b) self-interstitial, (c) substitutional impurity, (d) interstitial impurity, (e) divacancy, (f) substitutional impurity-vacancy pair. The open circles are silicon atoms and the filled circles are impurity atoms	47
1-15.	The vacancy in the silicon lattice. (a) The neutral vacancy V^o. Here there is one electron per dangling bond. The dangling bonds form two new bonds, thus leading to local distortion. (b) The positive vacancy V^+. (c) The negative vacancy V^-. The darkened bonds in (b) and (c) denote orbitals with unpaired spins, which makes the V^+ and V^- visible to electron paramagnetic resonance experiments. Since an electron is either missing or extra, the distortion is different than that of the V^o	48
1-16.	The divacancy configuration in the silicon lattice	48
1-17.	High symmetry interstitial sites in the silicon lattice. The dark spheres indicate the interstitial positions. (a) hexagonal, (b) tetrahedral	49
1-18.	The bond-centered interstitial configuration	50
1-19.	The interstitialcy defects. The two dark spheres represent the silicon interstitialcy defects if both of the dark spheres are silicon atoms. If one of the dark spheres is an impurity atom these are impurity interstitialcies *A I*	50
1-20.	Basic models of atomic diffusion mechanisms in a two-dimensional lattice. (a) The vacancy mechanism. (b) The interstitial mechanism. (c) The interstitialcy mechanism	53
1-21.	Diffusion by the concerted exchange mechanism	56
2- 1.	The Arsenic-Vacancy Cluster proposed by Fair and Weber	70

Figure		Page
2- 2.	Hu's model of an arsenic cluster in silicon. The open circles represent silicon atoms while the shaded circles represent arsenic atoms. In this diagram the four arsenic atoms form a tetrahedron with a normal interstitial site at its center	72
2- 3.	The electrical solubility concentration versus the annealing temperature	74
2- 4.	The average diffusivity versus the average arsenic concentration. At high arsenic concentration values the concentration enhancement is limited by clustering for anneals below 1050°C. For anneals above 1100°C concentration enhancement is very strong and a declustering mechanism is suggested	76
2- 5.	The sheet resistance of arsenic implanted silicon after high and low temperature anneals. The first and third anneals were done at 1100°C for 1 second. Second and fourth anneals were done at 800°C for 30 minutes	78
2- 6.	The data of Kamgar et al. [15] showing the three domains in the (a) sheet resistance and (b) the normalized fraction of nonsubstitutional to substitutional arsenic atoms as a function of anneal time. Note that f_{min} is the fraction of arsenic for the case where Rutherford Backscattering showed the highest degree of substitutionality	79
3- 1.	A schematic of a typical electrolytic cell used for anodization	91
3- 2.	A schematic of the cell used for anodic oxidation and oxide stripping	98
3- 3.	SIMS profile of the 1 X 10^{16} cm^{-2} arsenic implant	101
3- 4.	SIMS profiles of arsenic and oxygen after thermally growing a 600 Å oxide layer	102
3- 5.	SIMS profile after growing a 276 Å anodic oxide	103
3- 6.	SIMS profile after growing a 540 Å anodic oxide	104
3- 7.	Arsenic profile (by SIMS) after the 540 Å anodic oxide in Fig. 3-6 was removed	105
3- 8.	A schematic illustrating dopant profiling with the spreading resistance technique	109

Figure		Page
3- 9.	(a) The Gorey-Schneider Probe Grinder. (b) A schematic view of the grinder in use where "P" is the initial point contact between the probe and the sapphire plate	109
3-10.	Carrier concentration (electrically active arsenic) profiles obtained by spreading resistance. Between 800 and 900°C the tail-only samples (o) have deeper junctions than the total (+). Shown here are the 800°C profiles	112
3-11.	Carrier concentration profiles for the tail-only (o) and total (+) samples annealed at 1100°C	113
3-12.	Carrier concentration profiles for the tail-only (+) and total (Δ) samples rapid thermal annealed at 800°C for 10 seconds	115
3-13.	Carrier concentration profiles for the tail-only (+) and total (Δ) samples rapid thermal annealed at 1080°C for 10 seconds	116
3-14.	Spreading resistance data for the 1 X 10^{16} cm^{-2}, 100 keV total samples annealed by RTA for 10 seconds	117
3-15.	Spreading resistance data for the 1 X 10^{16} cm^{-2}, 100 keV tail-only samples annealed by RTA for 10 seconds	118
3-16.	The 800°C carrier concentration profiles for the 1 X 10^{15} cm^{-2} samples annealed by RTA for 10 seconds	120
3-17.	The 1080°C carrier concentration profiles for the 1 X 10^{15} cm^{-2} samples annealed by RTA for 10 seconds	121
3-18.	The 800°C carrier concentration profiles for the 1 X 10^{14} cm^{-2} samples annealed by RTA for 10 seconds	122
3-19.	The 1080°C carrier concentration profiles for the 1 X 10^{14} cm^{-2} samples annealed by RTA for 10 seconds	123
3-20.	Carrier concentration for the 1 X 10^{14} cm^{-2}, 50 keV total samples annealed by RTA for 10 seconds	125
3-21.	The Hall Effect	127
3-22.	The van der Pauw geometry	129
3-23.	The geometrical correction factor as a function of $\frac{R_1}{R_2}$	131

Figure | Page

3-24. The procedure to fabricate van der Pauw patterns 133

3-25. The new Hall measurement sample holder 135

3-26. Schematic diagram of the Hall effect measurement 136

3-27. The sheet resistivity of the 1 X 10^{15} cm^{-2} and 1 X 10^{16} cm^{-2} furnace annealed samples 140

3-28. Comparison of the total and tail-only electrically active concentration profiles after an 800°C, 30 minute anneal. Data are from differential Hall effect measurements.
(a) 1 X 10^{16} cm^{-2} 142
(b) 1 X 10^{15} cm^{-2} 143

3-29. Comparison of the total and tail-only electrically active concentration profiles after a 950°C, 30 minute anneal. Data are from differential Hall effect measurements.
(a) 1 X 10^{16} cm^{-2} 144
(b) 1 X 10^{15} cm^{-2} 145

3-30. Comparison of the total and tail-only electrically active concentration profiles after an 1100°C, 30 minute anneal. Data are from differential Hall effect measurements.
(a) 1 X 10^{16} cm^{-2} 146
(b) 1 X 10^{15} cm^{-2} 147

3-31. Hall mobility profiles for the 1 X 10^{16} cm^{-2} total samples 149

3-32. Hall mobility profiles for the 1 X 10^{15} cm^{-2} total samples 150

3-33. Hall mobility profiles for the 1 X 10^{16} cm^{-2} tail-only samples 151

3-34. Hall mobility profiles for the 1 X 10^{15} cm^{-2} tail-only samples 152

3-35. Hall mobility profiles for the samples annealed at 1100°C for 30 minutes. Shown here are profiles for the 1 X 10^{15} cm^{-2} (circles) and 1 X 10^{16} cm^{-2} (squares) samples. The tail-only samples are designated by open symbols while the total samples have filled symbols. The as-implanted arsenic profile (solid line) determined by SIMS is shown for comparisons 153

3-36. An illustration of the depletion (space charge) layer of a p^+n junction (a) before, (b) during, and (c) after a trap filling pulse 155

Figure | Page

3-37. A simple block diagram of a DLTS spectrometer. Shown in the insert are (from top) sample bias pulses, sample capacitance and typical spectrum as sample temperature is varied 157

3-38. Utilization of a rate window by means of a double boxcar averager. The output is the average difference in capacitance amplitudes at the sampling times t_1 and t_2 159

3-39. DLTS spectra for the 1 X 10^{15} cm^{-2} total samples annealed at 800°C and 1080°C for 10 seconds. Note that a third defect peak appears after the 1080°C anneal 162

3-40 A schematic representation of the principles of SIMS 166

3-41 SIMS data comparing the total and tail-only chemical concentration profiles after an 800°C, 30 minute anneal.
(a) 1 X 10^{16} cm^{-2} 169
(b) 1 X 10^{15} cm^{-2} 170

3-42 Comparison of the total and tail-only chemical concentration profiles after a 950°C, 30 minute anneal.
(a) 1 X 10^{16} cm^{-2} 172
(b) 1 X 10^{15} cm^{-2} 173

3-43 Comparison of the total and tail-only chemical concentration profiles after an 1100°C, 30 minute anneal.
(a) 1 X 10^{16} cm^{-2} 174
(b) 1 X 10^{15} cm^{-2} 175

3-44. (a) A schematic of a crystalline solid (o, host atoms) with a surface layer including heavy impurities that are in interstitial sites (□) and substitutional sites (Δ).
(b) The backscattering spectra for the random and aligned beams. In (a) the arrows show the directions of these beams 177

3-45. RBS random and aligned spectra for the as-implanted 100 keV, 1 X 10^{16} cm^{-2} sample. The aligned spectrum was taken along the <100> direction 180

3-46. The RBS spectra for the total samples after annealing at
(a) 800°C 181
(b) 950°C 182
(c) 1100°C 183

Figure Page

3-47. The RBS spectra for the tail-only samples after annealing at
(a) 800°C 184
(b) 950°C 185
(c) 1100°C 186

3-48. A schematic of an angular yield profile 190

3-49. Angular yield profiles for the 1100°C, 1 X 10^{16} cm^{-2} tail-only sample. Results from analysis about the
(a) <111> axis 193
(b) <110> axis 194

3-50. A flow chart describing the fabrication of the XTEM specimens 196

3-51. XTEM micrograph of the 1 X 10^{16} cm^{-2}, 800°C total sample 198

3-52. XTEM micrograph of the 1 X 10^{16} cm^{-2}, 800°C tail-only sample 200

3-53. XTEM micrograph of the 1 X 10^{16} cm^{-2}, 950°C tail-only sample 202

4- 1. Profiles determined by spreading resistance for 1 X 10^{14} cm^{-2}, 50 keV (open symbols) and 1 X 10^{15} cm^{-2}, 50 keV (filled symbols) implanted samples. These samples were rapid thermal annealed for 10 seconds at 800°C (circles) and 1080°C (boxes) 207

4- 2. Comparison of SIMS total chemical concentration data to a simulation by PREDICT for a 1 X 10^{15} cm^{-2} implant annealed for 30 minutes at
(a) 800°C 208
(b) 1100°C 209

4- 3. Comparison of the total chemical concentration to the electrically active concentration for the 1 X 10^{16} cm^{-2}, 800°C total sample
(a) SIMS and Hall effect data 212
(b) PREDICT Simulation 213

4- 4. Comparison of the total chemical concentration to the electrically active concentration for the 1 X 10^{16} cm^{-2}, 1100°C total sample
(a) SIMS and Hall effect data 214
(b) PREDICT Simulation 215

4- 5. Comparison of the total chemical concentration to the electrically active concentration for the 1 X 10^{15} cm^{-2}, 800°C total sample
(a) SIMS and Hall effect data 216
(b) PREDICT Simulation 217

Figure Page

4- 6. Comparison of the total chemical concentration to the electrically active concentration for the 1 X 10^{16} cm^{-2} tail-only samples
(a) 800°C 218
(b) 950°C 219
(c) 1100°C 220

4- 7. Comparison of the total chemical concentration to the electrically active concentration for the 1 X 10^{15} cm^{-2} tail-only samples
(a) 800°C 222
(b) 950°C 223
(c) 1100°C 224

4- 8. SIMS profiles for 140 keV arsenic implanted through 800 Å of silicon dioxide. Also shown are the recoil implanted oxygen profiles calculated by the method of Gibbons and Christel [12,13] 231

4- 9. SIMS profiles of furnace annealed through oxide arsenic implanted silicon
(a) 1 X 10^{15} cm^{-2} 232
(b) 5 X 10^{15} cm^{-2} 233

4-10. Carrier concentration profiles of rapid thermal annealed arsenic annealed implanted silicon
(a) 1 X 10^{15} cm^{-2} 234
(b) 5 X 10^{15} cm^{-2} 235

4-11. Fluences measured by SIMS for the 1 X 10^{16} cm^{-2}, 100 keV implanted and diffused profiles 237

5- 1. Mechanisms involved in damage annealing and arsenic diffusion for above amorphization doses of arsenic implanted into silicon 242

ABSTRACT

Ion implantation is one of the major processing steps used in the fabrication of integrated circuits. The principal advantages of this technique include control of the penetration depth of dopants, the possibility of forming shallow junctions, and the ability to introduce dopants to concentrations above their equilibrium solid solubility. Lattice damage is the main side effect and disadvantage encountered. A subsequent heat treatment can remove this damage.

The purpose of this dissertation is to examine the damage annealing, arsenic diffusion, and electrical activation of above-amorphization-dose arsenic implanted silicon after various thermal treatments. Several different techniques are used to analyze the results of the anneals. These include spreading resistance measurements, differential Hall effect measurements, deep level capacitance transient spectroscopy, cross-sectional transmission electron microscopy, Rutherford backscattering spectrometry and secondary ion mass spectrometry. Particular attention is given to the end-of-range (or tail) region of the implant. Tail-only samples were produced by an anodic oxidation and stripping technique after implantation or by implanting through a surface oxide. Arsenic in the tail-only samples is found to diffuse differently than the total implant samples, under both furnace and rapid thermal annealing conditions in the temperature range of 800°C to 1100°C.

The relationship of end-of-range damage to annealing and diffusion is examined. It is found that the amorphous layer must anneal before considerable arsenic diffusion can occur. The arsenic diffusion and electrical activation is also found to be strongly dependent upon implant dose. Excess silicon interstitials recoil-implanted from the surface region into the end-of-range region play an important role in the damage annealing, arsenic diffusion, and electrical activation. Results verifying a clustering/declustering mechanism are also reported. It is suggested that excess silicon interstitials play a role in the declustering mechanism.

Chapter 1

Fundamental Background

A fundamental and important physical phenomenon is the diffusion of one type of element or molecule in the matrix of another. The theories developed in the late 1800's have been the foundation of recent diffusion studies. Current studies range in scope from the diffusion of one metal into another to the diffusion of ion implanted species in their host lattice. This dissertation is a study of the diffusion of ion implanted arsenic in silicon, particularly the factors that affect the anomalous tail motion.

The current trend in very large scale integration (VLSI) circuitry is to seek means to reduce the minimum dimensions of the circuit below one micron, thus increasing packing density and improving circuit performance. According to device scaling "rules", as the lateral dimension is reduced the junction depth must also be reduced. This requires that both vertical and horizontal diffusion of the dopant species must be controlled. Ion implantation is used because of its precise control of both dose and depth of the dopant species. The type of thermal processing is also important because it activates the implanted dopants, anneals implant damage, and causes diffusion of the dopant. Furnace annealing has been the most common method of thermal processing used in diffusion studies. As the wafer size increases, however, radial heating and cooling effects cause warping or slipping when the wafers are heated or cooled too rapidly. These effects may influence the device yield and the arsenic diffusion. Another type of thermal processing is Rapid Thermal Annealing (RTA)

which involves heating with large area, incoherent energy sources. These sources heat the entire wafer at one time and thermally isolate the wafer so that the heating and cooling are dominated by radiation. The wafer is permitted to heat and cool rapidly and uniformly.

One of the major dopants used in the production of integrated circuits is arsenic. Arsenic is a group V element which yields n-type silicon. It is used in preference to other group V elements because it diffuses slowly in silicon, it has little misfit to the silicon lattice, and it can be doped in high concentrations. As the dimensions of VLSI devices decrease, a knowledge of how the implanted arsenic distribution diffuses becomes more important for dimensional control. In this dissertation the mechanisms of arsenic diffusion in silicon, especially in the tail region are examined. It will be shown that the tail diffuses differently than the total profile. Many factors play a role in this difference including damage annealing, concentration enhancement, and the remaining point defects after implantation.

In this chapter, the terms and concepts relevant to the understanding of ion implanted arsenic in silicon are presented. Ion implantation both introduces arsenic ions and damages the silicon substrate. Thermal treatments remove this damage and place the implanted arsenic on silicon lattice sites, thus making the arsenic electrically active. Many models have been proposed for the diffusion of arsenic in silicon. To understand these models the basic physical mechanisms by which atoms diffuse in solids are presented. The role of point defects, their charge state, the concentration of defects and dopant atoms, and the annealing temperature will be discussed.

1.1 Ion Implantation

In the first integrated circuits, dopants were diffused into the wafer from a surface

source, usually a doped glass. The dopant concentration at the surface was maintained at solid solubility to achieve reproducibility. This limited the possible dopant distribution. In the 1960's ion implantation was developed as a technique to reproducibly introduce a uniform and precise amount of dopant ($\leq$ 1% variation over a range of 10^{11} to 10^{18} cm^{-2}) into a semiconducting substrate. The current scientific and technological importance of this technique is evidenced by the number of recent volumes of conference proceedings published by the Materials Research Society [1-5].

When a substrate is bombarded by a beam of energetic ions it will retain some of the incident ions and lose some of its own atoms by sputtering. The incident ions that are retained are said to be implanted and the technique of using an energetic ion beam to introduce ions into a solid is called Ion Implantation (I^2). During implantation the dopant atoms are ionized, accelerated, and directed at the solid target. Upon entering the substrate lattice the ions collide with the substrate atoms, gradually lose energy, and finally come to rest at some depth below the surface. By adjusting the acceleration energy the average penetration depth is controlled. The dopant dose can be controlled by directly monitoring the ion beam current. Lattice damage, the principal side effect, can be removed by heat treatments. The following is a list of other advantages in using ion implantation.

- Dopant concentrations above the equilibrium solid solubility can be introduced.
- The dopant source purity is not as critical as doped glass diffusion sources, since exact mass separation can be done using a magnetic field.
- Shallow doped layers are possible. The penetration depth is a function of tilt angle, ion energy, ion mass, substrate and surface layer(s).

- Implantation at room temperature avoids a high temperature step during device fabrication.
- Many simple masking methods can control areal placement of the doping impurities.

As stated above, radiation damage is the principal disadvantage in using ion implantation. This byproduct of the implantation process makes a high temperature annealing step after implantation a requirement. Annealing restores the substrate crystallinity and moves implanted ions onto electrically active lattice sites. Other disadvantages of ion implantation include:

- The expected profile can be altered due to ion beam channeling (discussed later), beam heating and diffusion during annealing.
- Lateral movements of the ion under masking materials may occur.
- Thick doped layers (>10 μm) are not possible.
- Implanters are complex and require significant and costly maintenance and facilities.

The following sections will define and discuss the major concepts and results of ion implantation. Particular attention is focused on the implantation of arsenic into silicon.

1.1.1 Ion Implantation of Arsenic into Silicon

We will discuss the I^2 process using the specific example of implanted arsenic ions since most factors are also common to other implant species (P, B, Sb, etc.). As each implanted arsenic ion enters the silicon substrate, it experiences a series of collisions with the silicon atoms until it finally comes to rest, as shown in Fig. 1-1. This figure depicts a Monte Carlo calculation of fifty ion trajectories for

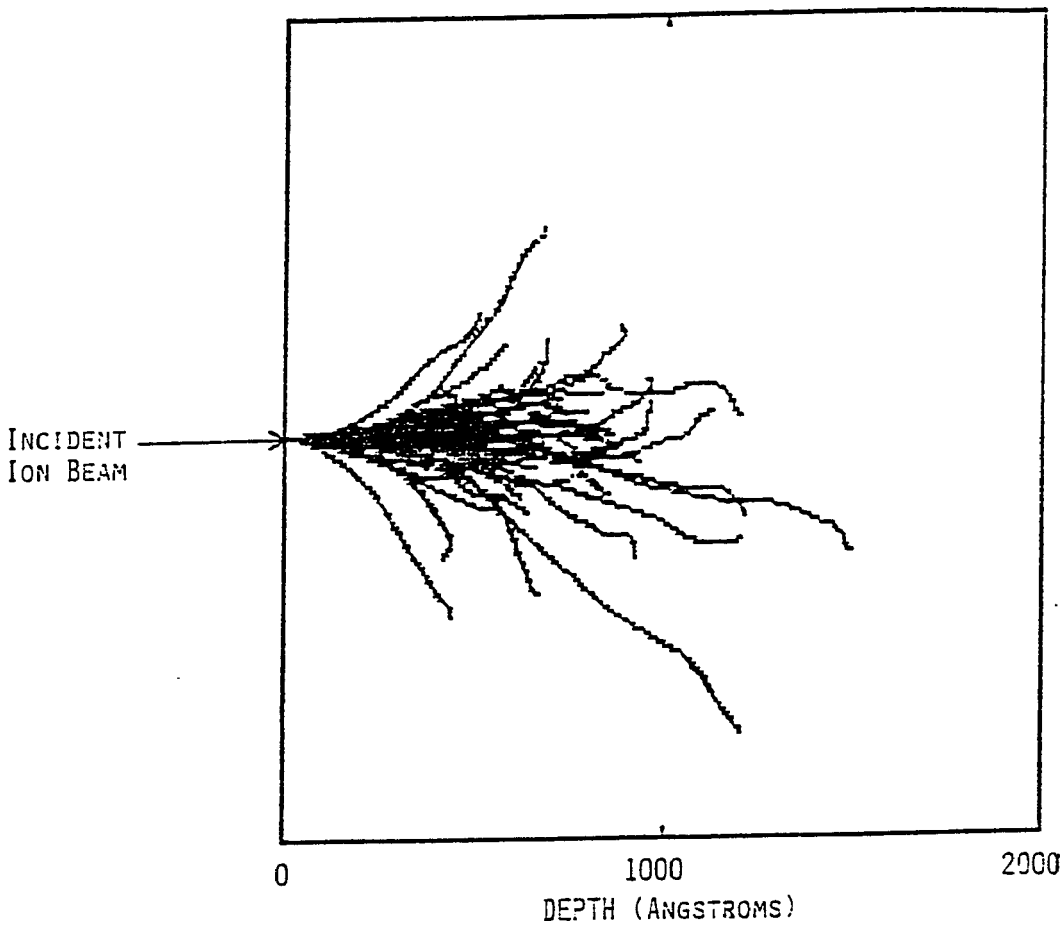

Figure 1-1. Fifty ion trajectories for 100 keV arsenic implanted into silicon. These trajectories were simulated by Monte Carlo calculations in the program TRIM-89 [6].

100 keV arsenic implanted into silicon. These trajectories were determined using the simulation program TRIM-89 [6]. The initial ion energy is much greater than the lattice binding energy. Therefore, the arsenic ion must come very close to a silicon atom if it is to interact and be deflected. The interaction of the ion with the solid depends largely on the ion energy and the proximity of the ion to the target atom and less so on the mass and charge of the ion and substrate atoms. A theory of ion scattering has been developed based on elastic collisions between pairs of nuclei and inelastic collisions between nuclei and electrons in the target [7]. The mass of the ion compared to that of the substrate plays an important role in determining the types of interactions experienced by the ions.

Two basic mechanisms are responsible for bringing energetic ions to rest in semiconductors: nuclear and electronic stopping. The ion trajectories, seen in Fig.1-1, are due to scattering associated with these interactions. It is customary to assume that the two forms of energy loss, nuclear $\left(\frac{dE}{dx}\right)_{nuclear}$ and electronic $\left(\frac{dE}{dx}\right)_{electronic}$, are independent of one another. The average energy loss per distance for a single incident projectile, $\frac{dE}{dx}$, is the sum of these two energy losses

$$-\frac{dE}{dx} = N\left[\left(\frac{dE}{dx}\right)_{nuclear} + \left(\frac{dE}{dx}\right)_{electronic}\right] = N\left[S_n(E) + S_e(E)\right] \qquad (1.1)$$

where N is the substrate atomic density and $S_n(E)$ and $S_e(E)$ are the nuclear and electronic stopping powers, respectively (in eV/Å or other equivalent units). Lindhard, Scharff, and Schiott [7] developed a theory (called LSS theory in the literature) based on equation 1.1 to determine the depths to which implanted ions

would travel before coming to rest in an amorphous or misaligned crystalline solid.

During nuclear stopping part of the kinetic energy of the incoming ion is transferred to the lattice nuclei absorbing the impact. This is theoretically treated as a screened Coulombic collision process, and the collision is elastic. In a first order approximation it is assumed that each target nucleus acts independently of all other target nuclei in slowing the incoming ion. The possible higher order interactions between target atoms in the stopping process are neglected.

Using classical mechanics a physical description of this scattering process can be obtained [8]. In the center-of-mass frame the scattering angle θ can be related to the energy lost by the ion τ:

$$\tau = \frac{4\, E_i\, M_i\, M_t}{(M_i + M_t)^2} \sin^2\left(\frac{\theta}{2}\right). \tag{1.2}$$

Here E_i is the initial ion energy and M_i and M_t are the atomic masses of the ion and target, respectively. The scattering angle is obtained using an atomic scattering potential of the form [8]

$$V(r) = \frac{q^2 Z_i Z_t}{r}\, f_s\,(r) \tag{1.3}$$

and integrating the equation of motion for the scattering trajectory. V(r) is a Coulombic - (Rutherford -) type potential where q is the charge magnitude of a single electron, Z_i and Z_t are the atomic numbers of the ion and target atoms respectively, r is the separation between nuclei, and f_s is the Thomas-Fermi electronic screening function [8,9]. The nuclear energy loss is then given by

$$-\frac{dE}{dx} = N \int_0^{T_{max}} T\, d\sigma \equiv N\, S\,(E) \tag{1.4}$$

where T_{max} is the maximum possible energy transfer per collision and $d\sigma$ is the differential cross section. The differential cross section, $d\sigma$, is the ratio of the number of scattered particles per unit time per unit scatterer, to the flux of incident particles with respect to the target which has units of area.

As the ions are stopped they are also deflected and can dislodge target nuclei from their original sites on the lattice, thus resulting in physical damage to the crystal. This damage can be in the form of point and line defects. For high doses amorphization results. The displaced nuclei may have enough energy to displace other nuclei leading to a "cascade" of recoiled atoms. Eventually the cascade ends when the energy given up per collision by the recoiled atom is less than the binding energy of the lattice.

The next form of energy loss is the electronic one. Electronic stopping is inelastic, with the energy lost by the incident ion being dissipated through the electron cloud as thermal vibrations of the target. As the ion loses energy it interacts with bound and free electrons in the target and the generation of electron-hole pairs is possible. In the LSS theory, a semiclassical approach has been found to give reasonable estimates for the energy loss rate due to these processes. This theory assumes that if the ion velocity is less than the velocity of an electron having an energy equal to the Fermi energy, then the electronic stopping power (S_e) is proportional to the ion velocity [7]. Therefore

$$S_e(E) = k E^{1/2} \tag{1.5}$$

where k is dependent upon the ion and target properties. The constant k is chosen to be consistent with the Thomas-Fermi picture [9] of the ion in the LSS theory and is a function of Z_i, Z_t, M_i, M_t, the atomic weights A_i and A_t of the two particles, and

the Thomas-Fermi screening radius a [7,9]:

$$k = Z_i^{1/6} \frac{0.0793\, Z_i^{1/2} Z_t^{1/2} (A_i + A_t)^{3/2}}{\left(Z_i^{2/3} + Z_t^{2/3}\right)^{3/4} A_i^{3/2} A_t^{3/2}} \frac{4\pi a^2 M_i M_t}{(M_i + M_t)^2}$$

$$\cdot \left(\frac{q^2}{a} \frac{Z_i Z_t \left(M_i + M_t\right)}{M_t}\right)^{1/2} \tag{1.6}$$

where q is the charge magnitude of a single electron. For silicon k is approximately 0.2×10^{-15} $(eV)^{1/2}$ cm^2.

Electronic stopping increases linearly with velocity over a wide range of energies (exceeding those encountered in typical ion implantation {> 300 keV}). At a very high energy (approximately 2×10^5 keV for arsenic in silicon [10]) $\left(\frac{dE}{dx}\right)_e$ passes through a maximum, and then falls off as E^{-1}. This is known as the " Bethe formula" region where the ion velocity exceeds that of the orbital electrons and hence moves as a fully ionized atom [10]. This energy range is far beyond the range of interest for most implants.

From the above equations, we see that the relative importance of nuclear and electronic stopping depends upon the energy and mass of the implanted ion, and the mass and atomic density of the solid target. Figure 1-2 shows the form of the nuclear and electronic stopping powers of arsenic in silicon as a function of ion energy. An important point to note is that for the heavier elements (such as arsenic) in silicon, nuclear stopping is the predominant mode of energy loss in the range of energies typically used for implantation (10 to 200 keV). The maximum energy loss by this mechanism occurs at 73 keV [10] and is designated as E_1 in Fig. 1-2. E_2 is the point at which the nuclear and electronic stopping powers are equal. This occurs at an

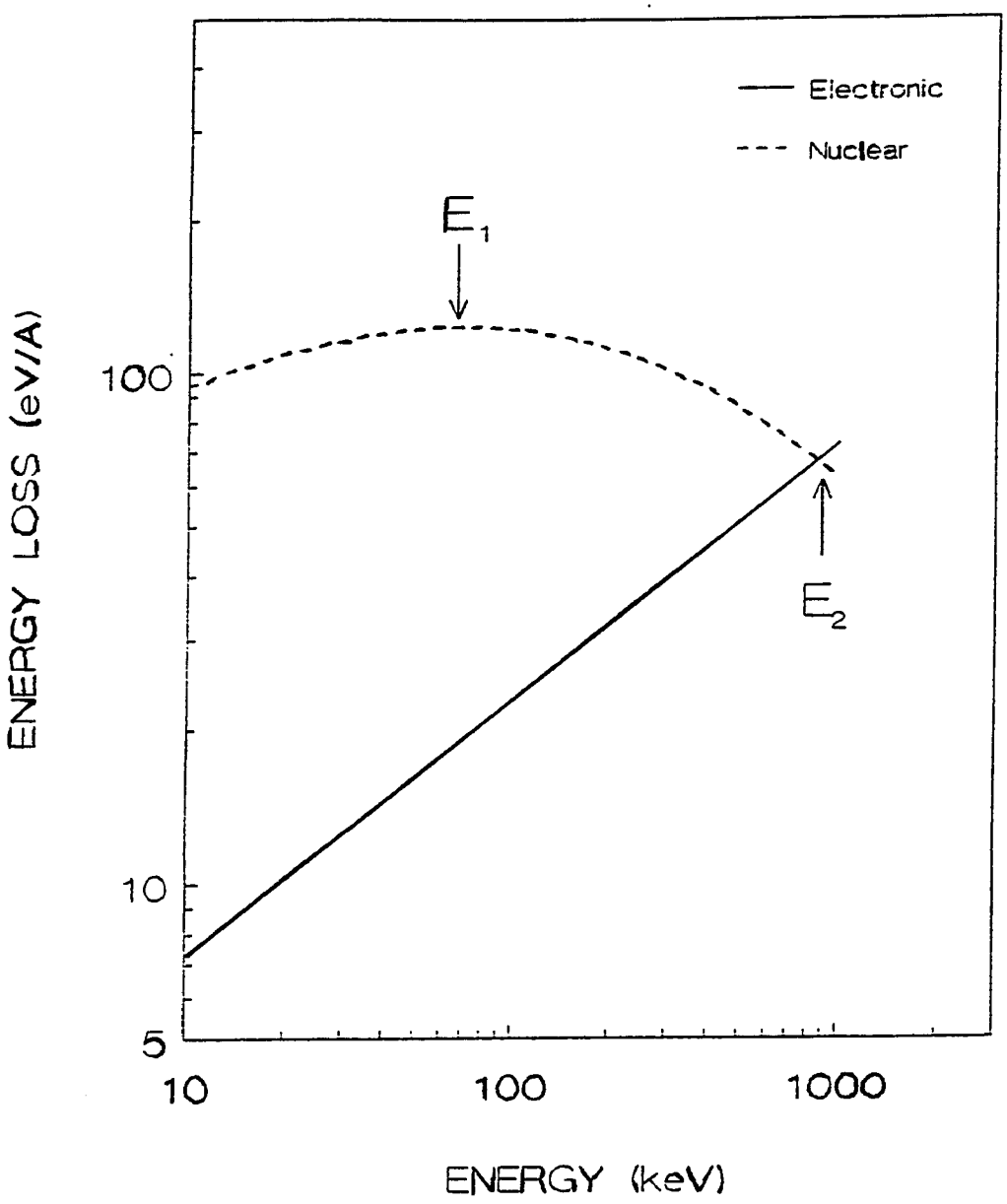

Figure 1-2. Energy loss due to nuclear (- - -) and electronic (—) stopping of arsenic in silicon. The maximum energy loss due to nuclear stopping occurs at ion energy E_1 (73 keV). E_2 (800 keV) is the ion energy where nuclear and electronic stopping are equal in value. Data for these curves was calculated by TRIM-89 [6].

enegry of 800 keV [10] for arsenic in silicon; an energy well beyond most technologically interesting implantations.

Integrating the stopping power to sum the energy losses determines how far an ion will travel in the substrate. The total distance traveled by the ion before coming to rest is known as the range R:

$$R = \frac{1}{N} \int_0^{E_i} \frac{dE}{S_n(E) + S_e(E)} \tag{1.7}$$

Because of the statistical nature of the implantation process, the range is characterized by its mean value and its standard deviation along the direction of the incident ion. The mean value and the standard deviation are usually referred to as the projected range, R_p, and the straggle, ΔR_p. A typical ion trajectory will also be displaced in the direction perpendicular to the incident ion direction. The value characterizing this motion is the lateral straggle $\Delta R_\perp$. Figure 1-3 is a schematic of a typical ion trajectory which defines these parameters. Values for these parameters have been calculated using TRIM-89 [6] and are shown in Figure 1-4 for the energy range of interest in ion implantation.

As discussed above, all ions of a given type and initial energy will not have the same range since the number of collisions and the energy transferred are random variables. For an amorphous target, the final distribution of the implanted ions can be described by a one-dimensional Gaussian distribution given by

$$N(x) = \frac{\Phi}{\sqrt{2\pi}\,\Delta R_p} \exp\left[-\frac{1}{2}\left(\frac{x - R_p}{\Delta R_p}\right)^2\right] \tag{1.8}$$

where Φ is the implantation fluence (or dose) in ions/cm^2. A lateral Gaussian

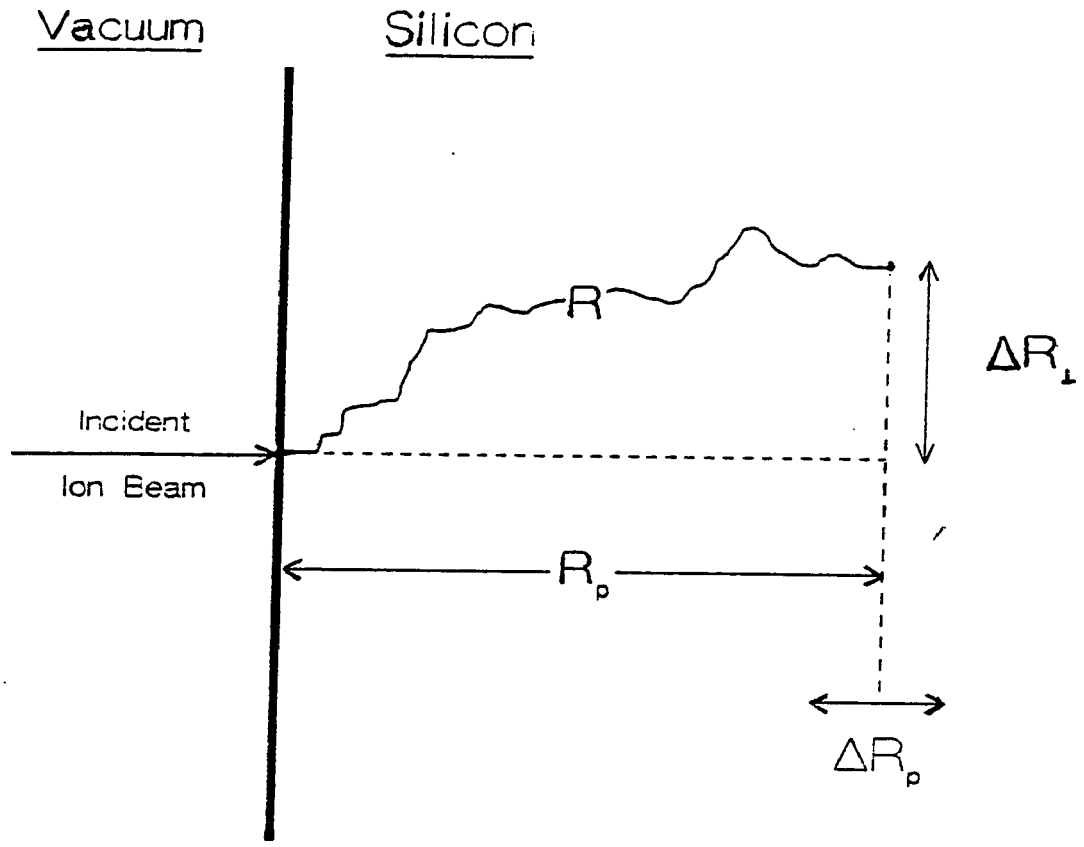

Figure 1-3. A single ion trajectory showing the range, R, projected range, R_p, straggle ΔR_p, and lateral straggle $\Delta R_\perp$.

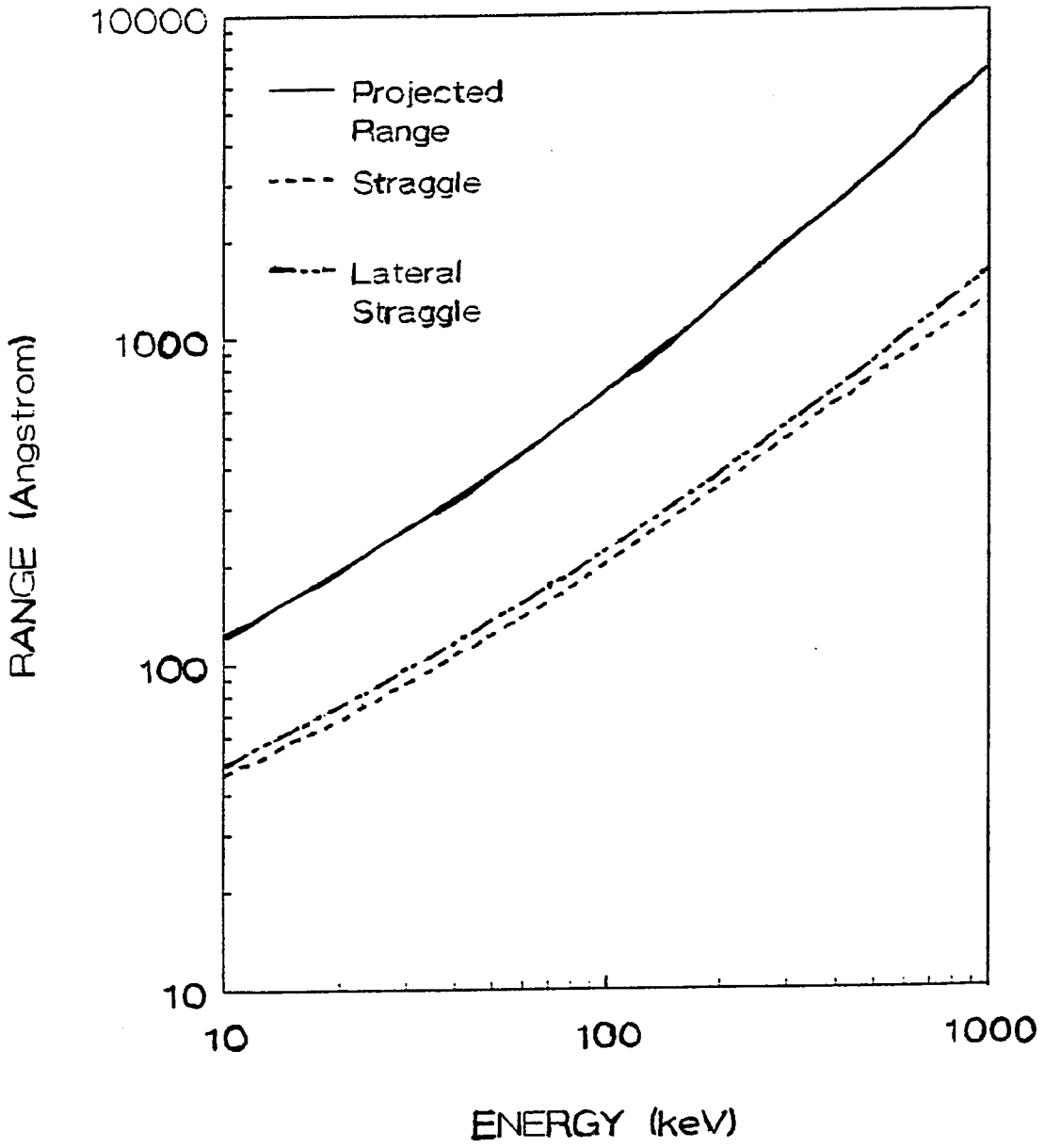

Figure 1-4. Monte Carlo calculations of the projected range, straggle, and lateral straggle of arsenic in silicon.

distribution can be multiplied to equation 1.8 to give a two-dimensional distribution. Since implantations in this dissertation were not done into defined areas, the two-dimensional distribution will not be a subject of our investigation.

The fluence or dose of ions, Φ, is determined experimentally by using the relationship

$$\Phi = \frac{Q}{q\,A} \quad \left[\text{ions/cm}^2\right] \tag{1.9}$$

where q is the total charge of the ion, A is the implanted surface area, and Q is the total integrated charge deposited into the substrate. Q is determined by measuring the beam current and is given by

$$Q = \int_0^t I \; dt \tag{1.10}$$

where t is the time for carrying out the implant. The wafer holder collects the beam current. This current is integrated by a current integrator in the implanter and thus the dose is determined.

For a single crystal target the implanted distribution depends upon the orientation of the crystal with respect to the ion beam, the surface condition of the crystal, and the substrate's processing history. The range distributions in single-crystal and amorphous targets are different primarily because of channeling. Channeling occurs when the incident ion beam is aligned to a major crystallographic axis or plane. Ions are steered for a considerable distance through the lattice with little energy loss. This results in an increased penetration depth (sometimes referred to as the channel tail) and reduced lattice disorder. To reduce this effect, most implantations are done at 7° from a major crystal orientation. At this angle the crystal appears to be almost amorphous. This can be seen in Fig. 1-5 where the

silicon lattice is viewed along the <100> direction and 7° from this direction.

The formation of a tail as the ions penetrate deeper into the solid is a result of channeling. Thus the implanted profile cannot be described as a pure Gaussian distribution. Sometimes better agreement is obtained by using a joined half-Gaussian distribution [11] or by taking into account higher order moments of the straggle [8]. These moments are known as skewness (second order) and kurtosis (third order), which affect the symmetry and tail shape of the distribution, respectively. An example of this is the Pearson IV distribution from statistics [12] used for boron. When the target has been damaged enough to be rendered amorphous, the profile is typically Gaussian and the channel tail is not observed.

1.1.2. Ion Implantation Damage

When an ion enters a solid, it is slowed by interactions with the lattice atoms. Sufficient energy may be transferred from the ion to displace an atom from its lattice site. Only nuclear collisions are responsible for the creation of lattice damage. The amount of damage is dependent upon the ion species, energy, and dose, and the substrate composition, temperature, and orientation to the ion beam. As can be seen in Fig. 1-2, for the energies typically used for implanting arsenic into silicon, nuclear stopping is the primary source of energy loss. In general, the concentration of defects increases with ion mass. Therefore, a great deal of damage is created when a massive ion such as arsenic is implanted into silicon.

Seidel [8] has estimated the amount of time required for an ion to come to rest and for the lattice to come back to equilibrium. By dividing the ion range by its

(a)

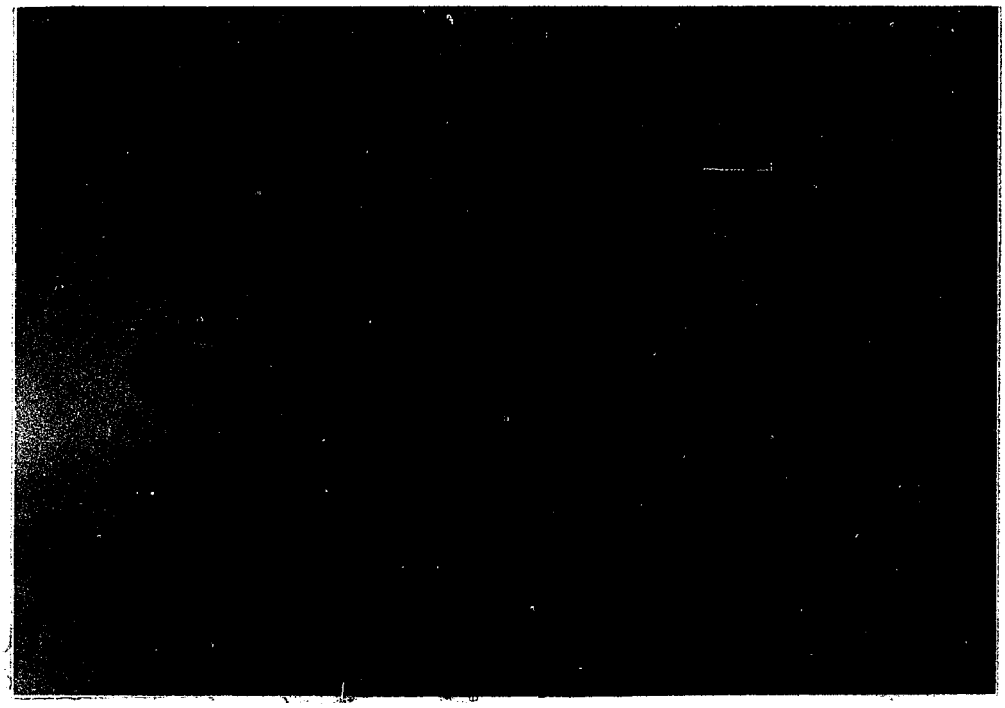

(b)

Figure 1-5. Model of the diamond lattice viewed along the (a) <100> direction and (b) 7° from the <100> direction.

velocity, the time for a typical ion to come to rest is approximately 10^{-13} seconds. In approximately 10^{-12} seconds thermal vibrations return to their equilibrium value. Many of the vacancies and interstitials created along the ion trajectory are estimated to recombine in approximately 10^{-9} seconds.

As an energetic ion enters the target the physical structure of the substrate changes near the ion trajectory. Close to the ion trajectory vacancy clusters are formed and interstitial clusters form around these. Wilson et al. [13] have found that the surface actually collapses to fill in the vacancies, forming a crater. The crater periphery is raised due to the extra planes of substrate atoms caused by the interstitial clusters. Recoiled substrate atoms produce side branches of damage to the ion trajectory.

The volume containing the ion trajectory and its branches is customarily called the "damage cluster" (see Fig. 1-1). This volume is dependent upon the mass and energy of the incident ion, the mass of the target atoms, and the target temperature [14]. No two ions will have exactly the same damage cluster shape due to the statistical nature of ion implantation. For heavy ions, such as arsenic, a single ion can create a defect cluster with a defect density so high that a spontaneous crystalline-to-amorphous transition occurs over most of the cluster. Many different defects are associated with the implantation process. These include vacancy-interstitial pairs (Frenkel defects), several charge states of vacancies, interstitials, vacancy-impurity pairs, divacancies, dislocation lines and loops, and vacancy and interstitial platelets [14].

As the implant fluence increases, the defect clusters overlap and eventually lead to a noncrystalline region with no long range order. This region is commonly referred to

as being amorphous. There is no single dose where an implanted surface layer transforms into a homogeneous amorphous layer. A series of gradual changes occur as the fluence is increased (see Fig. 1-6). Initially small pockets of isolated amorphous material are formed. A continuous layer of amorphous material is formed at the threshold fluence. For arsenic in silicon the threshold is 2.6 X 10^{13} ions cm^{-2} for the energy range typically used in implantation [15]. The buried amorphous layer continues to grow with increasing ion fluence. At a dose of 3 X 10^{14} As cm^{-2} the amorphous layer reaches the surface. Increasing the implantation dose continues to drive the lower amorphous/crystalline interface deeper into the silicon. Table 1-1 gives the fluence values for the formation of a continuous amorphous layer for the common implanted dopants in silicon.

Table 1-1. Fluence values at room temperature of the common dopants in silicon needed to create a continuous amorphous layer.

Element	*Amorphization Dose* [8,15] *(ions/cm^2)*
Arsenic	3×10^{14}
Antimony	1×10^{14}
Boron	$\gtrsim 2 \times 10^{16}$
Phosphorous	5×10^{14}

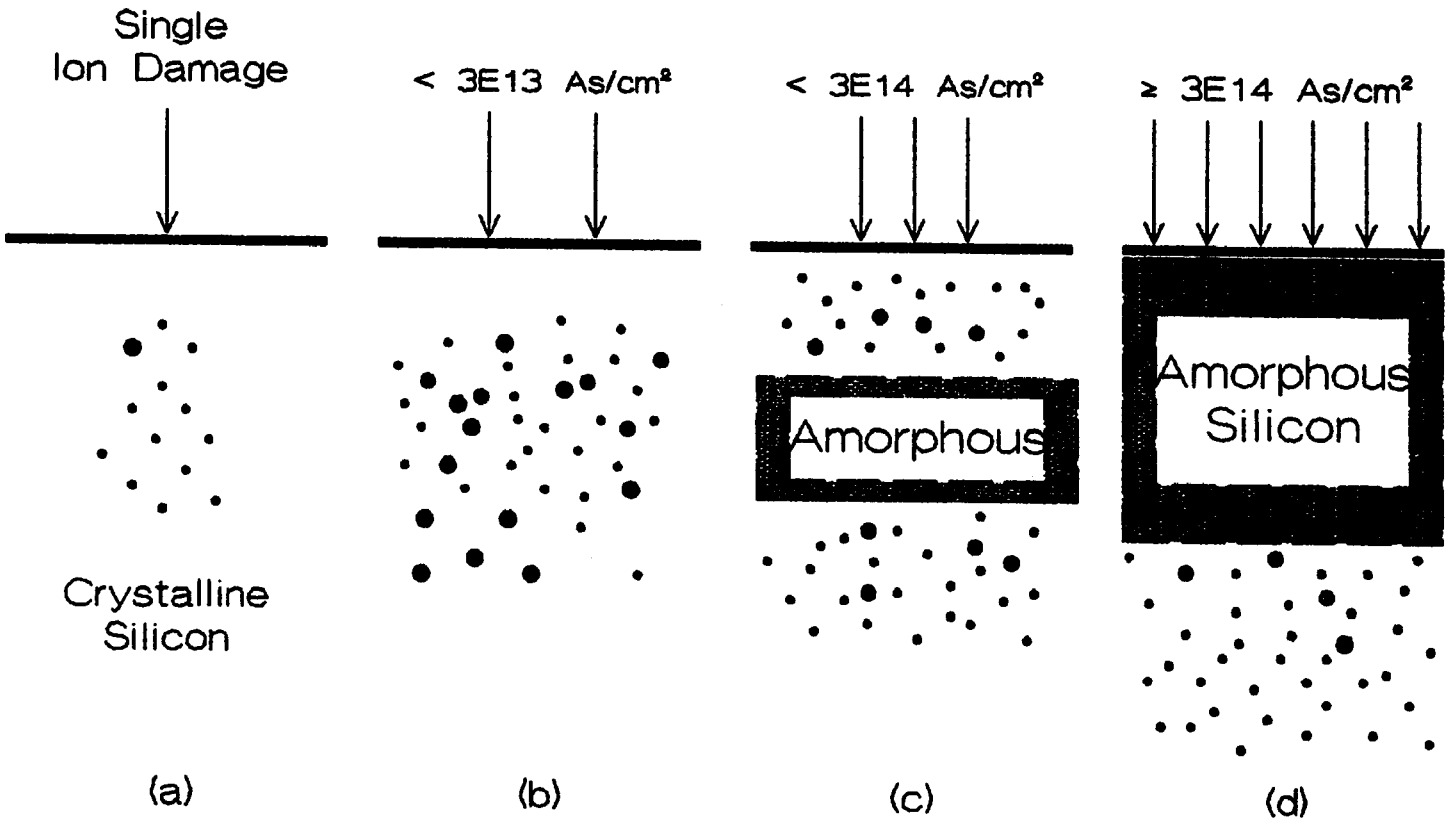

Figure 1-6. Schematic representation of how implantation damage builds up as a function of dose for 100 keV arsenic implanted into silicon. (a) Single ion damage, (b) Low dose damage, (c) A buried amorphous layer is formed, (d) Amorphous layer continues to grow until upper boundary reaches the silicon surface. Increasing the amount of arsenic continues the movement of the deeper amorphous/crystalline boundary. Doses were determined by Prussin et al. [15].

The atoms of a crystalline solid are bound to their lattice with a certain energy. When an ion collides with the atoms of the target, damage will only be produced when the energy transferred to a target atom exceeds its displacement threshold energy E_d. For silicon E_d is approximately 14eV [16]. Collisions with a transfer energy T greater than E_d will displace the atom from its lattice site and produce damage within the solid. The displaced atom will be a secondary projectile of energy $(T - E_d)$ and further displacements may occur. Thus, the doping characteristics of the implanted ions will be masked by the implantation-produced damage and the fact that most of the implanted ions occupy nonsubstitutional (electrically inactive) lattice sites.

Various methods [14,17-20] have been used to calculate the amount of damage created by an implanted ion. Inherent to all of these methods is a core set of assumptions. Channeling is usually neglected and collisions are treated as isolated two-body elastic scattering events. The form of the interaction potential does not play a major role in the calculation of the number of displaced atoms. When the energy transferred to the target atom T is less than the displacement energy E_d, the target atom is excited and no displacement occurs. A simple displacement occurs for the condition $2E_d > T \gtrsim E_d$. Under this condition the displaced atom does not have enough energy to produce a cascade. When $T \gtrsim 2E_d$ the initial displacement is followed by some secondary lattice disorder produced by energetic substrate atoms. Large amounts of disorder due to secondary displacements and cascading effects occur when $T \gg E_d$.

1.1.2.1 Kinchin and Pease Calculations of Damage

Kinchin and Pease [17] obtained one of the first estimates of the number of atoms displaced by an ion as it comes to rest. Along with the assumptions mentioned above they assumed that atoms are displaced by a Coulombic interaction between the nuclei and the effect of the screening electrons is to cut off this interaction at a radius of about $a_0/Z^{1/3}$ where a_0 is the Bohr radius and Z is the target atomic number. Using these approximations they determine that the number of target atoms displaced by a primary recoil is

$$N_d = \frac{E}{2E_d} \tag{1.11}$$

where E is the energy of the primary recoil. Equation (1.11) is valid when the ion energy is greater than $2E_d$. Note that this treatment neglects to consider any crystal lattice effects.

In many cases equation (1.11) overestimates the number of displaced target atoms. Sigmund [18] examined the validity of the Kinchin-Pease formula. In this treatment the elastic collision and hard-sphere scattering assumptions of Kinchin and Pease [17] were dropped and lattice effects were neglected. The amount of energy not lost to electronic excitation was included. Also included in this treatment was the assumption that the displacement energy depended upon the binding energy of the solid and the number of bonds to be broken to displace a target atom. If E_b is the bond energy then E_d is $4E_b$ in silicon. With these modifications the number of displaced target atoms becomes

$$N_d = 0.42\left(\frac{E}{E_d}\right) \tag{1.12}$$

Norgett et al. [21] modified the Kinchin-Pease model to more closely predict

(compared to timely computer simulations of radiation damage) the number of displaced atoms produced by a primary knock-on atom of known energy. Their formulation predicts the number of Frenkel pairs generated by a primary knock-on of initial kinetic energy E to be

$$N_d = \kappa \frac{\hat{E}}{2E_d} \tag{1.13}$$

where $\hat{E}$ is the energy available to generate atomic displacements by elastic collisions. This energy is given

$$\hat{E} = \frac{E}{[1 + kg(\epsilon)]} \tag{1.14}$$

where

$$g(\epsilon) = 3.4088\ \epsilon^{1/6} + 0.40244\ \epsilon^{3/4} + \epsilon \tag{1.15}$$

$$k = 0.1337\ Z_i^{1/6} \left(\frac{Z_i}{A_i} \right)^{1/2} \tag{1.16}$$

$$\epsilon = \left(\frac{A_t E}{A_i + A_t} \right) \left(\frac{a}{Z_i\ Z_t\ q^2} \right) \tag{1.17}$$

and

$$a = \left(\frac{9\pi^2}{128} \right)^{1/3} a_0 \left[Z_i^{2/3} + Z_t^{2/3} \right]^{-1/2} \tag{1.18}$$

The variables in these equations are the atomic numbers Z_i and Z_t and the mass numbers A_i and A_t of the projectile and target, respectively. The electronic charge is q and a_0 is the Bohr radius. The displacement efficiency κ is set to 0.8. Norgett et al. [21] do not give a reason for this assignment. This formulation is used by TRIM-89 [6] to give a quick calculation of the damage created by an ion. It should be noted that TRIM-89 can be also used to do a calculation of the trajectory of each displaced

silicon atom. This calculation requires significant computer time. Calculations by both methods will be discussed later in section 1.1.2.3.

1.1.2.2 Brice Method: Energy Deposition Distribution

Another way of ascertaining the amount of damage in an implanted substrate is by determining the depth distribution of energy deposited by an ion. Brice [19,20] has derived a direct method for obtaining the energy deposition distribution. This method accounts for multiple scattering of the ion beam and the partitioning of the energy of the recoiling target atoms. Therefore, energy is transported in the substrate by the recoiling target atoms. The depth distribution of energy deposited into atomic processes (i.e., damage) is determined to be [19,20]

$$Q_D(E,x) = \int_0^E S\,(E, E', x)\,\Sigma\,(E')\left(\frac{d\,R}{dE'}\right) dE' \tag{1.19}$$

where

$$S(E, E', x') = \int_{-\infty}^{\infty} P(E, E', x)\,D\,(E', x' - x)\,dx \tag{1.20}$$

In these equations $P(E, E', x)$ is the depth distribution of ions when their energy has been reduced from incident energy E, to E' and $S(E, E', x')$ is the relative depth distribution of damage energy for a distribution of ions $P(E, E', x)$ having energy E'. The rate an ion transfers damage into the lattice is

$$\Sigma(E') = N \int q\,(T)\,d\sigma\,(E', T) \tag{1.20}$$

where N is the atomic density of the target, T is the kinetic energy transferred to the recoiling target atom, and q(T) is the portion of T which will be deposited into atomic processes conventionally referred to as the damage energy of the recoiling target atom. The differential atomic cross-section for transfer of kinetic energy T in

the interval (T, T+ dT) to a recoiling target atom by an ion of energy E' is $d\sigma(E',T)$. $D(E', x' - x)$ is the final normalized distribution in depth, x', of the energy initially deposited at x and $d\bar{R}$ is the average distance traveled by an ion of E' in losing energy dE'. Brice [19] indicates that this method is most likely in error at low energies where the ion-target atom interaction is dominated by elastic collisions and the shape of the damage distribution becomes independent of ion energy. Seidel [8] approximates the density of displaced silicon by $\Phi\, Q_D/E_d$ where Φ is the implant fluence.

The fluence values given in Fig. 1-6 were determined by Prussin et al. [15] using the energy deposition tables calculated by Brice [20]. To determine these fluence values a total deposited damage energy was first calculated by

$$E_D(E) = \int_{-\infty}^{\infty} Q_D(E, x)\, dx \tag{1.21}$$

where $Q_D(E, x)$ is defined in equation (1.19). Measured positions of amorphous/ crystalline interfaces are compared to calculated damage density distributions and a threshold damage density is extracted which corresponds to the transition from crystallinity to amorphization. Using this procedure the threshold damage density for arsenic implanted into silicon was found to be 2.5×10^{20} keV/cm^3 [15]. An amorphous layer will form to a depth where the damage density drops below this threshold value. Since the heat of fusion of silicon is approximately 0.7×10^{20} keV/cm^3 [14], this threshold damage density value suggests that a phenomenon similar to melting occurs in the formation of an amorphous layer.

1.1.2.3 TRIM-89 Simulation: Resultant Profile and Damage

With the use of the Monte-Carlo simulation TRIM-89 [6] the damage created by ion implanting 100 keV arsenic into silicon was determined. These calculations were performed on a NEC 386 microcomputer with an Intel 80387 math co-processor. The shapes of the distributions of total target vacancies, silicon net displacement collisions, and replacement collisions were found to be approximately the same. Peak values for these curves were 1.75 vacancies/ion/Å, 2.15 silicon net displacements/ion/Å, and 0.4 replacements/ion/Å. These numbers were obtained by calculating the ion trajectory and each recoil trajectory. When a modified Kinchin-Pease calculation (similar to that of Norgett et al. [21]) was performed, 2.25 vacancies/ion/Å were predicted which overestimates the amount of damage determined above.

For heavy ions, such as arsenic, the peak in the damage distribution is closer to the surface than the ion distribution peak. This is depicted in Fig. 1-7. Here the ion travels mostly in its original direction and the energy loss per unit distance is large. Figure 1-8 shows the energy loss due to nuclear collisions. Note that the maximum value of total ion energy loss to recoils is approximately 120 eV/Å and extends over the first 400 Å. As a result of this energy loss, an arsenic ion will lose approximately 300 eV for each silicon atomic plane it passes. Most of this energy is transferred to a single lattice atom. Therefore the displaced silicon atom of energy $\sim$ 286 eV ($\sim$ 300 eV $-$ 14 eV) produces approximately 20 displaced lattice atoms. This is a great deal of damage. Calculations using TRIM-89 show that 1792 vacancies are created by a single arsenic ion on the average.

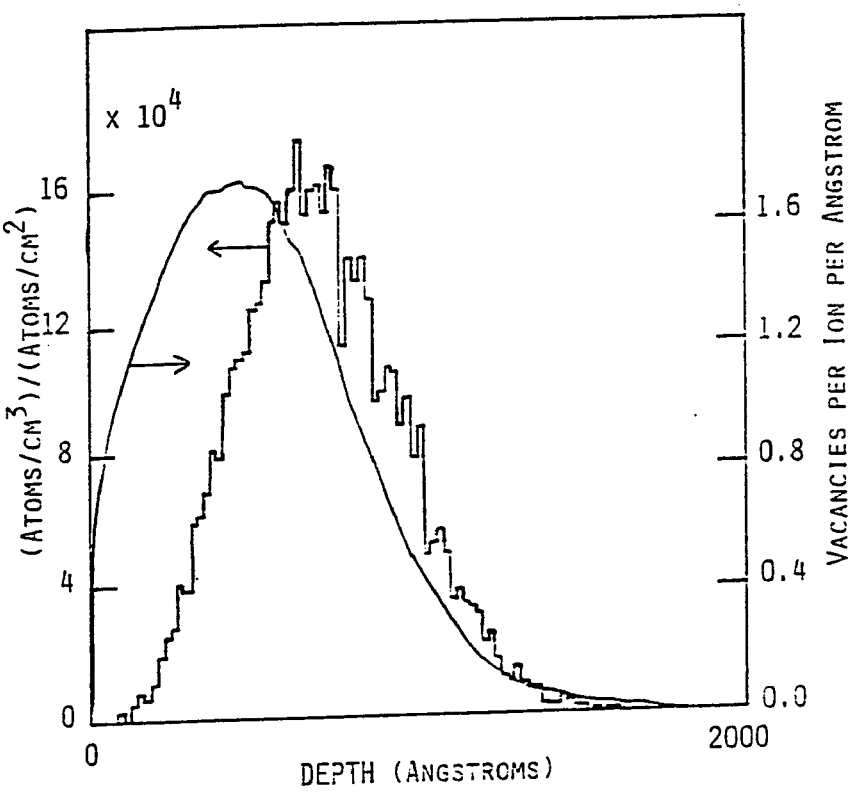

Figure 1-7. A comparison of the range distribution (histogram) and the damage distribution (solid line) for 100 keV arsenic in silicon. Note that the damage distribution peak depth is less than the projected range of the arsenic distribution. Five thousand trajectories were used in calculating these profiles by TRIM-89 [6].

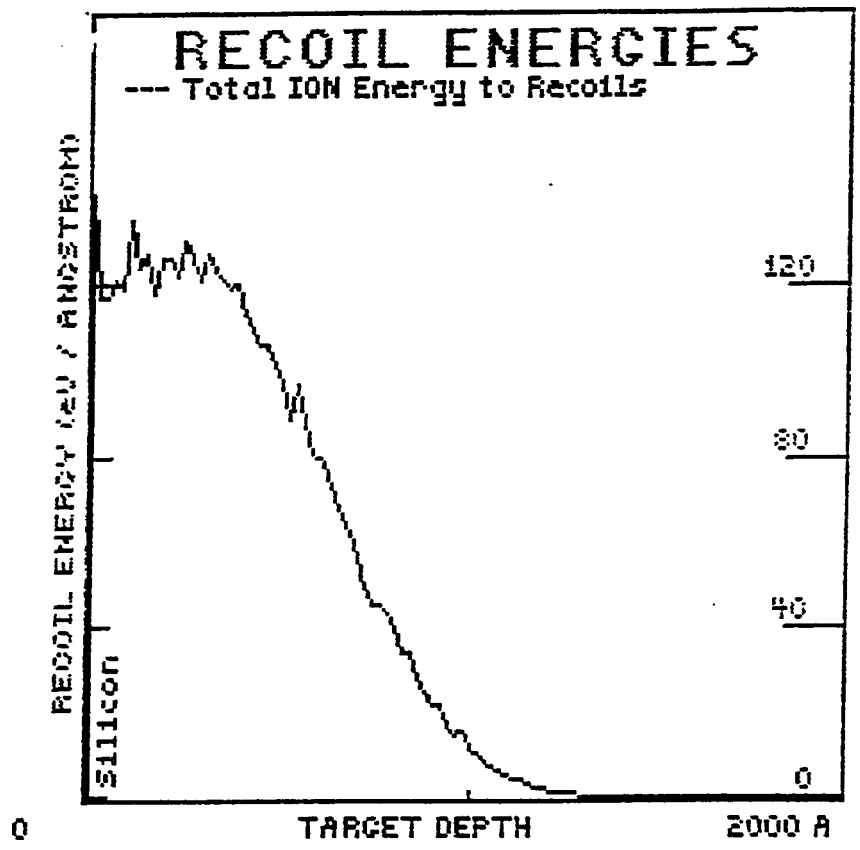

Figure 1-8. The distribution of energy given up in displacing a silicon atom by a 100 keV arsenic ion. This profile was calculated by TRIM-89 using 5000 trajectories.

1.2 Thermal Treatment of Implanted Silicon

In the previous sections it was shown that ion implantation creates substantial damage, thus degrading many properties related to device quality. Complete recovery of carrier activation, mobility, and minority carrier lifetime would occur if the damaged lattice could be returned to its original, single-crystal state. In practice, this can only be achieved by melting or epitaxial growth. Many methods exist to thermally treat implanted samples to anneal the damage and activate the implanted dopant. This section will review two of these methods (furnace annealing and rapid thermal annealing by incoherent radiation).

1.2.1 Furnace Annealing

The first method used to anneal implantation damage was furnace annealing. Here the implanted wafer is moved from room temperature into a furnace that is capable of maintaining a constant preset temperature. Heating is by convection. Most furnaces are designed to maintain the preset temperature within a few degrees Celsius after a warm-up period. The furnace used in this study is a Mini-Brute laboratory diffusion furnace, model MB-71 by Thermco Systems, Inc. The temperature remains stable within $\pm \frac{1}{4}$ °C according to the manufacturer.

Furnace annealing studies form the foundation of all of the annealing studies done on implanted silicon. The annealing characteristics depend on the dopant type [22,23] and the dose [22]. Csepregi et al. [22] have found that amorphous layers regrow by solid phase epitaxy (SPE). The amorphous/crystalline (a/c) interface moves toward the surface at a fixed velocity which is dependent upon annealing temperature, crystal orientation, and doping [23]. In <100> silicon it was found that the activation energy for SPE was approximately 2.35 eV for arsenic and phosphorous and 1.9 eV

for boron [22]. Impurities (such as arsenic, phosphorous, and boron) increase the growth rate, which is presumably due to substitutional impurities weakening bonds and increasing the likelihood of broken bonds [22].

There is a definite difference in annealing characteristics of silicon that has been made amorphous or partially disordered. When no amorphous layer exists the generation and diffusion of point defects repair the lattice damage. This occurs with an activation energy of approximately 5 eV [24]. Annealing a buried amorphous layer is more complex. Epitaxial annealing occurs at both interfaces and lattice mismatch can occur when the interfaces meet [8].

1.2.2 Rapid Thermal Annealing

Rapid thermal annealing (RTA) is the name given to many different techniques including beam annealing (by electrons, ions, and lasers) and incoherent light annealing (by flash lamps [25], graphite strip heaters [26,27,28], and tungsten-halogen or xenon lamps [29,30]). Typical anneal times range from fractions of a second to several hundred seconds. The lower time limit for furnace annealing is approximately 15 minutes since the wafer must be inserted and removed from the furnace without thermal stressing. Thus, RTA is more 'rapid' than furnace annealing.

RTA presents several advantages over conventional furnace annealing. At sufficiently high temperatures implantation damage is repaired much faster than the implanted species can diffuse. Thus, shallower junctions with dopant profiles similar to the implanted profile are possible. The process is 'cleaner' than furnace annealing since the walls of the anneal chamber remain cold. The major disadvantage of this process is the accuracy to which the wafer temperature can be measured [31,32]. This will be discussed below.

In this work, a Heatpulse 210M rapid thermal annealer manufactured by AG Associates was used. A schematic of the annealing chamber is shown in Fig. 1-9. Heating is accomplished by the use of tungsten-halogen lamps. The chamber walls are water cooled. Since the lamps are enclosed in a reflecting cavity, optical pyrometry is not possible. In the 210M, a thermocouple provides the only way to measure temperature. A SensArray series 1501A-3-0001 instrumented wafer was used as both the sample holder and temperature measuring device. Fig. 1-10 shows a cross-sectional view of this wafer where the thermocouple is bonded into the wafer surface. A type K (Chromel-Alumel) thermocouple was used. High temperature ceramic cement composed of 40% Al_2O_3 and 60% SiO_2 encapsulates the thermocouple junction and thermally bonds it to the silicon substrate. The coefficient of thermal expansion of the cement matches that of silicon over the operating temperature range of the 210M (200-1100 °C). This ensures that thermal contact is maintained within this range.

The silicon wafer is heated by the incoherent radiation produced by the tungsten-halogen lamps. These lamps yield a blackbody-like spectrum. Typical wafer temperature profiles are shown in Fig. 1-11.

Many absorption processes play a role in the heating of the wafer. These include free carrier absorption [31], interband processes, transitions between impurities and bonds, and coupling of lattice phonons to the incident photons [32]. All of these processes are wavelength dependent. A model has been developed [31,32,33] which assumes that the incident radiation is absorbed in a first pass into the wafer (i.e., multiple reflections are neglected). In this model, the temperature of

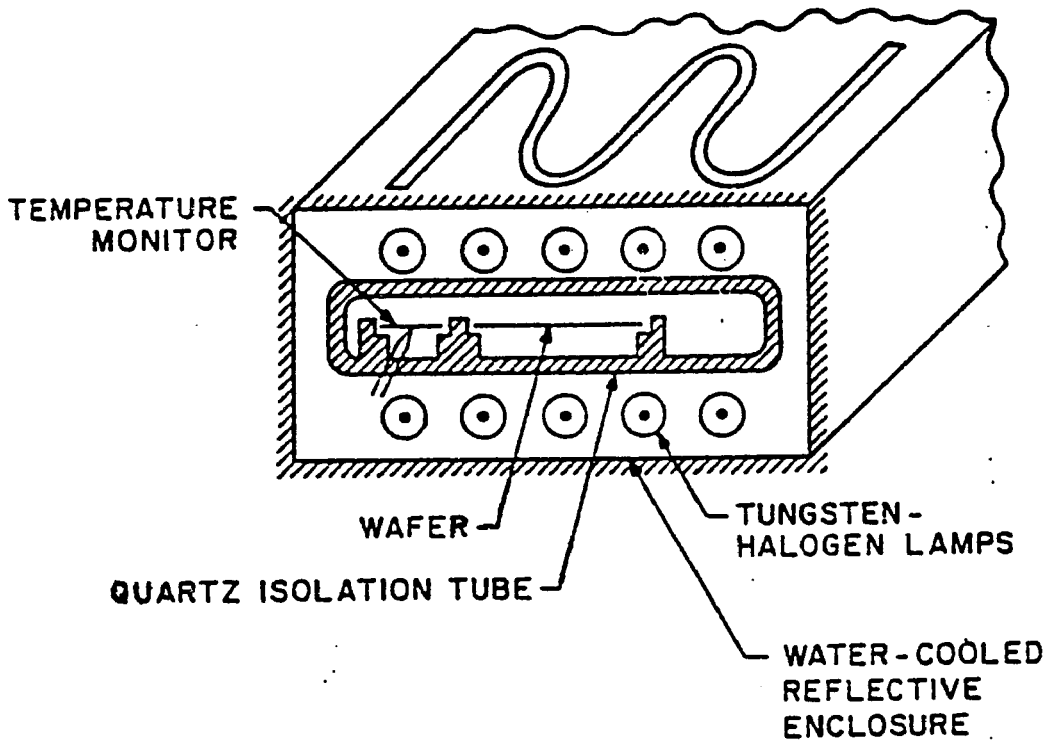

Figure 1-9. Schematic diagram of the Heatpulse 210M rapid thermal annealer. {From [8] (2nd edition)}

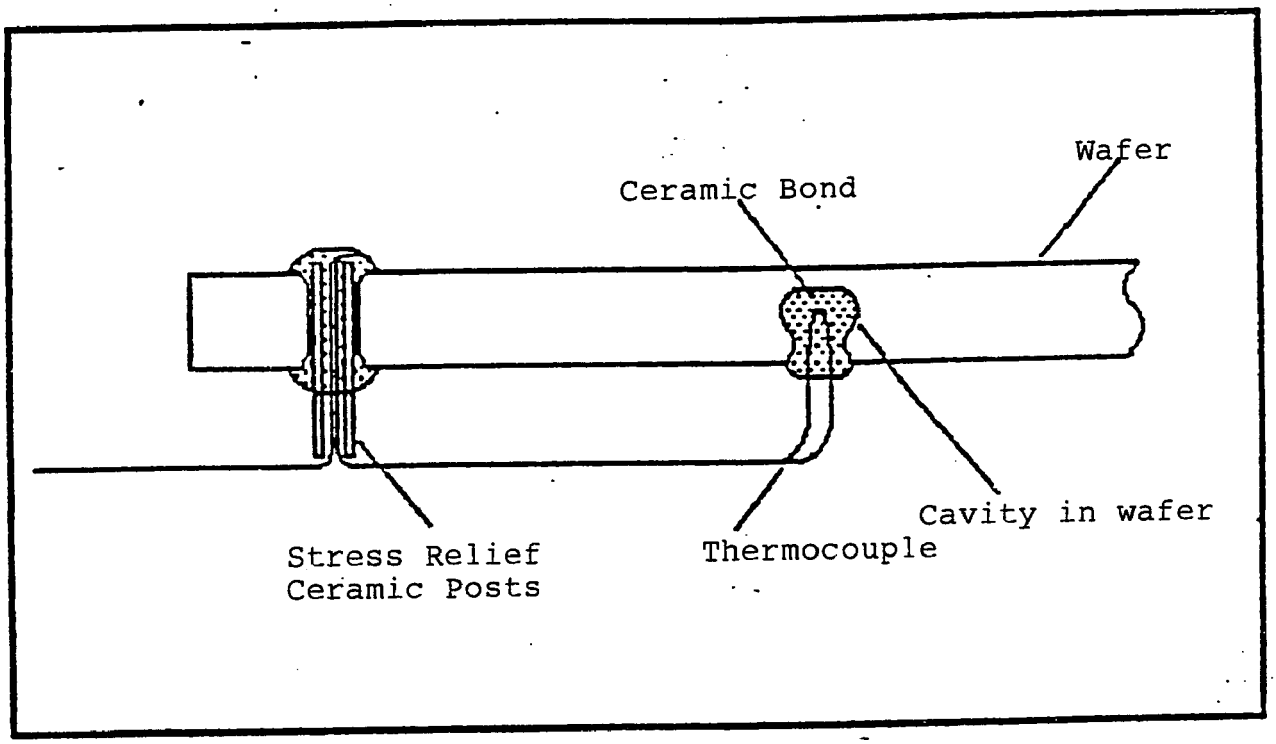

Figure 1-10. A cross sectional view of the SensArray series 1501A-3-0001 instrumental wafer.

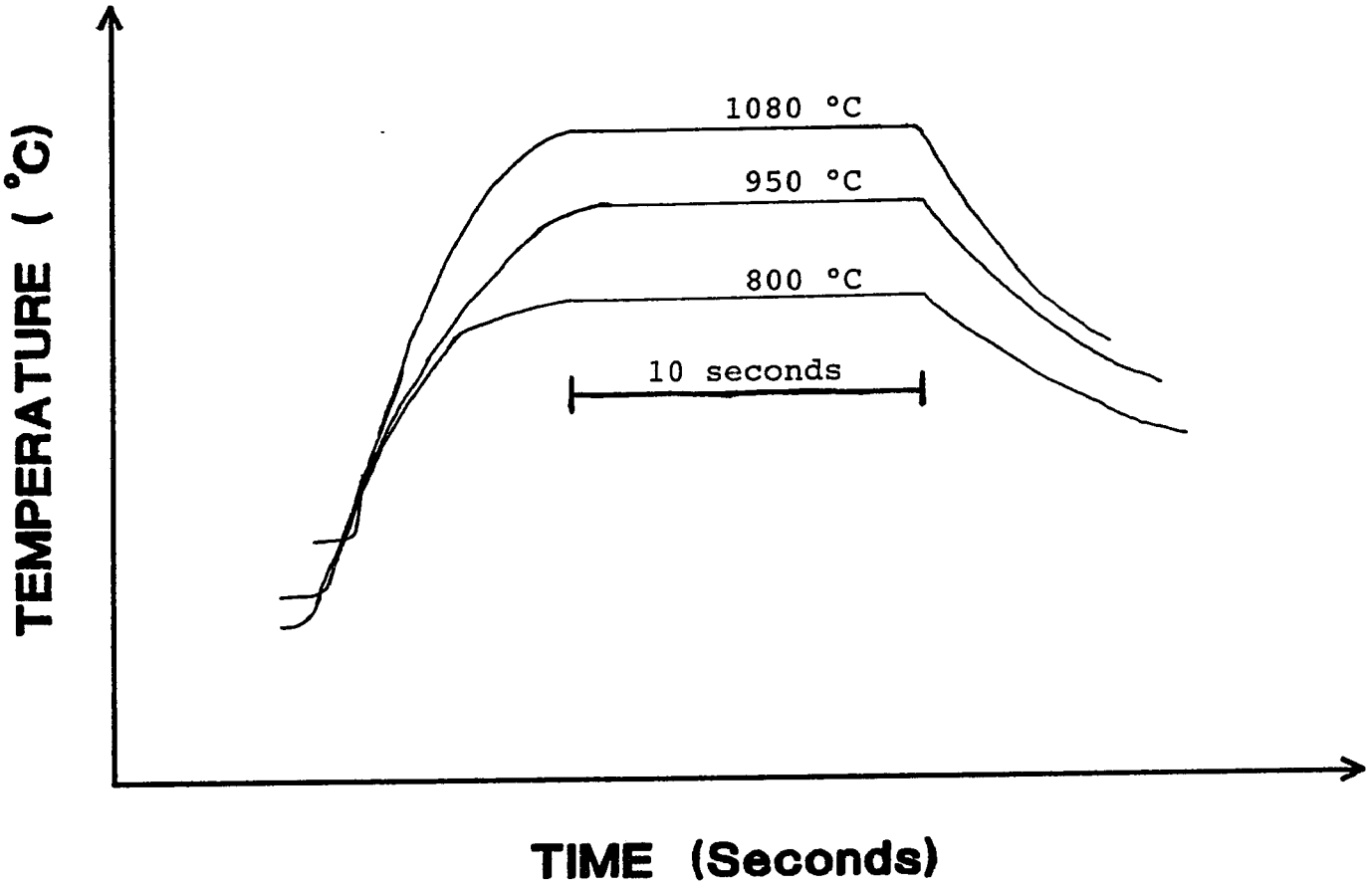

Figure 1-11. Thermocouple output voltage (temperature) versus time for various 10 second anneals.

the silicon wafer during power absorption is obtained by solving [33]:

$$C \frac{dT}{dt} = P_a - P_l \tag{1.22}$$

where C is the heat capacity per unit area, T is the temperature, t is the time, P_a is the instantaneous power absorbed, and P_l is the power lost by radiation or convection. The instantaneous power absorbed can be written as:

$$P_a = \int_0^{\lambda} I(\lambda) \left\{ 1 - R(\lambda,T) \right\} \left(1 - e^{-\alpha(\lambda,T)x} \right) d\lambda \tag{1.23}$$

where $I(\lambda)$ is the incident blackbody-like emission spectrum from the tungsten-halogen lamp, with a quartz window cutoff beyond 3.5 μm [33]. The reflectivity of the silicon is given by [34]

$$R(\lambda,T) = \frac{\left\{ n_r(\lambda,T) - 1 \right\}^2 + k(\lambda,T)^2}{\left\{ n_r(\lambda,T) + 1 \right\}^2 + k(\lambda,T)^2} \tag{1.24}$$

where $n_r(\lambda,T)$ is the index of refraction of silicon and $k(\lambda,T)$ is the wave vector. $\alpha(\lambda,T)$ is the spatially averaged absorption coefficient [32]. The term $\left\{1-R(\lambda,T)\right\} \times \left(1 - e^{-\alpha(\lambda,T)x}\right)$ is the power lost to the sample upon one pass through thickness x [33].

Along with the wavelength and temperature dependence of the absorbed power, Seidel, et al. [31,33] have experimentally shown a dependence on the doping level. It was also found that the heating rate was dependent upon the lamp intensity level [33]. In early RTA studies there was a controversy over the existence of a transient enhanced diffusion (TED) effect [31]. The effective diffusion rate during TED in the first few seconds of annealing was found to be much greater than usual for some dopants. This effect was due to wafer temperature uncertainty since the dopant level

effects were not included in some of these early experiments [31]. Discrepancies of this type for studies of arsenic in silicon will be discussed in a later section.

1.2.3 Annealing of Implanted Silicon

As discussed earlier, the annealing of implanted silicon has been the subject of a vast amount of research. Defects form in the silicon upon annealing and are related to the ion species and dose, the implant energy, the wafer temperature during implantation, and the annealing time and temperature. The most common types of defects formed include Frenkel pairs, point-defect clusters, and extended defects (such as extrinsic dislocation loops).

Prussin, Jones and coworkers have developed a classification scheme [35-42] for the secondary defects which arise or develop during annealing of implanted silicon. All secondary defects are grouped into five categories based on the origin of the implant damage. This scheme will form the foundation of this section. Figure 1-12 shows a schematic of the relationship between the effective threshold damage density and the damage density distribution. The curves are schematic and do not correspond to any particular species, dose, or energy. Also shown is the location of each category of defect. All of this work [35-42] was done at 900 °C for various anneal times.

Category I defects [35,42] are the result of annealing "subthreshold" damage (see Fig. 1-12a). Subthreshold damage occurs before there is sufficient damage to produce an amorphous layer. Transmission electron microscopy (TEM) studies have found elongated perfect dislocation loops centered near the projected range of the implant after annealing [35,42]. This study has also shown that there is a critical dose (or more specifically a critical peak concentration) which must be exceeded to form these

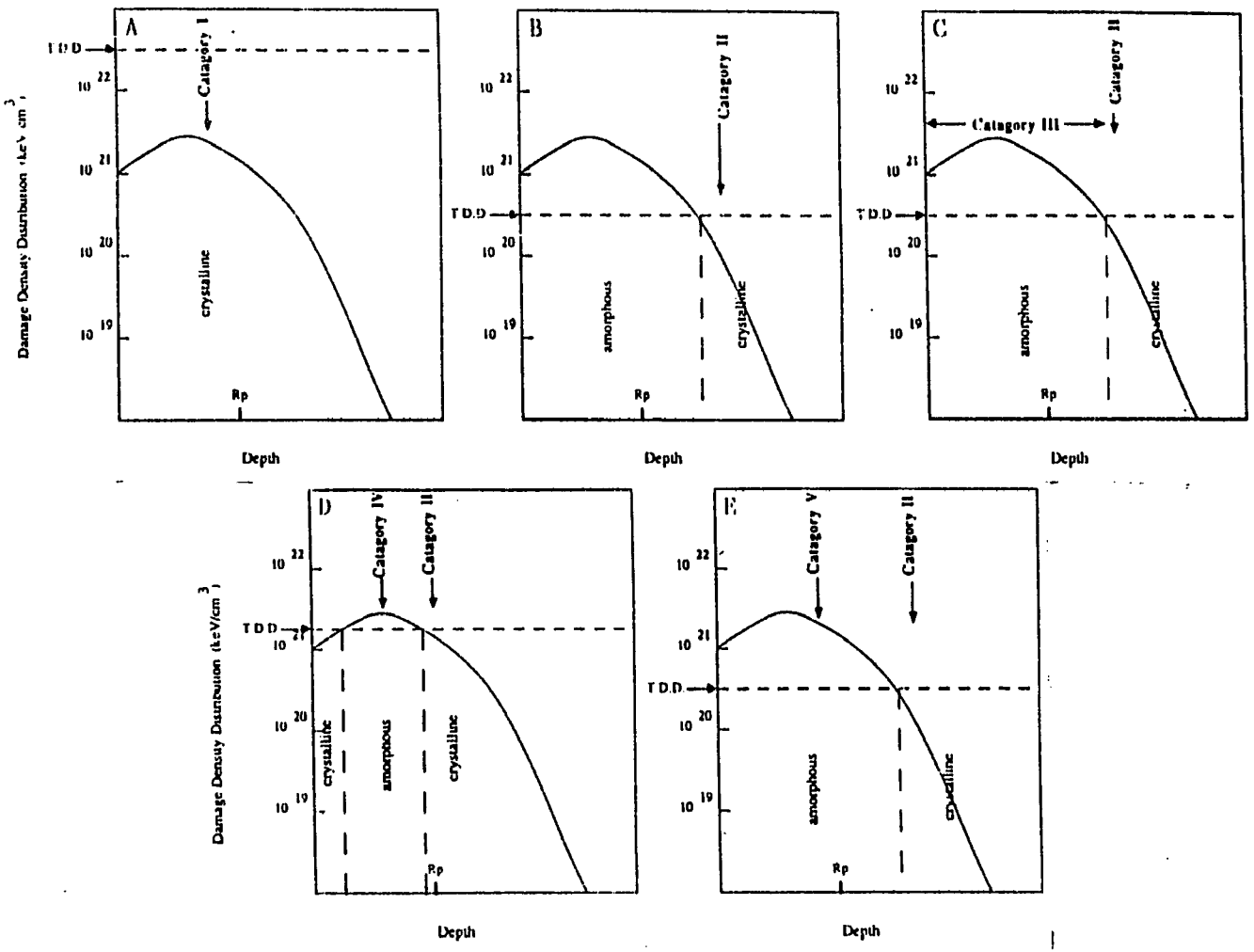

Figure 1-12. Schematics of the relationship between the effective threshold damage density (TDD) and the damage density distribution. The location of each category of defect is also shown. {From Ref. [42]}.

extended defects [42]. Below a dose of 2×10^{14} cm^{-2} no dislocation loops were observed. This finding is independent of implant species, energy, and wafer orientation. These results imply that the quantity of atoms introduced is more critical than the implant damage (for low doses) in determining whether extended defects will form (for energies < 200 keV). This supports a model that the higher density of the silicon lattice, due to the additional atoms, is primarily responsible for the category I defects. The extra atoms (either implanted ion or silicon interstitials) coalesce into the observed extrinsic dislocation loops.

When heavy ions (such as arsenic and antimony) are implanted at room temperature with energies less than 200 keV the peak of the damage density distribution exceeds the effective threshold damage density. This occurs when the dose is approximately 3×10^{13} cm^{-2} for arsenic [15] and 5×10^{13} cm^{-2} for antimony [42]. At these fluences and energies the peak of the impurity concentration is below the critical dose for category I formation. Therefore no dislocation loops form upon annealing. Instead, for these heavier ions an amorphous layer forms before reaching the critical dose for category I defect formation. Other defects (specifically category II and IV damage) will form. Thus, category I defects are not produced by room temperature (and below) implants for the heavier ions. Category I defects are typically associated with light ions since the threshold damage density is high and the critical dose can be exceeded without the formation of an amorphous layer.

Seshan and Washburn [43] have also studied the damage annealing after low dose (below amorphization) implantation of phosphorus. Anneals were performed between 200 and 800 °C in the time range of 15 to 30 minutes. From this study a model has been developed showing how the primary implant damage evolves into the category I

loops. A summary of this model is shown in Fig. 1-13.

At the lowest temperature in this study (200 - 350 °C) the Frenkel pairs created by the implantation are annihilated by the migration of one of more point defects. In the middle of this temperature range vacancies form divacancies and interstitials form di-interstitials. Near 350 °C, some of the divacancies and di-interstitials annihilate while others grow to include three or more defects.

The next stage of annealing occurs between 350 and 650 °C. Between 350 °C and 450 °C the smallest clusters dissolve with the release of mobile interstitials. These interstitials annihilate vacancies or cause interstitial cluster growth. More interstitials are produced as the temperature is raised. From 450 °C to 600 °C the damage silicon begins to recrystallize. The mobile point defects responsible for this recrystallization were not identified [43]. Between 550 °C and 650 °C clusters are converted to loops and linear defects.

Annealing the implanted samples between 650 °C and 800 °C exhibited a third stage in the annealing process. In this temperature range point defects move between small shrinking loops to larger growth loops. The dislocations which are present attract interstitials because of their large strain field [43]. Therefore, vacancy loops attract slightly more interstitials than vacancies causing them to shrink. Eventually the dopant atoms all become substitutional and there is a net excess of silicon interstitials.

Whenever an amorphous layer is formed category II damage is present (see Fig. 1-12 (b-e)) [35-37,40-42]. This damage occurs in the damaged crystalline material beyond the amorphous/crystalline (a/c) interface. Another name for this damage is "end-of-range" damage. When the amorphous layer is regrown by annealing at and

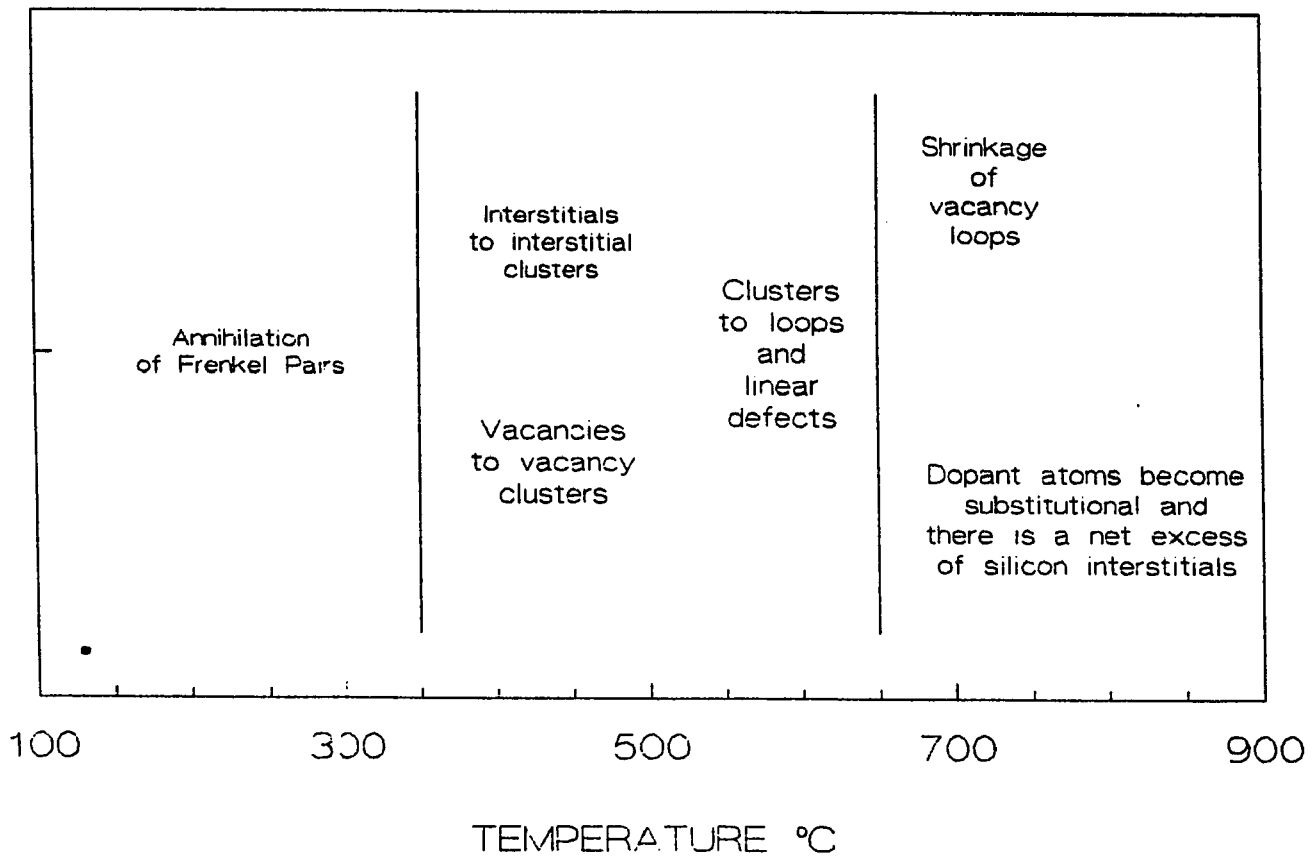

Figure 1-13. The model developed by Seshan and Washburn for low temperature anneals of below amorphization dose implants of phosphorous.

above 550 °C these defects evolve into extrinsic dislocation loops. It should be noted that the region where these defects are found is supersaturated with interstitials after implantation or becomes so after annealing. It has been found that category II defects do not form during category I formation. Jones et al. [42] suggest that category I defects act as sinks for the excess interstitials needed for category II formation.

Nemiroff and Speriosu [44] have found that two strain fields exist after annealing above amorphization doses of arsenic implanted silicon. The original amorphous region was found to be negatively strained while the category II region was positively strained. It is suggested that the positive strain is due to extra interstitials in this region [42,44].

The formation of extrinsic dislocation loops in the end-of-range region is energetically favorable with respect to the formation of a large cluster of interstitials. There is a large reduction in the strain energy associated with the formation of a plate. The dislocation loop has a strain field associated with it, and therefore it can attract impurities and implanted dopants [42]. Since dopants experience negligible diffusion during amorphous layer regrowth below 600 °C, the segregation to the category II loops after higher temperature anneals must result from impurity diffusion [45].

Wu et al. [46] have proposed a model to explain the extrinsic nature of the category II loops. In this model the loops form from the dissolution of amorphous islands below the a/c interface. For heavier ions, where the a/c interface is more abrupt, this model suggests that the concentration of loops should be less than for lighter ions. In addition, the concentration of atoms bound by dislocation loops is

predicted to decrease as the a/c interface becomes more abrupt with increasing dose. A more recent study by Jones et al. [42] contradicts these predictions.

Jones et al. [42] propose that the excess concentration of ions coming to rest beyond the a/c interface is one of the two sources for the formation of category II dislocation loops. It is suggested that since the implanted ions increase the density of the crystal lattice, the dislocation loops should be intrinsic. Statistically, the category II loops should be composed primarily of silicon interstitials since several hundred Frenkel pairs are created by one ion. Beyond the a/c interface there are more Frenkel pairs than implanted ions (up to 100 times as many Frenkel pairs). Both dopant and silicon interstitials prefer to occupy substitutional sites due to the high strain field associated with group III, IV, and VA interstitials in silicon. After annealing, the chances are greatest that silicon interstitials will remain. This effect may contribute to the number of atoms bound to dislocation loops for heavier atoms. But, this cannot account for the increase in bound atoms observed for increasing dose.

For heavier ions, Jones et al. [42] propose that a second factor may dominate at higher doses. This contribution comes from energy deposited into nuclear collisions within the amorphous layer. It is suggested that these elastic collisions may contribute to the total concentration of atoms in the loops by creating free atoms within the amorphous layer. These atoms either recoil or diffuse through the a/c interface to the category II region.

It has been proposed that surface image forces are responsible for the removal of the category II dislocation loops [46-48]. Pennycook et al. [48] have suggested that these loops glide to the surface under the action of image forces. For conventional implants (<200 keV) the category II damage removal takes place through the

annihilation of extended defects by incorporating intrinsic point defects. El-Ghor et al. [47] concluded that the activation energy for the removal of defects is the same as for silicon bulk diffusion, approximately 5 eV [48]. Also, for image forces to lead to defect removal the loops must lie within roughly twice their diameter from the sample surface [47]. Then the loops will glide to the surface. Glide, once initiated, is a runaway process since the image forces increase as the loops move closer to the surface.

The work of Ganin and Marwick [49] does not agree with the surface image forces model. In their work the surface proximity to the category II defects was studied. They found that the surface proximity did not affect the residual damage distribution. Instead, the ion beam energy was found to play a significant role in the formation of the end-of-range damage, far beyond its effect on amorphous layer thickness. From these studies we can see that there is still much to be learned as to how this region actually anneals.

Category III defects (see Fig. 1-12c) are associated with any imperfect SPE regrowth of the amorphous layer [35,42]. The most common forms of this damage are microtwins, hairpin dislocations, and segregation related defects. Many researchers have observed microtwins in <111> oriented wafers but not in <100> wafers [50]. Hairpin dislocations nucleate when the growing a/c interface encounters small misoriented (with respect to the bulk crystalline material) microcrystalline regions. As these regions are incorporated into the single crystal bulk a hairpin dislocation is nucleated. These dislocations propagate with the advancing a/c interface and become "V" in shape. Segregation defects also occur. These are associated with the rejection of an implanted species by the moving a/c interface and extend from the surface to

approximately 500 Å in depth. The most important aspect of such defects is that they can be avoided by using a cooled endstation waferholder during implantation [42].

The regrowth of a buried amorphous layer occurs by the motion of both a/c interfaces. When these two interfaces meet category IV defects are formed [35,37,42] (see Fig. 1-12d). These are sometimes called "clamshell" or "zipper" defects. Jones et al. [37,42] have found that upon annealing the buried amorphous layer large irregular dislocation loops were formed. These loops were found to be shear in nature, i.e., the Burgers vectors are in the plane of the loop and parallel to the surface. It is suggested that these defects arise from either a slight displacement of the two intersecting a/c interfaces or the coalescence of excess interstitials rejected by the advancing a/c interface. High temperature anneals (>550 °C) resulted in the category IV dislocation loops moving out of the plane parallel to the wafer surface. Eventually (annealing at 900 °C for 30 minutes) these loops dissolve with the growth of category II defects [37,42].

The final group of defects in this classification scheme are category V defects [35,42]. These defects arise when the solid solubility of the implanted species at the annealing temperature is exceeded. Their location is illustrated in Fig. 1-12e. These defects include precipitates and/or dislocation loops centered about the projected range of the implant [35,26,40,42,46,48,51-53] (where the maximum concentration occurs). Category V defect morphology usually consists of precipitates of the implanted impurity in silicon. These precipitates are believed to nucleate on category II defects.

Pennycook et al. [48] have reported that implantation of group V elements into

silicon results in the formation of extrinsic dislocation loops upon annealing. They have observed both extrinsic dislocation loops and precipitates for antimony and only dislocation loops for arsenic. Their results also suggest that the diffusivity is enhanced for group VA elements but not for group IIIA elements. The existence of a trapped group VA - silicon interstitial complex which survives SPE regrowth of the amorphous layer but dissociates in the temperature range 600 - 800 °C was proposed. This trapped complex would result in enhanced diffusivity and extrinsic dislocation loop formation. Jones et al. [42] suggest that this work could be in error since only plan-view micrographs were used. In these types of micrographs it is possible to confuse category II dislocation loops with category V defects.

Jones et al. [36,42] have used both plan-view and cross-sectional micrographs to study category V defects. For high dose arsenic implants the morphology of the category V defects consists of extrinsic dislocation loops and/or plate-like precipitates. The loops with Burgers vectors parallel to the surface become half-loop dislocations as annealing continues. These defects were observed to grow by a negative climb. For arsenic and other species implanted to high doses, they found no evidence to indicate glide occurs (as was suggested by Wu et al. [46] for category II loops). The half-loop dislocations were found to grow as the extrinsic category II loops were dissolved. This suggests that the source of the point defects resulting in half-loop growth is the declustering of arsenic precipitates. This effect was also observed for above solid solubility implants of gallium and phosphorous [42].

Hsu and Chen [53] have recently studied above solid solubility implants of arsenic into silicon. They find that upon exceeding a critical dose, the formation of loops at the projected range of the implant is inhibited. It is suggested that the category V

loops form by the agglomeration of self-interstitials mediated by the presence of a high concentration of electrically inactive arsenic in the region near the peak of the implant. This may occur through bond distortion and/or interface stress induced by the presence of the impurity. The mechanism does not exclude a small fraction of arsenic atoms precipitating during SPE. When the peak concentration exceeds a critical value, the precipitation starts to emit enough vacancies to inhibit the formation of interstitial (category V) loops and also retards SPE.

1.2.4 Diffusion of Dopants in Silicon

The major process by which atoms move in a crystal lattice is known as diffusion. Dopant diffusion in silicon is a subset of the classical field of study of diffusion in solids. This process is also of technological importance since it is an elementary processing step in the fabrication of integrated circuits. Whether the dopant has been introduced into the silicon lattice by ion implantation or from solid, liquid, or gaseous sources subsequent heat treatments are always used in the fabrication process. As a result, the dopant will diffuse.

In the simplest conceptual form, diffusion occurs as the impurity wanders through the silicon lattice in a series of random jumps. These jumps will occur in all three dimensions. If a concentration gradient exists a flux of the diffusing species will result. This process will be further affected by the concentration of point defects, the ambient temperature, the presence of an electrical field, and the charge state of point and extended defects in the substrate.

This section will lay the foundation for the diffusion studies presented throughout this dissertation. Since point defects play a major role in the diffusion phenomenon, vacancy- and interstitial-type point defects will be defined and some possible

configurations will be presented. The relationships between these defects and diffusion mechanisms will then be examined. A mathematical description of the diffusion process (Fick's law) will then be presented. From this description, the diffusion of an implanted profile will be examined.

1.2.4.1 Point Defects in Silicon

The simplest type of defect found in silicon is known as a point defect. These defects cause an interruption in the periodicity of the crystal lattice (see Fig. 1-14). Point defects are different than one-dimensional defects (eg., dislocations), two-dimensional defects (eg., grain boundaries), or three-dimensional defects (eg., voids, cavities). The concept of a "point" defect implies that the lattice perturbation remains localized to include an atom site and at most a few neighboring sites or atoms [54]. The associated electronic perturbation can extend to larger distances and can be delocalized.

There are three native point defects in silicon: the vacancy, interstitial and interstitialcy. The vacancy V is an empty lattice site and is formed when four bonds are broken to remove a silicon atom from its lattice site (see Fig. 1-14a). New bonds can be formed from the broken bonds (sometimes called dangling bonds) and lead to atomic displacement as shown in Fig. 1-15. The charge state of the vacancy determines this bonding and the atomic displacement of the neighboring atoms. When two neighboring atoms are removed a divacancy is formed (see Fig. 1-14e and Fig. 1-16).

When a silicon or impurity atom resides in one of the interstices of the silicon lattice it is known as an interstitial I (see Fig. 1-14 b and d). In a crystal lattice the stable interstitial sites occur at sites of high-symmetry where the total electronic

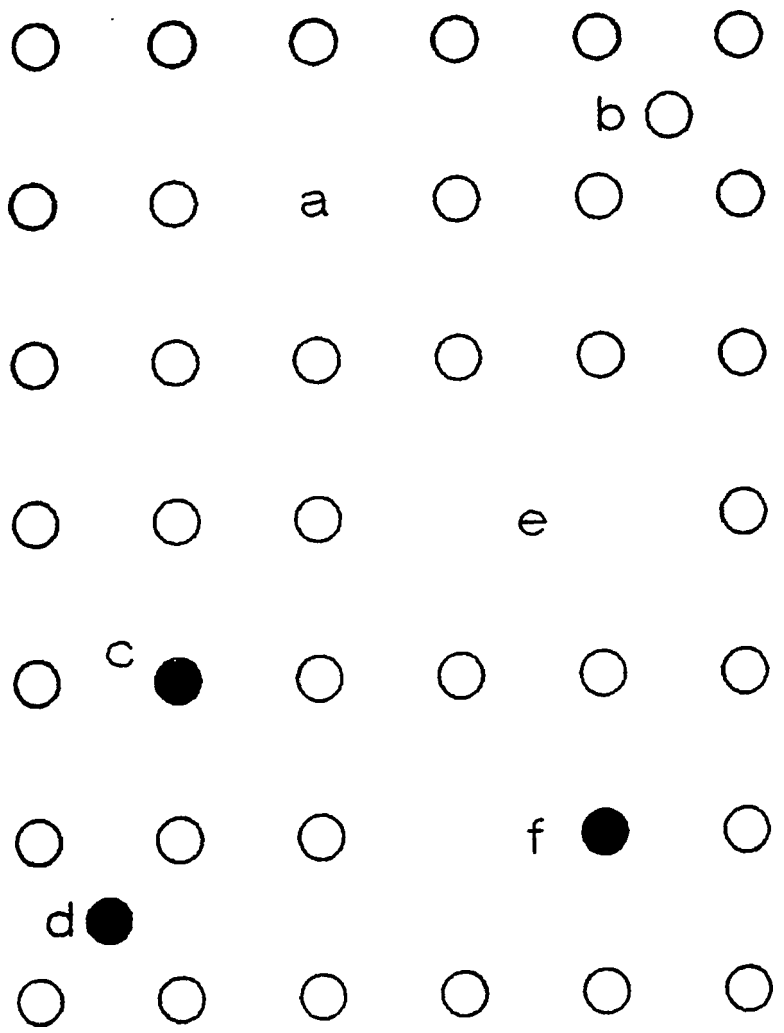

Figure 1-14 A two dimensional schematic representation of various simple point defects in a group IV semiconductor, (a) vacancy, (b) self-interstitial, (c) substitutional impurity, (d) interstitial impurity, (e) divacancy, (f) substitutional impurity-vacancy pair. The open circles are silicon atoms and the filled circles are impurity atoms.

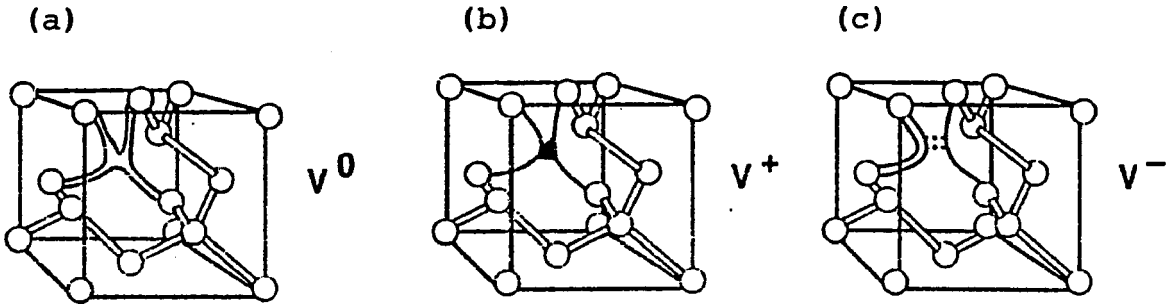

Figure 1-15 The vacancy in the silicon lattice. (a) The neutral vacancy V^o. Here there is one electron per dangling bond. The dangling bonds form two new bonds, thus leading to local distortion. (b) The positive vacancy V^+. (c) The negative vacancy V^-.

The darkened bonds in (b) and (c) denote orbitals with unpaired spins, which makes the V^+ and V^- visible to electron paramagnetic resonance experiments. Since an electron is either missing or extra, the distortion is different than that of the V^o. (After Ref. [55].)

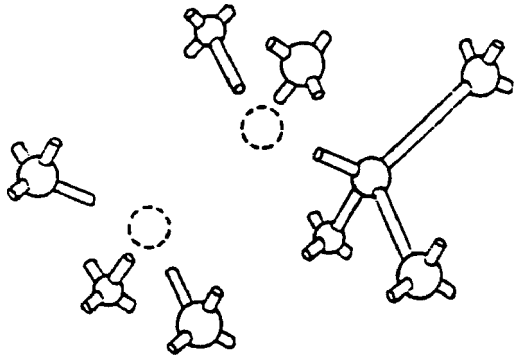

Figure 1-16 The divacancy configuration in the silicon lattice. (From Ref. [54].)

energy will be an extremum [54]. Since a crystal lattice has symmetry there may be several equivalent interstitial positions per unit cell. For the silicon lattice the sites of highest symmetry are the hexagonal and tetrahedral sites [54,55]. (See Fig. 1-17)

When an interstitial atom resides at the center of a bond, as in Fig. 1-18, it is called "bond-centered". This is another position of high symmetry. When the bond-centered configuration is distorted there is the possibility of the "split" interstitial configuration. Here the interstitial atom and one of its substitutional neighbors are displaced so that they form a dumbbell centered on the original substitutional site of the neighbor. Fahey et al. [55] have termed this type of defect the interstitialcy. It is formed by placing an extra atom about a lattice site. This is similar to a vacancy which is formed by removing an atom from a lattice site. Several configurations of this defect are shown in Fig. 1-19.

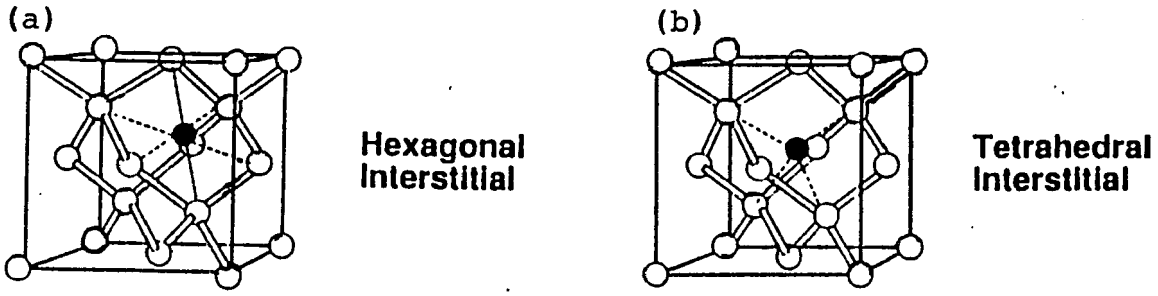

Figure 1-17. High symmetry interstitial sites in the silicon lattice. The dark spheres indicate the interstitial positions. (a) hexagonal, (b) tetrahedral. (From Ref. [55].)

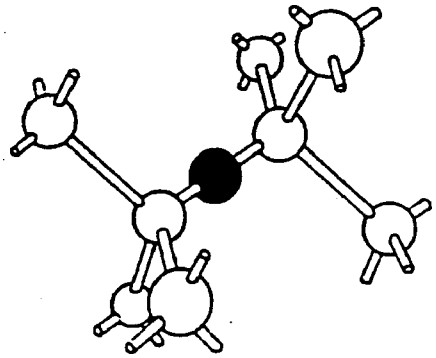

Figure 1-18 The bond-centered interstitial configuration. (From Ref. [54].)

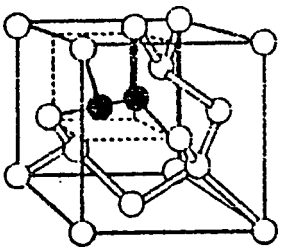

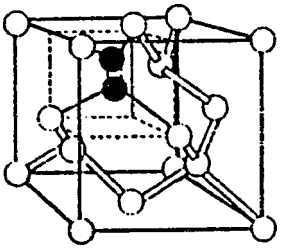

Figure 1-19 The interstitialcy defects. The two dark spheres represent the silicon interstitialcy defects if both of the dark spheres are silicon atoms. If one of the dark spheres is an impurity atom these are impurity interstitialcies *A I*. (From Ref. [55].)

Several other defects are considered to be point defects. A majority of these defects are associated with single dopant or other impurity atoms. These impurity atoms can be substitutional defects (Fig. 1-14c), interstitial defects (Fig. 1-14d), associated with a vacancy in a impurity-vacancy pair (Fig. 1-14f), or part of an interstitialcy defect called an impurity-interstitialcy pair (Fig. 1-19). The concept of an extended point defect has also been introduced. These defects are proposed to be similar in nature to the defects discussed in this section, but they are not as localized.

In many approaches to the study of diffusion, point defects are treated like atoms or molecules of foreign material in the crystal lattice. Their creation leads to the lowering of the free energy of the system. Point defects also lower the activation barrier for diffusion. Vacancies and interstitials are always present in crystals. The concentrations of these defects can affect the diffusion of impurities in the solid. The equilibrium concentrations can be determined from statistical thermodynamics. A discussion of this topic is beyond the scope of this dissertation. The interested reader is referred to the literature (see references [54-58]).

1.2.4.2 The Nature of Diffusion

In this section a nomenclature for the diffusing species and associated reactions is presented. To do this, symbols representing the various point defects discussed in the previous section must first be defined. A substitutional defect will be represented by A. The vacancy and impurity-vacancy pair will be symbolized by V and AV, respectively. An interstitial will be written as I and an interstitial impurity (dopant) as A_i. The interstitialcy type defect will be represented by the symbol AI.

Diffusion in a solid takes place as a series of random jumps. These jumps occur in all directions and, if there is a concentration gradient, results in a flux of the diffusing

species. There are several mechanisms by which these jumps take place. These diffusion mechanisms can be visualized as atomic movement of the diffusant in the crystal lattice aided by vacancies and interstitials. This section will describe these mechanisms.

When a substitutional atom (host or impurity) moves to a vacant neighboring lattice site this is known as the vacancy mechanism or substitutional diffusion. (see Fig. 1-20a). This mechanism is sometimes described by the reaction

$$A + V \longleftrightarrow AV \tag{1.25}$$

The jump process requires the breaking of covalent bonds and the making of others. If the potential barrier related to the process is E_b, the probability of atoms having a thermal energy greater than E_b is $e^{-E_b/kT}$ [60]. Note that a Boltzmann energy distribution has been assumed. The fraction of vacant sites is given by $e^{-E_v/kT}$, where E_v is the energy of formation of this defect. Since each site in the silicon lattice has four tetrahedrally situated neighbors, each jump can be made in one of four different ways. Assuming the jumps are uncorrelated, the jump frequency is given by [60]

$$\nu = 4\nu_0 e^{-(E_b + E_v)/kT} \tag{1.26}$$

where ν is the frequency with which thermal energy fluctuations occur with sufficient magnitude to overcome the barrier and have a neighboring vacancy. The frequency of lattice vibrations is ν_0 (typically in the 10^{13} to 10^{14} s^{-1} range), k is Boltzmann's constant, and T is the lattice temperature. For substitutional impurities $E_b + E_v$ typically has values of 3 to 4 eV [60]. This mechanism is the most general and important of all the diffusion mechanisms [61]. Until recently this has been the mechanism of choice to describe diffusion in silicon [55].

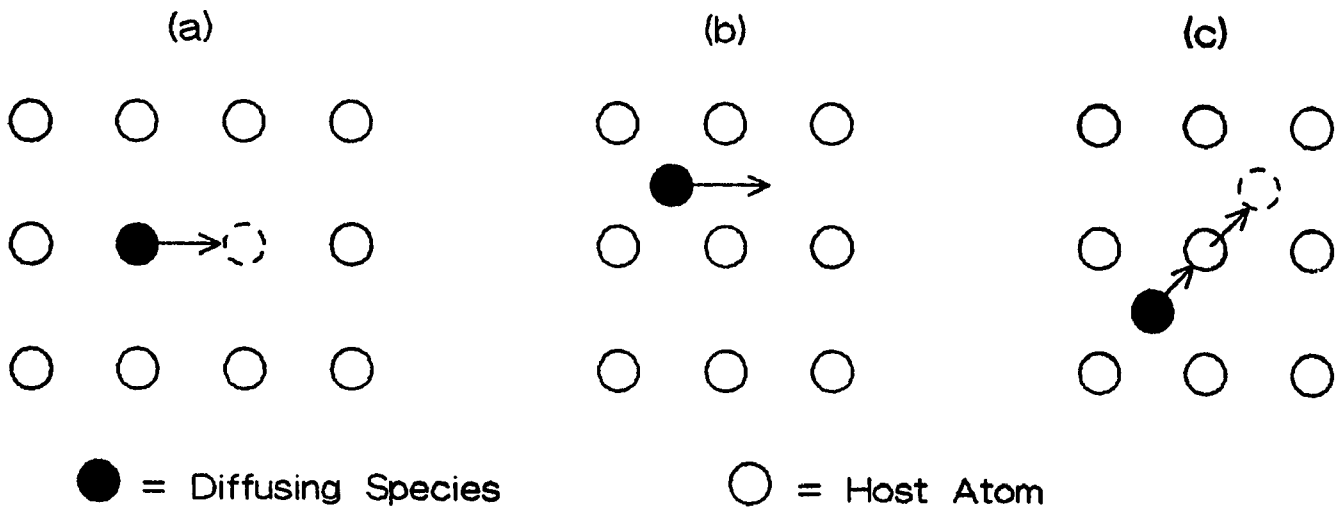

Figure 1-20. Basic models of atomic diffusion mechanisms in a two-dimensional lattice. (a) The vacancy mechanism. (b) The interstitial mechanism. (c) The interstitialcy mechanism. {After Ref. [59]}.

If an interstitial atom moves from one place to another without occupying a lattice site the diffusion is said to be by the interstitial mechanism. This process is depicted in Fig. 1-20b. The activation energy for this mechanism is lower than that of the vacancy mechanism since the formation of a vacancy is not required. Again assuming a Boltzmann energy distribution, the probability that the interstitial atom has an energy greater than the migration barrier, E_m, is given by $e^{-E_m/kT}$. In the silicon lattice atoms can jump from one interstitial site to another in four different ways. Assuming that all jumps are uncorrelated and that all interstitial sites are vacant, the frequency of jumping is given by [60]

$$\nu = 4\,\nu_0\, e^{-E_m/kT} \tag{1.27}$$

where ν is the frequency with which thermal energy fluctuations occur with sufficient magnitude to overcome the potential barrier. The migration energy E_m typically is in the 0.6 to 1.2 eV range [60].

The process of an interstitial atom displacing a substitutional atom into another interstice while it becomes substitutional is known as the interstitialcy mechanism (see Fig. 1-20c). Here it is assumed that the repulsive potential at the saddle point between lattice sites in a normal interstitial path is so high that it is energetically more favorable for the interstitial atom to move by pushing one of its neighboring lattice atoms into another interstice [58]. This mechanism can be described by two different reactions

$$A + I \longleftrightarrow AI \tag{1.28}$$

$$A + I \longleftrightarrow A_i \tag{1.29}$$

These are sometimes referred to as "kick-out" reactions.

Another common diffusion mechanism is the dissociative reaction given by

$$A \longleftrightarrow A_i + V \tag{1.30}$$

This reaction is commonly referred to as the Frank-Turnbull mechanism [62]. This mechanism was first used to describe the rapid diffusion of copper in germanium. It is now the accepted mechanism for gold diffusion in silicon [63,64]. The importance of this mechanism to dopant diffusion in silicon is controversial [55,65].

Another mechanism has been suggested for the diffusion of substitutional atoms in silicon, the concerted exchange (CE) mechanism [66]. This mechanism does not involve any defects and was shown by first-principle total-energy calculations to be energetically competitive with, or favored over, both the vacancy and interstitial mechanisms.

In the CE mechanism atoms move through a set of configurations so that, for energetic reasons, no more than two bonds are broken at one time and bond distortion is kept at a minimum. The mechanism is illustrated in Fig. 1-21 where the CE path for the diffusion of the black atom (B) to the gray atom (G) lattice site is shown. Pandey explains that the CE path can be described in terms of two rotations: a rotation about the original bond (ϕ) and a rotation of the black and gray atoms about their bond center (θ) in the plane of the paper. Note that all angles and energies are measured relative to the initial configuration. The initial movement of the B and G atoms is in the $\phi = 0$ plane. Two bonds (B-6 and G-5) are broken when θ is increased to 30° (Fig. 1-21b). As seen in Fig. 1-21c, bonds B-5 and G-6 have been made at $\theta = 60°$ and part of the exchange has been completed. In this configuration no bonds are broken, but bond angles are distorted. If θ is increased, the bonds B-5 and G-6 would be unduly compressed. To avoid this compression the B and G atoms are rotated in a plane parallel to $\theta = \phi$ (or $\theta = -\phi$). The midpoint of the exchange

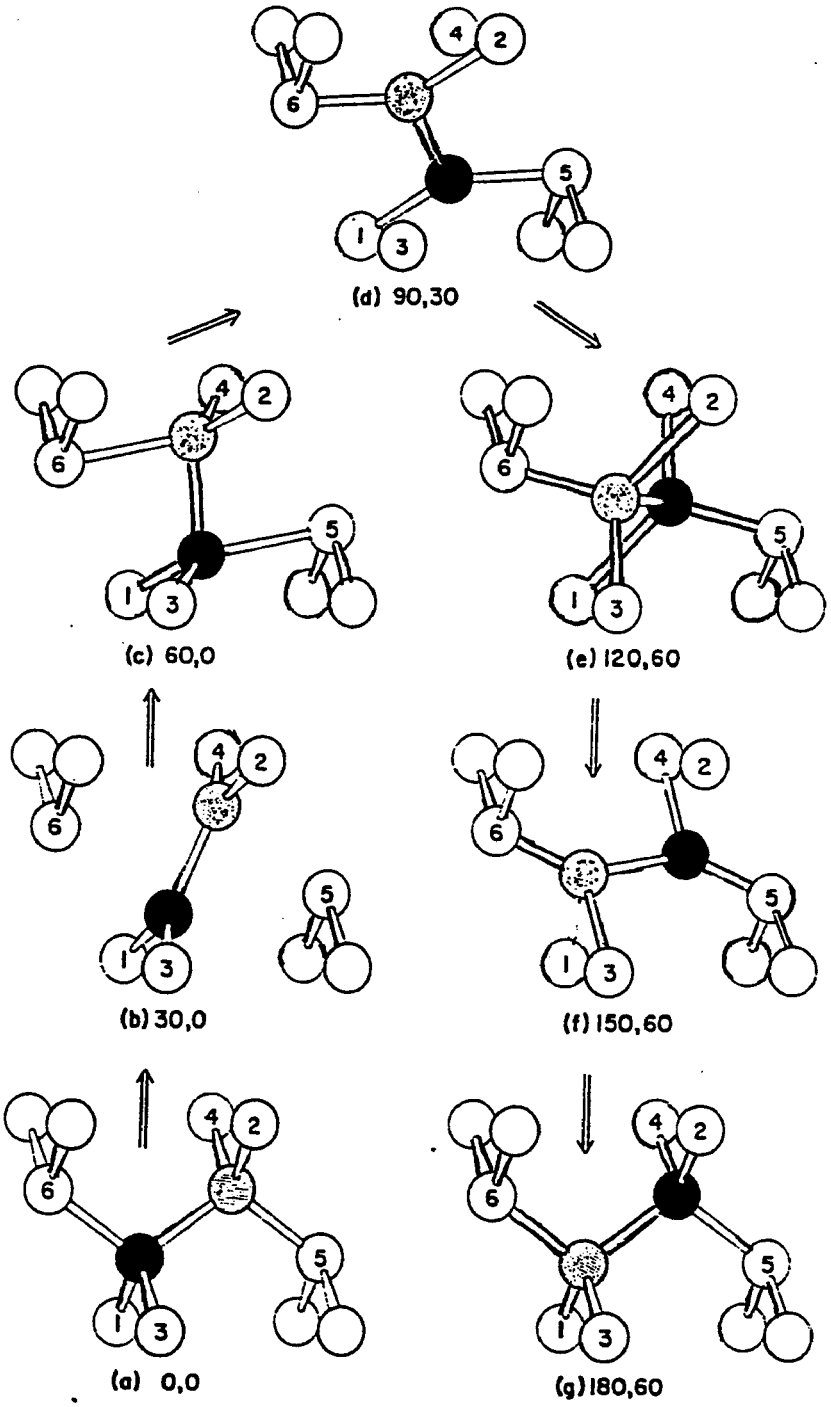

Figure 1-21 Diffusion by the concerted exchange mechanism. (From Ref. [66].)

process occurs at $\theta = 90^{\circ}$, $\phi = 30^{\circ}$ (Fig. 1-21d). Here, only two bonds (B-3 and G-4) are broken. Atoms B and G will continue to move in the plane parallel to $\theta = \phi$ until $\theta = 120^{\circ}$, $\phi = 60^{\circ}$ (Fig. 1-21e). Thereafter atoms B and G will move in the $\phi = 60^{\circ}$ plane until the exchange is completed. Pandey points out that from symmetry, the configurations (e), (f), and (g) are identical to (c), (b), and (a), respectively.

Recently, several studies have examined the mechanisms responsible for the diffusion of antimony, arsenic, boron, and phosphorous in silicon [55,65,67,68]. Each study has found that the CE mechanism plays only a minor role in the diffusion of these impurities in silicon.

1.2.4.3 Fick's Laws of Diffusion and the Diffusion Coefficient

In the previous section the atomistic view of diffusion was presented. These simple mechanisms are not adequate for describing diffusion when the impurity concentration is high, other impurities are present in high concentrations, or dislocations are present [59]. A phenomenological law of diffusion has been developed when both the impurity concentration and dislocation density are low. This mathematical description of diffusion is commonly known as Fick's law with a constant diffusivity. As the impurity concentration increases the diffusivity becomes concentration dependent which can be related to an assumed atomistic diffusion mechanism or mechanisms.

When there is a concentration gradient in the crystal, the random jump motion results in a net transport of impurities. The time rate of change of the number of impurities per unit area (flux density, J) has been determined to be [60]

$$J = -\frac{\nu d^2}{6} \frac{\partial C(x,t)}{\partial x} \tag{1.31}$$

where ν is the jump frequency as given by equations (1.26) and (1.27), d is the spacing between lattice sites, C is the impurity concentration and is assumed to be a function of x and t only, x is distance in the direction of impurity movement and t is the diffusion time. The term before the partial derivative in equation (1.31) is called the diffusivity or diffusion coefficient

$$D = \frac{\nu d^2}{6} \tag{1.32}$$

Equation (1.31) is known as Fick's first law. From this equation we see that, under diffusion conditions, the flux density is directly proportional to the concentration gradient. The negative sign in this equation indicates that the impurity flows in the direction of decreasing concentration.

Applying the law of conservation of matter, the change in the impurity concentration with time must be equal to the local decrease of the flux density, i.e.,

$$\frac{\partial C\,(x,t)}{\partial t} = -\frac{\partial J\,(x,t)}{\partial x} \tag{1.33}$$

Inserting equation (1.31) into equation (1.33) gives us Fick's second law

$$\frac{\partial C\,(x,t)}{\partial t} = \frac{\partial}{\partial x}\left[D\,\frac{\partial C\,(x,t)}{\partial x}\right] \tag{1.34}$$

A great deal of work has been done on this equation. Solutions with various simple initial and boundary conditions have been tabulated in the books by Boltaks [69] and Crank [70].

From the experimental point of view, the diffusion coefficient gives a great deal of information about the diffusion process. The diffusivity of many impurities in many materials has been determined over a wide range of temperatures [55-61]. Recalling equation (1.32) where the diffusion coefficient was defined and equations (1.26) and (1.27) (the jump frequencies related to vacancy and interstitial diffusion, respectively)

the diffusivity can be expressed as a function of temperature

$$D = \frac{4\nu_0 d^2}{6} e^{-E_a/kT} = D_0 e^{-E_a/kT} \tag{1.35}$$

Here E_a is termed the activation energy and D_0 is called the frequency factor. D_0 is usually considered to be temperature independent. The activation energy is related to the energies of motion and the energies of formation of defect-impurity complexes. It should be noted that, in most cases, the diffusivity is not a scalar quantity but is a second rank tensor. In crystals such as silicon it reduces to a single scalar quantity and the diffusion is isotropic [58].

If the impurity is ionized it will drift in an electric field in addition to the diffusion of equation (1.31). Hu and Schmidt [71] found that the flux density in equation (1.31) becomes (for the case of an internal electric field)

$$J_x = -D \frac{\partial C(x,t)}{\partial x} + Z \mu C(x,t) \mathcal{E}_x \tag{1.36}$$

where Z is the charge state of the impurity (usually $\pm$ 1 or $\pm$ 2), μ is the impurity mobility, $\mathcal{E}_x$ is the x-component of the electric field, and D and C(x,t) have been defined previously. (Note that if the doping level is high enough so that the silicon remains extrinsic at the diffusion temperature, the electric field will be internally generated during diffusion). If we use Einstein's equation ($qD = \mu kT$) and the local electrostatic field [71]

$$\mathcal{E}_x = \frac{-kT}{q} \frac{\partial}{\partial x} \left[\ln\left(\frac{n}{n_i}\right) \right] \tag{1.37}$$

(where n and n_i are the electron concentrations at the doping level concerned and the intrinsic level, respectively, at the diffusion temperature) the flux density becomes [57]

$$J_x = - hD \frac{\partial C}{\partial x} . \tag{1.38}$$

The term h is known as the electric-field enhancement factor where

$$h = 1 + Z\,C\left[\frac{\partial \ln\left(n/n_i\right)}{\partial C}\right] \tag{1.39}$$

At high doping levels h will approach a value of 2 [57].

Along with the impurity atoms being ionized, vacancies and interstitials can be charged and thus affect the impurity diffusion. In silicon, vacancies and interstitials can be neutral, singly charged, or doubly charged. It is very unlikely that these defects will have a charge state higher than 2. We will now look at the vacancy model of diffusion first proposed by Fair [57].

Vacancies with different charge states will interact with the diffusing impurity ions in different ways. As a result, the jump statistics, activation energy, and diffusion coefficient associated with each impurity-vacancy combination will be different. Assuming no correlation exists between the separate jump processes, the effective diffusion coefficient will be given by the sum of these terms taken over their respective contributions. At low impurity concentrations ($< n_i$) the diffusion is considered intrinsic and the intrinsic diffusion coefficient D_i is given by

$$D_i = D_i^o + D_i^+ + D_i^- + D_i^{2-} . \tag{1.40}$$

Here the intrinsic terms D_i^o, D_i^+, D_i^-, and D_i^{2-} are associated with the pair reactions $A\text{-}V^o$, $A\text{-}V^+$, $A\text{-}V^-$, and $A\text{-}V^{2-}$, respectively. For extrinsic doping concentrations ($> n_i$) the total diffusivity of the impurity in silicon becomes [57]

$$D = h\left[D_i^0 + D_i^+\left(\frac{n_i}{n}\right) + D_i^-\left(\frac{n}{n_i}\right) + D_i^{2-}\left(\frac{n}{n_i}\right)^2\right] \tag{1.41}$$

This expression is used to fit experimental profiles with defects of different charge states, but it does not specify the dominant diffusion mechanism. Therefore, this is a

phenomenological expression of the concentration dependence of the diffusion coefficient, and provides a description of the diffusion phenomena by extending Fick's laws. Fair [57] notes that multiplying all of the D_i terms by the electric-field enhancement factor h is not strictly correct. The internal electric field would not influence the diffusing pairs $A^+ V^-$ and $A^- V^+$ since they are neutral. Until recently (see for example reference [55]) this has been the generally accepted model for groups III and V impurity diffusion in silicon.

1.2.4.4 Diffusion of an Ion Implanted Distribution

In this dissertation we are particularly interested in the diffusion of the ion implanted distribution. Recall from equation (1.8) that the final ion distribution can be described by a one-dimensional Gaussian distribution given by

$$C(x) = \frac{\phi}{\sqrt{2\pi}\,\Delta R_p} \exp\left[-\frac{1}{2}\left(\frac{x - R_p}{\Delta R_p}\right)^2\right] \tag{1.42}$$

Seidel and MacRae [72] were the first to determine a solution to Fick's second law (equation (1.34)) subject to a position-independent diffusivity and equation (1.42) for the impurity distribution at time t = 0. A particular solution of the diffusion equation subject to the above conditions is

$$C(x) = \frac{\phi}{\sqrt{2\pi}(\Delta R_p^2 + 2Dt)^{1/2}} \exp\left\{-\frac{(x - R_p)^2}{2\Delta R_p^2 + 4Dt}\right\} \tag{1.43}$$

Seidel and MacRae [72] have also obtained a solution for no out-diffusion at the surface. They have assumed that no interactions occur at this surface except for atoms being perfectly reflected from it. In this case the particle current at the surface must be zero and so must $\frac{\partial C}{\partial x}|_{x=0}$. The solution then becomes

$$C(x) = \frac{\phi}{\sqrt{2\pi}\,(\Delta R_p^2 + 2Dt)^{1/2}} \cdot$$

$$\left[\exp\left\{ -\frac{\Delta R_p}{R_p} \frac{(x - R_p)^2}{2\Delta R_p^2 + 4Dt} \right\} + \exp\left\{ -\frac{\Delta R_p}{R_p} \frac{(x + R_p)^2}{2\Delta R_p^2 + 4Dt} \right\} \right] \quad (1.44)$$

Ghez et al. [73] have taken the analysis of Seidel and MacRae [72] a step further to include the temperature and time dependence of the diffusivity. They introduce a timelike variable λ

$$\lambda^2 = \int_0^t D\left(T\left(t'\right)\right) dt' \quad (1.45)$$

and normalized distance and time variables

$$\xi = \frac{x}{\sqrt{2}\,\Delta R_p} \quad (1.46a)$$

$$\mu = \frac{R_p}{\sqrt{2}\,\Delta R_p} \quad (1.46b)$$

and

$$\theta = 2\left(\frac{\lambda}{\Delta R_p}\right)^2 . \quad (1.46c)$$

The solution of the diffusion equation then becomes

$$\frac{C(\xi,\theta)}{C_m} = \frac{1}{2}\left(1 + \theta\right)^{-1/2} \cdot$$

$$\left[\exp\left\{ -\frac{(\xi-\mu)^2}{1+\theta} \right\} \operatorname{erfc}\left[\frac{-\xi-\mu\theta}{[\theta(1+\theta)]^{1/2}} \right] + \exp\left\{ -\frac{(\xi+\mu)^2}{1+\theta} \right\} \operatorname{erfc}\left[\frac{\xi-\mu\theta}{[\theta(1+\theta)]^{1/2}} \right] \right] \quad (1.47)$$

where C_m is the maximum concentration at R_p at time $t = 0$. To use this formation

the as-implanted data is analyzed using a linear regression to determine C_m, R_p, and ΔR_p which in turn allows μ to be determined. Next, the parameter θ in equation (1.47) is varied to minimize the sum of the squared relative differences with the annealed data. Once θ is obtained, λ and the diffusivity may be obtained.

To take into account the concentration dependence of the diffusivity Moroi and Hemenger [74] have derived an analytical solution to equation (1.34). Here $D = D\left[\, C(x,t);\, T(x,t)\right]$, that is, the diffusivity is a function of concentration, temperature, position, and time. New variables are also introduced

$$\tau = \tau\,(x,t) = \alpha^2 \int_0^t D\left[C(x,t');\, T(x,t')\right] dt' \tag{1.48a}$$

$$\zeta = \alpha\, x \tag{1.48b}$$

$$\Gamma = \Gamma(\zeta,\tau) = \alpha \int_0^{C(x,t)} D\left[\, C';\, T(x,t)\,\right] dc' \tag{1.48c}$$

where α is a constant with dimensions of reciprocal length (cm^{-1}). These variables allow the problem to be transformed to one where a linear simple diffusion equation must be solved. The formal solution is found to be [74]

$$\Gamma(\zeta,\tau) = \frac{1}{2\sqrt{\pi\tau}} \int_0^{\infty} d\zeta' \cdot$$

$$\left[\exp\left\{ -\frac{(\tau-\tau')^2}{4\tau} \right\} + \exp\left\{ -\frac{(\tau+\tau')^2}{4\tau} \right\} \right] \Gamma_0\,(\tau') \tag{1.49}$$

where $\Gamma_0\,(\tau') = \Gamma\,(\zeta', 0)$. In the case where $D = D\left(T(t)\right)$ this reduces to the solution found by Ghez et al. [73]. To actually determine the diffusivity by this method requires a numerical integration.

CHAPTER 1

References

1. Beam Solid Interactions: Physical Phenomena, J.A. Knapp, R.A. Zuhr, and P. Borgesen, eds., (Mater. Res. Soc. Proc., Pittsburgh, PA, 1990) to be published.

2. Ion Beam Processing of Advanced Electronic Materials, N. Cheung, J. Roberto, and A. Marwick, eds., (Mater. Res. Soc. Proc. Vol. 147, Pittsburgh, PA, 1989).

3. Processing and Characterization of Materials Using Ion Beams, L.E. Rehn, J. Greene, F.A. Schmidt, eds., (Mater. Res. Soc. Proc. Vol. 128, Pittsburgh, PA, 1989).

4. Fundamentals of Beam-Solid Interactions and Transient Thermal Processing, M.J. Aziz, L.E. Rehn, and B. Stritzker, eds., (Mater. Res. Soc. Proc. Vol. 100, Pittsburgh, PA, 1988).

5. Beam-Solid Interactions and Transient Processes, M.O. Thompson, S.T. Picraux, and J.S. Williams, eds., (Mater. Res. Soc. Proc. Vol. 74, Pittsburgh, PA, 1987).

6. J.F. Ziegler, J.P. Biersack, and U. Littmark, The Stopping and Range of Ions in Solids, (Pergamon Press, New York, 1985); and J.P. Biersack and L.G. Haggmark, *Nucl. Instrum. and Methods* 174, p. 257 (1980).

7. J. Lindhard, M. Scharff, and H. Schiott, *Mat. Fys. Medd. Dan. Vid. Sclsk.*, 33, 1 (1963).

8. T.E. Seidel, in VLSI Technology, S.M. Sze, ed., (McGraw-Hill, New York, 1983), p. 219.

9. J.F. Gibbons, *Proc. IEEE* 56, 295 (1968).

10. J.W. Mayer, L. Erikson, and J.A. Davies, Ion Implantation in Semiconductors, (Academic Press, New York, 1970).

11. J.F. Gibbons and S. Mylroie, *Appl. Phys. Lett.* 22, 568 (1973).

12. For a review of the Pearson IV distribution and mathematical descriptions of skewness and kurtosis see Reference 8.

13. I.H. Wilson, N.J. Zheng, U. Knipping, and I.S.T. Tsong, *J. Vac. Sci. Technol. A* 7, 2840 (1989).

14. J.F. Gibbons, *Proc. IEEE* 60, 1062 (1972).

15. S. Prussin, D.I. Margolese, and R.N. Tauber, *J. Appl. Phys.* 57, 180 (1985).

16. R.L. Novak, *Bull. Am. Phys. Soc.* 8, 235 (1963).

17. G.H. Kinchin and R.S. Pease, *Rep. Progr. Phys.* 18, 1 (1955).

18. P. Sigmund, *Appl. Phys. Lett.* 14, 114 (1969).

19. D.K. Brice, *J. Appl. Phys.* 46, 3385 (1975).

20. D.K. Brice, Ion Implantation Range and Energy Deposition Distributions, (Plenum, New York, 1975).

21. M.J. Norgett, M.T. Robinson, and I.M. Torrens, *Nucl. Eng. and Design* 33, 50 (1975).

22. L. Csepregi, E.F. Kennedy, T.J. Gallagher, J.W. Mayer, and T.W. Sigmon, *J. Appl. Phys.*, 48, 4234 (1977).

23. L. Csepregi, E.F. Kennedy, J.W. Mayer, and T.W. Sigmon, *J. Appl. Phys.*, 49, 3906 (1978).

24. T.E. Seidel and A.U. MacRae in, First International Conference on Ion Implantation, Thousand Oaks, F. Eisen and L. Chadderton, eds., (Gordon and Breach, New York, 1971), p. 149.

25. R.L. Cohen, J.S. Williams, L.C. Feldman, and K.W. West, *Appl. Phys. Lett.* 33, 751 (1978).

26. B.Y. Tsaur, J.P. Donnelly, J.C.C. Fan, and M.W. Geis, *Appl. Phys. Lett.* 39, 93 (1981).

27. R.T. Folks, C.J. Russo, P.R. Hanley, and T.I. Kamins, *Appl. Phys. Lett.* 39, 604 (1981).

28. S.R. Wilson, W.M. Paulson, R.B. Gregory, A.H. Hamdi, and F.D. McDaniel, *J. Appl. Phys.* 55, 4162 (1984).

29. A. Gat, *IEEE Electron Device Lett.* EDL-2, 85 (1981).

30. A. Nylandsted Larsen and L. Correra, *Rad. Eff. Lett.* 76, 67 (1983).

31. T.E. Seidel, D.J. Lischner, C.S. Pai, R.V. Knoell, D.M. Maher, and D.C. Jacobson, *Nucl. Instrum. and Methods* B7/8, 251 (1985).

32. A. Feygenson and J.N. Zemel, *Thin Solid Films* 165, 109 (1988).

33. T.E. Seidel, D.J. Lischner, C.S. Pai, and S.S. Lau, *J. Appl. Phys.* 57, 1317 (1985).

34. J.I. Pankove, Optical Processes in Semiconductors (Dover Publications, Inc., New York, 1975). 99

35. S. Prussin, D.I. Margolese, R.N. Tauber, and W.B. Hewitt, *J. Appl. Phys.* 56, 915 (1984).

36. K.S. Jones, S. Prussin, and E.R. Weber in, Proc. 14^{th} Intl. Conference in Defects in Semiconductors, H.J. von Bardeleben, ed, Materials Science Forum Vol. 10 (Trans. Tech. Pub, Aedermannsdorf, 1986) p. 751.

37. K.S. Jones and S. Prussin in, Materials Issues in Silicon Integrated Circuit Processing, M. Wittner, J. Stimmell, and M. Strathman (Mater. Res. Soc. Proc. Vol. 71, Pittsburgh, PA, 1986) p. 173.

38. S. Prussin and K.S. Jones, *Nucl. Instrum. and Methods* B21, 496 (1987).

39. K.S. Jones, S. Prussin, and E.R. Weber, *Nucl. Instrum. and Methods* B21, 499 (1987).

40. K.S. Jones, S. Prussin, and D. Venables in Ref [4], p. 277.

41. S. Prussin and K.S. Jones, Abstract 176 in Extended Abstracts of the Electrochem. Soc., Vol. 88-1, ECS Spring Meeting, May 1988, p. 271.

42. K.S. Jones, S. Prussin, and E.R. Weber, *Appl. Phys.* A45, 1 (1988).

43. K. Seshan and J. Washburn, *Rad. Eff.* 37, 147 (1978).

44. M. Nemiroff and V.S. Speriosu, *J. Appl. Phys.* 58, 3735 (1985).

45. D.K. Sadana, J. Washburn, and C.W. Magee, *J. Appl. Phys.* 54, 3477 (1983).

46. N.R. Wu, P. Ling, D.K. Sadana, and J. Washburn, in Defects in Silicon, W.M. Bullis and L.C. Kimerling, eds., (Proc. Electrochem. Soc. Vol. 83-9, Pennington, N.J., 1983) p. 366.

47. M.K. El-Ghor, S.J. Pennycook, and R.A. Zuhr, in Ref [2], p. 19.

48. S.J. Pennycook, R.J. Culbertson, and J. Narayan, *J. Mater. Res.* 1, 476 (1986).

49. E. Ganin and A. Marwick, in Reference [2], p. 13.

50. See Ref [42] and references therein.

51. J. Narayan, O.W. Holland, R.E. Eby, J.J. Wortman, V. Ozguz, and G.A. Rozgonyi, *Appl. Phys. Lett.* 43, 957 (1983).

52. N.R. Wu, D.K. Sadana, and J. Washburn, *Appl. Phys. Lett.* 44, 782 (1984).

53. S.N. Hsu and L.J. Chen, *Appl. Phys. Lett.* 55, 2304 (1989).

54. M. Lannoo and J. Bourgoin, Point Defects in Semiconductors I: Theoretical Aspects (Spinger-Verlag, New York, 1981).

55. P.M. Fahey, P.B. Griffin, and J.D. Plummer, *Rev. Mod. Phys.* 61, 289 (1989).

56. S.M. Hu, in Atomic Diffusion in Semiconductors, D. Shaw, ed., (Plenum Press, New York, 1973), p. 217.

57. R.B. Fair in Impurity Doping Processes in Silicon, F.F.Y. Wang, ed., (North-Holland, New York, 1981), p. 315.

58. D.A. Antoniadis, in Process and Device Simulation for MOS-VLSI Circuits , P.A. Antognetti, D.A. Antoniadis, R.W. Dutton, and W.G. Oldham, eds., (Martinus Nijhoff Publishers, Boston, 1983), p.1.

59. J.C.C. Tsai, in VLSI Technology, S.M. Sze, ed., (McGraw-Hill, New York, 1983), p. 169.

60. S.K. Ghandhi, VLSI Fabrication Principals, (John Wiley and Sons, New York, 1983).

61. R.J. Borg and G.J. Dienes, An Introduction to Solid State Diffusion, (Academic Press, New York, 1988), Chapter 3.

62. F.C. Frank and D. Turnbull, *Phys. Rev.* 104, 617 (1956).

63. U. Gösele, W. Frank, and A. Seeger, *Appl. Phys.* 23, 361 (1980).

64. See Ref. [61] pp. 202-205.

65. N.E.B. Cowern, *J. Appl. Phys.* 64, 4484 (1988).

66. K.C. Pandey, *Phys. Rev. Lett.* 57, 2287 (1986).

67. C.S. Nichols, C.G. Van de Walle, and S.T. Pantelides, in Atomic Scale Calculations in Materials Science, J. Tersoff, D. Vanderbilt, and V. Vitek, eds., (Mater. Res. Soc. Proc. Vol. 141, Pittsburgh, PA, 1989).

68. C.S. Nichols, C.G. Van de Walle, and S.T. Pantelides, *Phys. Rev. Lett.* 62, 1049 (1989).

69. B.I. Boltaks, Diffusion in Semiconductors, (Academic Press, New York, 1963).

70. J. Crank, The Mathematics of Difffusion, Second Edition, (Oxford University Press, New York, 1975).

71. S.M. Hu and S. Schmidt, *J. Appl. Phys.* 39, 4272 (1968).

72. T.E. Seidel and A.U. MacRae, *Trans. Met. Soc. AIME*, 245, 491 (1969).

73. R. Ghez, G.S. Oehrlein, T.O. Sedgwick, F.F. Morehead, and T.H. Lee, *Appl. Phys. Lett.* 45, 881 (1984).

74. D.S. Moroi and P.M. Hemenger, *Appl. Phys. Lett.* 50, 155 (1987).

Chapter 2

Arsenic in Silicon: Electrical Activation and Diffusion

In this chapter we will focus our attention on the introduction of arsenic into silicon. Particular consideration will be given to factors that have been proposed as to how arsenic becomes electrically inactive and diffuses in silicon. These factors include clustering, declustering, precipitation, phase transformation, concentration dependent diffusion, and exceeding the solid solubility limit of arsenic in silicon at the diffusion temperature. The chapter will be concluded with the purpose of the present study.

2.1 Arsenic Clustering/Complexing

Early work performed on chemical source deposited arsenic which was subsequently furnace annealed provided some interesting insights into the electrical activation and diffusion of arsenic in silicon. Masters and Fairfield [1] demonstrated experimentally that the diffusion coefficient of arsenic in silicon is linearly proportional to the electrically active arsenic concentration for electrically active doses below 10^{20} cm^{-3}. The arsenic diffusion was explained by a single-level vacancy mechanism. A short time later Schwenker, et al. [2] observed a large decrease in conductivity during heat treatments in the 500 to 970°C temperature range. The relationship between the electrically active arsenic and total arsenic was found to be consistent with a model of substitutional arsenic atoms being nonionized when in a "cluster" involving one or more vacancies. Their analysis suggested that, on the average, two arsenic atoms were involved with the cluster. Thus the first arsenic clustering model was proposed.

Fair and Weber [3] were next to propose a cluster. Their results suggested that a complex of two arsenic atoms and a vacancy are formed in silicon (VAs_2). This structure is depicted in Fig. 2-1. It was also suggested that the clustering reaction could reduce the arsenic diffusion. Chu et al. [5,6] agree in part with the work of Fair and Weber [3]. Using an ion channeling technique they found that the arsenic is located between 0.15 Å and 0.2 Å off of the lattice site. They suggest that a cluster is formed similar to that shown in Fig. 2-1, with a doubly charged vacancy located at the center of a tetrahedral site and with two charged arsenic ions located at any of the four tetrahedral sites.

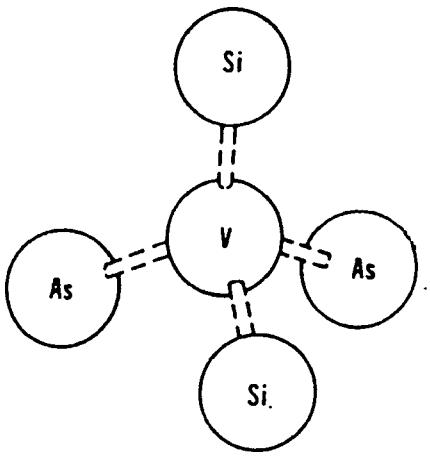

Figure 2-1. The Arsenic-Vacancy Cluster proposed by Fair and Weber [3]. {From Reference [4]}.

From the Fair point of view [3,4] we can see how clustering affects the diffusivity. In this approach the total arsenic concentration can be expressed as the sum of the monatomic As^+ and the arsenic-vacancy pairs:

$$C_T = C_{As} + C_{VAs} + C_{VAs^-} + C_{VAs_2} \tag{2.1}$$

where the possibility of V^-As^+ and $V^=As^+$ pair formation has been included. Using Fick's first law (see equation 1.31) the effective arsenic diffusivity becomes

$$D_{As} \equiv - J \left(\frac{\partial C_T}{\partial x}\right)^{-1} \tag{2.2}$$

Assuming that J is the flux density of monatomic, active arsenic, C_{As}, then

$$J = - D_i^- \frac{C_{As}}{n_i} \frac{\partial C_{As}}{\partial x}$$

$$= - D_i^- \frac{C_{As}}{n_i} \frac{\partial C_{As}}{\partial C_T} \frac{\partial C_T}{\partial x} \tag{2.3}$$

where D_i^- is the arsenic diffusivity where V^- vacancies are involved. Thus, as electrically inactive stationary arsenic complexes are formed the flux of diffusible ions is reduced.

In an analysis of arsenic vapor pressure data Hu [7] found that the arsenic diffusivity decreased for arsenic concentrations greater than 3×10^{20} cm^{-3}. He explains this phenomenon based on a cluster model consisting of four arsenic atoms forming a tetrahedron either with a normal interstitial site (shown in Fig. 2-2) or with a silicon atom at its center. The cluster becomes electrically inactive with the formation of two As—As covalent bonds. This model was arrived at by analyzing various models from As_2 to As_5 and finding the one that best fit vapor pressure data. Within this analysis it was assumed that only one complex structure would dominate in a particular temperature range.

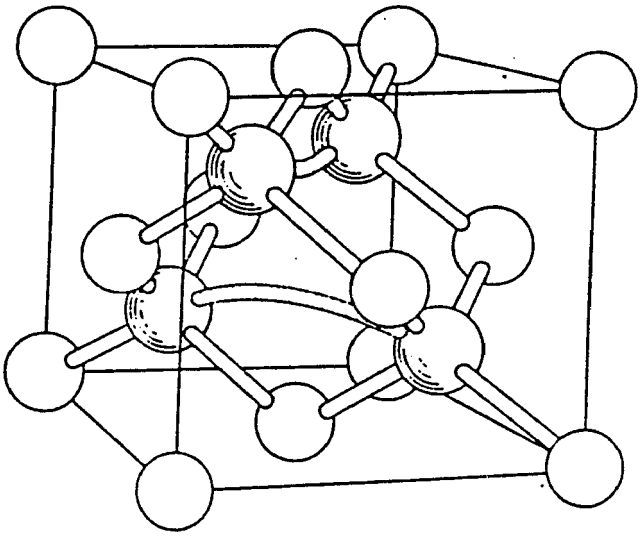

Figure 2-2. Hu's model of an arsenic cluster in silicon. The open circles represent silicon atoms while the shaded circles represent arsenic atoms. In this diagram the four arsenic atoms form a tetrahedron with a normal interstitial site at its center. {From Reference [7]}

Tsai et al. [8] have simulated high dose arsenic diffusion in silicon with a computer program which simulates both concentration dependent diffusion and arsenic clustering. Also included in the program is the internal field effect diffusion (discussed in Chapter 1) and vacancy-enhancement diffusion [9]. A new arsenic clustering model is introduced to describe the clustering effect more accurately than the two [2-4] or four [7] arsenic clustering models. This model assumes that clustering of arsenic occurs through the reaction

$$3\,As^{+} + e^{-} \underset{\text{Temperature}}{\overset{\text{Annealing}}{\longleftrightarrow}} As_3^{+2} \xrightarrow{25^{\circ}C} As_3 \qquad (2.4)$$

Here three arsenic ions are clustered with an electron at annealing temperatures and the cluster is electrically active. At room temperature the cluster is electrically inactive. The total arsenic concentration can then be expressed as

$$C_T = C_{As} + 3\,C_{As_3^{+2}} \qquad (2.5)$$

Thus, inserting this into equations (2.2) and (2.3) we see that the diffusivity will be affected by this clustering model.

Further work on clustering along the lines of Tsai et al. [8] has been performed by Guerrero et al. [10]. They have shown that the basic qualitative behavior of clustering with increasing arsenic concentration depends on the sign of the charge of the clusters and the number of electrons or vacancies taking part in the formation of the clusters. A major conclusion from this study is that a saturation value of unclustered (electrically active) atoms C_{As}^{max} always exists if negative charges in the form of electrons or vacancies participate in the formation of positive arsenic clusters. It is therefore conjectured that C_{As}^{max} is independent of the number of clustering arsenic atoms. This maximum solubility is then reported to be given by

$$C_{As}^{max} = 1.89637 \text{ X } 10^{22} \exp\left[-\frac{0.453}{k\,T}\right] \qquad (2.6)$$

This expression is plotted in Fig. 2-3. They conclude that their work supports the model by Tsai et al. [8].

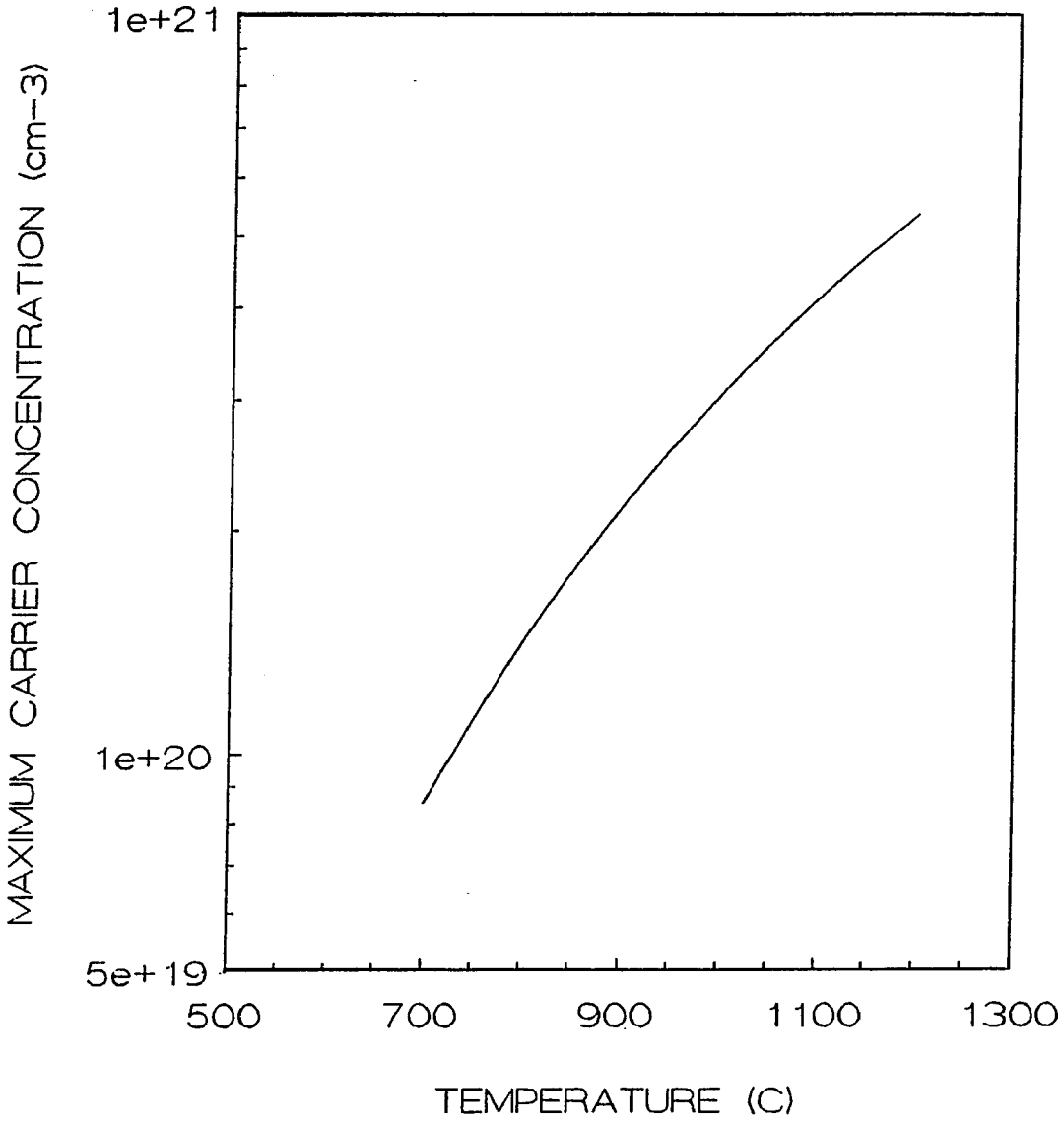

Figure 2-3. The electrical solubility concentration versus the annealing temperature {after Reference [10]}

Recently a new arsenic cluster has been proposed [11]. Using first-principles total-energy calculations [11] and extended x-ray-absorption fine-structure (EXAFS) measurements [12] a $V-As_4$ complex is suggested to explain the electrical deactivation of heavily arsenic doped silicon. This complex was found to be energetically favored over substitutional, isolated arsenic in silicon and substitutional $Si-As_4$ configurations. This is reported to agree with the previously mentioned channeling studies of Chu et al. [5,6] who found the arsenic to be displaced approximately 0.15 Å from the lattice site. It is also conjectured that this defect is only the first step in the growth of larger complexes such as V_2-As_6 and the eventual precipitation of arsenic.

Seidel et al. [13] have also studied the clustering mechanism using both furnace and rapid thermal annealing. In this study arsenic implants were performed at energies in the range of 50 to 200 keV with fluences between 10^{15} and 10^{16} cm^{-2}. Figure 2-4 shows the results of this study. Also shown as solid curves are data from the literature. Note that the average diffusivity rises more rapidly than linearly with average arsenic concentration for anneals at and above 1100°C. Below 1050°C a saturation and reduction in the average diffusivity with concentration is observed. The saturation is associated with clustering, while the higher temperature results are associated with "no clustering" or declustering. It was suggested that the high temperature data could be possibly related to a doubly charged vacancy mechanism.

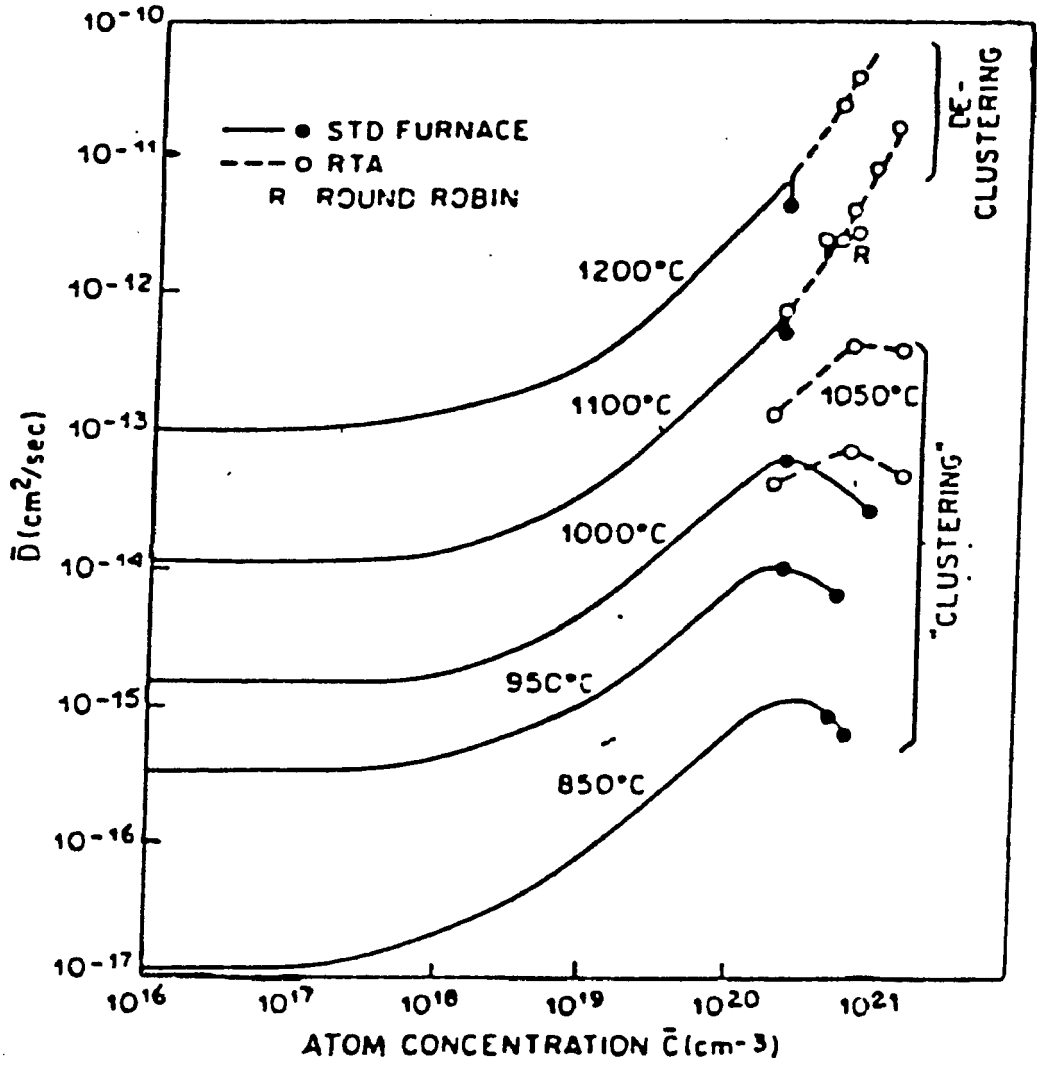

Figure 2-4. The average diffusivity versus the average arsenic concentration. At high arsenic concentration values the concentration enhancement is limited by clustering for anneals below 1050°C. For anneals above 1100°C concentration enhancement is very strong and a declustering mechanism is suggested. {From Reference [13]}

2.2 Metastability

Another interesting effect associated with high arsenic concentrations is metastability [13]. Here a sequence of anneals is performed with an initial high temperature anneal followed by a low temperature anneal. After the first high temperature step the measured sheet resistance is low (as expected). A subsequent low temperature step increases the sheet resistance. As seen in Fig. 2-5 the cycle is reversible. This effect has been observed by several authors [13-15]. Seidel et al. [13] suggest that this demonstrates the ability to induce declustering and clustering. Therefore the initial high-temperature short-time anneal achieves a high solubility in a state of metastable activation.

Further work by Kamgar et al. [14,15] has characterized this metastable state. Using rapid thermal annealing (RTA) experiments they have found that the metastable activation is not necessarily due to the high temperature used, but rather the short time used. In this work high solubility was also attained during the initial few seconds of relatively low temperature anneals. These observations allowed the sheet resistance versus time to be divided into three separate domains as shown in Fig. 2-6(a). The normalized fraction of nonsubstitutional to substitutional arsenic atoms as a function of anneal time is shown in Fig. 2-6(b). The RTA power used in this experiment corresponded to a steady-state temperature of 950°C.

In the first domain the resistance drops from its high nonannealed magnitude to a local minimum of about 73 Ω/□. While annealing in Domain I the amorphous silicon recrystallizes and the arsenic atoms occupy predominantly substitutional sites. Therefore the arsenic becomes electrically active and the sheet resistance drops.

Between 10 and approximately 30 seconds (Domain II) the arsenic is conjectured to cluster. Here the sheet resistance increases while there is little diffusion at the

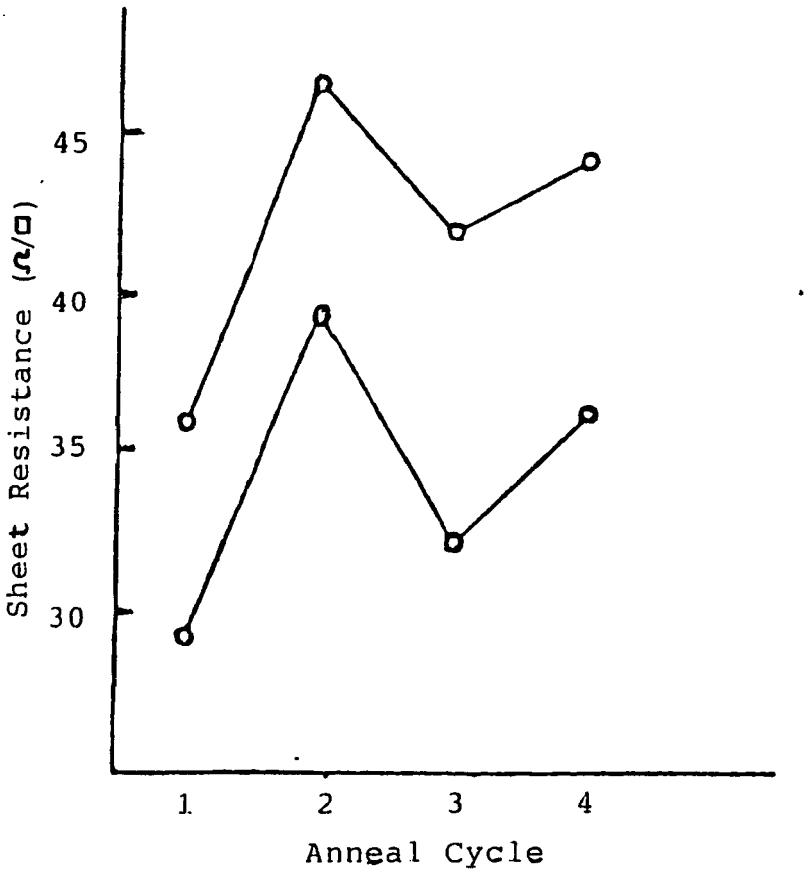

Figure 2-5. The sheet resistance of arsenic implanted silicon after high and low temperature anneals. The first and third anneals were done at 1100°C for 1 second. Second and fourth anneals were done at 800°C for 30 minutes. {After Reference [13]}

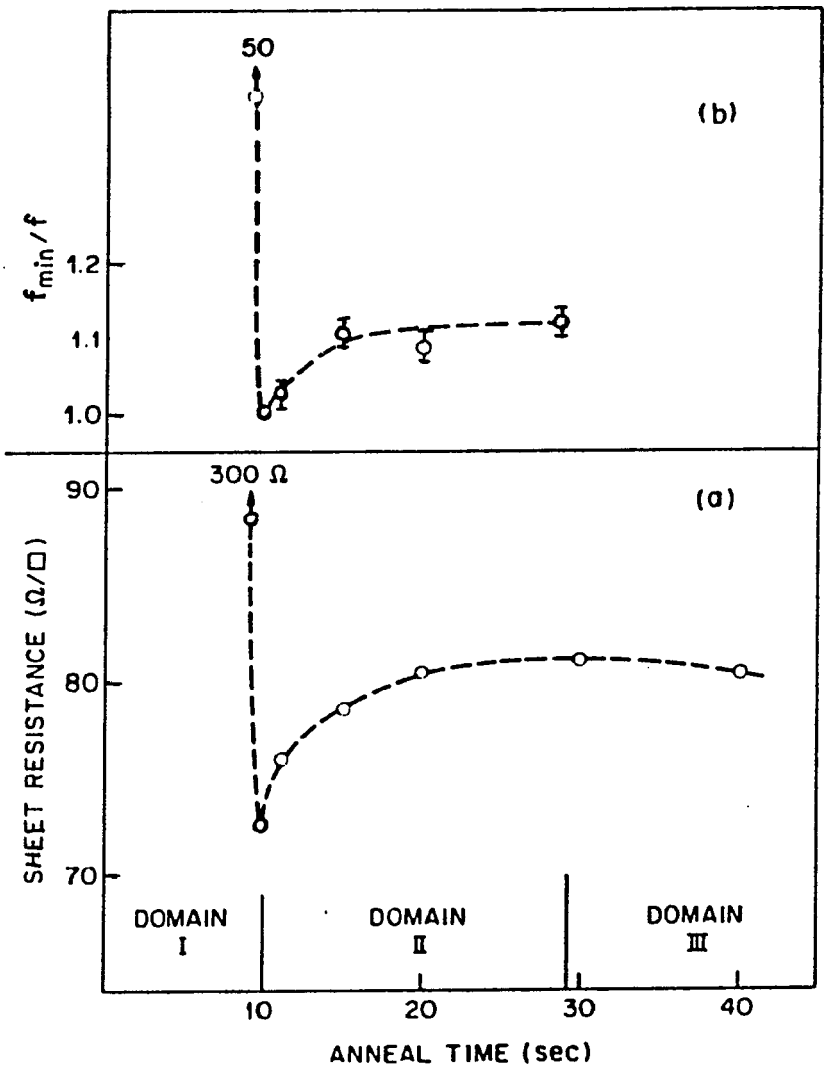

Figure 2-6. The data of Kamgar et al. [15] showing the three domains in the (a) sheet resistance and (b) the normalized fraction of nonsubstitutional to substitutional arsenic atoms as a function of anneal time. Note that f_{min} is the fraction of arsenic for the case where Rutherford Backscattering showed the highest degree of substitutionality.

same time the channeling measurements (Fig. 2-6(b)) show substantial changes in the fraction of substitutional arsenic. In this figure f_{min}/f represents the percent increase in the fraction of nonsubstitutional arsenic normalized to the fraction at the local sheet resistance minimum. From their RBS work [14] on samples in this domain they have observed a peak in the silicon spectrum at the projected range of the arsenic. They conclude that this indicates the formation of As—Si complexes associated with arsenic clustering [15]. By observing the temperature dependence of the sheet resistance rise the activation energy for arsenic clustering was determined to be 1.1 ± 0.15 eV [14,15].

Above 30 seconds the sheet resistance begins to drop. This has been designated as Domain III. In this domain declustering is reported to occur as the arsenic further diffuses [15]. It is suggested that when the arsenic begins to diffuse its atomic concentration decreases, thus reducing the clustering. One should note that as the annealing temperature is increased the time of each domain is shortened.

2.3 Precipitation

Nobili et al. [16] were first to suggest a phenomenon different from clustering to explain the discrepancy between the concentration of carriers and that of the arsenic atoms at high doping levels. This phenomenon is precipitation, which is an alternate suggestion to the clustering/complexing hypothesis. They suggest that a constant As^+ equilibrium concentration cannot result from a point defect reaction and only a two-phase equilibrium (precipitate formation) is compatible with their results. These precipitates are reported to be silicon arsenide. They proposed that if these precipitates are coherent and keep the lattice structure of the silicon (or closely match it) then this phenomenon is compatible with Chu's channeling results [5,6]. Using small angle x-ray scattering (SAXS) measurements they find that most of the

precipitates conform to the silicon lattice with a mean radius of approximately 40 Å. It is further suggested that because of this feature and the similarity of the tetrahedral radii of arsenic and silicon, only a fraction of the precipitated dopant is observable by channeling. This also hinders observation by transmission electron microscopy. The electrically active concentration was determined to be only dependent upon temperature.

Angelucci et al. [17] extended the work of Nobili et al. [16] to less heavy doping of arsenic in silicon. By decreasing the arsenic concentration from 3.2 to 1.1 X 10^{21} cm^{-3} they observed a decrease in the population of particles of small size and a corresponding increase in the fraction of particles with radii of approximately 150 Å. Concurrently the precipitate shape evolved from that of a thin platelet to that of a sphere. The influence of the precipitation on the diffusivity was also considered. It was found that at high temperatures (1000°C) the diffusivity is concentration dependent and the shift of the junction depth and carrier profile was not appreciably dependent upon the amount of precipitates. Analysis of the arsenic diffusivity showed good agreement with the well known model of arsenic diffusion by ionized point defects proposed by Fair [4].

Zhiheng [18-20] has studied silicon heavily doped with arsenic. In this work a coherent phase transformation is observed [19,20]. A theoretical derivation is presented following Cahn's theory of spinodal decomposition [21]. Comparison of theoretical and experimental results demonstrated that the electrically inactive arsenic resulted from an uphill diffusion. That is, spinodal decomposition induced heavily arsenic doped regions into small areas alternating with both high and low concentrations. Calculations of precipitate size were also possible. The mean size of the coherent precipitates was found to be between 15 and 23 Å [18]. Transmission

electron microscopy work has shown a periodic structure with period of 17 to 23 Å [19,20].

2.4 Arsenic Diffusion Simulations

It is important to know how these arsenic diffusion models are used in common device processing simulations. In this section we will examine the simulation of arsenic diffusion by the two most popular simulation programs. The first, SUPREM III [22], is probably the most widely used simulation. Also presented is the PREDICT [23] formulation since it has become popular in recent years.

The SUPREM III simulation [22] involves the solution of the complete one-dimensional continuity equation

$$\frac{\partial C_T}{\partial t} = \frac{\partial}{\partial x}\left(D_{As} \frac{\partial C_T}{\partial t}\right) \pm \frac{q}{kT} \frac{\partial}{\partial x}\left(D_{As} C_A \frac{\partial \Phi}{\partial x}\right) \tag{2.7}$$

where D_{As} is the effective diffusivity, and C_T and C_A are the total and electrically active arsenic concentrations, respectively. Here the potential Φ is given by

$$\Phi = \frac{kT}{q} \ln \frac{n}{n_i} \tag{2.8}$$

where n and n_i are the electron and intrinsic carrier concentrations, respectively. In equation (2.7) the first term represents a concentration gradient driven diffusion with the inclusion of a non-constant diffusivity. The electrostatic potential gradient driven flux with non-constant diffusivity is given by the second term.

Although there is the possibility that both interstitials and vacancies play a role in arsenic diffusion, the model in SUPREM III is based upon vacancy diffusion mechanisms. Here the arsenic is assumed to diffuse with V^0 and V^- vacancies. The diffusivity is then given by

$$D_{As} = D_i^0 + D_i^- \left(\frac{n}{n_i}\right)$$

$$= 0.066 \exp\left(\frac{-3.44\ eV}{kT}\right) + 12.0 \left(\frac{n}{n_i}\right) \exp\left(\frac{-4.05\ eV}{kT}\right) \qquad (2.9)$$

At moderate doping levels the net electron concentration is taken to be equal to the arsenic concentration. With high doping levels the electron concentration deviates from that of the total arsenic C_T. Arsenic in excess of the solid solubility limit is assumed to precipitate and is considered not diffusible and not contributing to the n value in the above equations. SUPREM III follows the work of Fair [4] by assuming that as the solubility limit is approached n becomes less than C_T due to complex formations. The net electron concentration becomes

$$n = C_{As^+} - C_{As^+V^=} \qquad (2.10)$$

After further analysis the dependence of C_T on n is then given by

$$C_T = n + \left[0.41 \times 10^{-44} \exp\left(\frac{0.33}{kT}\right)\right] n^3 \qquad (2.11)$$

PREDICT [23] uses a different technique to simulate arsenic diffusion. In this simulation the continuity equation

$$\frac{\partial C_T}{dt} = \frac{\partial}{\partial x}\left(h\ D_{As}\ \frac{\partial C_T}{dx}\right) \qquad (2.12)$$

is numerically integrated using a finite difference technique. The term h in equation (2.12) is the electric field effect term as described in Chapter 1. Again assuming

diffusion by V^0 and V^- vacancies the diffusivity becomes

$$D_{As} = D_i^0 + D_i^- \left(\frac{n}{n_i}\right)$$

$$= 0.25 \exp\left(\frac{-3.58\ eV}{kT}\right) + 22.9 \left(\frac{n}{n_i}\right) \exp\left(\frac{-4.1\ eV}{kT}\right) \quad (2.13)$$

When the arsenic dose exceeds 2×10^{14} cm^{-2} (note that this dose produces a continuous amorphous layer) arsenic clustering is taken into account. The effective diffusivity then becomes

$$D_{As} = \frac{D_i^-\left(\frac{n}{n_i}\right)}{1 + \frac{4\ K_c(T)\ n^3}{1+3\ K_b(T)\ n^2}} \quad (2.14)$$

where

$$D_i^- = 22.9 \exp\left(\frac{-4.1\ eV}{kT}\right) \quad (2.15)$$

and the equilibrium coefficients derived using the law of mass action are

$$K_b(T) = 1.39 \times 10^{-49} \exp\left(\frac{1.51\ eV}{kT}\right) \quad (2.16)$$

and

$$K_c(T) = 1.78 \times 10^{-70} \exp\left(\frac{2.14\ eV}{kT}\right) \quad (2.17)$$

2.5 Arsenic Tail Diffusion

Fair [24] has attempted to characterize the implanted arsenic profile as it diffuses with increasing temperature. Examining the results of Shibayama et al. [25] he notes an enhanced diffusion in the "tail" region and a reduction in the surface electron concentration n_s for anneals between 500 and 700°C. The tail region in this use is the region of deepest penetration beyond the peak concentration.

In earlier work on phosphorous diffusion it was noted that a "kink" and a tail region appeared at 1100°C. This feature became more prominent as the diffusion temperature was decreased. The appearance of this tail was related to the number of $V^{=}P^{+}$ pairs in the surface region. Since a kink and tail region was observed for arsenic it was inferred that arsenic in the low temperature regime (below 700°C) diffused very much like phosphorous does below 1100°C. It was also conjectured that above 1100°C, phosphorous would diffuse very much like arsenic does above 700°C. Relating this information to that of Fair and Tsai [26] it was deduced that arsenic tail diffusivity was proportional to the cube of the surface electron concentration [24], i.e.,

$$D_{As}^{tail} \propto n_s^3 \tag{2.18}$$

and a pair-dissociation mechanism was involved. It is concluded that the concentration of VAs^{-} pairs below approximately 700°C is sufficient to cause tail region enhanced diffusion through a pair-dissociation process. The formation of VAs_2 perturbs the vacancy concentration and results in the enhancement factor being relatively independent of temperature below 800°C.

2.6 Purpose of the Present Investigation

The technological importance of using ion implantation of arsenic into silicon has been well established. Since arsenic is a major dopant in silicon it is important in the fabrication of VLSI circuitry. Ion implanted arsenic is extremely attractive since shallow junctions are possible; it can be introduced to levels above solid solubility; and it is a slow diffuser. The significance of arsenic to VLSI technology can be seen in its current uses as a dopant of emitters, resistors, and contacts.

From the material presented in Chapter 1 it was determined that implanted

arsenic produces a great deal of damage. The implant fluence was seen to play an important role in damage annealing. In this chapter we have seen that this dose also has an effect on the arsenic diffusion and the models proposed for the electrical activation. Therefore, to be able to understand the way implanted arsenic is incorporated into the silicon lattice during various thermal treatments one must examine damage annealing, arsenic diffusion, and arsenic electrical activation.

In the present work, an evaluation of these properties has been undertaken on a systematic basis. This investigation centers on samples implanted to a fluence of 1 X 10^{16} cm^{-2} at 100 keV since this dose is known to produce a continuous amorphous layer [27]. Both furnace and rapid thermal annealing have been used. Lower fluences have also been studied to determine concentration effects.

Particular attention is given to the end-of-range (or tail) region of the implant. Tail samples were produced by an anodic oxidation and stripping technique after implantation or by implanting through a surface oxide. Arsenic in this region is found to diffuse differently than the total implant samples. It has been found that damage near the peak of boron profiles does not affect the tail region [28]. One of the aims of this work is to see if this also holds true for arsenic. The relationship of end-of-range damage to annealing and arsenic diffusion will also be examined.

CHAPTER 2

References

1. B.J. Masters and J.M. Fairfield, *J. Appl. Phys.* 40, 2390 (1969).

2. R.O. Schwenker, E.S. Pan, and R.F. Lever, *J. Appl. Phys.* 42, 3195 (1971).

3. R.B. Fair and G.R. Weber, *J. Appl. Phys.* 44, 273 (1973).

4. R.B Fair, in "Impurity Doping Processes in Silicon", F.F.Y. Wang, ed., (North Holland Pub., Amsterdam, 1981) p. 351.

5. W.K. Chu and B.J. Masters, in Laser-Solid Interactions and Laser Processing-1978, S.D. Ferris, H.J. Leamy, and J.M. Poate, eds., (AIP Conference Proceedings No. 50, New York, 1979) p. 305.

6. W.K Chu, in Laser and Electron Beam Processing of Electronic Materials, L.L. Anderson, G.K. Cellar, and G.A. Rozgonyi, eds., (Proc. Electrochem. Soc. Vol. 80-1, Pennington, N.J., 1980) p. 361.

7. S.M. Hu, in Atomic Diffusion in Semiconductors, D.Shaw, ed., (Plenum Press, New York, 1973) Chapter 5.

8. M.Y. Tsai, F.F. Morehead, J.E.E. Baglin, and A.E. Michel, *J. Appl. Phys.* 51, 3280 (1980).

9. S.M. Hu and S. Schmidt, *J. Appl. Phys.* 39, 4272 (1968).

10. E. Guerrero, H. Potzl, R. Tielert, M. Grasserbauer, and G. Stingeder, *J. Electrochem. Soc.* 129, 1826 (1982).

11. K.C. Pandey, A. Erbil, G.S. Cargill, R.F. Boehme, and D. Vanderbilt, *Phys. Rev. Lett.* 61, 1282 (1988).

12. A. Erbil, W. Weber, G.S. Cargill, and R.F. Boehme, *Phys. Rev. B* 34, 1392 (1986).

13. T.E. Seidel, C.S. Pai, D.J. Lischner, D.M. Maher, R.V. Knoell, J.S. Williams, B.R. Penumalli, and D.C. Jacobson, in Energy-Beam Solid Interactions and Transient Thermal Processing, D.K. Biegelsen, G.A. Rozgonyi, and C.V Shank, eds., (Mater. Res. Soc. Proc. Vol. 35, Pittsburgh, PA, 1985) p. 329.

14. A. Kamgar and F.A. Baiocchi, in Rapid Thermal Processing, T.O. Sedgwick, T.E. Seidel, and B.-Y Tsaur, eds., (Mater. Res. Soc. Proc. Vol 52, Pittsburgh, PA, 1986) p. 23.

15. A. Kamgar, F.A. Baiocchi, and T.T. Sheng, *Appl. Phys. Lett.* 48, 1090 (1986).

16. D. Nobili, A. Carabelas, G. Celotti, and S. Solmi, *J. Electrochem. Soc.* 130, 922 (1983).

17. R. Angelucci, G. Celotti, D. Nobili, and S. Solmi, *J. Electrochem. Soc.* 132, 2726 (1985).

18. Lu Zhiheng, *Phys. Stat. Sol.* (a) 98, 471 (1986).

19. Zhiheng Lu, *J. Appl. Phys.* 62, 1756 (1987).

20. Lu Zhiheng, *Vacuum* 39, 159 (1989).

21. J.W. Cahn, *Trans. Met. Soc. AIME* 242, 166 (1968).

22. C.P. Ho, S.E. Hansen, and P.M. Fahey, SUPREM III-A Program for Integrated Circuit Process Modeling and Simulation, (Stanford Technical Report No. SEL84-001, 1984).

23. R.B. Fair and R. Subrahmanyan, *Proc. SPIE*, Vol. 530, 88 (1985).

24. R.B Fair, in Semiconductor Silicon 1981, H.R. Huff, R.J. Kriegler, and Y. Takeishi, eds., (*Proc. Electrochem. Soc.* Vol. 81-5, Pennington, N.J., 1981) p. 963.

25. H. Shibayama, H. Masaki, H. Ishikawa, and H. Hashimoto, *J. Electrochem. Soc.* 123, 742 (1976).

26. R.B. Fair and J.C.C. Tsai, *J. Electrochem. Soc* 124, 1107 (1977).

27. S. Prussin, D.I. Margolese and R.N. Tauber, *J. Appl. Phys.* 57, 180 (1985).

28. L.C. Hopkins, T.E. Seidel, J.S. Williams, and J.C. Bean, *J. Electrochem. Soc.* 132, 2035 (1985).

Chapter 3

Experimental Details and Results

Many experimental techniques were used to examine arsenic diffusion and implant damage annealing. In this chapter we will discuss these techniques and the resulting knowledge gained from each of them. Before doing so, anodic oxidation will be examined. This technique is an integral part in the preparation of the "tail only" samples. It is also used to controllably remove small layers of silicon during the differential Hall effect measurements.

Spreading resistance and Hall effect measurements are used to investigate the electrical activity of the arsenic after various heat treatments. Deep level capacitance transient spectroscopy (DLTS) allows the determination of deep level states that may exist after processing. Many of the arsenic diffusion models presented in Chapter 2 related to vacancy diffusion and clustering of arsenic with vacancies. Several of these defects have been observed with DLTS.

Several techniques using ion or electron beams have been utilized. Rutherford backscattering spectrometry (RBS) and transmission electron microscopy are complementary methods for examining damage annealing. RBS channeling experiments allow for the determination of the arsenic substitutionality in the silicon lattice. Arsenic diffusion is examined with secondary ion mass spectrometry (SIMS).

3.1. Anodic Oxidation

Anodization of silicon is one way to produce an oxide on the semiconductor surface. A surface oxide may be formed which can grow to considerable thickness

provided that there is an adequate rate of ionic conduction through the film to carry the current for continued oxide growth. Film growth stops when all of the current through the film becomes electronic. The most important characteristic of the anodic oxidation process to this study is that it is carried out at room temperature. An oxide produced on silicon by this technique is not of device quality, but serves as a way to controllably remove measurable thicknesses of the silicon surface at room temperature. Alternatively, this technique has been used to produce high-quality oxides on gallium arsenide. In this section an elementary overview of the principles of anodization and oxide growth will be given. Also covered are the way the oxides have been grown for this work and the experiments done on these oxides.

3.1.1 Principles of Anodic Oxidation

Anodic oxidation, or anodization, is conducted in an electrolytic cell, as shown in Fig. 3-1. The silicon becomes the anode by connecting it to the positive terminal of the power supply. Platinum, or another noble metal, is connected to the negative terminal of the supply, thus serving as a cathode. Anodization can occur at constant voltage by keeping the source impedance of the power supply low; or it can occur at constant current by keeping the source impedance high.

Many electrolyte formulations have been used to perform the anodization. Water is the primary oxidizing component of all of these, dissociating into H^+ and $(OH)^-$. The dissociation reaction is written as

$$H_2O \longleftrightarrow H^+ + (OH)^- \tag{3.1}$$

Usually a conductivity/pH modifier is added to the system to vary the resistance of the electrolyte and/or the dissolution rate of the oxide in it. Very small amounts of these modifiers are usually required for pH control. The anodization process is also

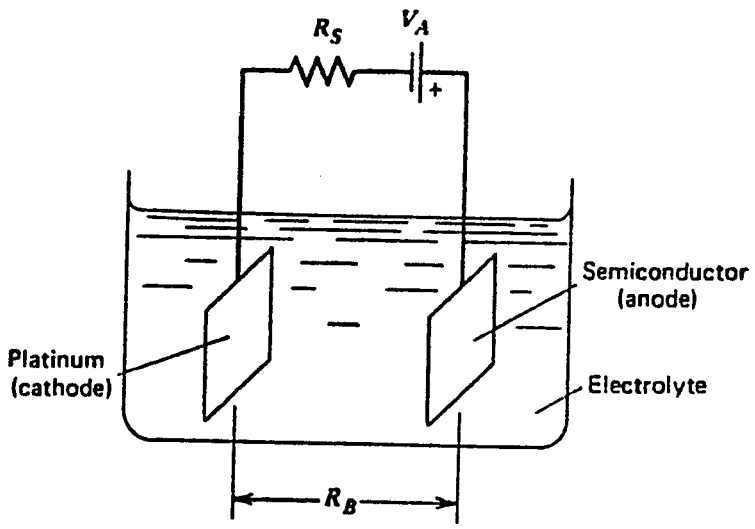

Figure 3-1. A schematic of a typical electrolytic cell used for anodization. {From Reference [1]}

possible in a nonaqueous electrolyte. Ethylene glycol or propylene glycol are often used as the nonaqueous medium. The requirement for this electrolyte is that one of its dissociation products be the $(OH)^-$ ion. The solution used in this dissertation consists of a mixture of ethylene glycol, KNO_3, and water.

The reactions leading to the anodic oxidation of silicon are as follows [1]:

(i) Dissociation of water in the electrolyte medium into H^+ and $(OH)^-$

$$2H_2O \longleftrightarrow 2H^+ + 2(OH)^- \tag{3.2}$$

(ii) Charge transfer from the silicon to the electrolyte occurs until equilibrium is reached leaving the surface layer partially depleted of electrons [2]. This effect is due to the difference in electrochemical potentials between the silicon and the electrolyte. The surface silicon atoms are promoted to a higher oxidation state during anodization since holes are supplied from the bulk of the semiconductor to the silicon-electrolyte interface.

$$Si + 2h^+ \longrightarrow Si^{2+} \tag{3.3}$$

(iii) A hydroxide is formed by combining Si^{2+} with $(OH)^-$

$$Si^{2+} + 2(OH)^- \longrightarrow Si(OH)_2 \tag{3.4}$$

(iv) By releasing hydrogen the $Si(OH)_2$ forms SiO_2,

$$Si(OH)_2 \longrightarrow SiO_2 + H_2 \tag{3.5}$$

The overall reaction is written as

$$Si + 2h^+ + 2H_2O \longrightarrow SiO_2 + 2H^+ + H_2 \tag{3.6}$$

The continuous supply of holes to the reaction interface ceases in the absence of an external energy source since the concentration of the thermally generated holes is not sufficient to form SiO_2 beyond a few monolayers. A power supply or light source provides the holes needed to support the anodic reaction and sustain the process of oxide growth. The H^+ ion drifts to the cathode, where it evolves as molecular hydrogen by the addition of electrons

$$2H^+ + 2e^- \longrightarrow H_2 \tag{3.7}$$

Both n-type and p-type silicon have been anodized in this study. The anodization of p-type semiconductors is easily accomplished since holes are readily transferred to the surface of the semiconductor by an energy source. On the other hand, the situation for an n-type semiconductor is somewhat more complex [3].

In order to carry out the anodization of an n-type semiconductor at a reasonable rate, some means of increasing the hole concentration at the surface must be found. Initially, as thermal equilibrium is established, charge transfer from the semiconductor

to the electrolyte creates a depletion layer in the semiconductor, and a barrier to the flow of holes. This is like a Schottky diode with the electrolyte being the "metal". The growing oxide reduces the available voltage across the depletion layer and anodization will stop when the voltage across this layer falls below the breakdown voltage of the semiconductor-electrolyte system.

Holes can be supplied to the surface in several ways: (1) illuminate the surface; (2) heat the semiconductor; (3) apply sufficient voltage to the electrodes to cause avalanche breakdown in the space charge layer; or (4) increase the surface generation rate of electron-hole pairs with surface damage produced by abrasion or by high energy particle bombardment (ion implantation). High-intensity illumination provides the best way of producing a large number of holes uniformly in the surface region. Light with wavelengths less than 1.2 micrometers is capable of producing electron-hole pairs in silicon. When light was used longer wavelengths were not filtered out since a high-intensity light source was not used. If a high-intenstity light source were used, a major concern would have been the overheating of the silicon and the electrolyte, thus the use of a filter would have been required. Heating of the silicon, to increase the number of holes, was not done since there is the possibility of diffusion. Avalanche breakdown occurs when the cell voltage is raised to a critical value at which holes diffusing from the silicon bulk are accelerated in the space-charge region to kinetic energies sufficient to produce hole multiplication. Because this breakdown does not occur uniformly over the silicon surface it was not used.

The number of holes available at the silicon surface is increased if the surface hole generation (recombination) velocity is increased by surface damage. This condition lasts until the damaged surface material is removed; then the anode current is limited by the rate of hole diffusion from the bulk. In all cases in this study the bulk samples

have been implanted with arsenic which creates a great deal of damage throughout the implanted range. It is therefore likely that this damage plays a role in the anodization process, especially for samples anodized immediately after implantation and before any other processing step.

3.1.2 Oxide Growth Principles

Initial oxide growth in an anodizing cell is by formation of oxide islands on the semiconductor surface [1]. A continuous oxide film is formed by nucleation. Once a film is formed oxidation proceeds by transport of the semiconductor through the oxide to the oxide-electrolyte interface, or by transport of the $(OH)^-$ ion through the oxide to the semiconductor. Oxidation is governed by Faraday's law of electrolysis. This law states that the number of grams W of material consumed per Coulomb of charge is given by

$$W = \frac{W_e}{qN} \tag{3.8}$$

where W_e is the electrochemical equivalent weight in grams of the material involved, q is the electronic charge, and N is Avogadro's number. The electrochemical weight of an element is its atomic weight divided by the change in valence involved in the reaction. During anodization silicon undergoes a valence change of 2+ (see equation 3.6). From Faraday's Law, the amount of silicon consumed per Coulomb of charge is about 1.46×10^{-4} g [1].

Before continuing the discussion of oxide growth, a few terms should be defined. The formation rate of an oxide, a, is the increase in film thickness per unit charge, passing through unit area. The oxide dissolution rate, f_d, is the change in the film thickness as a function of time, if left in the electrolyte without any applied voltage. There are a few potentials involved in the anodization process. One of these is the

applied voltage, V_a. For a p-type semiconductor V_r is the rest potential of the anodizing cell; that is, the reverse e.m.f. generated when the cell is used as a battery. In the case of an n-type semiconductor V_r is the sum of the rest potential and the breakdown voltage associated with its depletion layer. R_S and R_B are defined as the resistance of the circuit and the bath, respectively.

During anodization, current flow through the oxide is basically ionic. Assuming unit area for the electrodes, the initial current flow I_o is given by

$$I_o = \frac{(V_a - V_r)}{(R_S + R_B)} \tag{3.9}$$

and the equivalent dissolution current, I_d, is given by

$$I_d = \frac{f_d}{a} \tag{3.10}$$

For high fields, as in the case of anodization of silicon where the electric field during anodization, E_{ox}, is on the order of 2×10^7 V/cm, it can be assumed that there is a constant electric field across the oxide during film growth. Using this assumption, the final thickness of the oxide formed is

$$x_f = \frac{(V_a - V_r)\ (I_o - I_d)}{E_{ox}\ \ I_o} \tag{3.11}$$

By writing Kirchhoff's Law for the anodizing circuit the growth rate of the oxide can be determined. Thus

$$V_a - V_r = i\,(R_S + R_B)\ + a\,E_{ox} \int_0^t i\,dt \tag{3.12}$$

A solution of this equation is

$$x = x_f\,(1 - e^{-t/\tau}) \tag{3.13}$$

where the time constant for growth τ is given by

$$\tau = \frac{(R_S + R_B)}{a\, E_{ox}} \tag{3.14}$$

Oxide thickness builds up exponentially until a final value, prescribed by the applied voltage, is reached. Typically the final oxide thickness is 3 Å/V for silicon.

When a constant current source is used for anodization, Faraday's Law requires that the oxide thickness vary linearly with time. The voltage drop across the oxide will also increase linearly with time since the field across the oxide is constant. This behavior allows the monitoring of the film thickness; i.e., monitoring the linear increase in voltage with time, and then stopping the process at some preset voltage produces a given oxide thickness.

3.1.3 Silicon Dioxide Growth by Anodic Oxidation

Studies on the anodic oxidation of silicon were performed in the 1960's. The reason for doing these studies was to find a way to remove successive layers of silicon and measure the dopant profile.

Results were not reproducible for n-type silicon. It was found that a solution of 10 percent by volume water in ethylene glycol and 4.0 g KNO_3 in 1000 ml solution provided the best results [4], [5]. The electrolyte is best prepared by dissolving the KNO_3 in the water and then adding the ethylene glycol to the solution. When less water was used peeling and variable thicknesses occurred. Using larger percentages of water led to etching.

Making reproducible oxide thicknesses depends upon (1) the chemical pretreatment of the silicon surface, (2) the intensity of any illumination used, and (3) thermal stability during anodization (accumulation of bubbles on the silicon surface

should be avoided). A current density of 5 to 10 mA/cm^2 proved to be the best for providing reproducible results. The starting voltage of the reaction is strongly dependent upon the chemical surface treatment and illumination. One case where illumination is not necessary is when an n-type surface layer has been produced by either implantation or diffusion of donor type impurities into p-type silicon.

The ratio of the reacted silicon to the thickness of the oxide grown is important in this study. For thermal oxides this ratio is approximately 0.44. Bunsen and Linzey [4] found this ratio to be between 0.6 and 0.8 for short time anodization and about 0.4 for reactions that consume 300 Å of silicon. Later in this section it will be shown that our results give a ratio of about 0.44, i.e., that of thermal silicon dioxide.

3.1.4 Anodizing Systems Used

Several systems were used to perform anodic oxidation throughout this study. These systems included both constant voltage and constant current supplies. Also used were different anodizing cells.

Different supplies were used at different times during this study. The first supply used was a constant voltage supply. This system was used to do an anodization and stripping technique for the initial differential Hall effect measurements. A diagram of the cell used for this technique is shown in Fig. 3-2. The area anodized in this cell was about 30 mm^2. When the area for anodization was increased to about 20 cm^2 a very nonuniform oxide layer was produced. This was corrected by forming the platinum wire into a flat spiral.

Further improvements included designing and building a constant current supply and a new anodizing cell. The constant current supply has a current range of 0 to 90 mA and a voltage range of 0 to 145 volts. This supply allows more control over the

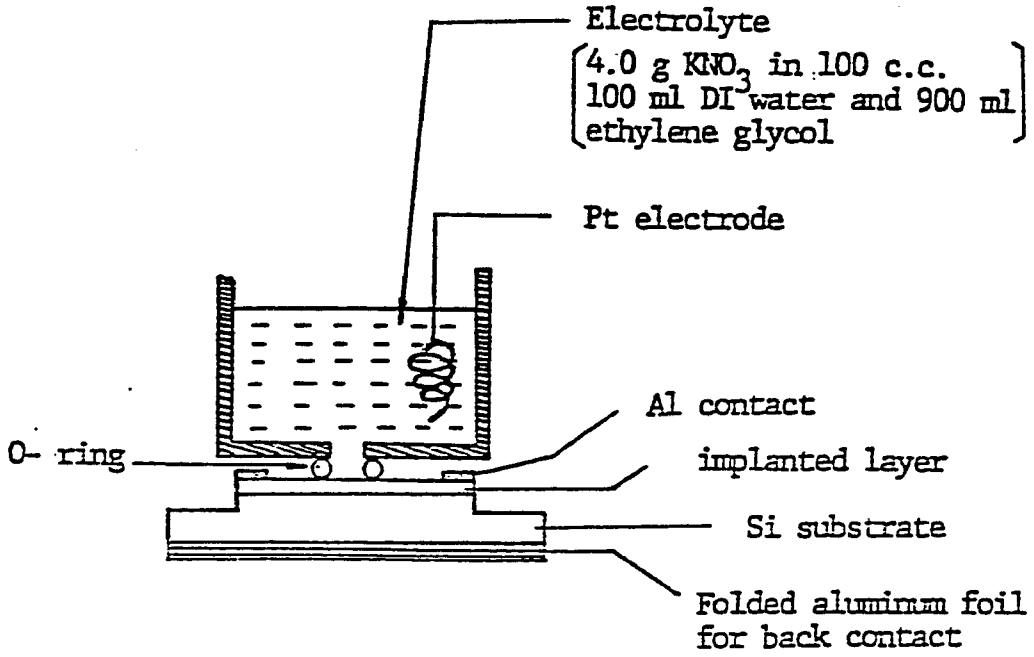

Figure 3-2. A schematic of the cell used for anodic oxidation and oxide stripping.

anodization process and better reproducibility. Larger areas than previously mentioned can now be anodized. A cell similar to that in Fig. 3-2 was fabricated with a 5 cm opening. This allowed anodization of a 5 cm diameter region on a silicon wafer.

3.1.5 Experimental Results

How the anodizing process affects the implanted and/or diffused arsenic profile must be examined. The profiles after the anodic oxide growth were studied by Secondary Ion Mass Spectrometry (SIMS), Auger Spectroscopy, and lapping and staining.

SIMS studies were performed on three samples: a 600 Å thermal oxide made at 900 °C for 75 minutes in dry oxygen and two anodic oxides of 276 ± 2 Å and 540 ±

30 Å. All analyses were made on a Cameca IMS-3F with an O_2^+ beam at AT&T Bell Laboratories, Allentown. Results are shown in Figures 3-3 through 3-6 for the as-implanted profile, the thermal oxide, and the anodic oxides, respectively. From the results in Fig. 3-4 we see that the thermal oxide is very abrupt. The 600 Å oxide thickness, measured by ellipsometry, is shown on the figure. Figures 3-5 and 3-6 show the results for the 276 Å and 540 Å oxides, respectively. These oxide thicknesses were measured by ellipsometry and are shown on the figures. From these figures we can see that the anodic oxides are not as abrupt as the thermal oxide. By comparing the as-implanted profile of Fig. 3-3 with the profiles of Figures 3-4 through 3-6 we can draw the following conclusions: (1) during thermal oxidation the implanted arsenic distribution diffuses significantly; (2) no diffusion occurs during the anodic oxidation within the error of the SIMS measurement (±50 Å); (3) the silicon dioxide - silicon interface is in the same general location (within experimental error) measured by SIMS and ellipsometry; and (4) the transition regions from oxide to silicon are different for thermal and anodic oxides.

Part of the 540 Å anodic oxide was etched in 10% HF for approximately 45 seconds until the surface was hydrophobic. The SIMS concentration profile for this sample is shown in Fig. 3-7. Comparison of this figure with Fig. 3-3 shows that approximately 238 Å of silicon has been removed from the surface of the implanted wafer. This number is in agreement with the 540 Å oxide grown since we had assumed that the thickness of silicon removed (reacted) was 44% of the grown oxide thickness as in the case of a thermal oxide.

Auger spectroscopy was performed on the same set of samples. The conclusions from this study are the same as those drawn in the SIMS study.

A lapping and staining experiment was done to see the effects of the anodization

on the electrically active profile. Windows of bare silicon were anodized. Before anodization the junction below the window was the same as the junction under the insulator. The samples were then lapped and stained with 49% HF. The junction under the silicon window did not diffuse during the anodization. This again showed that the junction depth was not affected by the anodic oxidation process.

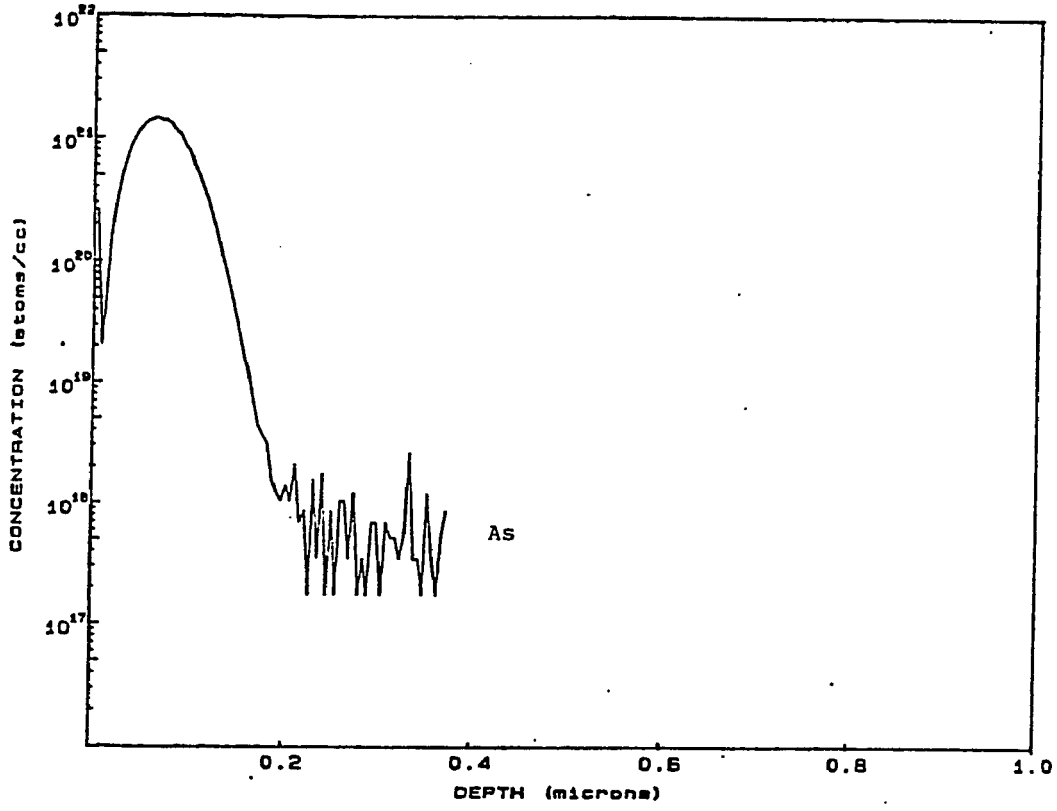

Figure 3-3. SIMS profile of the 1 X 10^{16} cm^{-2} arsenic implant.

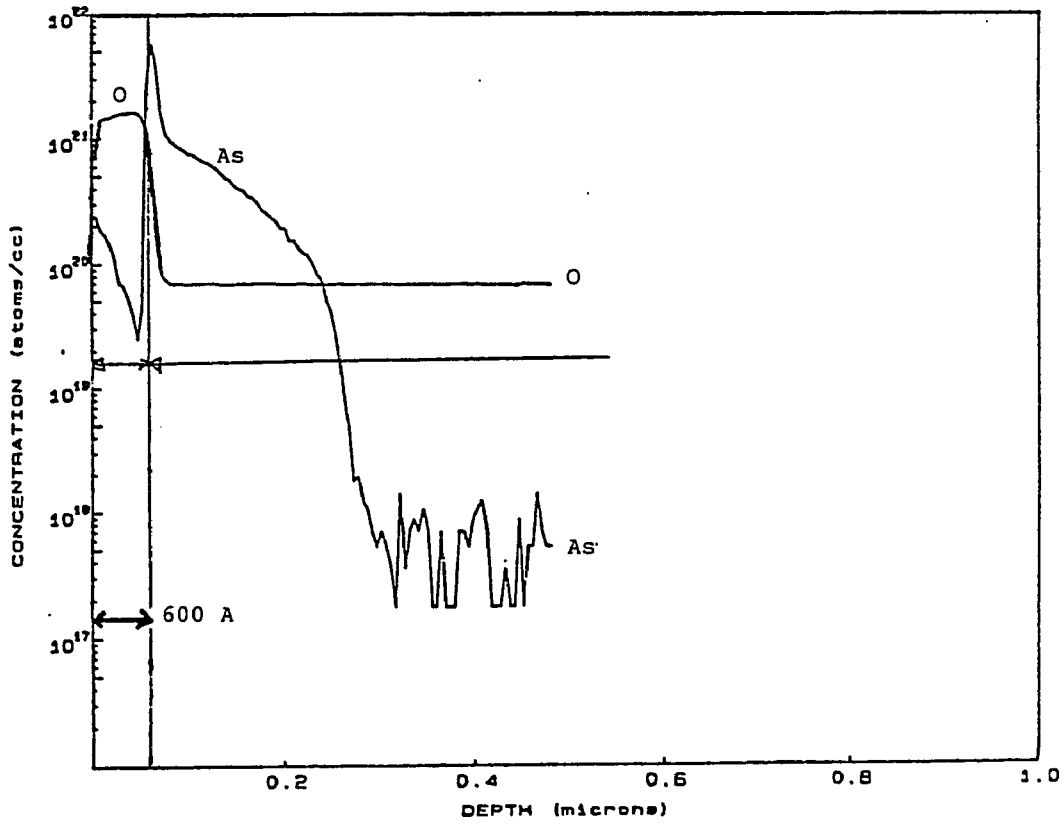

Figure 3-4. SIMS profiles of arsenic and oxygen after thermally growing a 600 Å oxide layer.

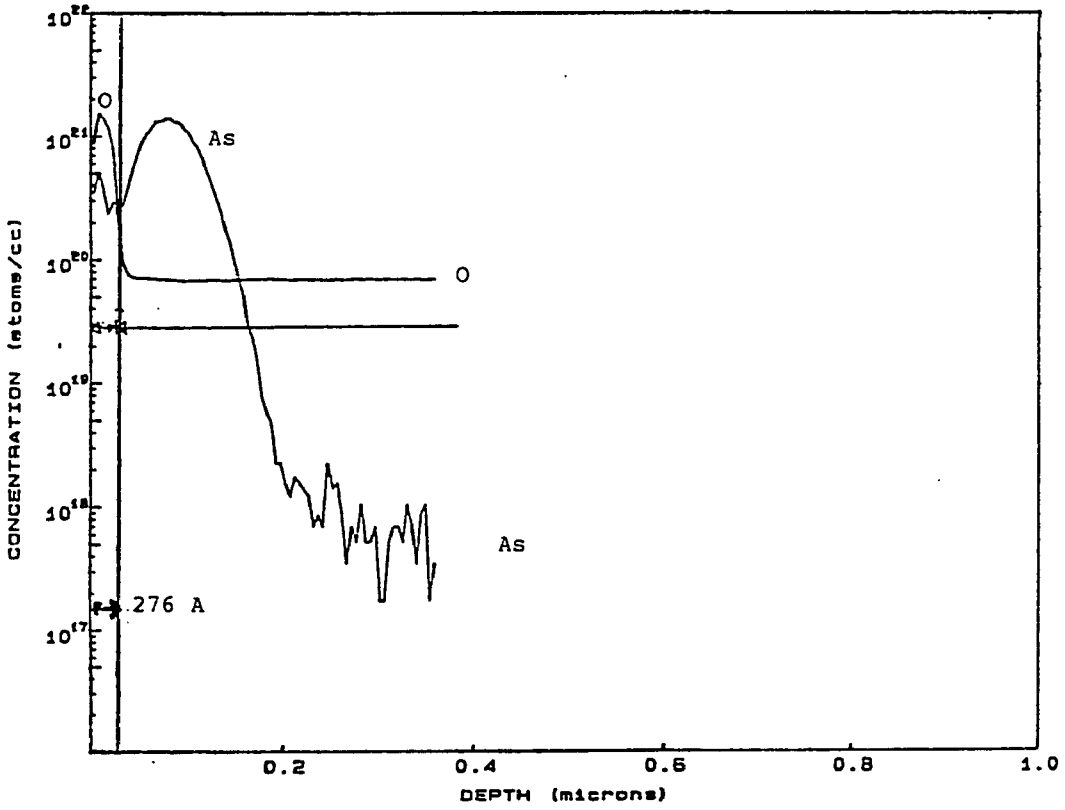

Figure 3-5. SIMS profile after growing a 276 Å anodic oxide.

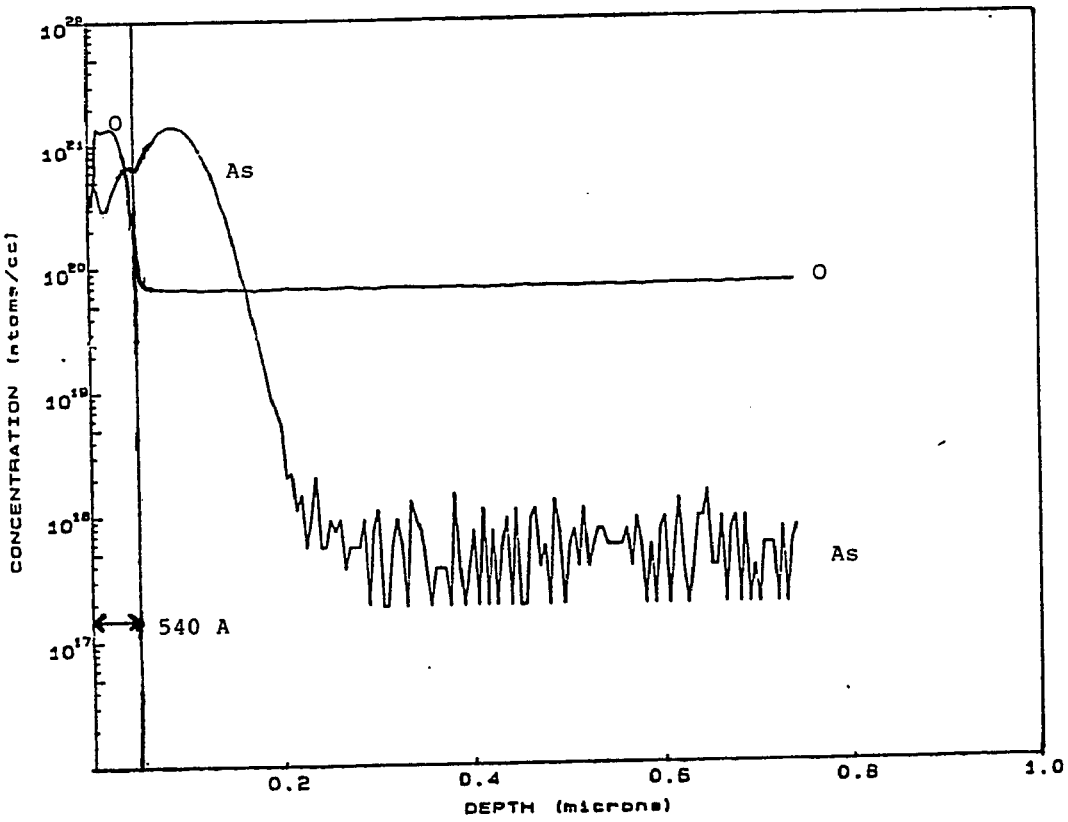

Figure 3-6. SIMS profile after growing a 540 Å anodic oxide.

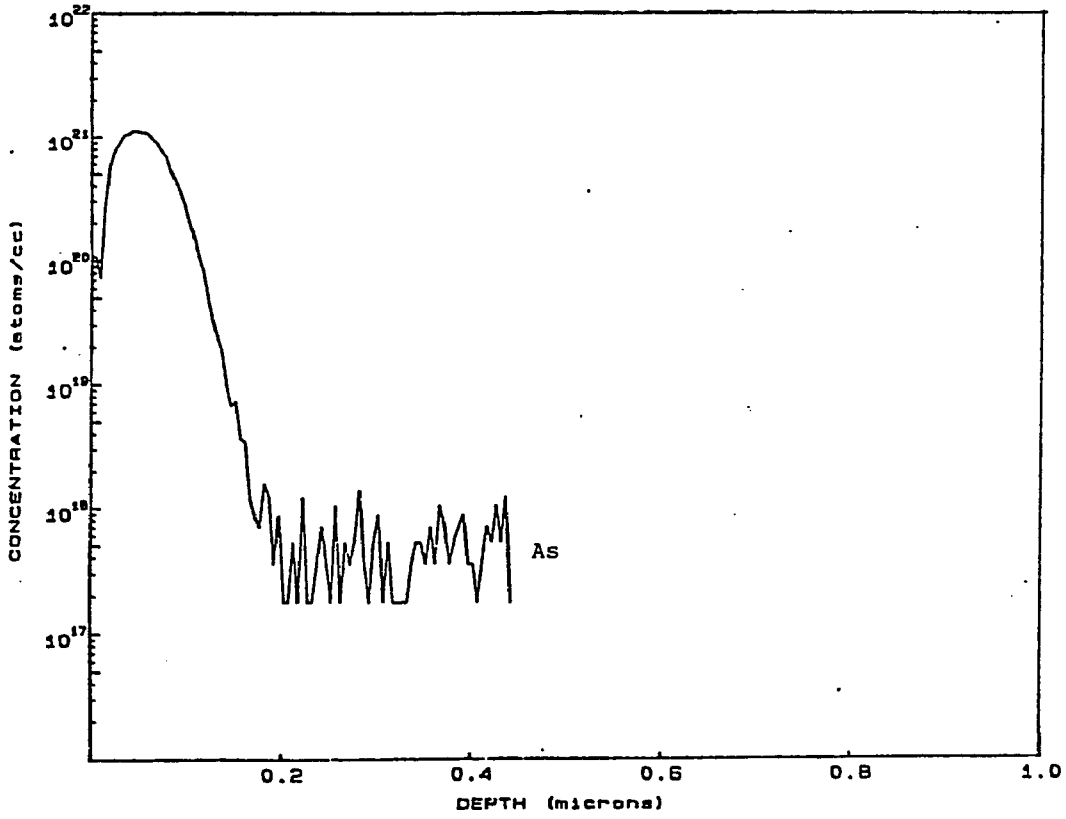

Figure 3-7. Arsenic profile (by SIMS) after the 540 Å anodic oxide in Fig. 3-6 was removed.

3.2 Sample Preparation

The majority of samples analyzed for this dissertation were above the amorphization dose for arsenic implanted <100> silicon. Samples implanted at 100 keV to a fluence of 1 X 10^{16} cm^{-2} served as the core of this work. It is known that a fluence above 3 X 10^{14} cm^{-2} will create a continuous amorphous layer [6]. Most of the other samples were implanted to fluences between these two values.

In this dissertation the implant tail region will be the region beyond the projected range plus the straggle ($R_p + \Delta R_p$). This region is below the amorphous region and beyond the peak arsenic concentration. To fabricate "tail-only" samples the damaged and peak concentration region are remove by the anodization and stripping technique discussed in the previous sections. In most cases over 1100 Å of silicon have been removed. Thus only the tail of the arsenic distribution and end-of-range damage remain in the tail only samples before the heat treatment.

Several studies were also performed on samples implanted through a surface oxide. In these studies 1 X 10^{15} and 5 X 10^{15} cm^{-2}, 140 keV implants were done through an 800 Å thermal oxide. This allowed a majority of the arsenic to be implanted into the oxide. Most of the implant damage was also confined to the oxide region. The silicon substrate then consisted of an arsenic tail and recoil-implanted oxygen. Before any other processing, the surface oxide was removed in a 10% HF etch until the silicon became hydrophobic. This removed any possible doped oxide effect in subsequent heat treatments.

All samples were capped with a layer of spin-on-glass. This was accomplished by applying ACCUGLASS 102 while the sample was spun at 5500 r.p.m. for 20 seconds. ACCUGLASS 102 is manufactured by Allied Chemicals. This spin-on-glass is a solution of silicon-oxygen polymeric materials in an alcohol/ketone solvent system.

After spinning, all samples were heated to 100°C for 10 minutes. This is the standard prebake suggested by the manufacturer. This process yields high quality films of essentially pure silicon dioxide.

Samples were annealed in the temperature range of 800°C to 1100°C. All furnace anneals were performed for 30 minutes in a Mini-Brute model MB-71 laboratory diffusion furnace by Thermco Systems, Inc. High purity nitrogen was introduced into the furnace at a rate of 1 l/min during annealing. Prior to annealing samples were placed at the furnace opening for one minute and then moved to the central zone at a rate of one inch every three seconds. After the 30 minute anneals, the samples were removed by reversing the first two steps.

Rapid thermal annealing (RTA) was performed in the same temperature region as the furnace anneals. The annealer was a Heatpulse 210M by AG Associates as described in Section 1.2.2. A majority of the anneals were performed for 10 seconds in a 1 l/min flow of high purity nitrogen. Actual temperature profiles can be seen in Fig. 1-11. Any deviations from the processing described in this section will be denoted in the appropriate discussion.

3.3 Electrical Measurements

In this section we will discuss the electrical characterization of implanted and annealed arsenic in silicon. Each technique used examines different aspects of the electrical activity of arsenic in silicon.

3.3.1 Spreading Resistance Measurements

The spreading resistance technique has been used for many years as a way to measure resistivity and electrically active dopant profiles. This method is based on a low voltage measurement of the contact resistance of a small area contact on a

specially-prepared silicon surface. It is referred to as "spreading resistance" because the dominant resistance of a point contact diode occurs in a very small volume beneath the probe, where the current spreads out into the sample. For a flat circular contact of radius a on a sample of resistivity ρ , the measured spreading resistance (from theory) should be [7].

$$R_m = \frac{\rho}{4a} \tag{3.15}$$

In actuality this is a very complex function of a number of variables including sample conductivity type, crystallographic orientation, surface finish and the mechanical micro-structure of the probe tip. Figure 3-8 illustrates a schematic of dopant profiling with the spreading resistance technique.

It is important to realize that this is a comparison technique. Therefore, calibration curves for a particular pair of probes at a particular time must be generated using a set of known resistivity samples of the same type, orientation, and surface finish as the samples to be profiled. The known resistivity samples are NBS standards that may be obtained through Solid State Measurements, Inc. Once data is obtained from the test samples, a comparison is made with the calibration curves to determine the local resistivity. In most cases a correction factor C must be determined to obtain the resistivity from the measured spreading resistance [9,10], thus

$$\rho = \frac{2aR_m}{C} \tag{3.16}$$

Since this technique is comparative in nature, it is of the utmost importance to have reproducible contacts. The first step to assure reproducibility is to determine that each probe has the same load. In our case this is 10g. Next the probes must be "conditioned". The device used in this process is called the Gorey-Schneider probe grinder (shown in Fig. 3-9). This device has two sapphire plates; one for 1 micron

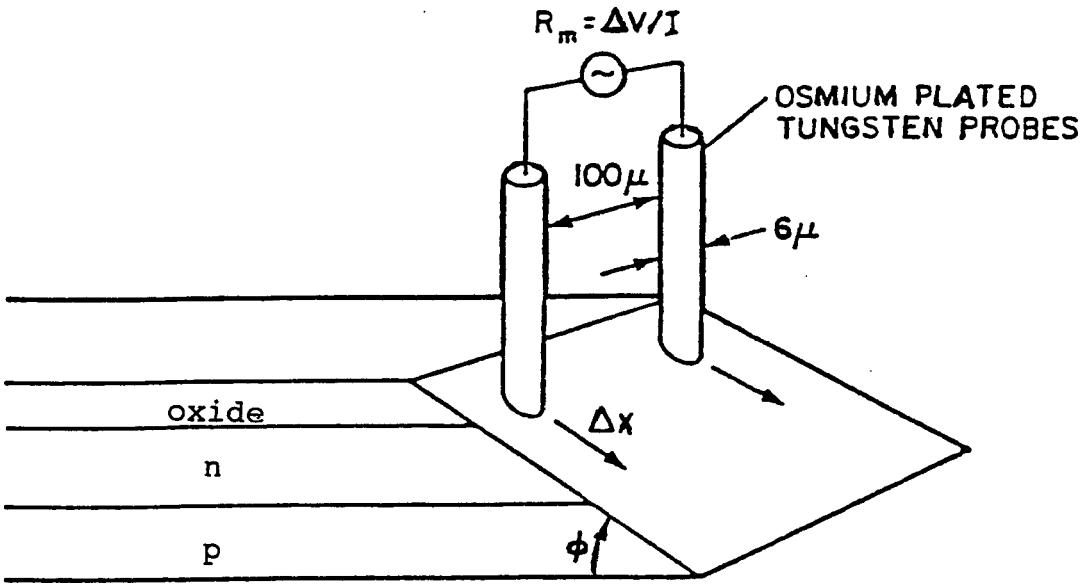

$$\Delta y = \Delta x \sin \phi$$

$$\phi = 16' \qquad \Delta x = 5\mu \rightarrow \Delta y = 233\,\text{Å}$$

Figure 3-8. A schematic illustrating dopant profiling with the spreading resistance technique. {After Reference [8]}

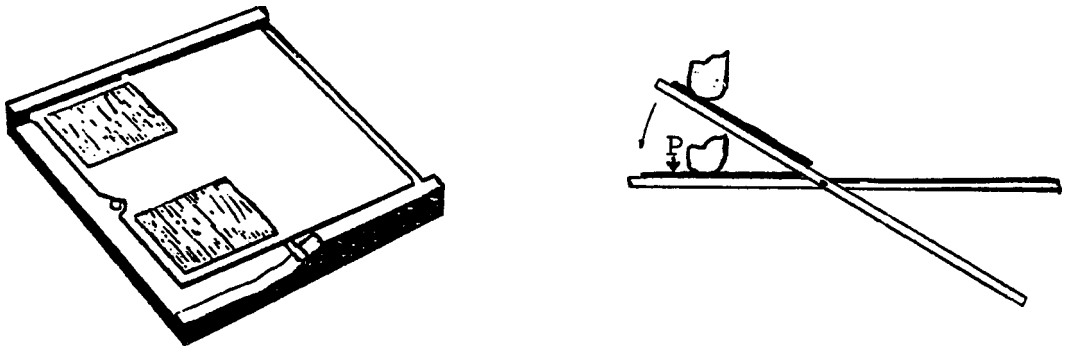

Figure 3-9. (a) The Gorey-Schneider Probe Grinder. (b) A schematic view of the grinder in use where "P" is the initial point contact between the probe and the sapphire plate. {From Reference [7]}

diamond paste and the other for Y_4 micron paste. The grinder is mounted similar to that of a sample and a single spreading resistance probe tip is set on one of the sapphire plates. Usually the probe is set down on the pivoting sapphire surface several times before rotating the grinder and repeating the process. The probe tips are then cleaned with an organic solvent. Measurements are then made on qualification samples to assure proper contact and penetration. If the measured resistance is not within the error noted on the standard qualification samples, the probe must undergo further conditioning.

Once both probes are qualified, then measurements on the NBS standards may be performed and recorded. [This step was not possible on the ASR-100 (Solid State Measurements, Inc.) at Lehigh, but was possible on the ASR-130 at Bell Laboratories in Allentown, PA.] After this step it is possible to convert the measured spreading resistance into electrically active (or carrier) concentration with the aid of a computer program.

The surface finish of the sample after beveling is also important. In this study samples were polished with 1/10 micron diamond paste and oil to bevel angles between 4′ and 16′. After polishing, the samples were cleaned with a cotton swab and alcohol to prevent the possibility of oxidation created by water cleaning. Oxidation would change the measured electrical activity. Also note in Fig. 3-8 that the original sample surface is covered with spin-on-glass. This eliminates the possibility of measuring on a rounded bevel near the surface. It also offers the advantage of knowing when the probes have crossed from the high resistivity oxide into the low resistivity implanted region.

To make a profile measurement the probes are stripped across the bevelled surface. Although it is possible to make very small steps, in this work we have chosen

to use step sizes of 2.5 microns or larger. Below 2.5 microns the probe damage can overlap [8] and result in erroneous data. As shown in Fig. 3-8 a 5 micron step on a 16' bevel results in a vertical step of 233 Å.

To determine the actual vertical step size the bevel angle on the silicon sample must be measured after polishing. The may be determined by two different techniques. The first method is the use of a patented device (called the SAM ring) available from Solid State Measurements, Inc. Use of this technique is described in Ref. [8]. The other method is to reflect a collimated light source from the bevel surface, measure the distance between the incident light beam and the reflected beam, and use trigonometry to determine the angle. The latter method was used because of its accuracy and it requires less time.

3.3.1.1 Experimental Results

This initial investigation of damage annealing , arsenic diffusion, and electrical activation was conducted on the core set of samples (100 keV arsenic implanted to a fluence of 1 X 10^{16} cm^{-2} into <100> p-type silicon). Both total and tail-only samples were furnace annealed for 30 minutes in the temperature range of 800 to 1100°C. Spreading resistance measurements were performed on these samples. In Fig. 3-10 the tail-only sample is more electrically active and has diffused further into the original sample than the total. This was typical of samples annealed between 800 and 900°C. At 950°C and above the total profile has diffused deeper than the tail. This can be see in Fig. 3-11 for samples annealed at 1100°C. Note that the peak carrier concentration is the same for both the total and tail and that the total has diffused significantly (approximately 3000 Å more than the tail). This suggests that the amorphous layer remaining in the total samples must anneal before significant activation and diffusion can occur. Since the tail samples do not have an amorphous

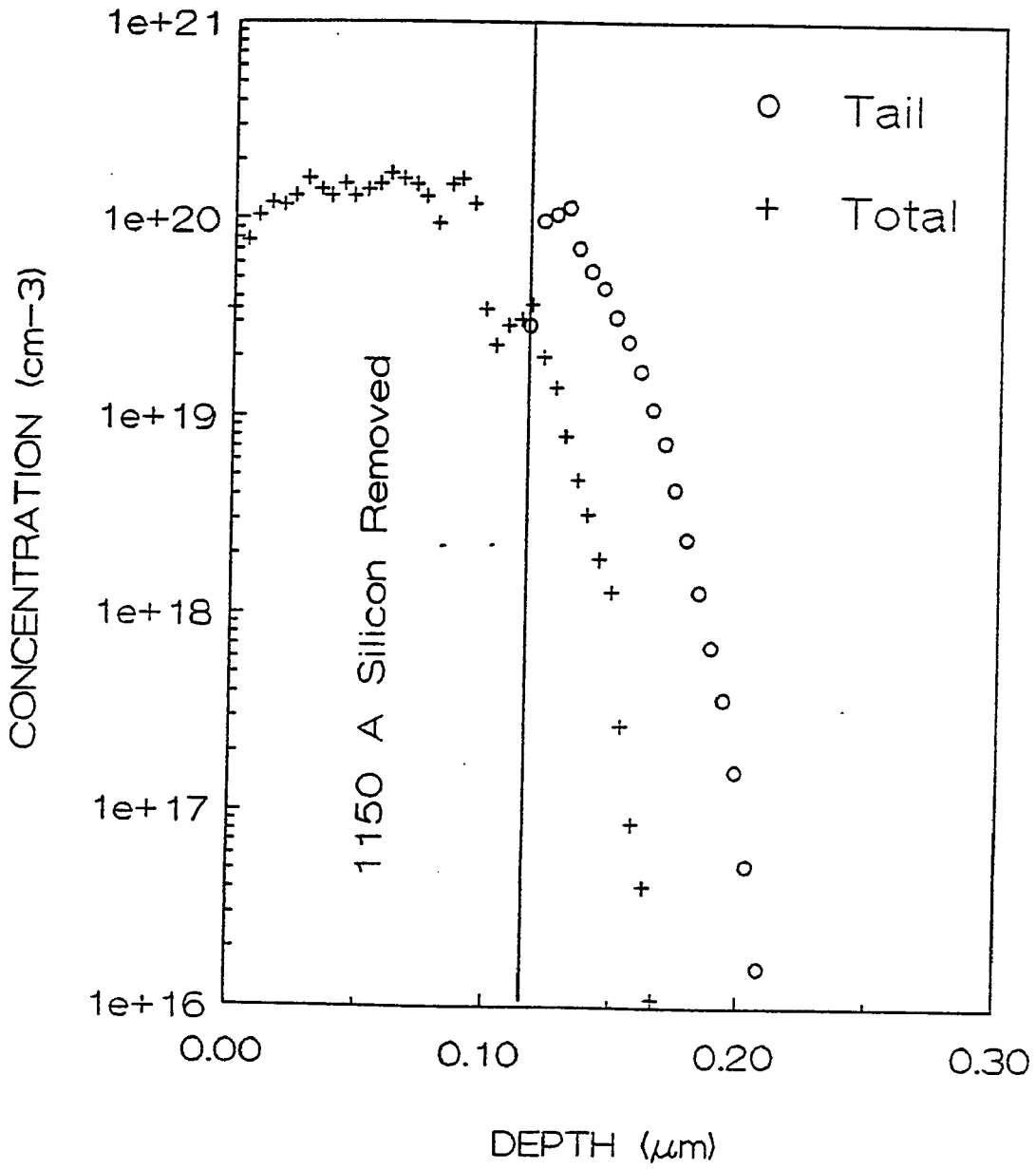

Figure 3-10. Carrier concentration (electrically active arsenic) profiles obtained by spreading resistance. Between 800 and 900°C the tail-only samples (o) have deeper junctions than the total (+). Shown here are the 800°C profiles.

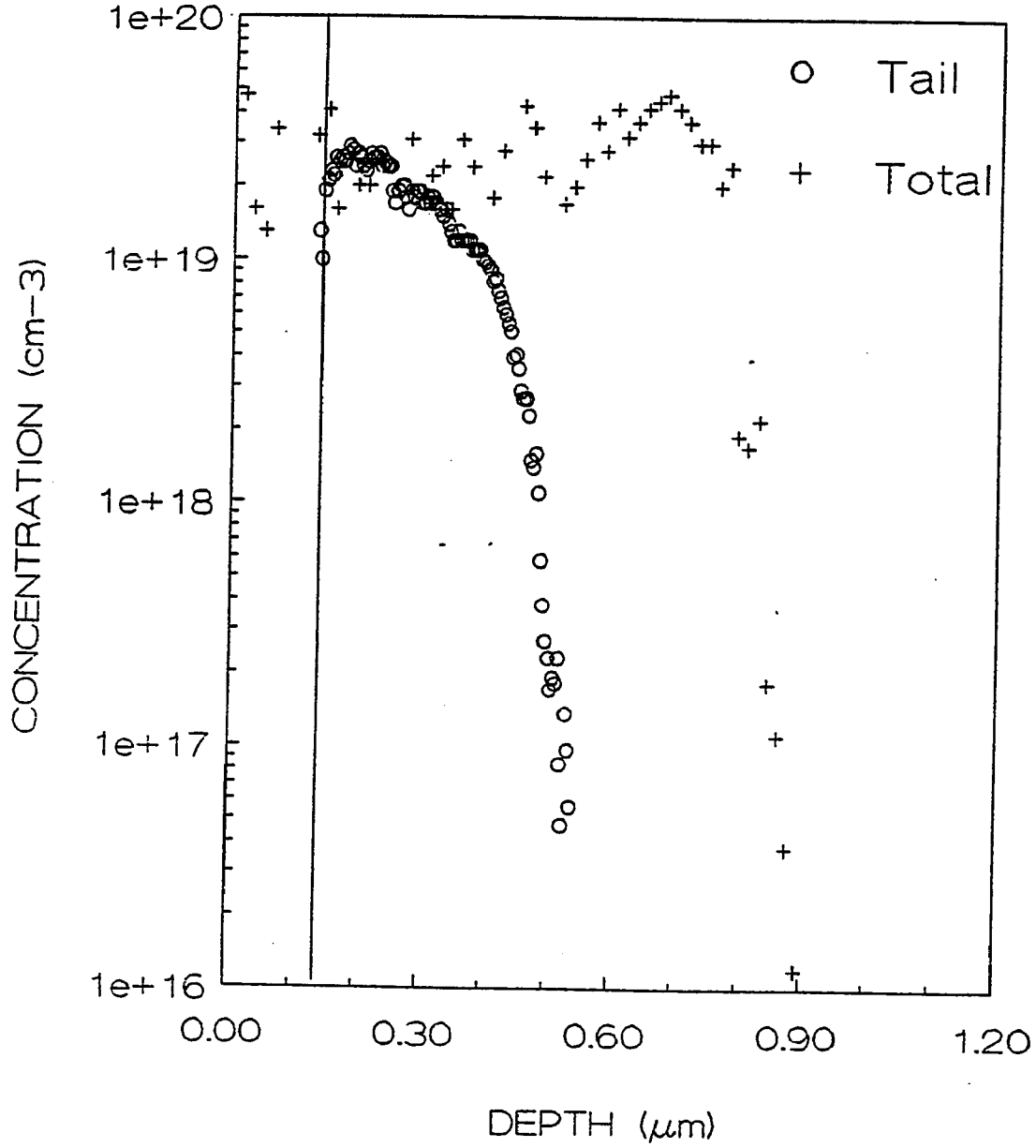

Figure 3-11. Carrier concentration profiles for the tail-only (o) and total (+) samples annealed at 1100°C.

layer, diffusion and electrical activation proceeds differently than the total.

To determine if this effect was time dependent, 10 second rapid thermal anneals were performed on the core set of samples in the same temperature range as the furnace annealed samples. Again at 800°C the tail-only sample has diffused deeper and became more electrically active than the total (see Fig. 3-12). As in the furnace annealed case, annealing at and above 950°C resulted in the total diffusing deeper than the tail (see Fig. 3-13). Contrary to the furnace annealed case, the peak tail carrier concentration at 1080°C is lower than the peak total concentration. At this point several different interpretations may be proposed. (1) Under rapid thermal annealing the amorphous layer has recrystallized after the 10 second anneal at 1080°C whereas the end-of-range damage in the tail-only sample has not. If this is true, the high concentration in the total profile sample would diffuse by a concentration dependent diffusion. (2) The lower activity in the tail region could be due to defects that remain after annealing, which thereby decrease the electrical activity. These points will be discussed in the next chapter after results from the various studies are presented.

Another question may be asked about these data. That is, when the temperature is increased from 800 to 1080°C does the electrically active concentration increase? In Fig. 3-14 the carrier concentration profiles for the total samples are plotted. The results for the tail-only samples are shown in Fig. 3-15. As expected, the arsenic becomes more electrically active and diffuses as the anneal temperature is increased.

To examine the concentration dependence on the tail diffusion several other implants were performed. These new conditions and their peak (volume) concentrations are shown in Table 3-1. Included in this table are the condition for the core set of samples.

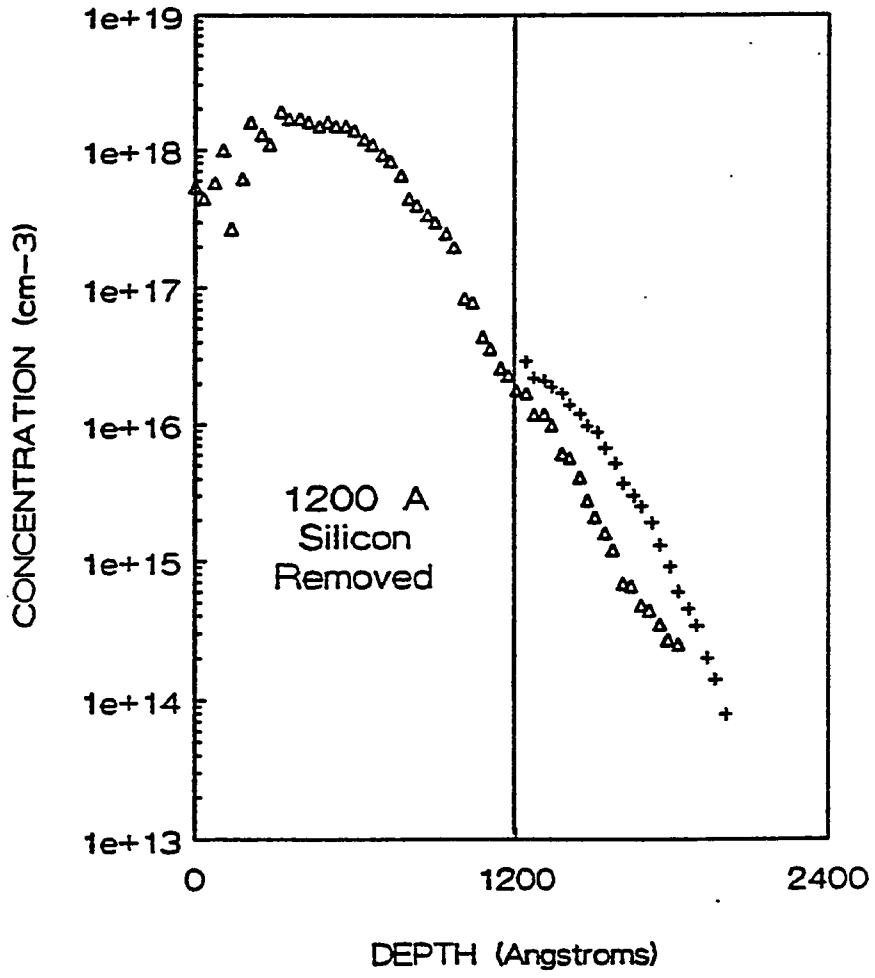

Figure 3-12. Carrier concentration profiles for the tail-only (+) and total (Δ) samples rapid thermal annealed at 800°C for 10 seconds.

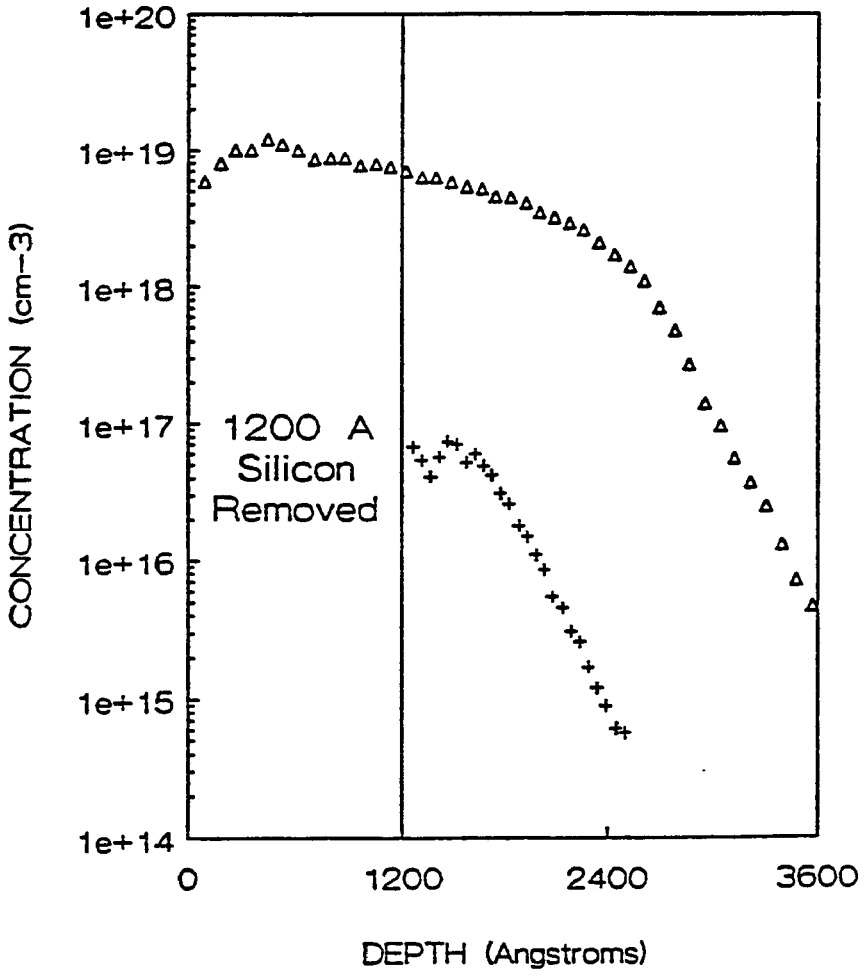

Figure 3-13. Carrier concentration profiles for the tail-only (+) and total (Δ) samples rapid thermal annealed at 1080°C for 10 seconds.

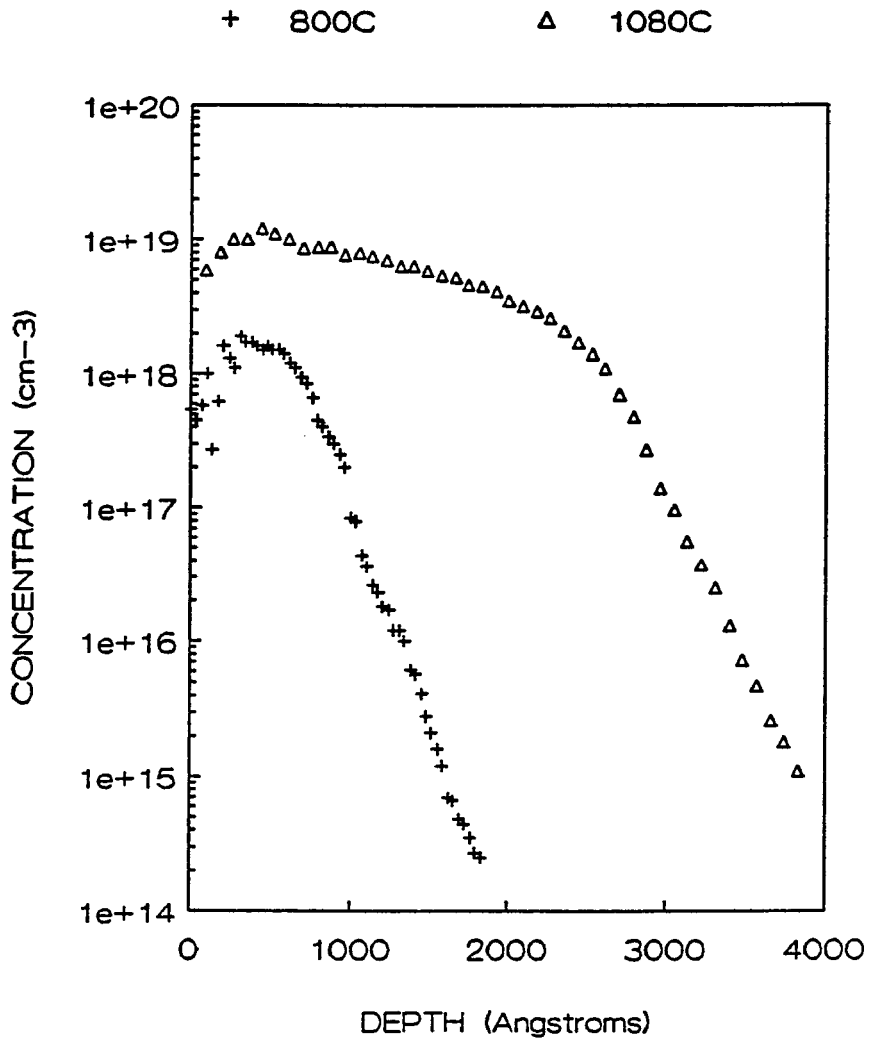

Figure 3-14. Spreading resistance data for the 1 X 10^{16} cm^{-2}, 100 keV total samples annealed by RTA for 10 seconds.

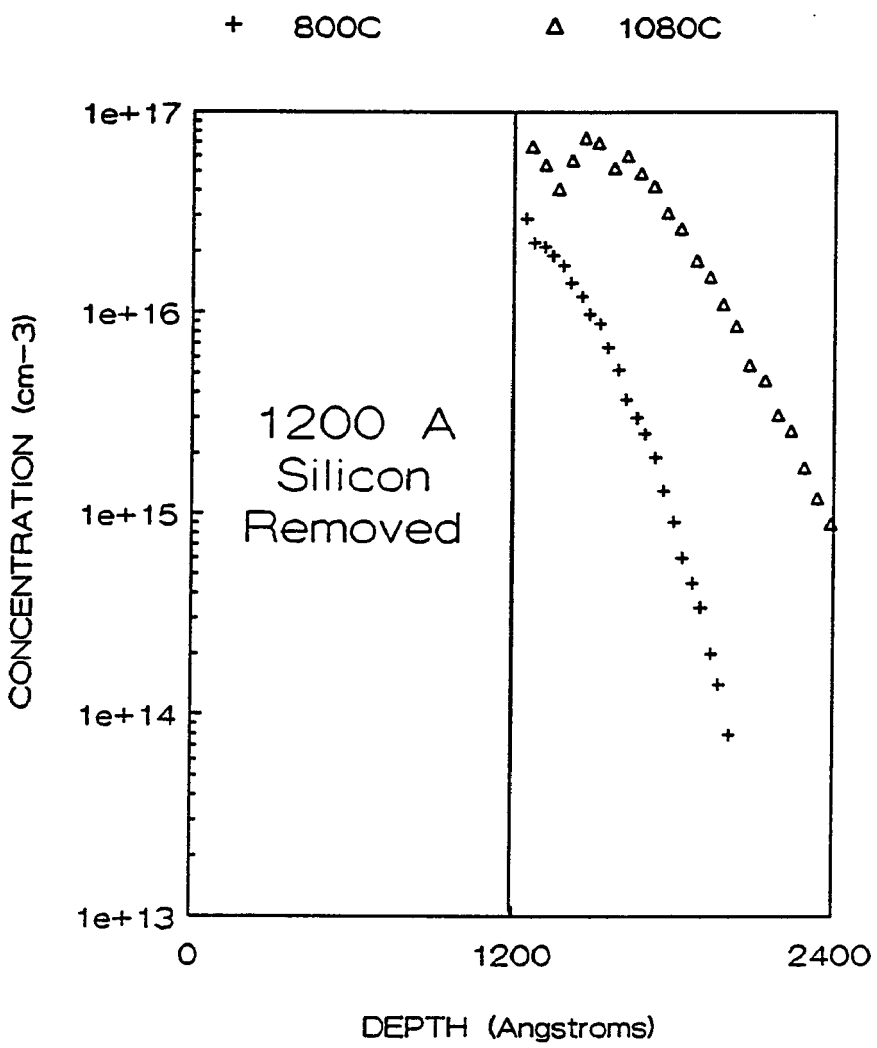

Figure 3-15. Spreading resistance data for the 1 X 10^{16} cm^{-2}, 100 keV tail-only samples annealed by RTA for 10 seconds.

Table 3-1. Implant Conditions Used in the RTA Studies.

Dose (cm^{-2})	*Energy* (*keV*)	*As-Implanted Peak Concentration* (cm^{-3})
1×10^{16}	100	1.98×10^{21}
1×10^{15}	50	3.25×10^{20}
1×10^{14}	50	3.25×10^{19}

Figures 3-16 through 3-19 show the results of the 10 second RTA treatments on the 1×10^{15} cm^{-2} and 1×10^{14} cm^{-2} samples. For the 1×10^{15} cm^{-2} case, annealing at 800°C for 10 seconds produced the same result as previously discussed (see Figs. 3-10 and 3-12), i.e., the tail has diffused deeper and become more electrically active than the total. Contrary to the earlier results, a 1080°C, 10 second anneal is required for the total to diffuse deeper and become more electrically active (in the tail region) than the tail. This may be due to the decrease in arsenic concentration. As shown in Table 3-1 the peak concentration for the 1×10^{15} cm^{-2} implant is 3.25×10^{20} cm^{-3}. For the temperature range studied (800 to 1080°C) the solid solubility range is 1.4 to 3.9×10^{20} cm^{-3}. (see Chapter 2) Therefore the peak concentration of the 1×10^{15} cm^{-2} implant is very close to the solubility limit, whereas the 1×10^{16} cm^{-2} implant has an initial peak volume concentration far above the solubility limit.

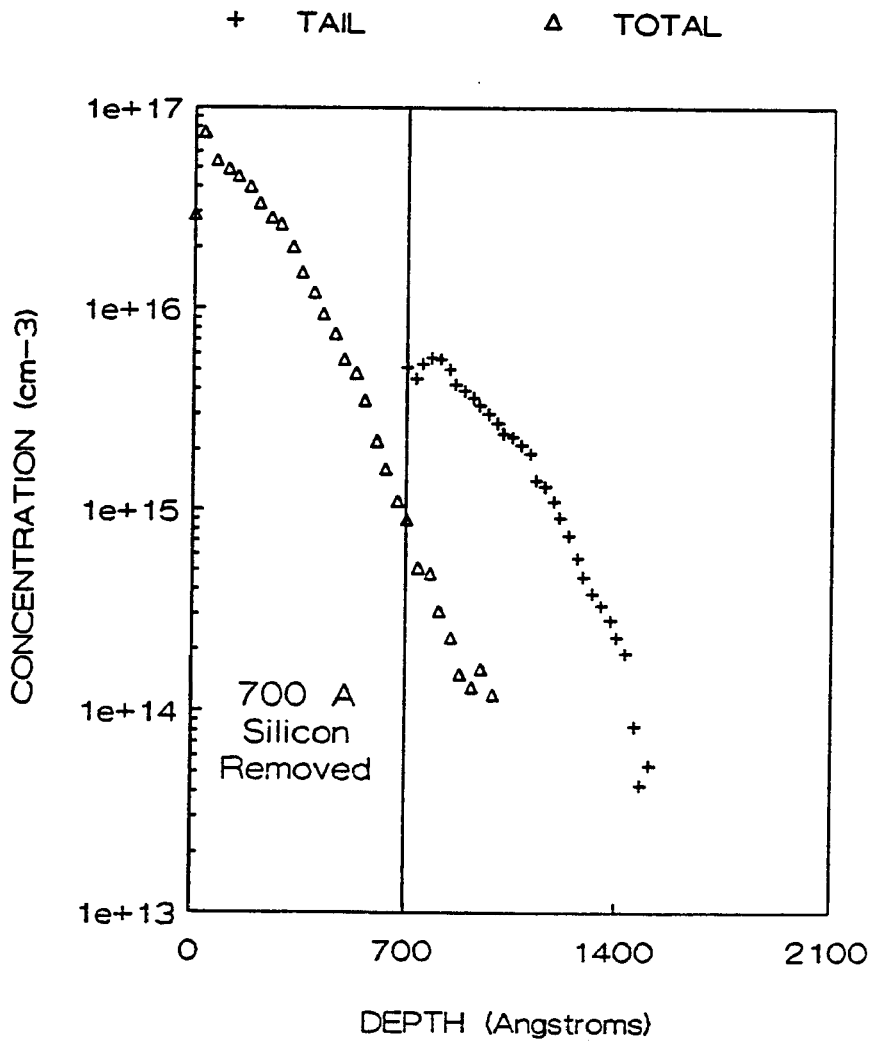

Figure 3-16. The 800°C carrier concentration profiles for the 1 X 10^{15} cm^{-2} samples annealed by RTA for 10 seconds.

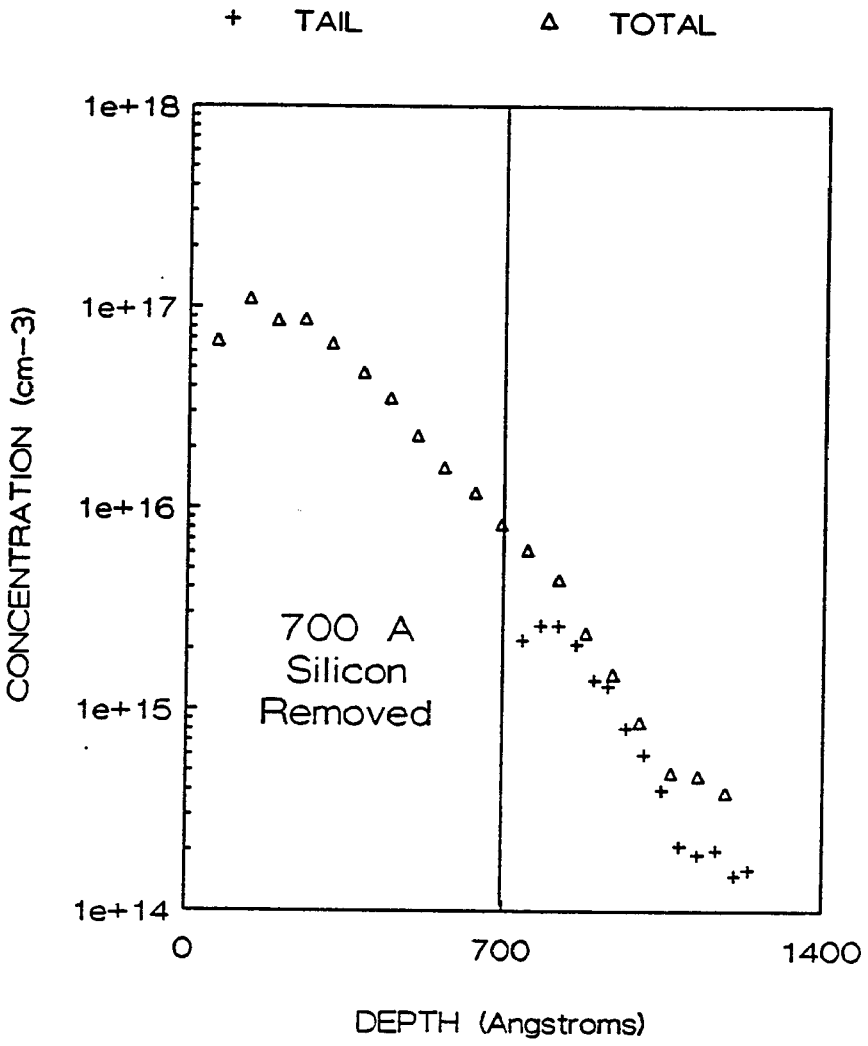

Figure 3-17. The 1080°C carrier concentration profiles for the 1 X 10^{15} cm^{-2} samples annealed by RTA for 10 seconds.

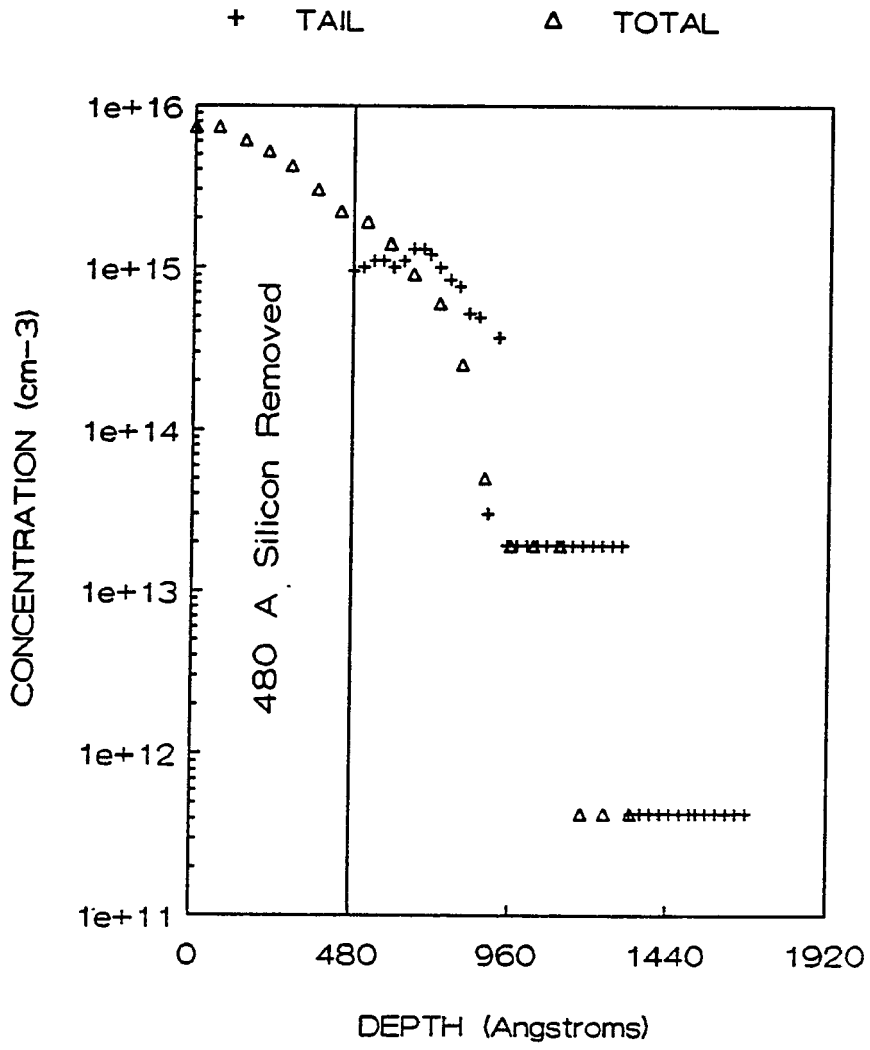

Figure 3-18. The 800°C carrier concentration profiles for the 1×10^{14} cm^{-2} samples annealed by RTA for 10 seconds.

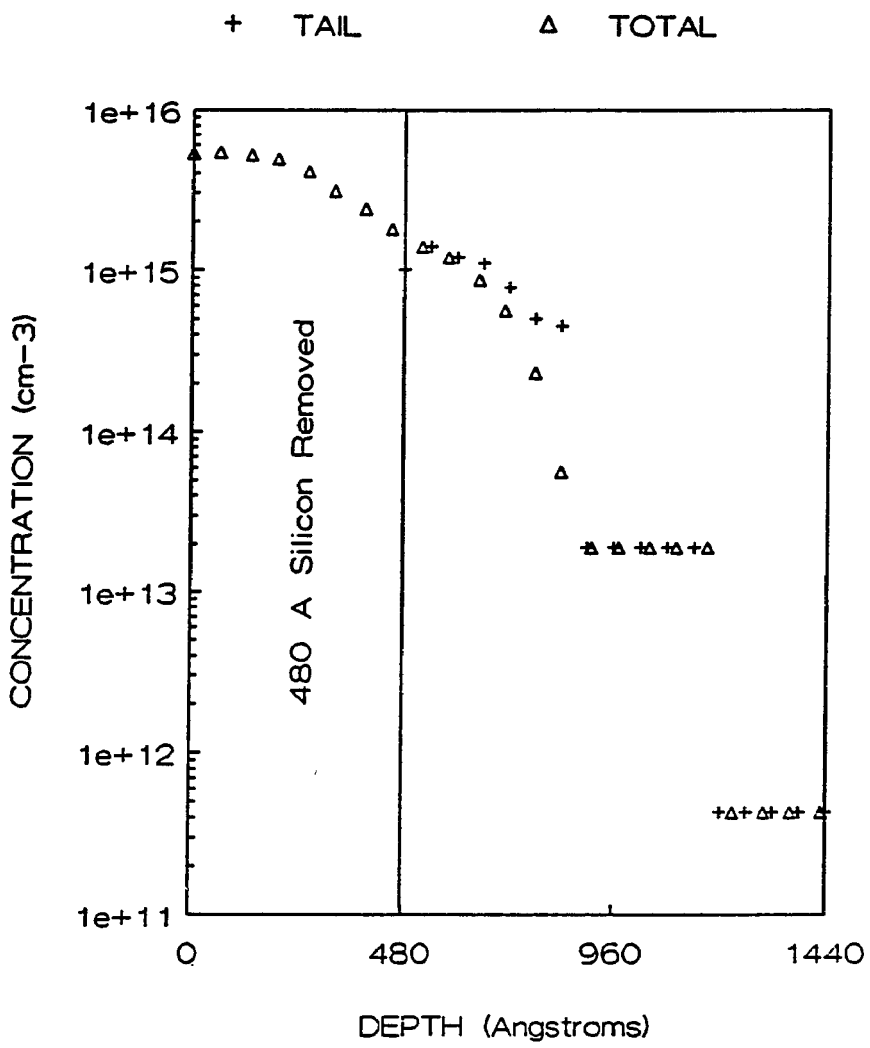

Figure 3-19. The 1080°C carrier concentration profiles for the 1 X 10^{14} cm^{-2} samples annealed by RTA for 10 seconds.

As the implant fluence is further decreased to 1 X 10^{14} cm^{-2} the peak concentration drops below the solubility limit for the temperature range studied. (by almost a factor of 10). It is also known that this implant condition produces a buried amorphous layer [6]. After a 10 second RTA treatment at 800 and 1080°C (Figs. 3-18 and 3-19, respectively) the tail and total profiles are approximately the same (within experimental error) in the tail region. This suggests that there is concentration dependent diffusion and electrical activation, consistent with the models presented in Chapter 2. Comparing the total samples after 800 and 1080°C, 10 second anneals (Fig. 3-20) shows negligible diffusion and/or electrical activation in this temperature range. This suggests that for this low dose the diffusion is intrinsic in nature.

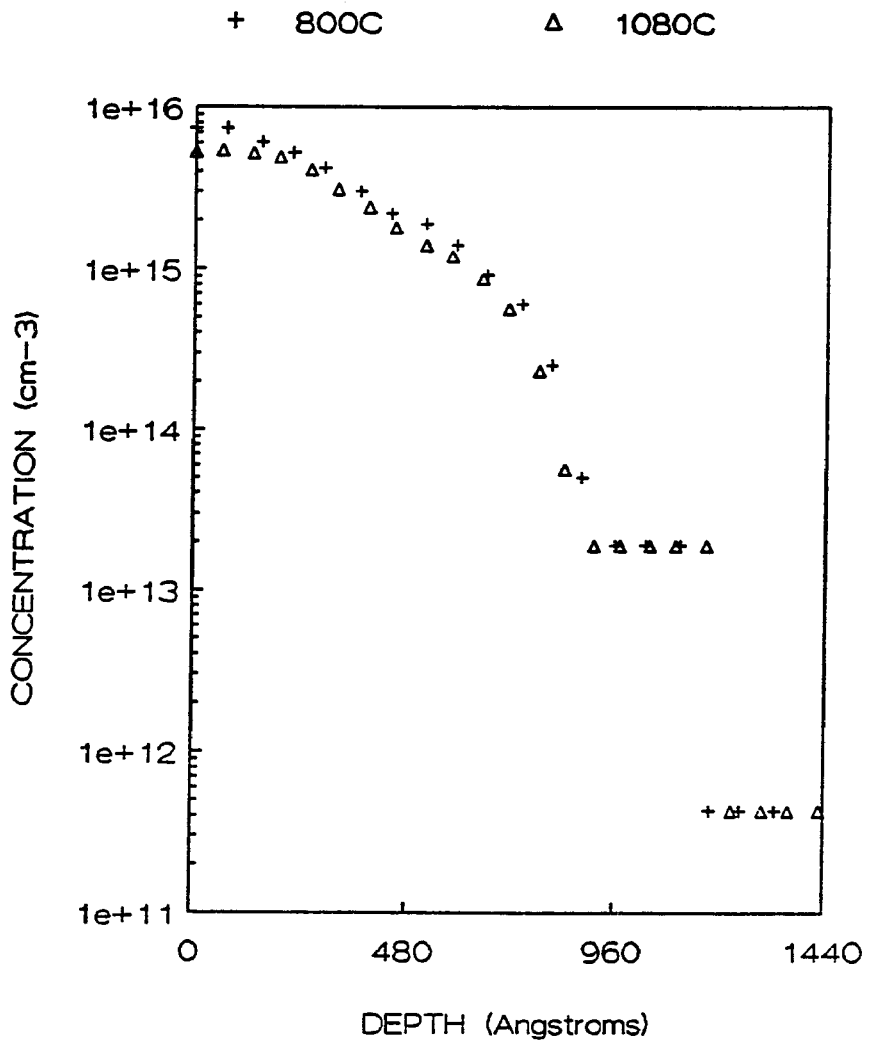

Figure 3-20. Carrier concentration for the 1 X 10^{14} cm^{-2}, 50 keV total samples annealed by RTA for 10 seconds.

3.3.2 Hall Effect Measurements

3.3.2.1 The Hall Effect

When a magnetic field is applied perpendicular to the direction of current flow, an electric field is established in the direction orthogonal to both the direction of the magnetic field and the current. This is known as the Hall effect [11,12]. It is the most common method used to directly measure the carrier concentration in semiconductors.

To examine the Hall effect consider an electron in a solid. This is depicted in Fig. 3-21 . An electron travelling with a velocity $\vec{v}$ will experience the Lorentz force q ($\vec{v}$ × $\vec{B}$), where q is the magnitude of the electronic charge and $\vec{B}$ is the magnetic induction. In free space the electron will be deflected in a direction perpendicular to the $\vec{v}$,$\vec{B}$ plane. However, inside a solid the current is constrained within the bounds of the solid. Initially electrons will be deflected by the magnetic field, creating an electric field. This counterbalances the Lorentz force acting on the bulk of the carriers (electrons), and the current flows as before. Equating these two forces gives the electric field

$$q\,(\vec{v} \times \vec{B}) = q\vec{E} \tag{3.17}$$

So, referring to Fig. 3-21 , the net force in the y-direction, F_y, is zero and

$$E_y = v_x B_z \tag{3.18}$$

The establishment of the electric field E_y is know as the Hall Field effect, and the resulting voltage $V_{ab} = E_y$. The relation between current density $\vec{J}$ and the electron's velocity is

$$\vec{J} = nq\vec{v} \tag{3.19}$$

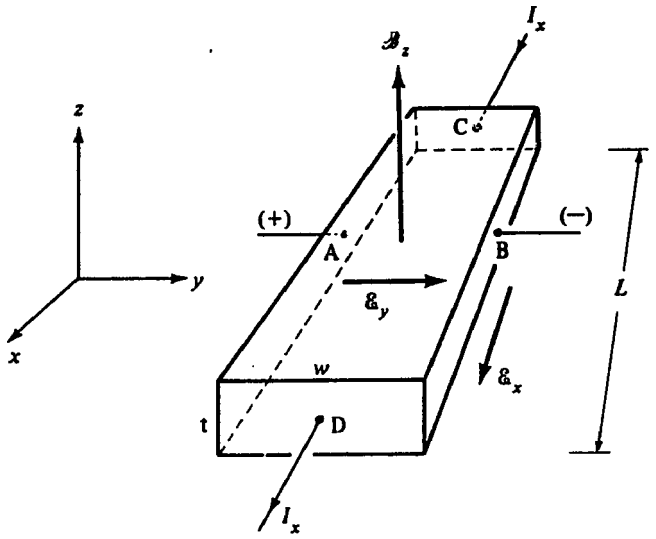

Figure 3-21. The Hall Effect. {From Reference [13]}

where n is the concentration of electrons. Therefore, from (3.17) and (3.18)

$$E_y = \frac{-1}{(nq)} J_x B_z \tag{3.20}$$

Thus the Hall field is proportional to the product of the current density and the magnetic induction. The constant of proportionality is defined as

$$R \equiv \frac{1}{(nq)} \tag{3.21}$$

and is called the Hall coefficient. The adopted convention is that when q is negative R is taken to be negative. Once the Hall coefficient is known, the carrier concentration may be obtained.

Another important quantity may be obtained from these measurements, the Hall mobility. To determine this mobility which is different from the conductivity mobility we must first look at the electrical conductivity σ, which is the inverse of the resistivity. The conductivity is defined by

$$J_x \equiv \sigma E_x \tag{3.22}$$

so,

$$\sigma = nq \frac{v_{ab}}{E_x} \tag{3.23}$$

If Ohm's law is obeyed then σ is independent of E and may be written as

$$\sigma = nq\mu \tag{3.24}$$

where μ is the electron drift velocity per unit electric field, or the mobility. Equation (3.22) shows that the conductivity depends upon the density of the charge carriers and their mobility. The combination of the Hall effect and the conductivity measurements yield a mobility. From equations (3.20) and (3.22)

$$|R|\,\sigma = \mu \tag{3.25}$$

By convention μ is a positive quantity regardless of the sign of R.

Since this section took a very elementary approach to define these quantities it must be pointed out that the quantity in equation (3.25) is referred to as the Hall mobility and the quantity in equation (3.24) is the conductivity mobility. In many cases these are not equivalent. It should be noted that the elementary approach given in this section is valid for the experimental results in this dissertation since high magnetic fields are used. For a more detailed description of the Hall effect see [11,12].

3.3.2.2 The Sheet Hall Coefficient and Resistivity

Measurements of the Hall effect and sheet resistivity can be used to determine the electrically active concentration and the carrier mobility. Van der Pauw [14] developed a method that allows measurements on diffused and ion implanted samples. A typical van der Pauw geometry is shown in Fig. 3-22. Details for fabricating this structure will be discussed in a later section. Convenient measurements of the sheet

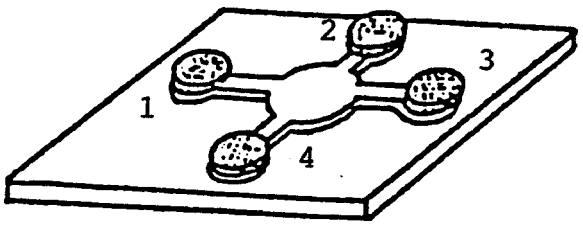

Figure 3-22. The van der Pauw geometry.

Hall coefficient and the sheet resistivity are facilitated by the use of a van der Pauw pattern.

The Hall effect is utilized to determine the sheet Hall coefficient. A current I_{13} is passed between two opposite contacts and a measurement is made of the voltage between the other contact pairs, V_{24}. The magnetic induction is then applied and another measurement of V_{24} is taken. The difference between these two voltages, ΔV_{24}, is then calculated [15]. The sheet Hall coefficient is then given by

$$R_s = 10^8 \times \frac{\Delta V_{24}}{B\, I_{13}} \tag{3.26}$$

in units of volts, Gauss, and amperes.

The van der Pauw pattern also allows the determination of the sheet resistivity, ρ_s. For a symmetrical pattern, ρ_s is obtained by measuring the potential difference occurring between two adjacent contacts (V_{34}) when a current (I_{12}) is passed between the two other contacts. Thus,

$$\rho_s = \frac{\pi}{2\ln 2}\ \frac{V_{34}}{I_{12}} \tag{3.27}$$

Note that ρ_s is related to the sheet conductivity by the simple relation $\rho_s = \frac{1}{\sigma_s}$. Van der Pauw [14] derived the correction for nonsymmetrical patterns. Then the sheet resistivity is determined by

$$\rho_s = \frac{\pi}{2\ln 2}\ (R_1 + R_2)\ \ F\left(\frac{R_1}{R_2}\right) \tag{3.28}$$

where $R_1 = \frac{V_{34}}{I_{12}}$, $R_2 = \frac{V_{41}}{I_{23}}$ and $F\left(\frac{R_1}{R_2}\right)$ is the geometrical correction factor. The correction factor is shown in Fig. 3-23 as a function of $\frac{R_1}{R_2}$.

From the measurements summarized above, the sheet carrier concentration N_s and the Hall mobility μ_h may be determined. For a sample with a uniform carrier concentration to a depth t the sheet carrier concentration is given by

$$N_s = n\ t = \frac{r}{R_s q} \tag{3.29}$$

where $r = \frac{\mu_h}{\mu}$ is the ratio of the Hall mobility ($\mu_h = \frac{R_s}{\rho_s} = R_s\sigma_s$) and the conductivity mobility ($\mu = \frac{1}{qN_s\rho_s} = \frac{\sigma_s}{qN_s}$). The theoretical value of r depends upon the impurity concentration and scattering mechanisms. For this study a unity mobility ratio is assumed [15]. This assumption is valid since high magnetic fields are used and the implant regions have large carrier concentrations compared to the bulk carrier concentrations.

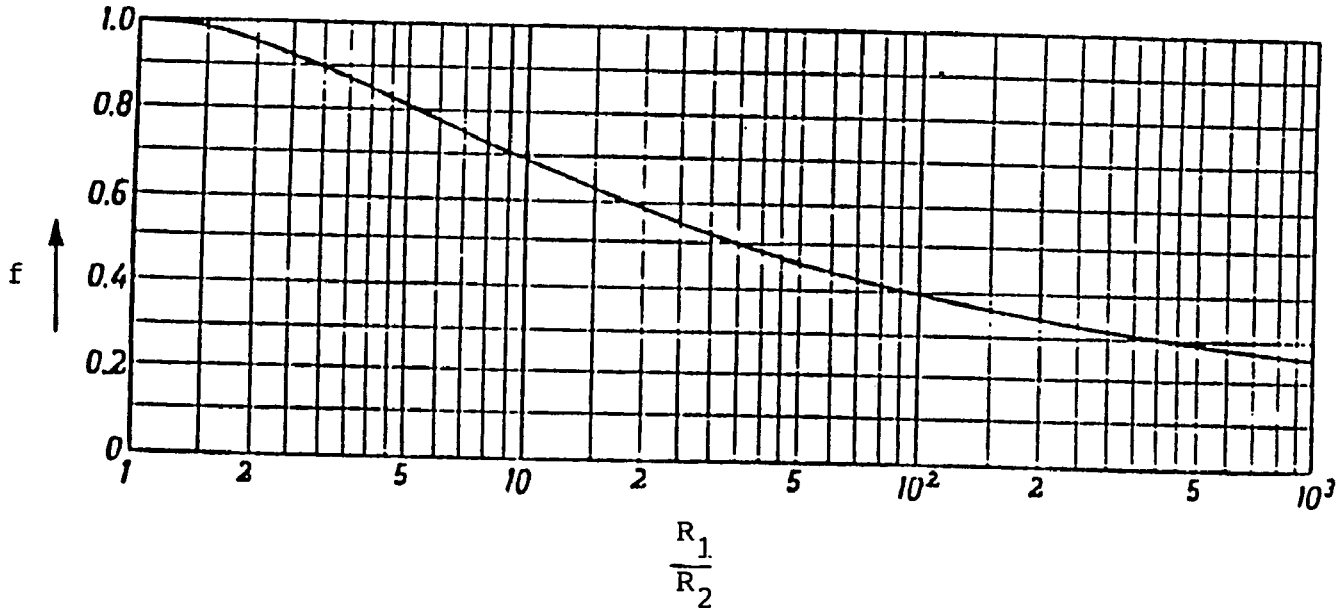

Figure 3-23. The geometrical correction factor as a function of $\frac{R_1}{R_2}$. {From Ref. [14]}.

3.3.2.3 Van der Pauw Sample Fabrication

In this section the procedures for fabricating the van der Pauw pattern will be discussed. Figure 3-24 is a schematic showing the fabrication procedure. This process offers two advantages over the conventional technique outlined in reference [16]. First, precise photolithographic alignment is unnecessary since the aluminum is evaporated through a shadow mask. Secondly, the processing time is shorter.

The first step in the pattern fabrication is aluminum metallization. A clean, annealed sample was immersed in 10% HF solution until the surface became hydrophobic. This ensured good ohmic contact of the aluminum to the silicon. After rinsing thoroughly in DI water and blow drying with nitrogen, the sample was then quickly transferred to a vacuum evaporator in order to deposit a layer of aluminum (about 250 nm in thickness) through a shadow mask.

If the electrical measurements are to be meaningful, the ion implanted and diffused layer must be electrically isolated from the bulk of the semiconductor material. Forming a mesa structure reduces the possibility of surface leakage currents. The aluminum van der Pauw patterns act as the mask to form the mesa structure. A plasma of SF_6 was used to etch the exposed silicon surface. The etching conditions are shown in Table 3-2.

Contact pads were then defined by photolithography. Hunt 204 positive photoresist was spun on the samples at 5000 r.p.m. for 40 seconds. A prebake was performed for 30 minutes at 80° C. The samples are then exposed to UV light through a mask of dots. This is the only step requiring alignment - the dots over the contact pads. After development, the aluminum in the central region is removed by a PAN etch. The PAN etch consisted of phosphoric acid (85%): HNO_3 (70%): CH_3COOH: DI water = 16:1:1:2. The photoresist was then stripped.

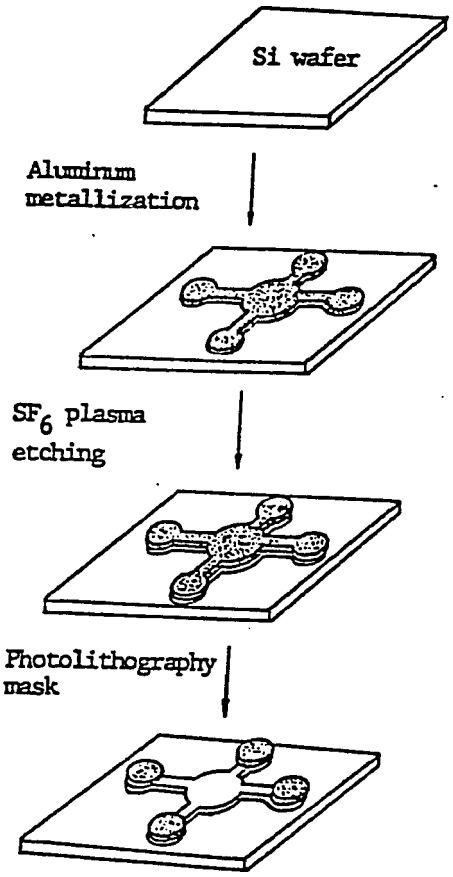

Figure 3-24. The procedure to fabricate van der Pauw patterns.

Table 3-2. Plasma etching conditions for forming the mesa van der Pauw pattern for Hall effect measurements. A PlasmaTherm 2400 plasma etching system was used.

gas:	SF6
pressure:	300 mtorr
flow rate:	50 sccm
etching time:	30 minutes
power:	300 W
temperature:	23° C

3.3.2.4 Experimental Procedures

To facilitate the Hall effect and resistivity measurements a sample holder was designed. This is shown in Fig. 3-25. The holder was fabricated from teflon. Small gold plated probes made electrical contact to the aluminum pads on the sample. This eliminated the bonding of wires to the pads on the van der Pauw pattern. The probes were manufactured by IDI Interconnect Devices, Inc. part number S1C-2-G with maximum contact resistance of 50 milliohms.

Figure 3-26 shows the schematic of the circuit used for the measurements. A switch box allowed different combinations of contacts to be selected so Hall effect and resistivity measurements could be made and checked by varying the contact configuration.

The magnetic field was produced by a Varian 4004 four inch electromagnet. A typical value of the magnetic induction used was 6000 ± 60 G, with a variation of less than 1 Gauss across the diameter of the magnetic pole piece. A one hour warm-up of the magnet maintained the field drift to less than 1 Gauss/hour. The magnetic induction was measured using a Bell 640 Incremental Gaussmeter.

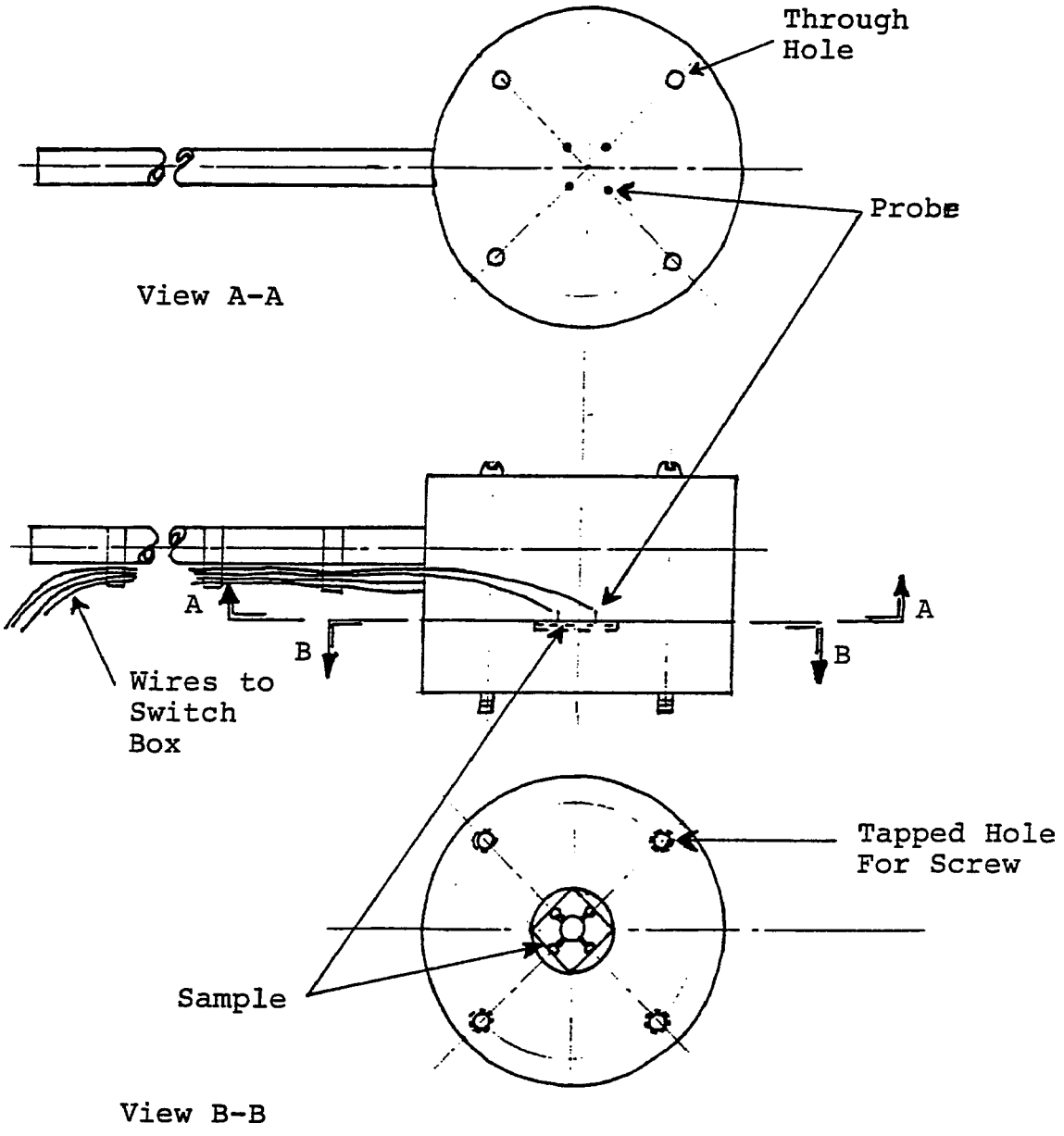

Figure 3-25. The new Hall measurement sample holder.

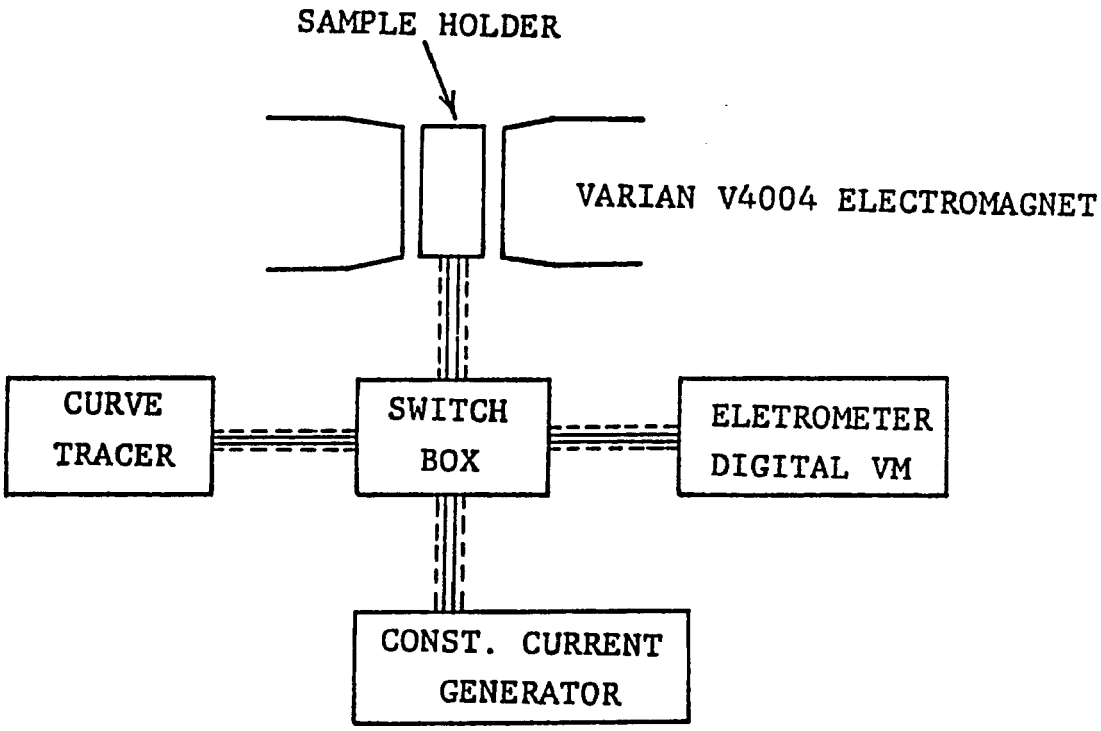

Figure 3-26. Schematic diagram of the Hall effect measurement.

Current was supplied by a Power Design Model 6010 Universal DC source, used in the constant current mode. The current was monitored by a Fluke 8060A digital multimeter. Typical input currents were in the range of tenths of microamperes to a few milliamperes (± 0.1%). Lower input currents are generally used to prevent current injection into the substrate and Joule heating.

The Hall voltage is then measured as the voltage change before and while a magnetic field is applied. During this time current is passed through the specimen in a direction perpendicular to the voltage measurement. Typical values of ΔV range from 0.01 to 10 mV (± 0.1%). As the value of the surface carrier concentration increases, ΔV decreases. In practice, higher currents will be used to increase the value of ΔV [15]. Larger currents were needed when the carrier concentration was very high. In general, the Hall effect is not the only source for the observed voltage change when a magnetic induction is applied [11,12,15]. Other contributions to ΔV comes from other galvanomagnetic and thermomagnetic effects. The most important of these effects are the Nernst, Righi-Leduc, and Ettinghausen effects. In the Nernst effect electrons attempt to diffuse down a temperature gradient. They are deflected by the magnetic field and a transverse electric field is produced, balancing the Lorentz force as in the Hall effect. The Righi-Leduc effect depends upon the distribution of electron velocities. The effect produces a transverse temperature gradient. In the Ettinghausen effect slow electrons tend to suffer a greater deflection than fast ones when a magnetic field is applied. More energy will be transported to one side of the solid than to the other and a transverse temperature gradient will be established [11].

These galvanomagnetic and thermomagnetic effects can be eliminated, except for the Ettinghausen effect. Measuring ΔV with the current in one direction and then reversing it allows cancellation of some of these effects. Reversing the direction of the

magnetic field while making measurements of ΔV for forward and reverse currents eliminates other effects. Averaging these four readings eliminates all errors except that produced by the Ettinghausen effect [11,17]. This last effect is negligible for silicon since its thermoelectric power is so small [11,15].

3.3.2.5 Profiling by Layer Removal

The values of the carrier concentration and Hall mobility as defined in Section 3.3.2.2 are average values. To obtain direct measurements of these values, a combination of a layer removal technique and the Hall and sheet resistivity measurements was used [15,16]. The technique used for layer removal was by anodic oxidation and stripping. Anodization produced a thin oxide film which consumed a layer of silicon at the surface. The oxide thickness was measured by ellipsometry. Thus, the thickness of silicon removed could be determined as discussed in Section 3.1. Before Hall measurements were made, the oxide was removed so that any spurious charge in the oxide was eliminated.

The number of carriers and their mobility in the i^{th} layer may be obtained from [15,16]

$$\frac{(R_s)_i}{(\rho_s)_i^2} - \frac{(R_s)_{i+1}}{(\rho_s)_{i+1}^2} = qn_i\mu_i^2 t_i \tag{3.30}$$

and

$$\frac{1}{(\rho_s)_i} - \frac{1}{(\rho_s)_{i+1}} = qn_i\mu_i t_i \tag{3.31}$$

giving

$$\mu_i = \frac{\Delta(R_s/\rho_s{}^2)_i}{\Delta(1/\rho_s)_i} \tag{3.32}$$

and

$$n_i = \frac{\Delta(1/P_s)_i}{qt_i\mu_i} \tag{3.33}$$

$(R_s)_i$ and $(\rho_s)_i$ are the sheet Hall coefficient and the sheet resistivity measured after the i^{th} layer with thickness t_i was removed. A full derivation of these equations may be found in reference [16].

3.3.2.6 Experimental Results

The Hall effect measurements were performed on high dose, furnace annealed samples. As was seen in Section 3.3.1.1, samples implanted above the fluence required to form a continuous amorphous layer (>3 X 10^{14} cm^{-2}) displayed some interesting characteristics. That is, for high dose samples the tail-only samples diffused differently than the total samples. To further investigate this phenomenon <100> p-type silicon was implanted at 100 keV to fluences of 1 X 10^{15} cm^{-2} and 1 X 10^{16} cm^{-2}. From these samples a set of tail-only specimens was prepared. All samples were then furnace annealed for 30 minutes at temperatures between 800 and 1100°C.

As discussed in Section 3.3.2.2 the sheet resistivity may be obtained by utilizing the van der Pauw geometry. Random errors in sheet resistivity were determined to be 1% of the measured value. Figure 3-27 depicts the results of this measurement on the above samples. In all cases the sheet resistivity decreases with increasing annealing temperature. This is what one would logically expect. Note that the tail-only samples have higher resistivities than the total samples. Keeping in mind that the tail-only samples do not have the high peak concentration of the total samples, it is reasonable to expect that the resistivity would be higher for the tail-only samples since resistivity is inversely related to the concentration. Also note that there is no indication of the unusual diffusion and electrical activation behavior (observed by

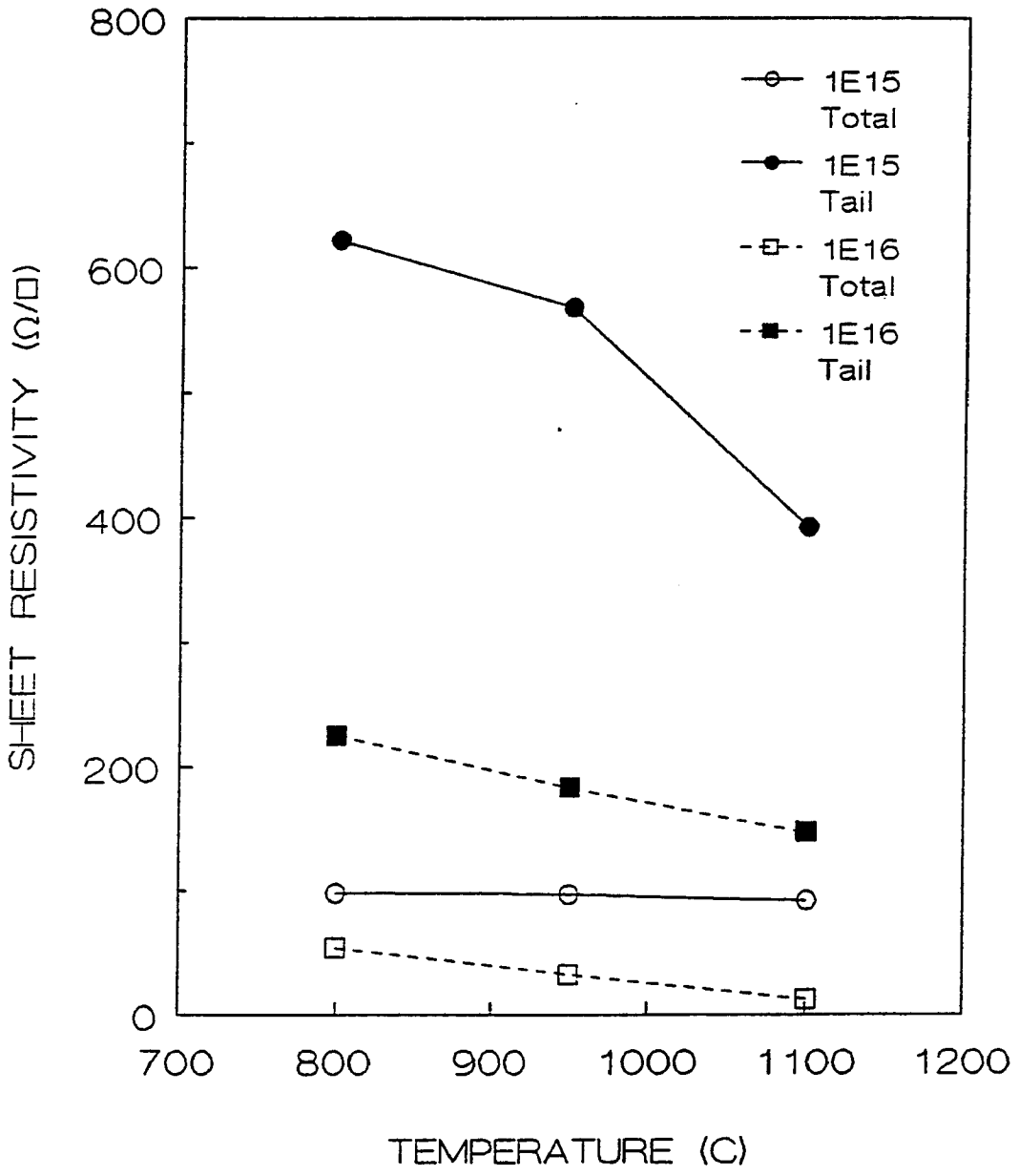

Figure 3-27. The sheet resistivity of the 1 X 10^{15} cm^{-2} and 1 X 10^{16} cm^{-2} furnace annealed samples.

spreading resistance) in these data.

By performing differential Hall effect measurements, as described in the previous sections, carrier concentration profiles may be determined. Random errors in carrier concentration were determined to be 3% of the measured value. Figure 3-28 shows the results of the 800°C anneal. As was found by the spreading resistance measurements (see Fig. 3-10) the tail is more electrically active than the total for the 1 X 10^{16} cm^{-2} implant. This is also true for the 1 X 10^{15} cm^{-2} implant (Fig. 3-28b). It should be noted that one of the reasons for performing Hall effect measurements is that the carrier concentration can be directly determined (as opposed to spreading resistance which is a comparative technique). In comparing the Hall effect data to the spreading resistance data junction depths may also be different. This difference has been attributed to "carrier spilling" [18,19] on beveled samples. It has been shown that near the bevel surface lines of constant potential, corresponding to lines of constant carrier concentration, bend to be perpendicular to the surface [18,19]. Therefore, the junction depth measured by spreading resistance may differ from that obtained by the differential Hall effect method. From these data it can therefore be said that the effects seen by either technique will be qualitatively in agreement.

As discussed in Section 3.3.1.1, the total profile is more electrically active, and has diffused more, than the tail by 950°C. This is also observed by the Hall effect measurements on the 1 X 10^{16} cm^{-2} samples (Fig. 3-29a). Note that this is not true for the 1 X 10^{15} cm^{-2} samples (Fig. 3-29b). For this lower dose, an anneal at 1100°C is required for the total profile to diffuse further than the tail (Fig. 3-30b). From Fig. 3-30a we can see the dramatic effect above solid solubility arsenic concentration has on the diffusion and electrical activation. Here the 1 X 10^{16} cm^{-2} total sample is above the solubility limit (approximately 4 X 10^{20} cm^{-3}) while the 1 X 10^{15} cm^{-2}

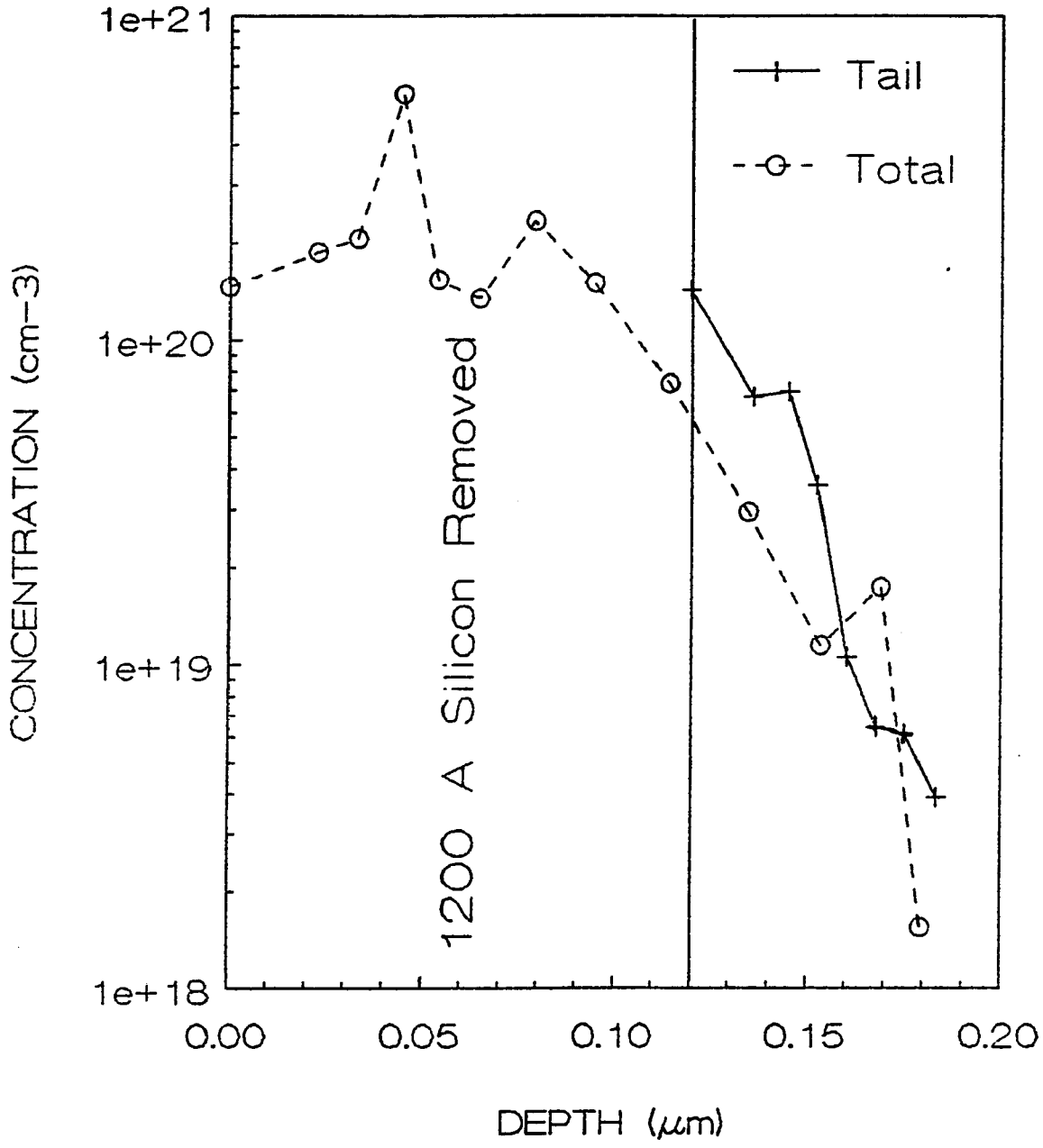

Figure 3-28. Comparison of the total and tail-only electrically active concentration profiles after an 800°C, 30 minute anneal. Data are from differential Hall effect measurements. (a) 1 X 10^{16} cm^{-2}.

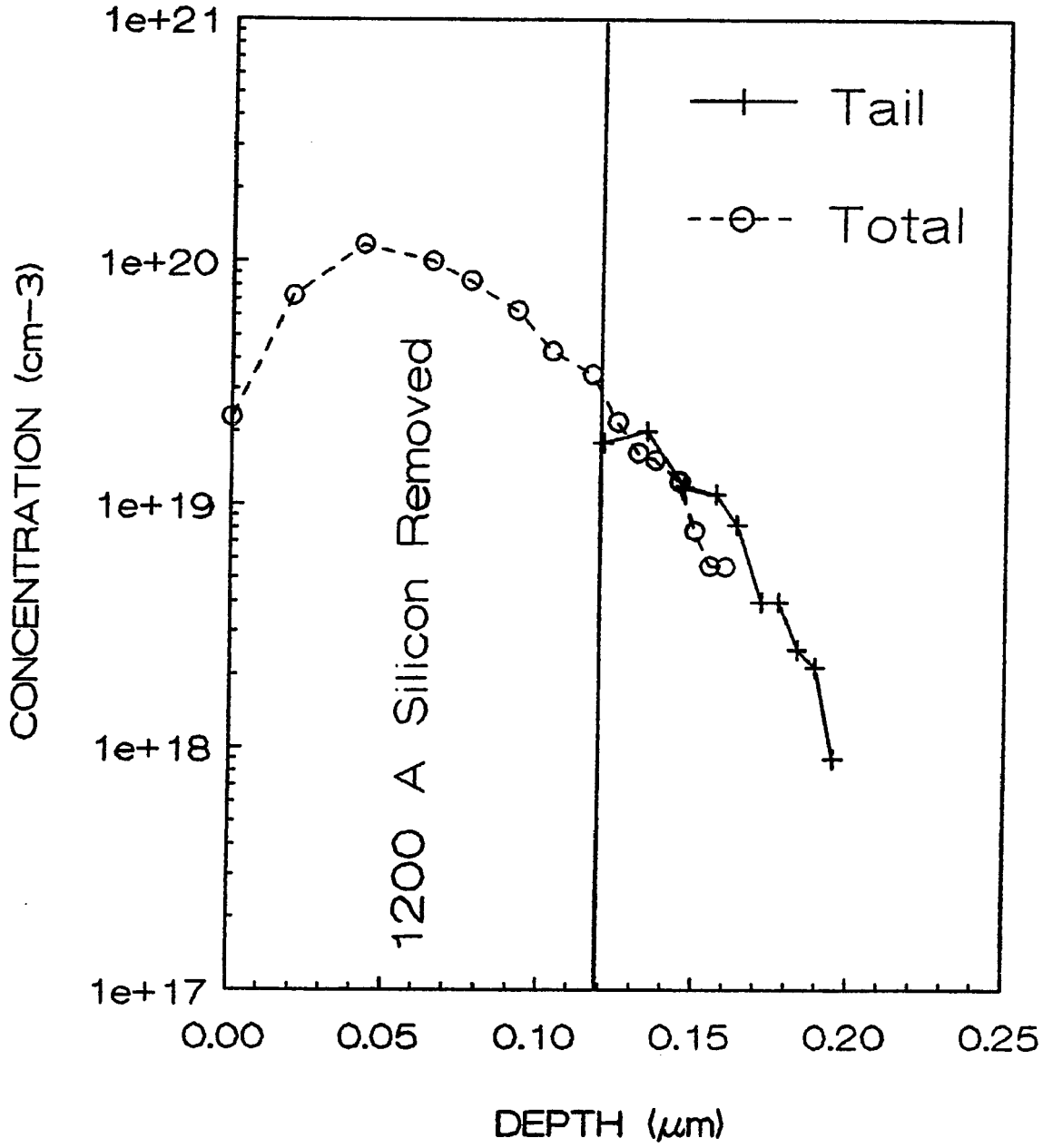

Figure 3-28. (b) 1 X 10^{15} cm^{-2}.

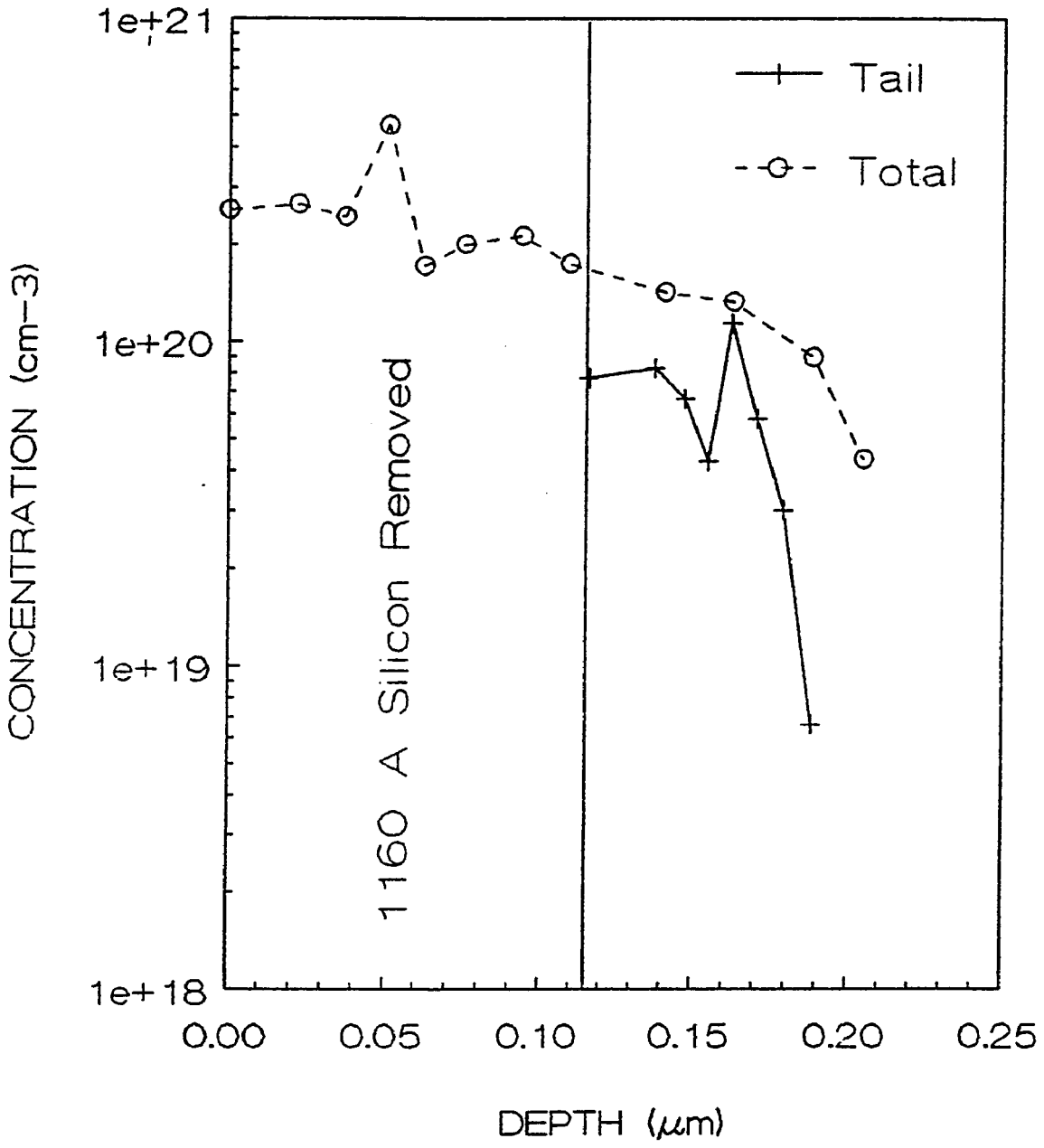

Figure 3-29. Comparison of the total and tail-only electrically active concentration profiles after a 950°C, 30 minute anneal. Data are from differential Hall effect measurements. (a) 1 X 10^{16} cm^{-2}.

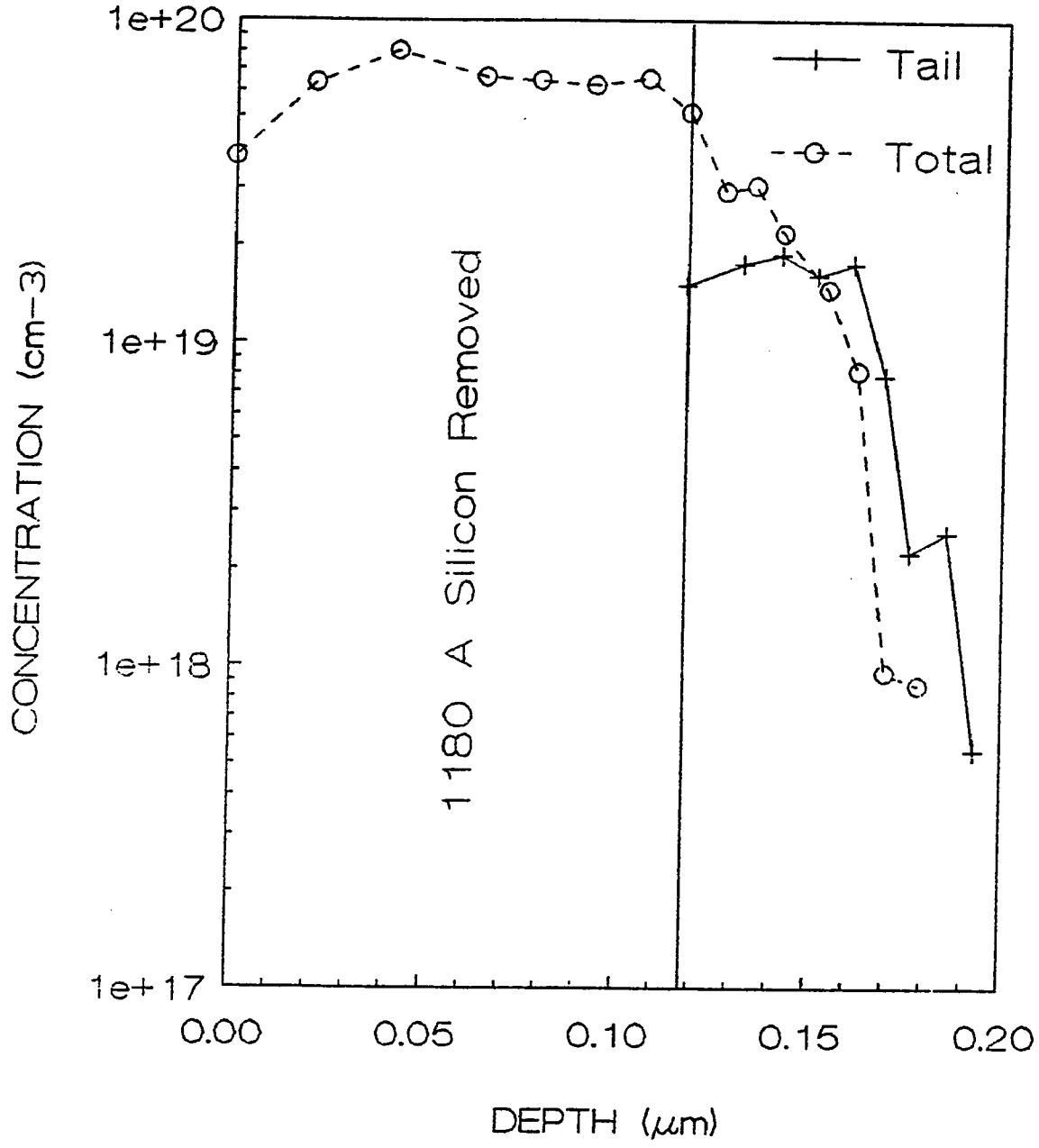

Figure 3-29. (b) 1 X 10^{15} cm^{-2}.

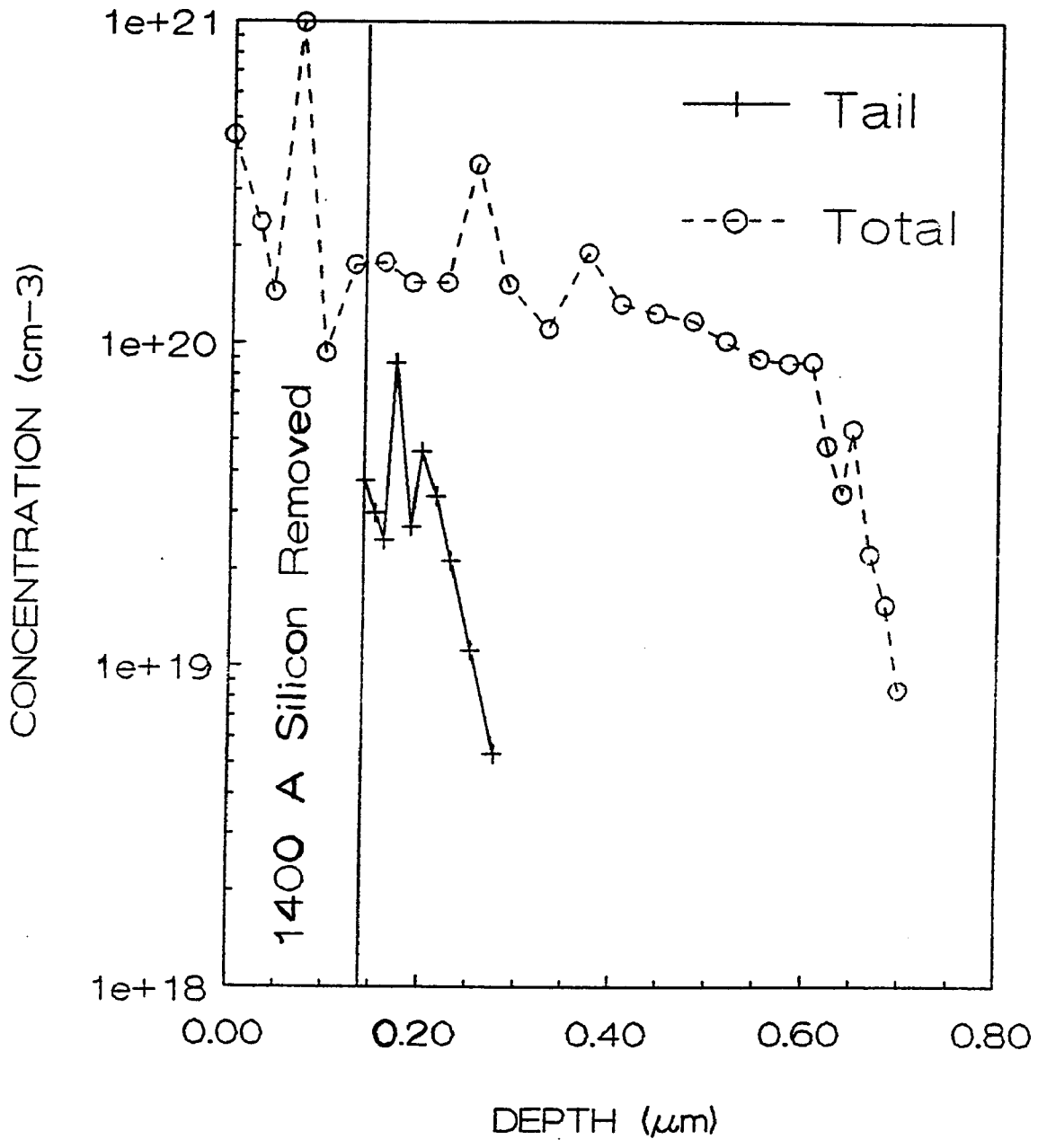

Figure 3-30. Comparison of the total and tail-only electrically active concentration profiles after an 1100°C, 30 minute anneal. Data are from differential Hall effect measurements. (a) 1 X 10^{16} cm^{-2}.

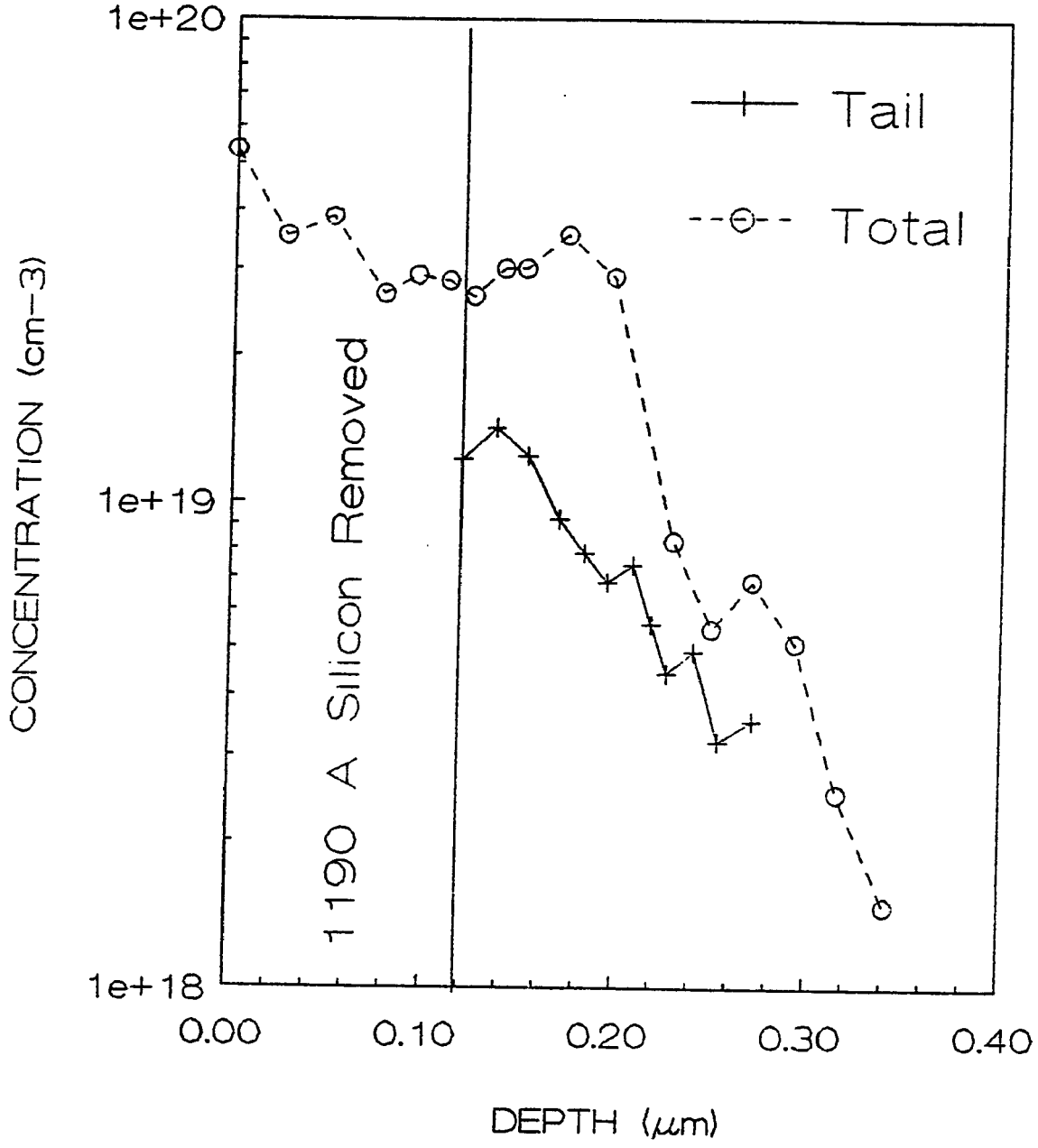

Figure 3-30. (b) 1 X 10^{15} cm^{-2}.

sample is not.

Another benefit of Hall effect measurements is that a mobility profile may be obtained. Random errors in the Hall mobility were determined to be 1% of the measured value. Mobility profiles for samples analyzed by this technique are shown in Figs. 3-31 through 3-34. The mobilities for the high dose implants are lower than those obtained for the lower dose (1 X 10^{15} cm^{-2}) samples. These mobility values are consistent with those found in the literature for high arsenic doses [20]. Also note that the tail mobilities (Fig. 3-33 and 3-34) are higher than the total samples.

A particularly interesting result of this investigation is shown in Fig. 3-35. Here the tail and total profiles, for both implant conditions studied, after the 1100°C anneal are shown. Note that in every profile a kink appears in the region between 0.2 and 0.3 μm. This suggests that there is a change in scattering mechanisms in the end-of-range region. One possible reason for this may be found in the work of Servidori, et al. [22] who have found two distinct regions of strain for above-amorphization-dose implants. In this work a negatively strained region is found near the surface. In the end-of-range region is found a positively strained region. The surface strain disappears after a 900°C, 30 minute anneal, while the end-of-range region does not change. Therefore it is suggested that the kink appearing in Fig. 3-35 may be due to lattice distortion in this region.

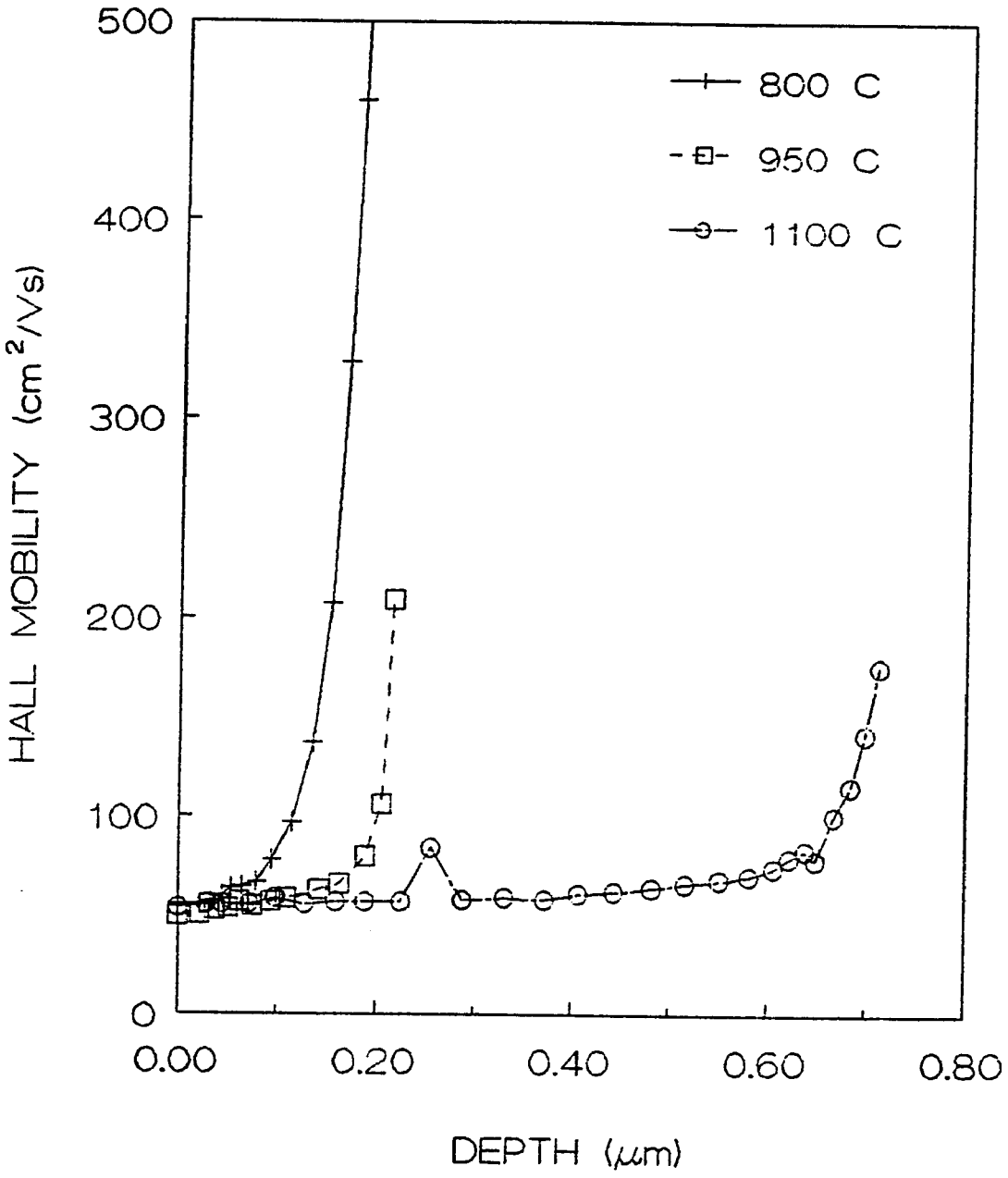

Figure 3-31. Hall mobility profiles for the 1 X 10^{16} cm^{-2} total samples.

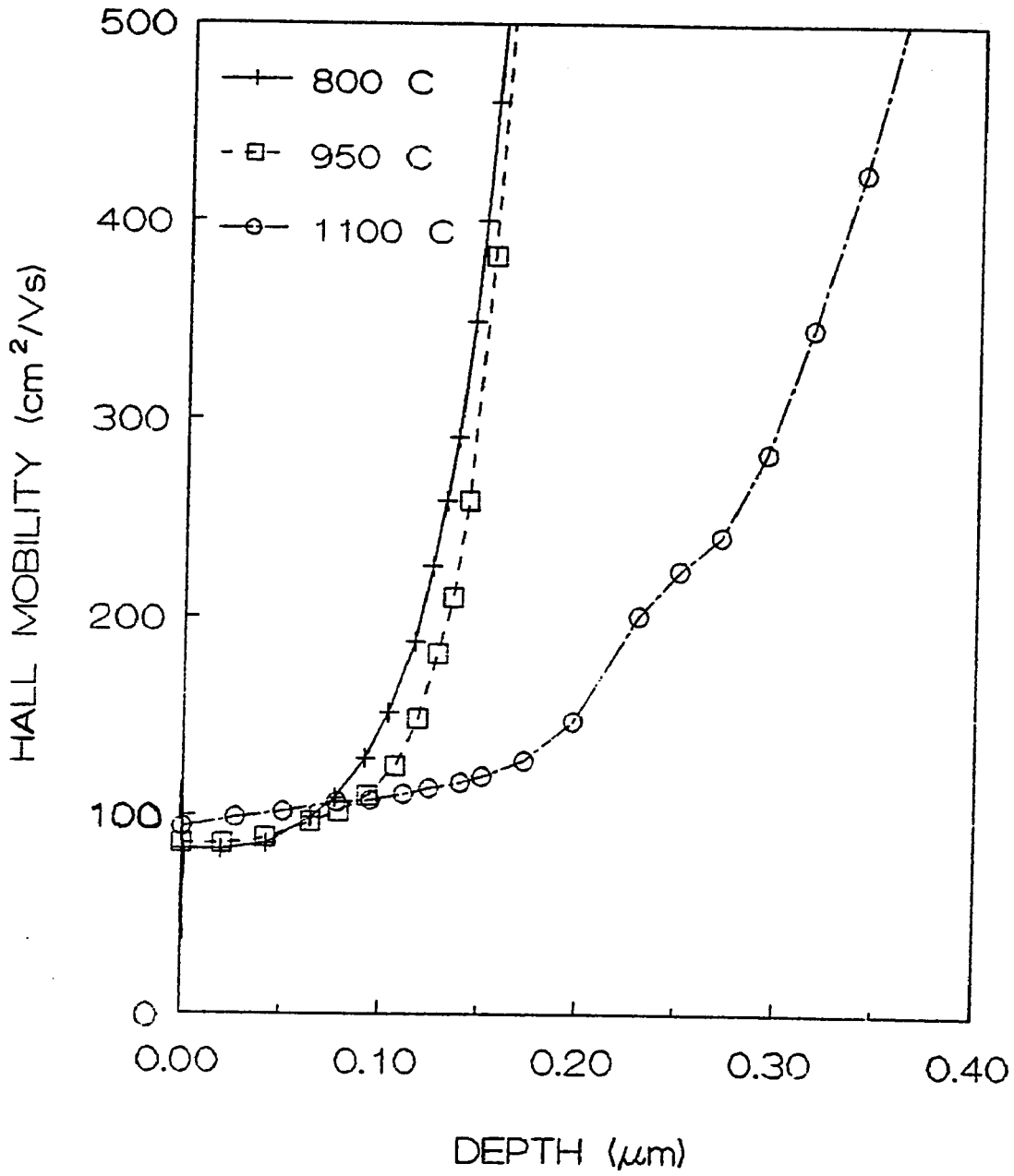

Figure 3-32. Hall mobility profiles for the 1 X 10^{15} cm^{-2} total samples.

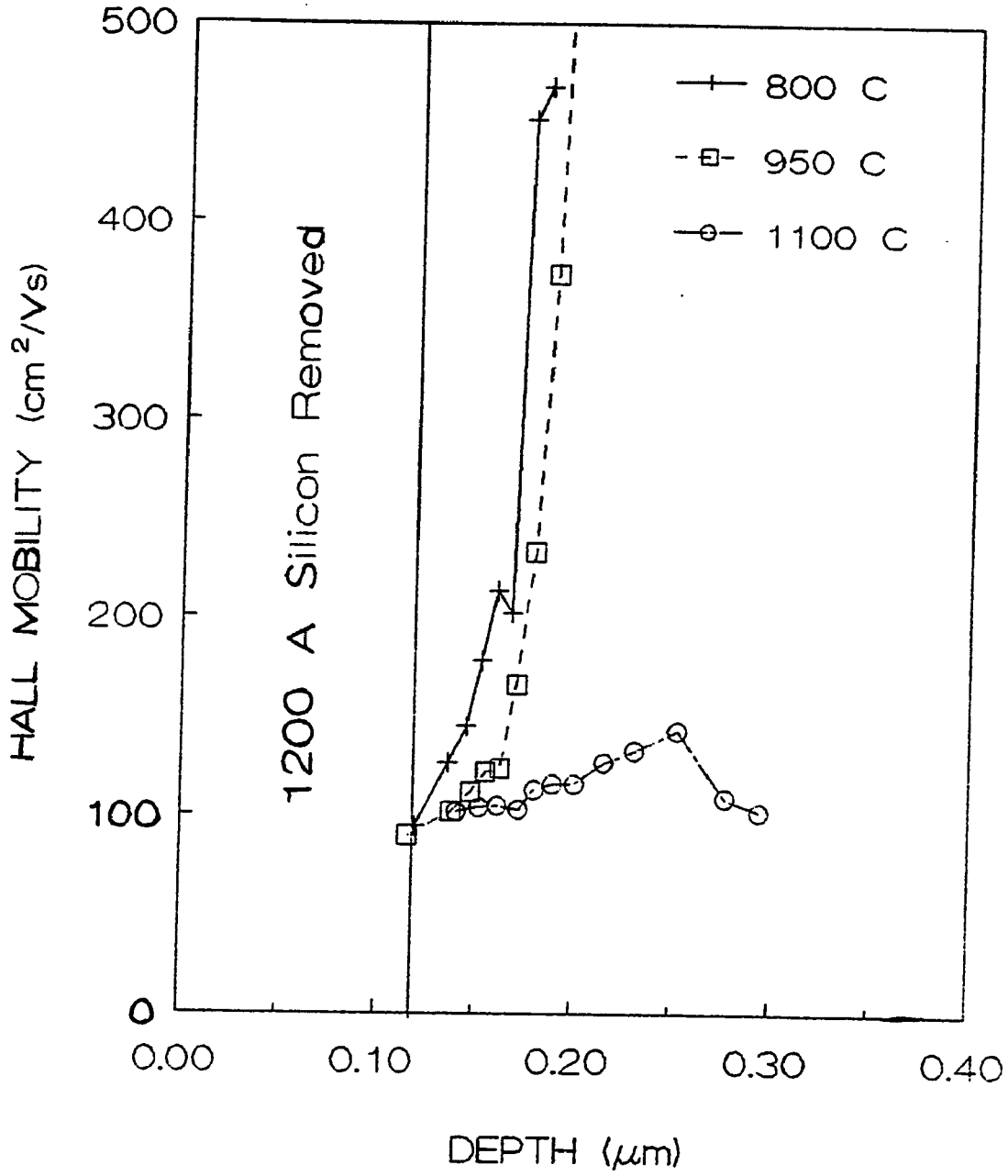

Figure 3-33. Hall mobility profiles for the 1 X 10^{16} cm^{-2} tail-only samples.

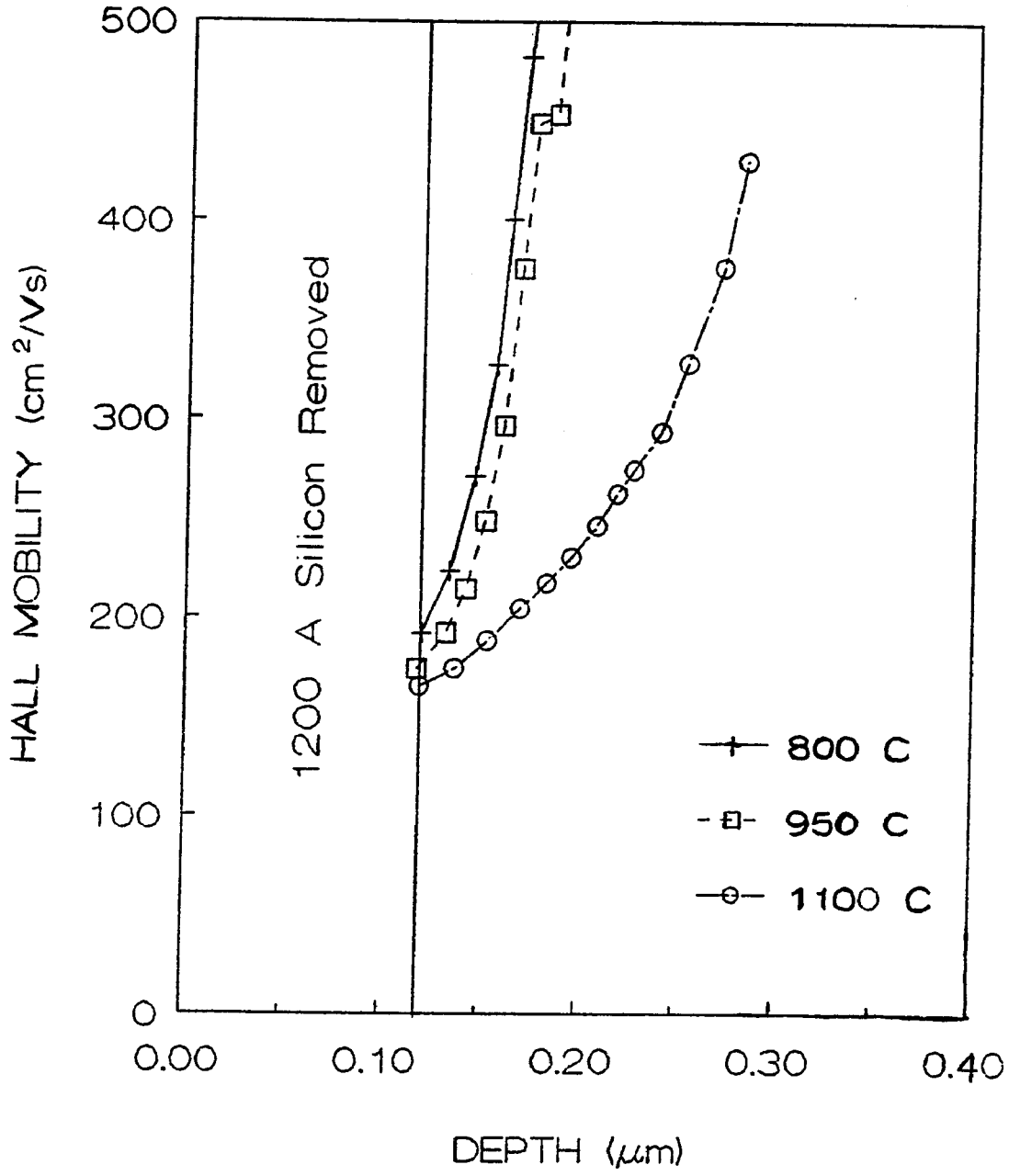

Figure 3-34. Hall mobility profiles for the 1 X 10^{15} cm^{-2} tail-only samples.

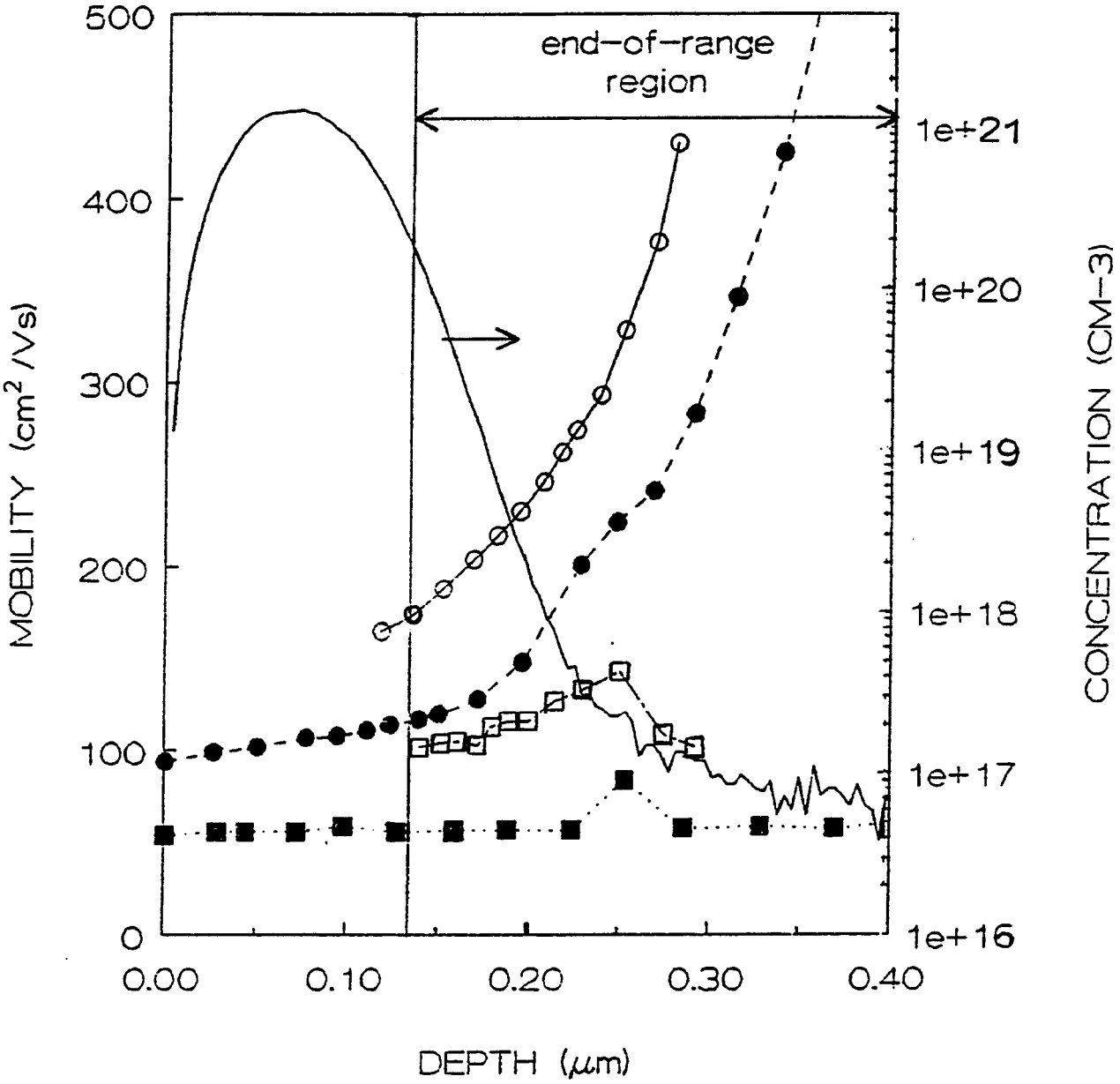

Figure 3-35. Hall mobility profiles for the samples annealed at 1100°C for 30 minutes. Shown here are profiles for the 1 X 10^{15} cm^{-2} (circles) and 1 X 10^{16} cm^{-2} (squares) samples. The tail-only samples are designated by open symbols while the total samples have filled symbols. The as-implanted arsenic profile (solid line) determined by SIMS is shown for comparisons.

3.3.3 Deep Level Capacitance Transient Spectroscopy

In 1974 D.V. Lang [22] reported a technique named Deep Level Capacitance Transient Spectroscopy (DLTS). SInce that time DLTS has become a well established technique for studying electrically active defects and impurities in semiconductors. Several excellent detailed reviews are available [23,24].

To illustrate the basics of this technique, consider a p^+n diode as shown in Fig. 3-36. For simplicity the band bending is not shown. Figure 3-36a depicts the steady state reverse bias condition. Under ideal conditions (no traps) the depletion (or space charge) region has a width W given by [23,24]

$$W = \sqrt{\frac{2\epsilon\epsilon_0(V_{bi} + V_a)}{q\,N_+}} \tag{3.34}$$

where ϵ is the relative dielectric constant (11.7 for silicon), ϵ_0 is the permittivity of free space $\left(8.854 \text{ X } 10^{-14} \ \frac{\text{Farads}}{\text{cm}}\right)$, V_{bi} is the built-in junction potential, V_a is the applied reverse bias voltage, q is the electronic charge, and N_+ is the concentration of positive charge due to the ionized shallow donors. The capacitance associated with this junction is then given by [23,24]

$$C = \frac{\epsilon\epsilon_0 A}{W} \tag{3.35}$$

where A is the area of the capacitor.

In most practical cases deep levels will also be present. One trap is depicted in Fig. 3-36 at an energy of $E_T = E_C - E$. Under steady state reverse bias conditions (Fig. 3-36a) no free carriers will be found in the depletion region, and the traps are empty. Reducing the reverse bias (Fig. 3-36b) reduces the width W of the depletion region. Now some of the traps which were in the depletion region are in neutral material so that the traps are below the Fermi level. While the bias is at this lower

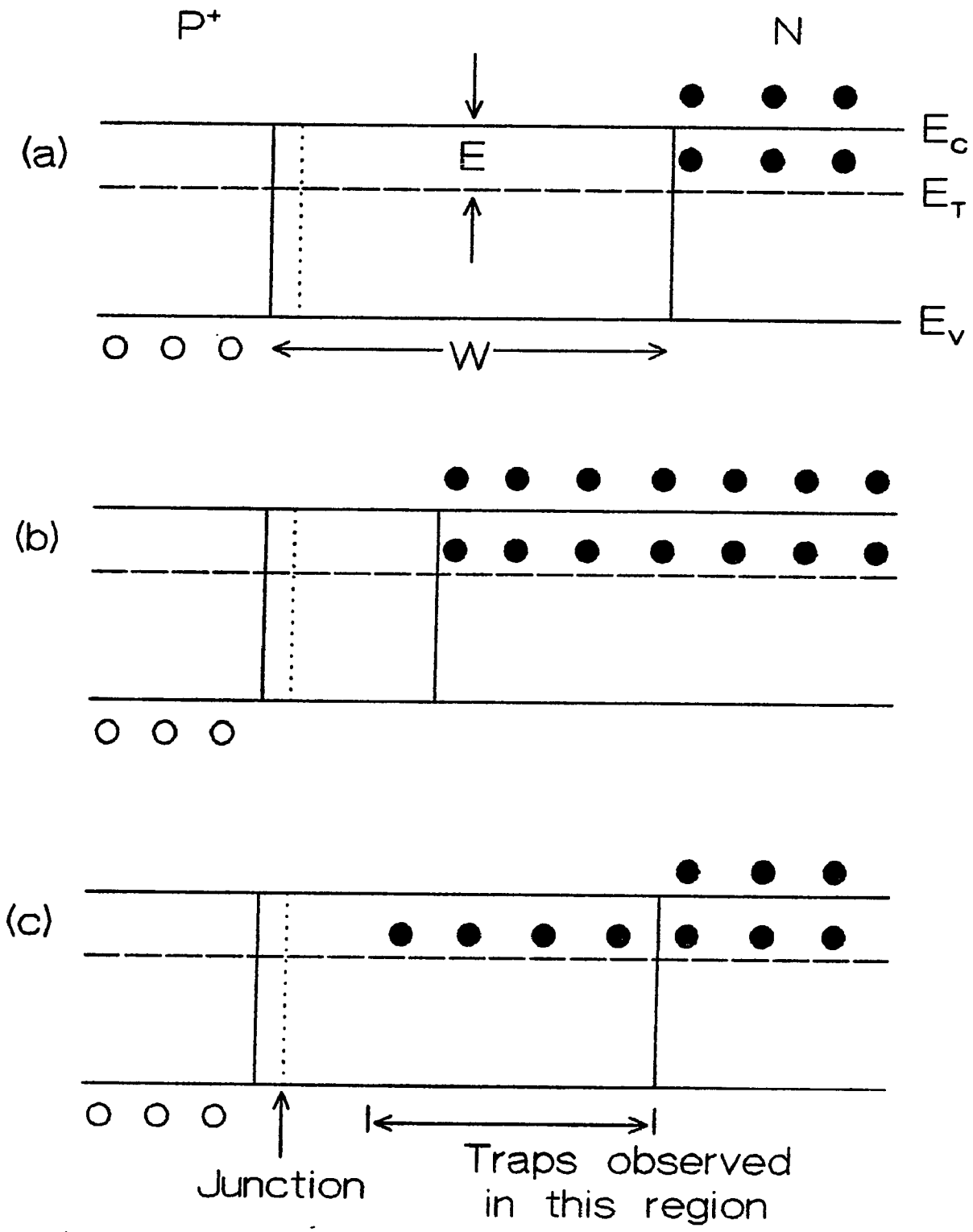

Figure 3-36. An illustration of the depletion (space charge) layer of a p^+n junction (a) before, (b) during, and (c) after a trap filling pulse. {After Reference [24]}

value the deep levels may capture carriers and become filled. Returning the reverse bias to its original value (Fig. 3-36c) places the filled traps into the depletion region. Since the traps in the depletion region are now filled the capacitance will differ from the steady state value. These carriers can be emitted by thermal excitation and a capacitance transient will be produced. The diode capacitance can then be written as [25]

$$C = \left[\frac{\epsilon\epsilon_0 A^2 q}{2} \quad \frac{\left(N_+ + N_T(t)\right)}{\left(V_{bi} + V_a\right)} \right] \tag{3.36}$$

where $N_T(t)$ represents the effective density of deep levels. Since carriers will be emitted from deep levels this quantity will change with time. Therefore the capacitance transient is a monitor of carrier emission from deep levels. In general more than one trap may exist making the transient a composite of several individual transients from each type of defect.

The basic concept behind the DLTS technique is the use of a "rate window" to determine the time constant of the capacitance transient. Analysis of the capacitance versus time from the transient capacitance experiment is done by selecting a specific decay rate which will produce a maximum output. Then the sample is gradually raised in temperature while continually pulsing the sample (as depicted schematically in Fig. 3-37). As the temperature is increased the transient time constant will change. This is directly related to the emission rate, which for electrons is given by

$$e_n = \sigma_n \, \langle v_{th} \rangle \, N_C \exp\left(-\frac{E}{kT}\right) \tag{3.37}$$

where e_n is the emission rate of electrons, σ_n is the capture cross-section for electrons, $\langle v_{th} \rangle$ is the average thermal velocity of electrons, N_C is the effective mass density of states in the conduction band, E is the energy level in the band gap with respect to

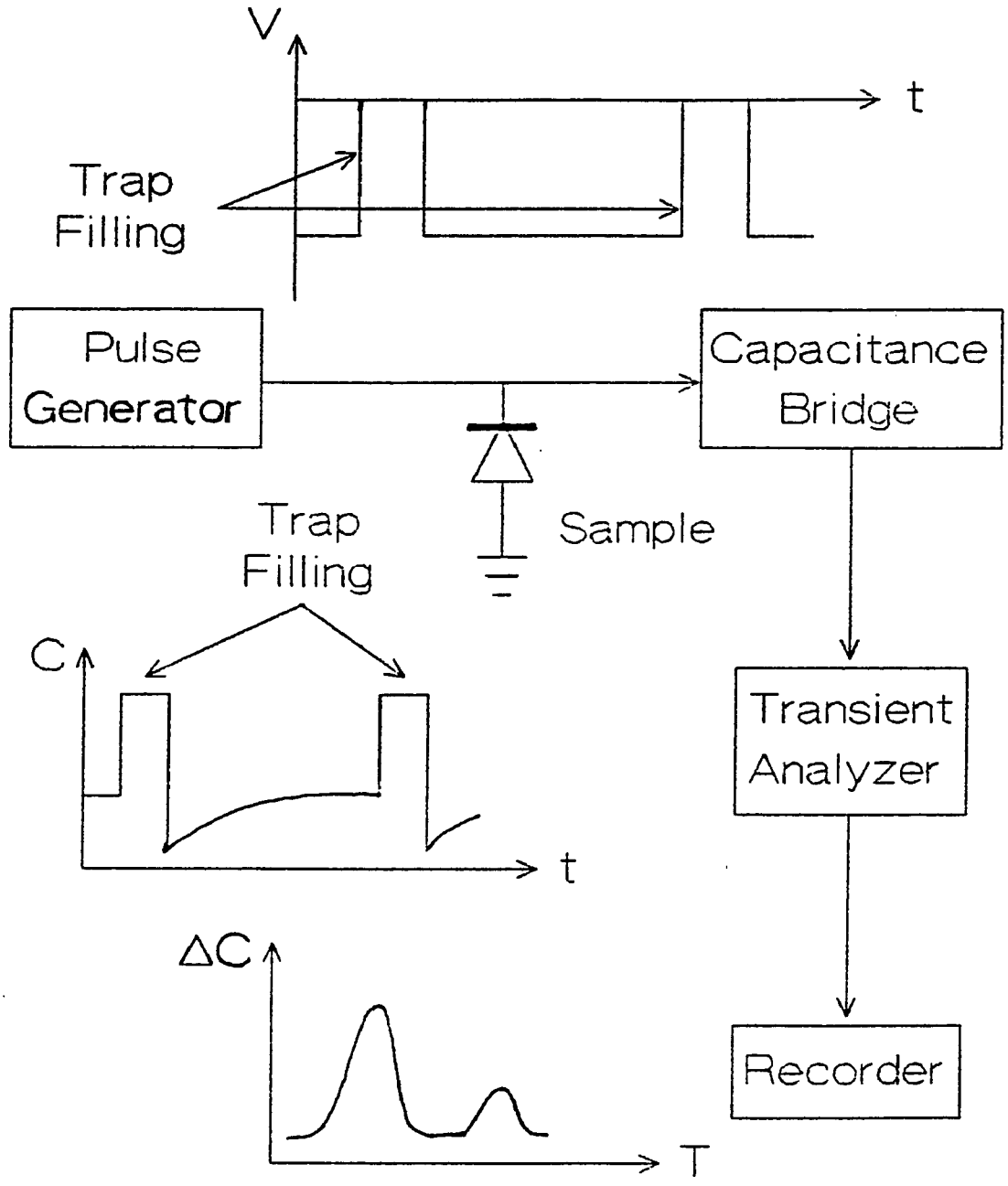

Figure 3-37. A simple block diagram of a DLTS spectrometer. Shown in the insert are (from top) sample bias pulses, sample capacitance and typical spectrum as sample temperature is varied.

the nearest band edge $\left(E = E_C - E_T \text{ for electrons}\right)$, k is Boltzmann's constant, and T is the absolute temperature. (A similar expression can be written for holes [25]).

To generate spectra from the transient capacitance experiments the rate window is implemented by a double boxcar averager. As shown in Fig. 3-38, the capacitance transient is analyzed at two times t_1 and t_2 and the double boxcar averager produces an output proportional to the average capacitance difference (the DLTS signal). When the transient time constant is close to that of the gate separation $(t_2 - t_1)$ the boxcar output passes through a maximum as a function of temperature (Fig. 3-38). The maximum of this output is known as the DLTS peak.

3.3.3.1 Sample Fabrication

A process similar to the fabrication of van der Pauw patterns (Section 3.3.2.3) was used to produce mesa structure diodes. First the back side of the wafer was abraded with 400 grit emery paper to improve back side contact. After cleaning, the sample was immersed in 10% HF until it became hydrophobic. After rinsing in DI water and blow drying with nitrogen, the sample was placed in the vacuum evaporator to deposit aluminum on the front side of the wafer. Then the sample was flipped over, and aluminum was evaporated on the back side. An array of dots was defined on the front side of the surface by photolithography. These dots served as the mask during the SF_6 plasma etching describe in Table 3-2.

The initial set of samples ($1 \text{ X } 10^{16} \text{ cm}^{-2}$, furnace annealed) were analyzed at Lehigh University. These samples were mounted on a TO5 header with silver epoxy. Thin aluminum wires were ultrasonically bonded to several diodes and the header base (back contact). Samples analyzed at Bell Laboratories, Allentown (RTA study) did not require the TO5 header.

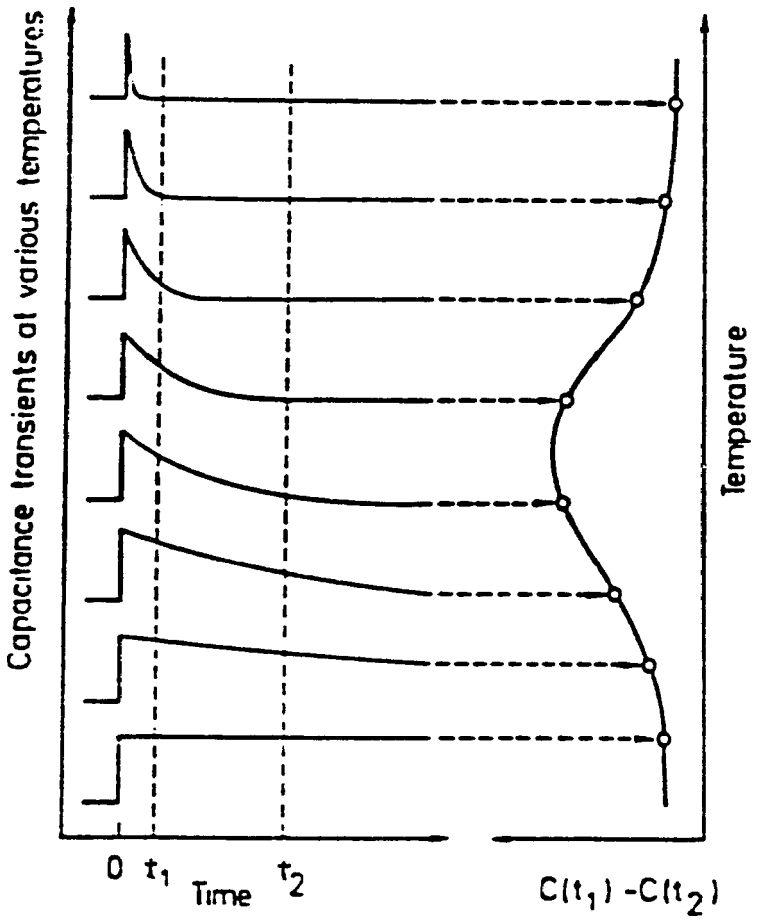

Figure 3-38. Utilization of a rate window by means of a double boxcar averager. The output is the average difference in capacitance amplitudes at the sampling times t_1 and t_2. {From Reference [24]}

3.3.3.2 Experimental Results

The initial DLTS experiments were done at Lehigh University. These experiments were performed on the core set of samples (1 X 10^{16} cm^{-2}, 100 keV, furnace annealed). In these experiments the reverse bias was set at 4V, the pulse height was 3V and the pulse width was 1ms. A low broad peak was observed at about 0.3 eV for each of the total samples. At 1100°C a second peak at 0.2 eV appeared in the spectra. It is suggested that this supports a declustering mechanism at anneals about 1050°C [26]. In all cases peaks were low and broad, suggesting that low concentrations of electrically active defects with a spread in energy were present. For the tail-only samples no peaks were observed. Several reasons are suggested to explain why there are no electrically active defects detected in the tail-only samples: (1) No electrically active traps exist in these samples. (2) Since these samples are highly doped shallow junctions, the space charge region only extends into the low boron (p-type) doped material and not into the tail region. The second suggestion is most probable.

A rapid thermal annealing study was also performed on the samples listed in Table 3-1. This allowed the study of arsenic defects for a range of doses annealed for a short time (10 seconds). These samples were analyzed at AT&T Bell Laboratories, Allentown. The pulse generator maintained a reverse bias of 5V and produced 5V pulses with a 0.05 ms width.

Results from the above amorphization dose implants are shown in Table 3-3. Once again additional peaks are observed in the samples annealed at a temperature above 1050°C (in this case 1080°C). Figure 3-39 depicts the spectra observed for the 1 X 10^{15} cm^{-2} total samples. Anneals at 950°C resulted in spectra similar to the 800°C spectra.

Table 3-3. Results from the DLTS study of 10 second rapid thermal annealed arsenic implanted samples.

Sample	$E_C - E_T$ (eV)	*Comments*
800°C/10^{16} cm^{-2} (and 950°C)		
TAIL	—	Nothing Detected
TOTAL	—	Nothing Detected
1080°C/10^{16} cm^{-2}		
TAIL	—	Nothing Detected
TOTAL	0.18 ± 0.01	Oxygen-Vacancy Pair (Wang, et al. [27])
		Carbon-Carbon Pair (Song [29])
	0.33 ± 0.01	Unknown
800°C/10^{15} cm^{-2} (and 950°C)		
TAIL	0.06 ± 0.02	Unknown
	0.28 ± 0.01	Unknown
TOTAL	0.04 ± 0.02	Unknown
	0.29 ± 0.01	Unknown
1080°C/10^{15} cm^{-2}		
TAIL	0.08 ± 0.02	Unknown (Harris [28])
	0.32 ± 0.01	Arsenic related (Troxell [25])
	0.35 ± 0.01	Carbon-Arsenic Complex (Song [29])
TOTAL	0.06 ± 0.02	Unknown
	0.24 ± 0.01	Doubly charged V—V (Troxell [25])
	0.32 ± 0.01	Arsenic related (Troxell [25])

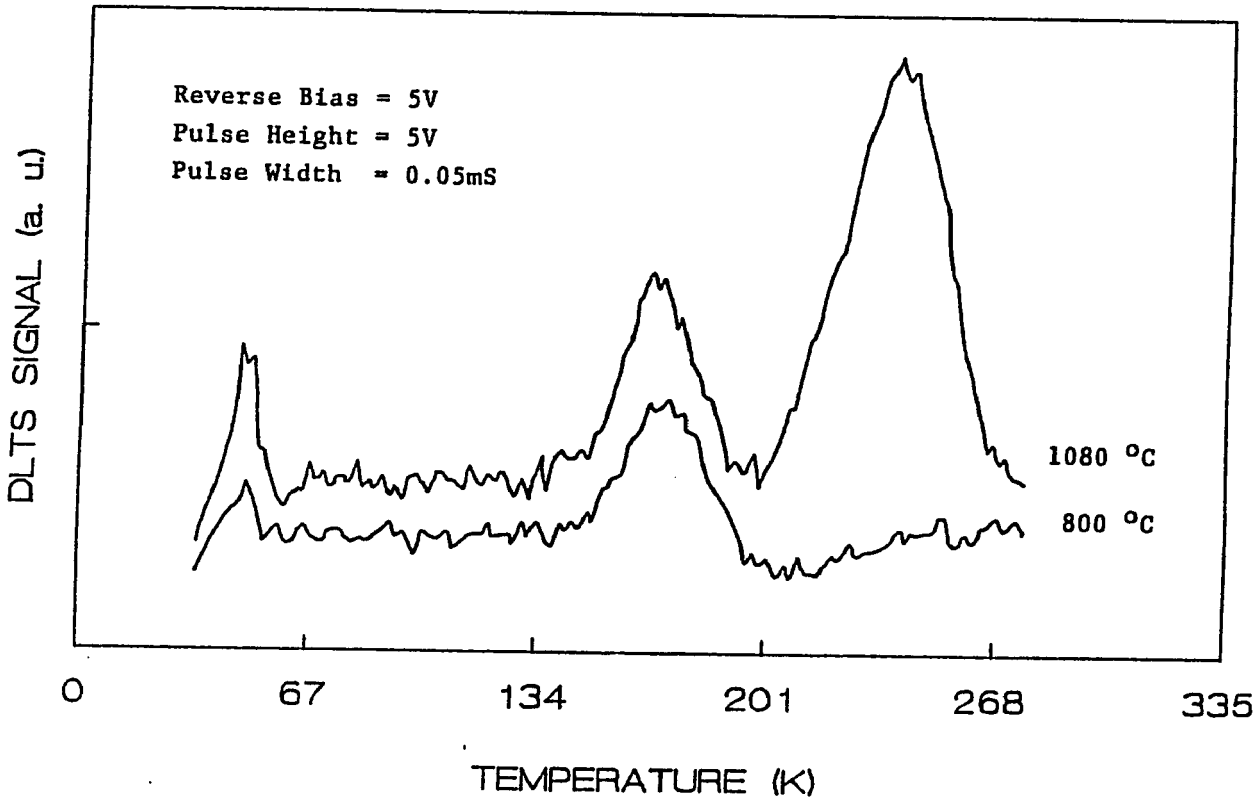

Figure 3-39. DLTS spectra for the 1 X 10^{15} cm^{-2} total samples annealed at 800°C and 1080°C for 10 seconds. Note that a third defect peak appears after the 1080°C anneal.

For the 1 X 10^{16} cm^{-2} samples the results in Table 3-3 are similar to those reported for the furnace annealed samples. No peaks were observed in the 800°C annealed samples and the 1080°C tail sample. After annealing the junctions are very shallow and most of the arsenic is electrically active. Therefore mostly the p-type region is probed without observation of arsenic and damage related defects. The possibility that the defect population is below the DLTS detection limit must also be considered. Note that two energy levels are detected in the 1080°C sample. These levels are similar in energy to those observed after furnace annealing. In searching the literature it was found that a level at 0.18 eV was observed in arsenic doped silicon after electron irradiation [27,29]. This was attributed to the oxygen-vacancy pair[27] or a carbon-carbon pair [29]. Thus it is suggested that the level observed at 0.18 eV in this experiment may be related to this defect. No match was found for the 0.33 eV level, therefore it is designated as unknown.

Reducing the implant fluence to 1 X 10^{15} cm^{-2} and repeating the RTA treatment allowed the study of a lower dose of arsenic while maintaining an amorphous layer. The lower dose allowed more of the implanted region to be probed by DLTS. As shown in Table 3-3 and Fig. 3-39 two defects are present in both total and tail samples after an 800°C anneal. Comparing the higher energy levels for the tail and total samples, it is observed that they are the same, within experimental error. The same can be said of the low energy levels. This suggests that similar mechanisms are related to the diffusion and electrical activation of the tail and total samples. (This does not rule out that diffusion is these regions is different as seen in Sections 3.3.1.1 and 3.3.2.6. What it does say is that these are some similarities, as would be expected).

At 1080°C some differences between tail and total samples and annealing

temperatures are observed. As previously discussed, an extra peak is observed in the high temperature case. Upon closer examination of the data in Table 3-3, the energy levels reported for the tail and total samples (at 1080°C) are different. The lowest energy level for each of these samples may be the same defect since they are within experimental error of each other [30]. Also note that these energies are approximately the same as the lowest energy levels for the 800°C tail and total samples.

Evidence of the defects at 0.28 eV and 0.29 eV in the 800°C samples has disappeared by 1080°C. In their place two new levels are observed. One level, at 0.32 eV, is present for both the tail and total samples. This level has been determined to be arsenic related [25]. The tail defect level at 0.35 eV has been observed and related to a vacancy complex [29]. A doubly charged divacancy gives a deep level at 0.24 eV, which is also observed in the total sample. It is suggested that this data supports the idea that there exist differences and similarities in the damage annealing and arsenic diffusion for the two types of samples (tail and total). This data also lends support to a declustering mechanism above 1050°C [26]. Diffusion including a doubly charged vacancy mechanism at high doses and temperatures [26,30] is also supported.

To further examine the effects of implant fluence 1 X 10^{14} cm^{-2} total samples were also rapid thermal annealed for 10 seconds at 800°C and 1080°C. At 800°C one level was observed at 0.45 eV. After annealing at 1080°C this level is not detected, but a new level at 0.29 eV is. It should be noted that at this dose only a buried amorphous layer is formed, which is known (see Section 1.2.3) to anneal differently than a continuous amorphous layer. Therefore this difference in deep levels may be either related to damage annealing (as the two a/c interfaces meet and interact), or a clustering/declustering mechanism.

In summary, the DLTS work presented here shows evidence of a

clustering/declustering mechanism which is dependent upon arsenic concentration, the degree of amorphization, and the anneal temperature. The actual defects formed are not known, since many of the levels observed have not been seen before or correlated to structure determining experiments. Since some arsenic and vacancy related defect energy levels are observed the damage annealing and arsenic diffusion must be associated with these defects. This is in agreement with the models presented in Chapter 2. It should be noted that the damage created by ion implantation produces both vacancies and interstitials. Therefore a fraction of the arsenic diffusing by an interstitial mechanism cannot be ruled out.

3.4 Ion Beam Analysis

Two analytical techniques which utilize ion beams to determine various aspects of materials were used in this dissertation. Secondary ion mass spectrometry (SIMS) was employed because of its ability to determine chemical concentrations of impurities in a host solid to a high degree of sensitivity. Rutherford backscattering spectrometry (RBS) measurements were used to examine the substitutionality of the arsenic in silicon.

3.4.1 Secondary Ion Mass Spectrometry

Secondary ion mass spectrometry (SIMS) is used in this dissertation since it allows the chemical characterization of the implanted and diffused arsenic in silicon. In this section the essential features of SIMS will be discussed. Several excellent reviews detailing the principles, instrumentation, and applications of SIMS are available in the literature [32-35].

As depicted in Fig. 3-40, a primary energetic ion beam is directed at the surface of the sample to be analyzed. This beam typically has an energy in the range of 0.5 to

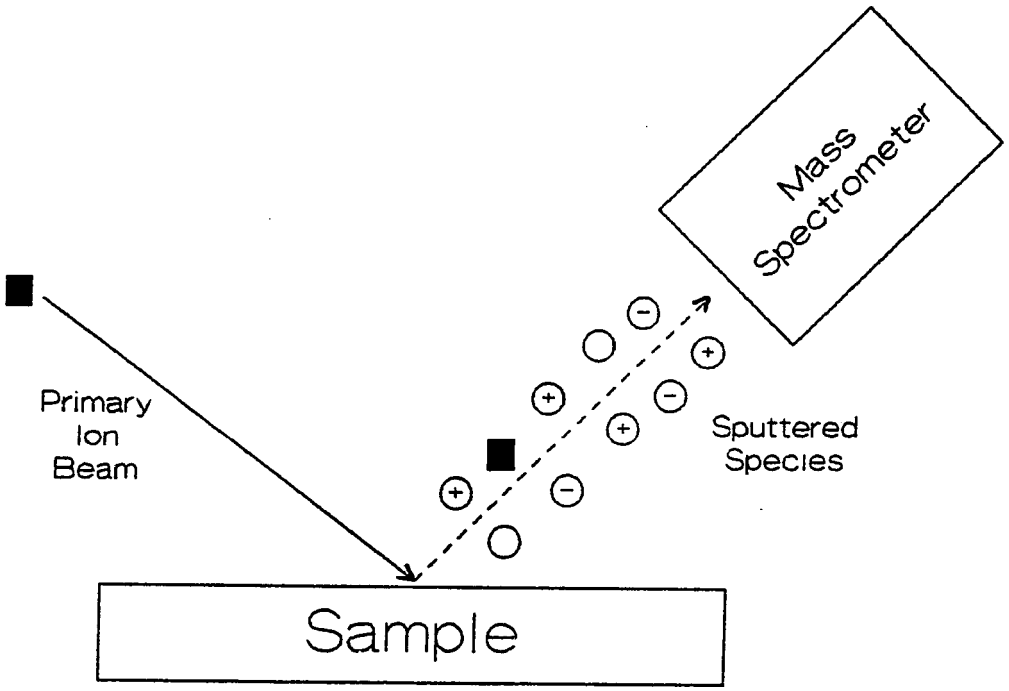

Figure 3-40. A schematic representation of the principles of SIMS.

20 keV [33-35]. At these energies the more important interaction between the primary ion beam and the solid surface is momentum transfer from the incident ion to the target atoms. This in turn leads to ion implantation, electronic excitation, lattice damage, and sputtering.

In SIMS the sputtered particles are of most interest. Most of the material leaves as neutral particles (circles in Fig. 3-40), but a small fraction are positive or negative ions (circles with + or − respectively in Fig. 3-40). Some of the primary ions (filled squares) may also backscatter. The ejected (secondary) ions are then focused into a mass spectrometer. Here mass/charge separation occurs and a spectrum is obtained.

To obtain an in-depth analysis of the particular species of interest, a detector is focused on the peak(s) of interest by use of an energy prefilter. The intensity I of this peak(s) is monitored as a function of sputter time. Therefore a double calibration is required to obtain a concentration C versus depth x profile. The sputter time is related to the sputter depth by measuring the sputter crater depth with a profilometer. The sputter rate (in Å/sec) is then determined.

The conversion of ion intensity I into concentration C is somewhat more complex. This intensity is actually a secondary ion current I_i which is related to the ion concentration C_i by [34]

$$I_i = I_p \; S \; \gamma_i \; C_i \; \eta \tag{3.38}$$

where I_p is the primary ion beam current, S is the sputter yield, γ_i is the ionization efficiency for the ion of interest, and η is an instrumental factor dependent upon the collection, transmission, and detection efficiency of the instrument. It should be noted that the sputter yield is dependent on the substrate and primary ion [35,36]. Therefore, prior to making a measurement on a processed wafer a standard ion

implanted sample is analyzed so a calibration constant K can be determined [34]. The calibration constant K is then used to convert the measured secondary ion current I_i into absolute concentration (in atoms/cm^3)

$$C_i = \frac{I_i}{K} \tag{3.39}$$

In this work, this conversion is done by a computer system provided with the SIMS system.

3.4.1.1 Experimental Results

SIMS characterization was performed at AT&T Bell Laboratories, Allentown. All analyses were made with a 14.5 keV Cs^+ primary ion beam on a Cameca IMS-3f with a C. Evans and Assoc. computer system. A Cs^+ beam with detection of $AsSi^-$ secondary ions was used to profile the arsenic. It has been shown that this system has a higher yield and lower detection limit than a primary beam of O_2^+ with detection of As^+ [36]. All data were normalized to $^{28}Si^+$.

SIMS was performed on high dose, furnace annealed samples. As in the differential Hall effect measurements, (Section 3.3.2.6) <100> p-type silicon was implanted with arsenic to fluences of 1 X 10^{15} cm^{-2} and 1 X 10^{16} cm^{-2} at 100 keV. All samples were furnace annealed for 30 minutes at temperatures between 800°C and 1100°C. These experiments were performed to gain insight into the chemical concentration aspects of arsenic diffusion as opposed to the electrically active data presented in Section 3.3.

As in the results from the other profiling techniques, the tail and total results after annealing at a certain temperature will be compared. SIMS data from the 800°C, 30 minute annealed samples are presented in Fig. 3-41. In the 1 X 10^{16} cm^{-2} data the tail-only sample profile matches that of the total, whereas the 1 X 10^{15}

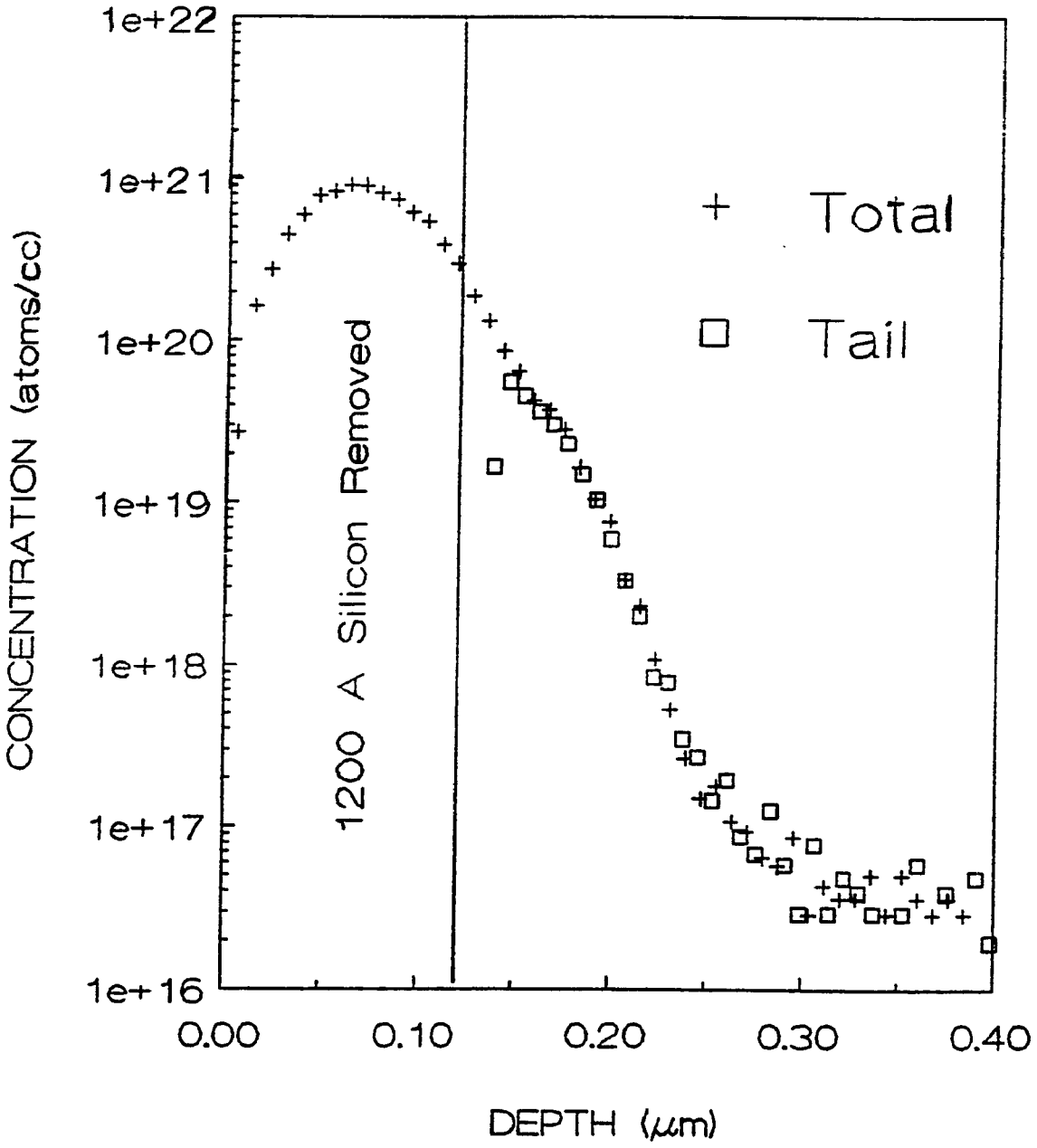

Figure 3-41. SIMS data comparing the total and tail-only chemical concentration profiles after an 800°C, 30 minute anneal. (a) 1 X 10^{16} cm^{-2}.

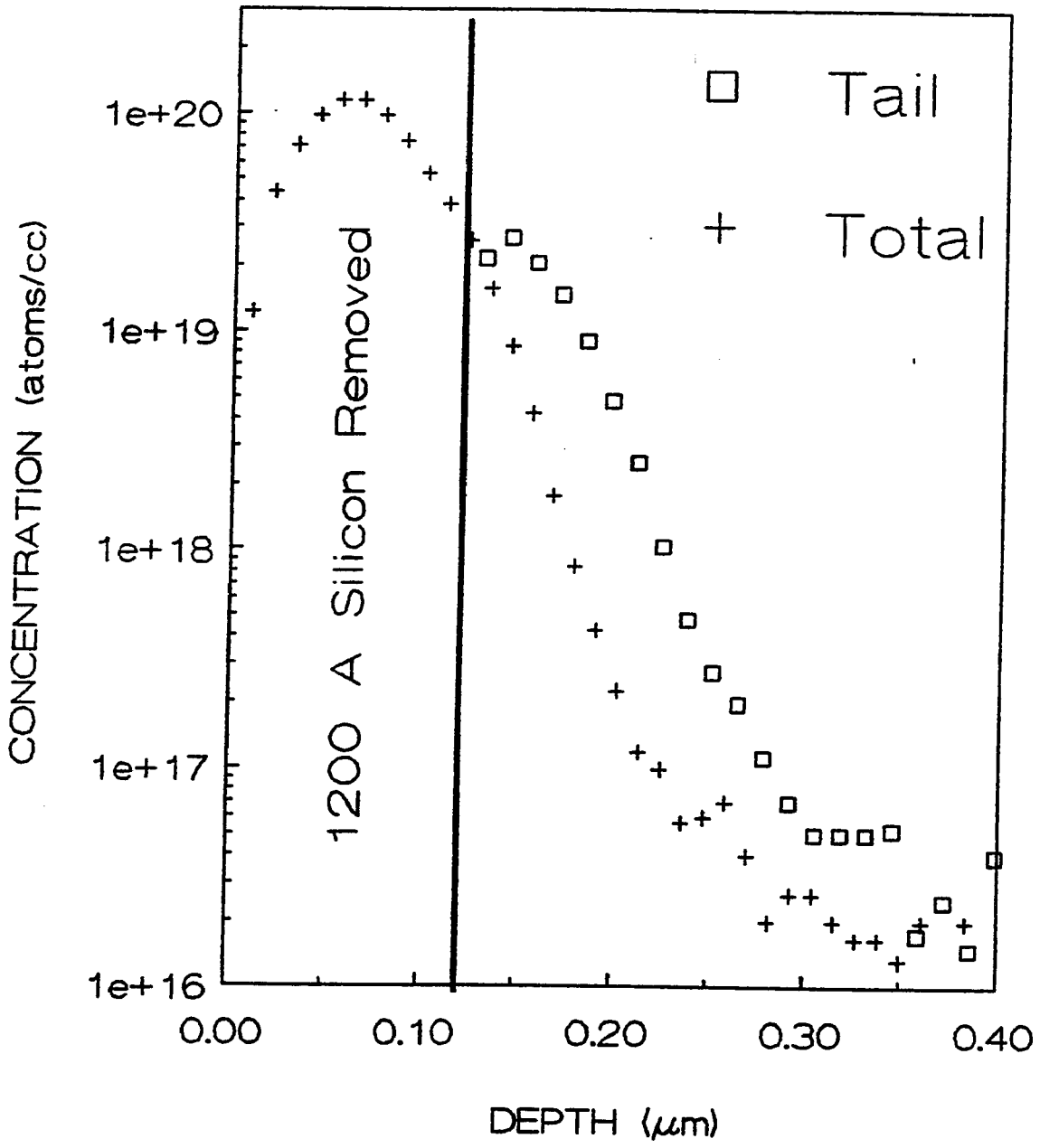

Figure 3-41. (b) 1 X 10^{15} cm^{-2}.

cm^{-2} tail-only sample has diffused deeper than its corresponding total sample. These data are consistent with the Hall data in Fig. 3-28.

Although similar junction depths are found in both Fig. 3-28a and 3-41a, the tail in Fig. 3-28a is more electrically active than the total sample. This suggests that different mechanisms are involved with the tail-only and total sample tail (end-of-range) region diffusion and electrical activation. Also note in Fig. 3-41b that the arsenic in the tail-only sample has diffused deeper into the original sample than the total sample, thus suggesting that the implant concentration is also important.

The results of the 950°C, 30 minute anneal (Fig. 3-42) are similar to those at 800°C. Once again the 1 X 10^{16} cm^{-2} tail is coincident with the total profile, and the 1 X 10^{15} cm^{-2} tail is deeper than its corresponding total sample. Upon comparing Fig. 3-42a with Fig. 3-29a, one finds that the data in these figures could lead to conflicting interpretations. The discussion of these differences will be left for later when more data will be available to explain the discrepancies.

By 1100°C profiles of both total samples are deeper than their corresponding tail-only samples (Fig. 3-43). Qualitatively this is also in agreement with the results presented in Fig. 3-30. Also note the dramatic difference in junction depths of the 1 X 10^{16} cm^{-2} and 1 X 10^{15} cm^{-2} total profiles. Here the peak arsenic concentration of the 1 X 10^{16} cm^{-2} implant (1.98 X 10^{21} cm^{-3}) is above the solid solubility limit of arsenic in silicon at 1100°C (approximately 4 X 10^{20} cm^{-3}), while the peak concentration of the 1 X 10^{15} cm^{-2} implant (1.98 X 10^{20} cm^{-3}) is below. This shows the effect a high arsenic concentration will have on the diffusivity at high temperatures. Also note the "smoothness" of the profiles in Fig. 3-43. Comparing these to Fig. 3-35 suggests that the kink in the mobility profiles between 0.2 and 0.3 μm is not due to the arsenic in this region.

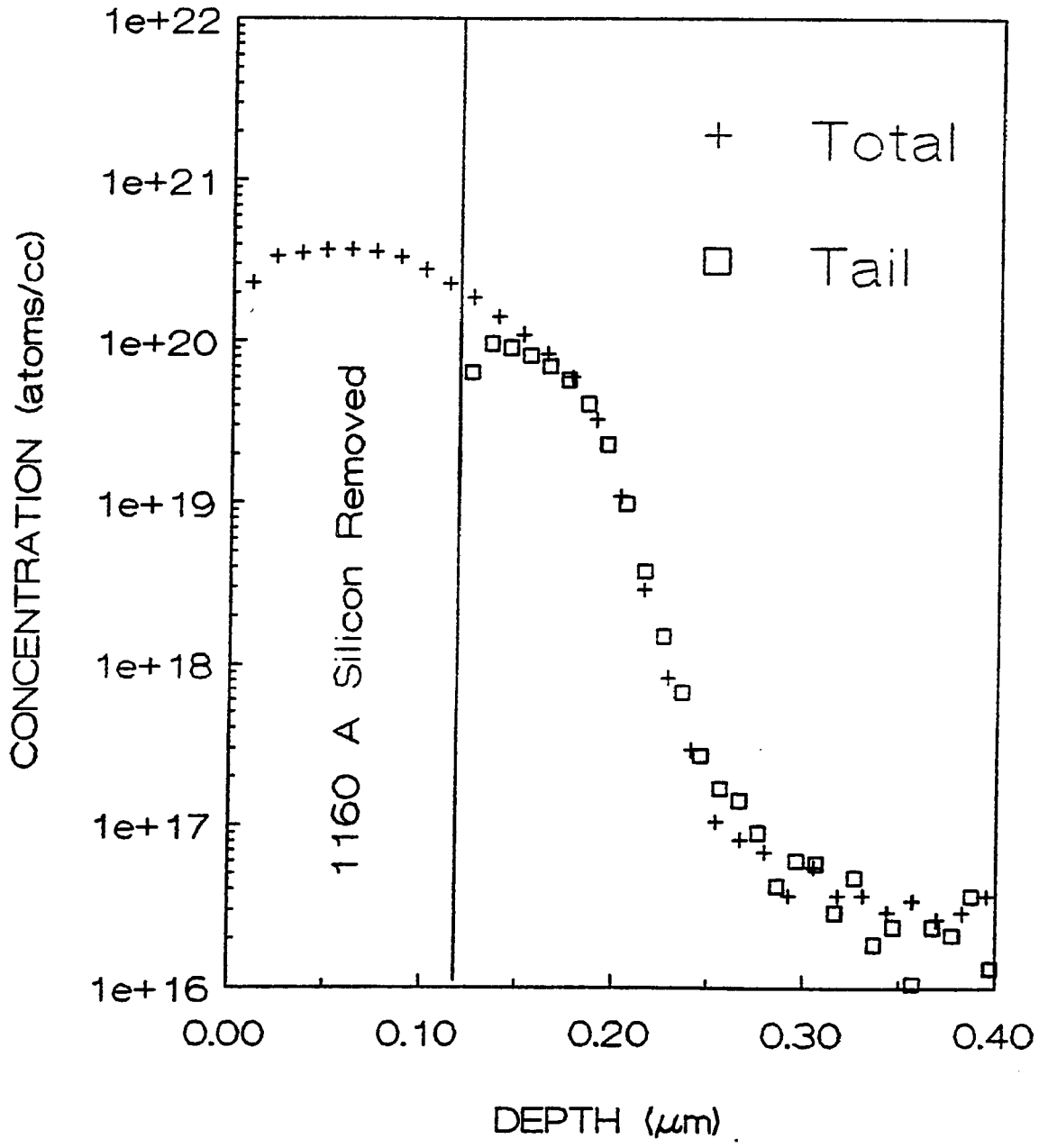

Figure 3-42. Comparison of the total and tail-only chemical concentration profiles after a 950°C, 30 minute anneal. (a) 1 X 10^{16} cm^{-2}.

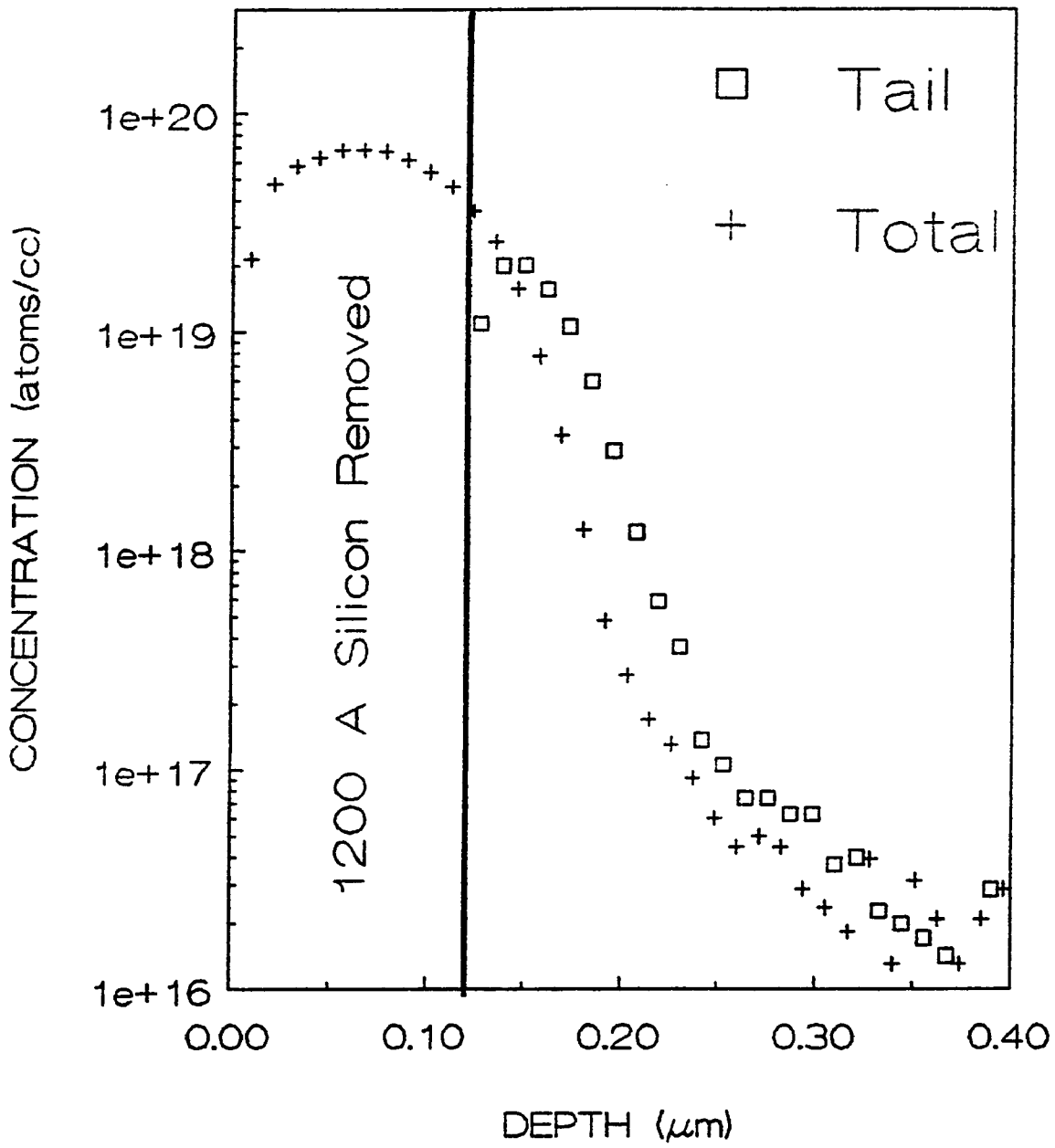

Figure 3-42. (b) 1 X 10^{15} cm^{-2}.

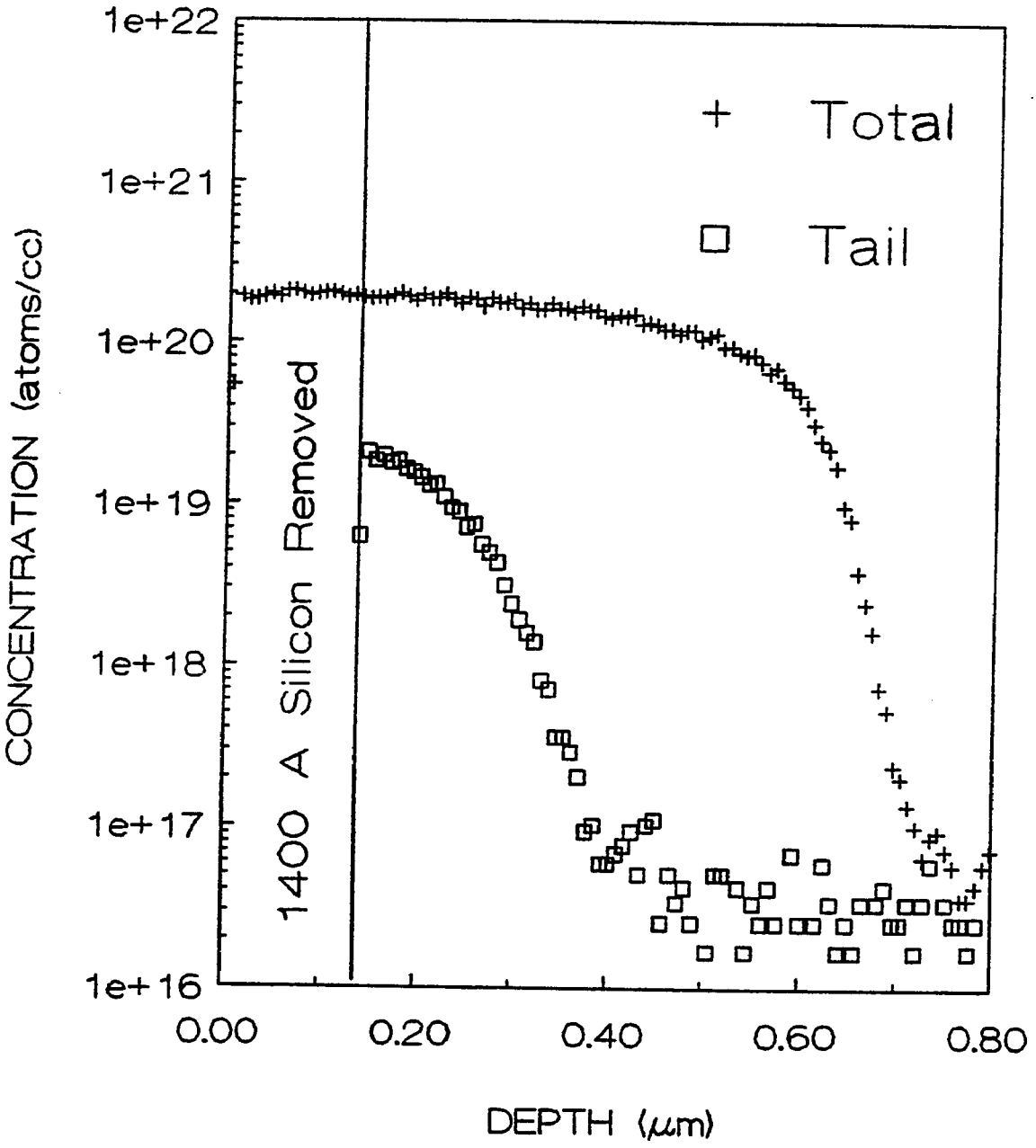

Figure 3-43. Comparison of the total and tail-only chemical concentration profiles after an 1100°C, 30 minute anneal. (a) 1 X 10^{16} cm^{-2}.

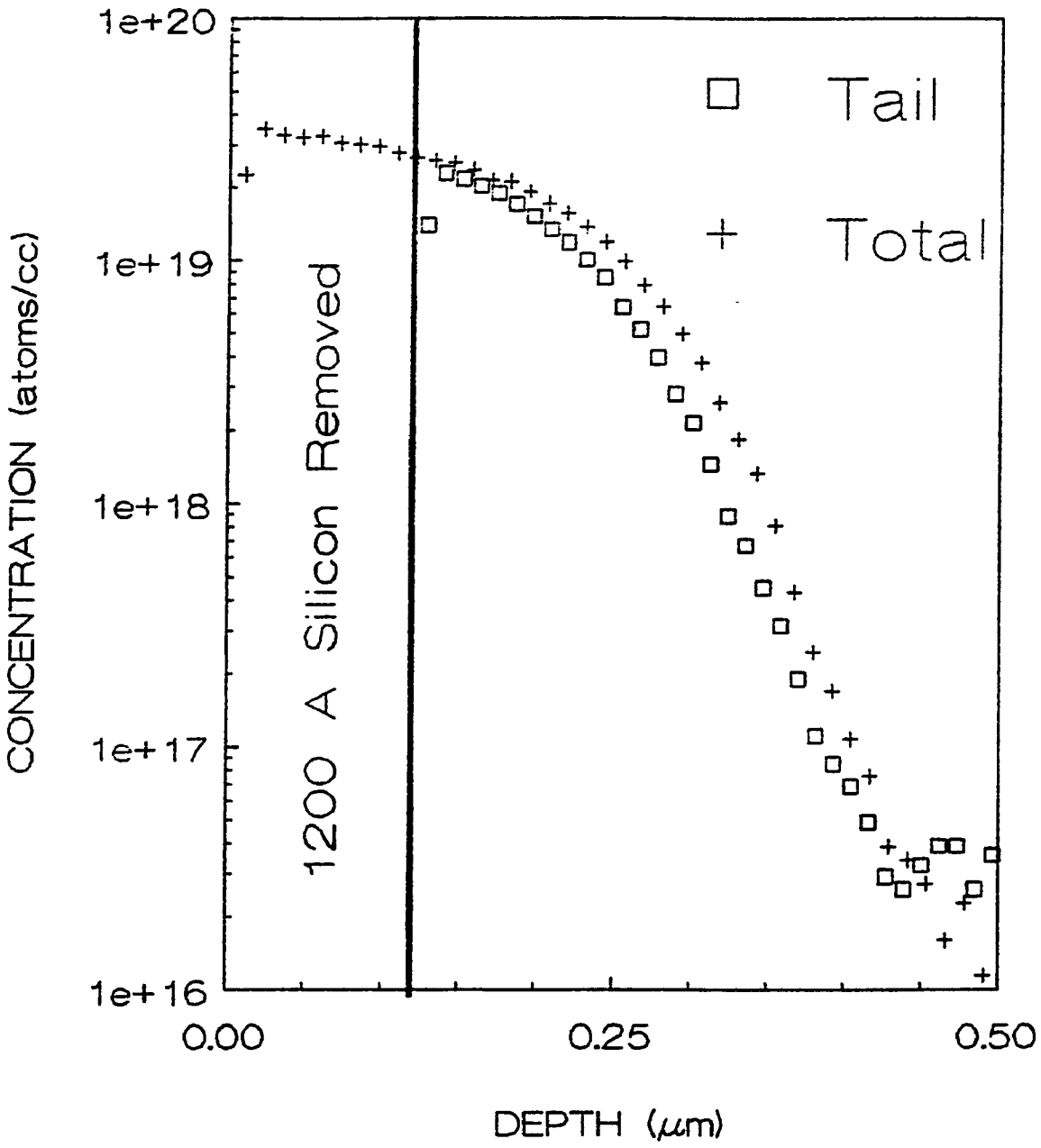

Figure 3-43. (b) 1 X 10^{15} cm^{-2}.

3.4.2 Rutherford Backscattering Spectrometry

Scattering of energetic particles by solids has been extensively used in the field of nuclear physics since the early part of this century. More recently, a great deal of interest has been shown for its application as a thin film analysis technique [37,38]. In these studies the energetic beam (usually protons or alpha particles) is directed perpendicular to the surface of the sample to be studied and backscattered particles are detected. Therefore the technique is called Rutherford Backscattering Spectrometry (RBS). Rutherford is honored in this name due to his early scattering work.

The basic idea behind this technique is that the incident particle is backscattered due to elastic scattering. A typical energy used is 1 MeV for a $^4He^{2+}$ particles. This is in the elastic scattering regime and nuclear reactions do not occur. Usually 1 in every 10^4 particles will be backscattered (that is, deflected more than 90° from the incident direction). The energy of the backscattered ion will be dependent upon the mass and depth of the scattering atom in the solid. An excellent overview of the physics behind this process may be found in the book by Chu et al. [37].

The energy spectrum of backscattered particles from a crystalline solid with a surface layer of randomly oriented impurities is shown in Fig. 3-44. Here the impurity atoms (squares and triangles) have a higher atomic mass than the host atoms (circles). Therefore the incident particle will recoil with a higher energy from the impurities than from the host surface atoms. Incident ions can also be scattered from atoms deeper in the solid and emerge at lower energies. Since the impurities are only in the surface region, scattering from these impurities only occurs over a limited energy range and therefore results in peaks. By contrast, the scattering from the host atoms results in a continuum of energies.

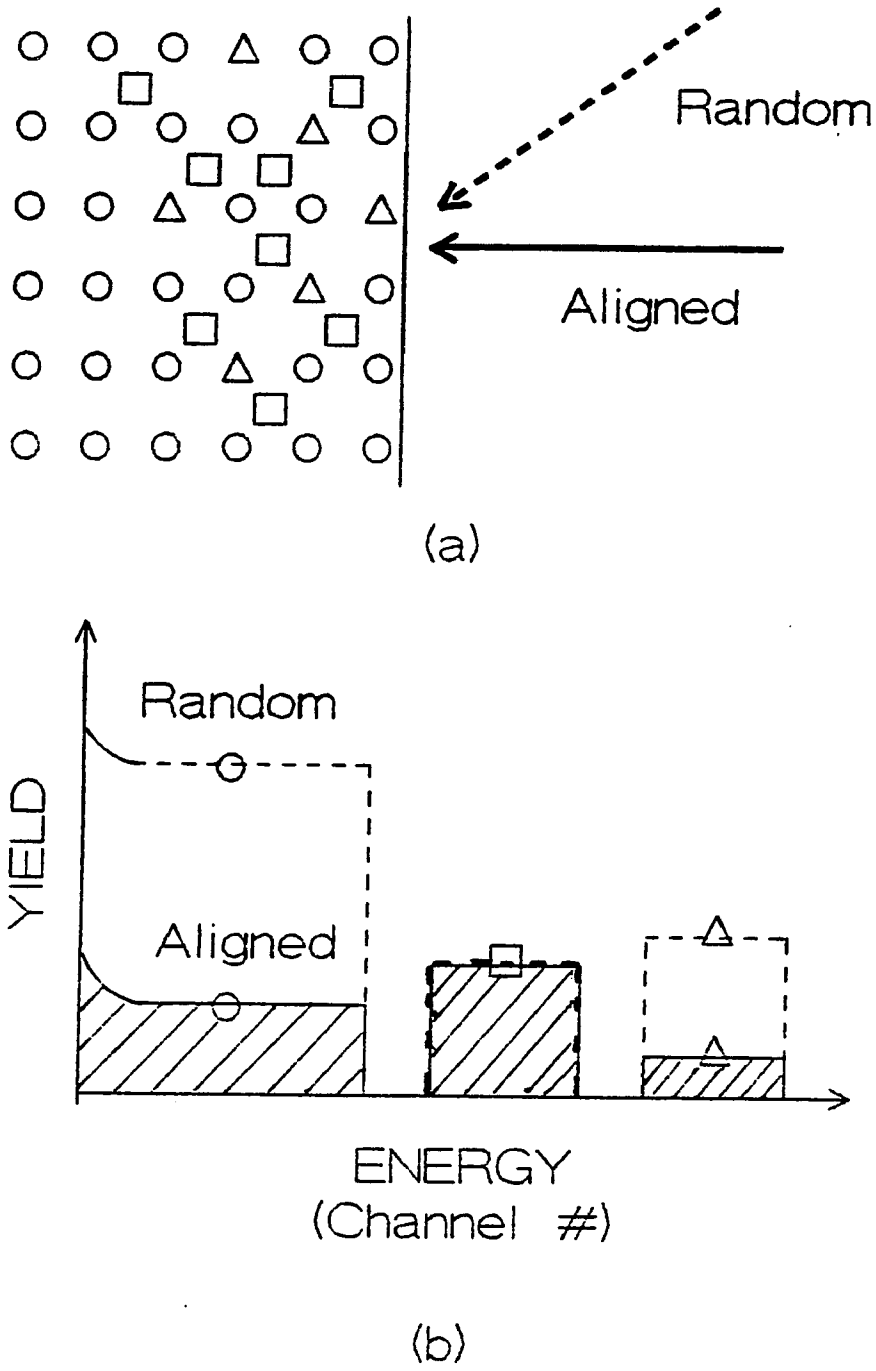

Figure 3-44. (a) A schematic of a crystalline solid (o, host atoms) with a surface layer including heavy impurities that are in interstitial sites (□) and substitutional sites (△).
(b) The backscattering spectra for the random and aligned beams. In (a) the arrows show the directions of these beams.

The most common RBS experiment involves the determination of two spectra: the aligned and the random. In the aligned experiment the incident beam is directed along a major orientation of the crystal (e.g., <100>) and a spectrum is obtained. For the random spectrum the sample is rotated so that the incident beam is not directed along a major orientation. The crystal may also be rotated while the spectrum is acquired [37]. In either case channeling effects are minimized since the beam "sees" a random arrangement of atoms.

Performing both a random and an aligned experiment allows one to determine whether an atom is substitutional or interstitial. When an atom is substitutional the spectra will appear as the triangle peak in Fig. 3-44. If the atom is purely interstitial its spectra for the random and aligned experiments will be coincident (see the square spectra in Fig. 3-44).

In most cases impurity atoms will not be totally interstitial or substitutional. A quantity termed the substitutional fraction f may be determined. This is given by the equation [37,38]

$$f = \frac{1 - \chi_{min}^{impurity}}{1 - \chi_{min}^{host}} \tag{3.40}$$

where $\chi_{min}^{impurity}$ $\left(\chi_{min}^{host}\right)$ is the minimum yield of the impurity (host). The minimum yield is given by the ratio of the height of the aligned spectra to the height of the random spectra in the near surface region. This formula gives a rough estimate as to the number of substitutional impurity atoms [38].

3.4.2.1 Experimental Results

The 1 X 10^{16} cm^{-2}, furnace annealed samples were studied by RBS. This work was performed at AT&T Bell Laboratories, Allentown on a General Ionex System. A

2.25 MeV $^4He^{2+}$ ion beam was used for the analysis with a detector placed at 164° from the incident directions.

The aligned and random spectra for the as-implanted sample are shown in Fig. 3-45. Note that part of the aligned silicon spectrum (left hand part of Fig. 3-45) is coincident with the random spectrum. This indicates that silicon in the surface region is randomly distributed throughout this surface layer. Also note that the random and aligned arsenic spectra (right-hand part of Fig. 3-45) are essentially the same. These spectra indicate that a great deal of disorder is present in the silicon surface, as would be expected for an amorphous layer.

The spectra for the annealed total and tail-only samples are shown in Figs. 3-46 and 3-47, respectively. Comparing Fig. 3-45 to these figures, it is quite evident that by 800°C most of the implantation damage has annealed. This is supported by the dramatic decrease in the aligned spectra yield. Especially note the decrease in the silicon aligned yield between 800°C and 950°C for the total samples (Fig. 3-46). This indicates that the 800°C sample is not totally annealed.

By observing the arsenic random spectra the arsenic diffusion can be observed. As observed in the SIMS work, very little arsenic diffusion occurs between 800°C and 950°C. At 1100°C a great deal of diffusion occurs, thus these results are consistent with the previous work.

In Fig. 3-47c two peaks are observed in the silicon aligned spectrum and one in the random spectrum. These peaks are due to a thin layer of silicon dioxide that was not completely etched from the surface before analysis. For comparison, the 950°C, tail-only sample (Fig. 3-47b) was analyzed with the spin-on-glass still intact. This oxide layer was approximately 1000 Å thick. Comparing these two figures the oxide peaks in Fig. 3-47c reside between channel numbers 175 and 200, while the oxide

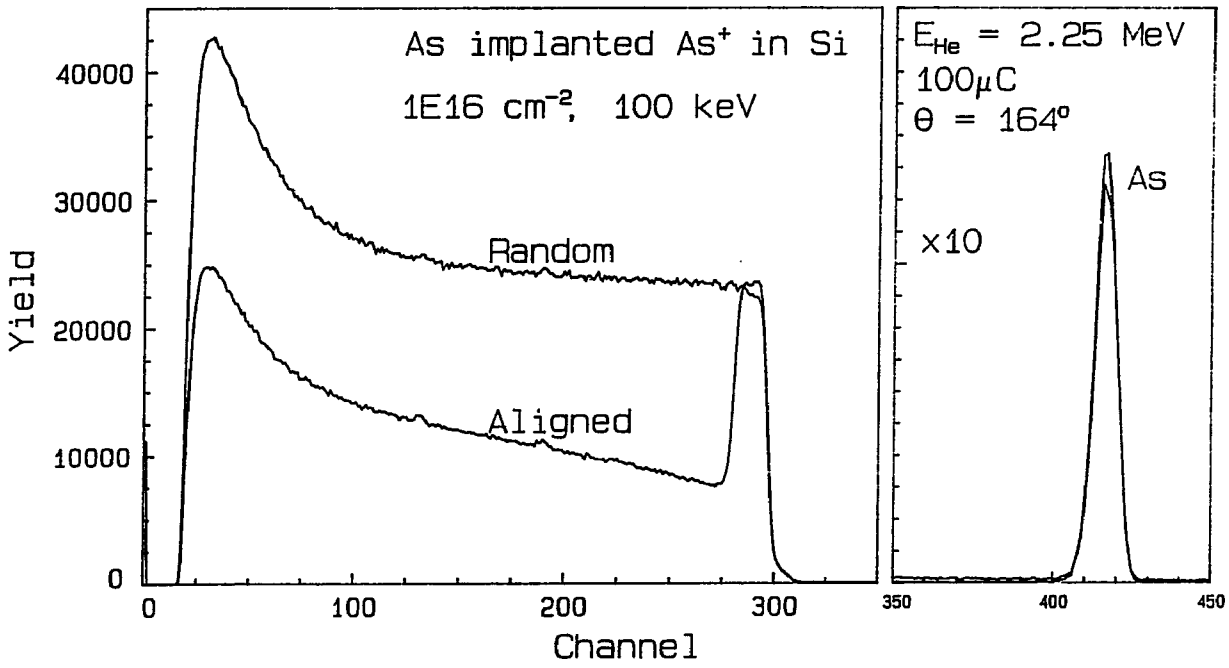

Figure 3-45. RBS random and aligned spectra for the as-implanted 100 keV, 1 X 10^{16} cm^{-2} sample. The aligned spectrum was taken along the <100> direction.

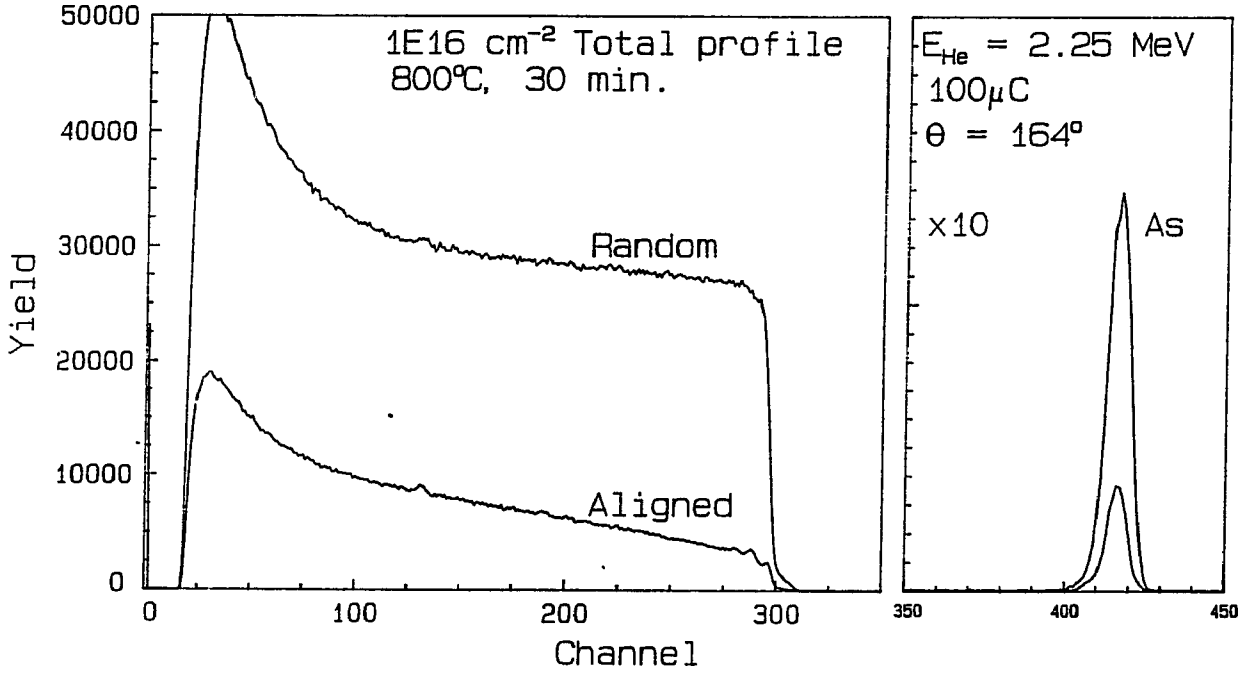

Figure 3-46. The RBS spectra for the total samples after annealing at (a) 800°C.

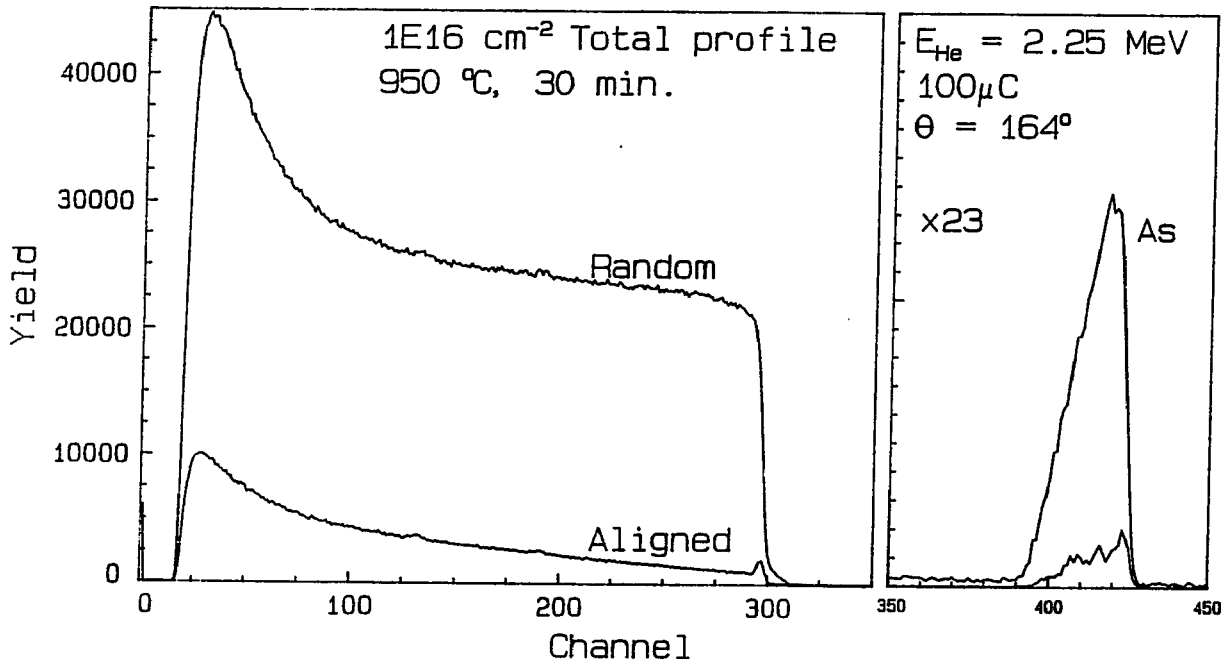

Figure 3-46. The RBS spectra for the total samples after annealing at (b) 950°C.

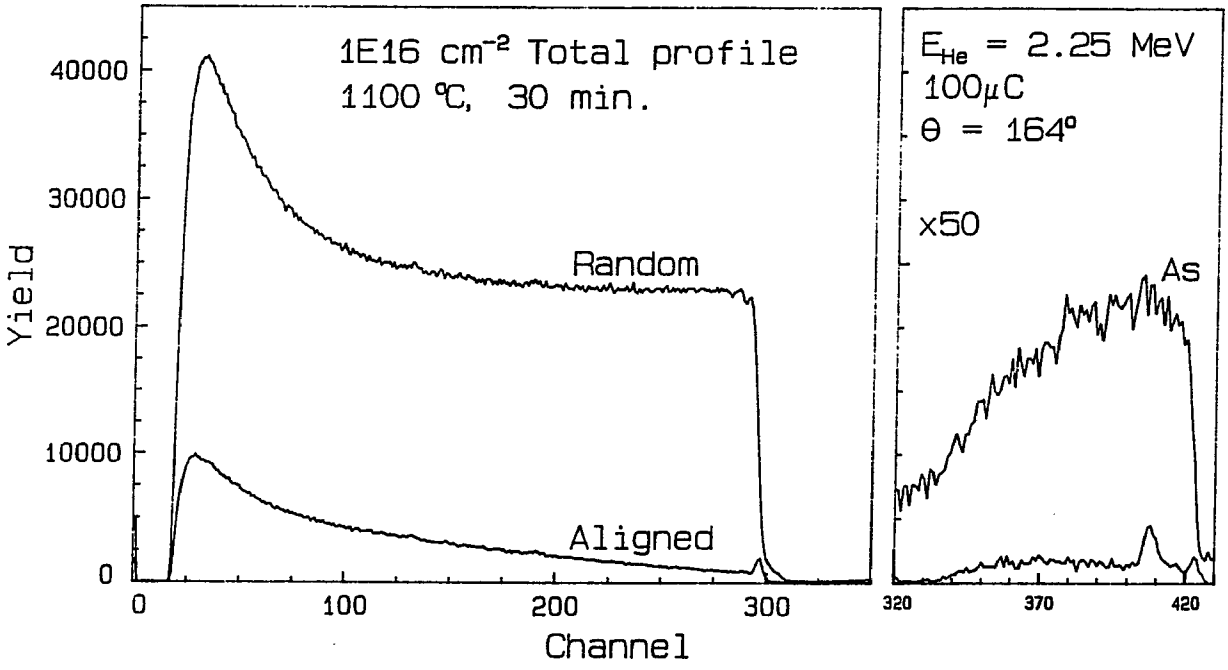

Figure 3-46. The RBS spectra for the total samples after annealing at (c) 1100°C.

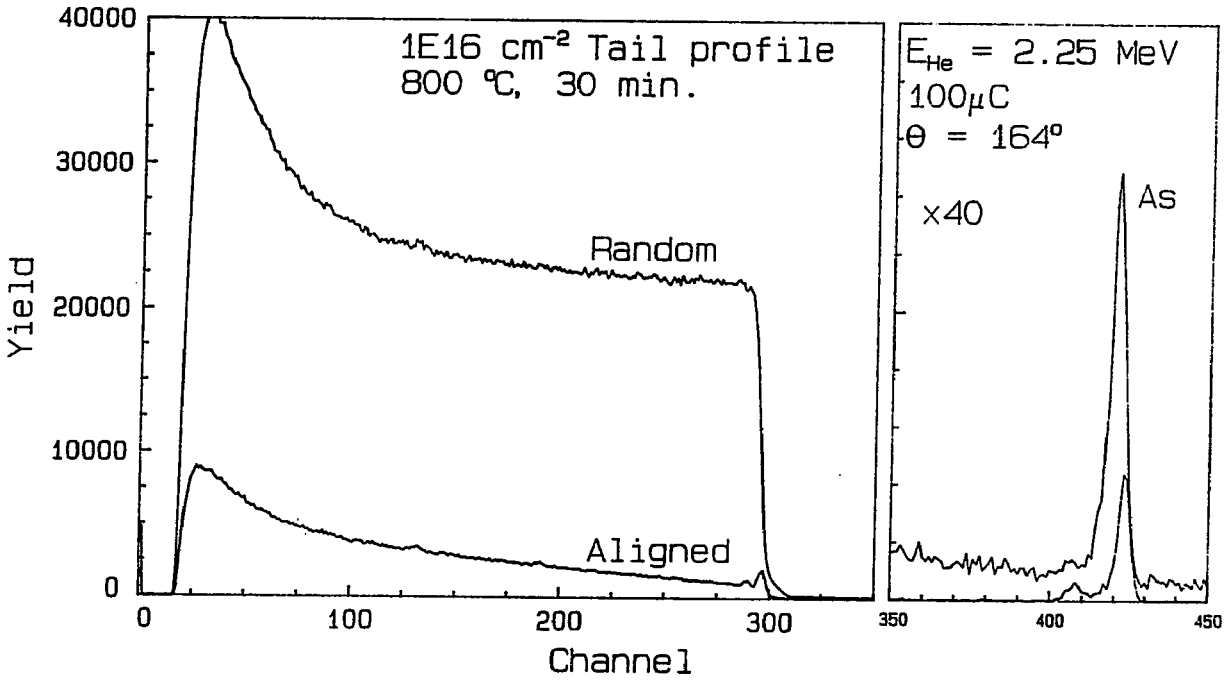

Figure 3-47. The RBS spectra for the tail-only samples after annealing at (a) 800°C.

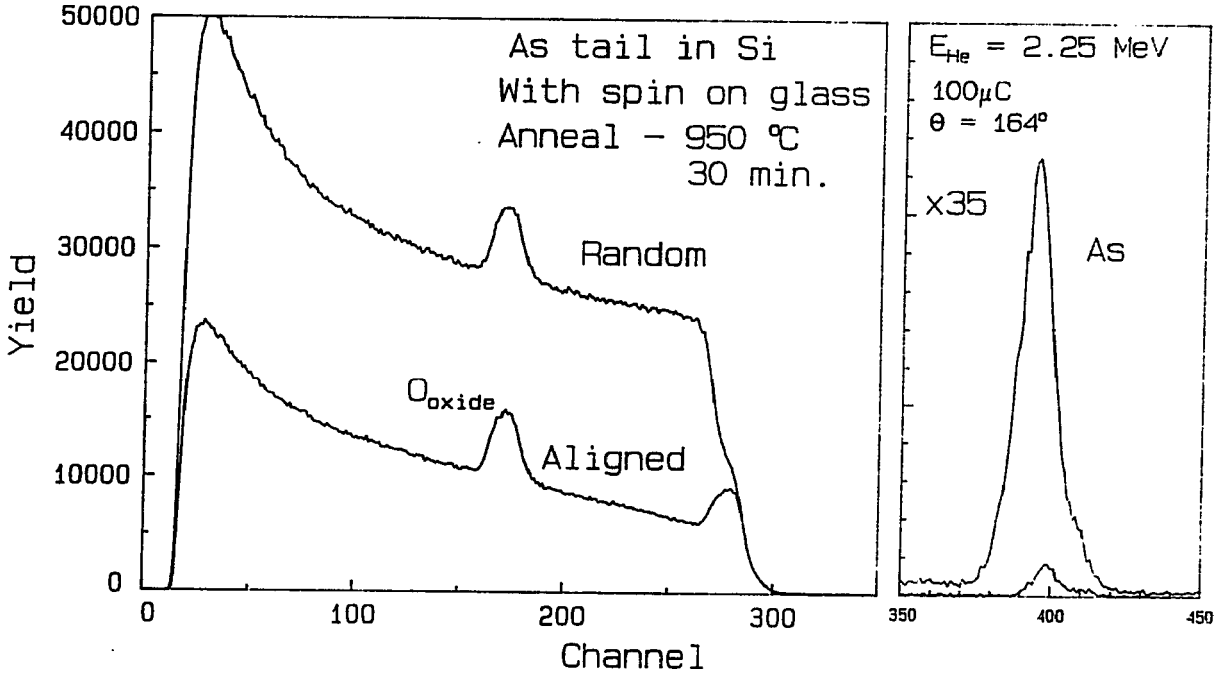

Figure 3-47. The RBS spectra for the tail-only samples after annealing at (b) 950°C.

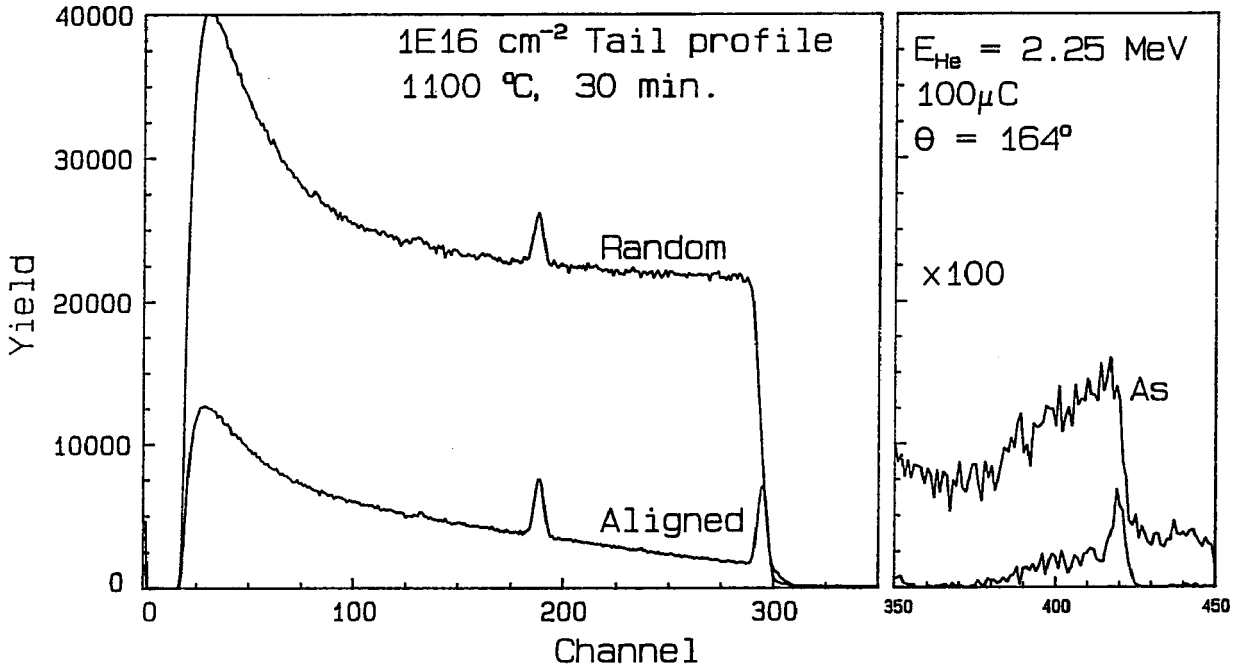

Figure 3-47. The RBS spectra for the tail-only samples after annealing at (c) 1100°C.

peaks in Fig. 3-47b reside between 150 and 200. Thus the oxide peak in Fig. 3-47c is a remnant of the original capping oxide. Also note that a peak occurs in both figures below channel 300. This is indicative of randomly distributed silicon (compared to the substrate) as would be expected in an oxide.

From these spectra and aligned spectra obtained in the <111> and <110> directions the substitutional fraction was determined. These results are shown in Table 3-4. As would be expected, the arsenic in the total samples becomes more substitutional for a temperature increase from 800°C to 950°C. These results also show that, with this temperature increase, the arsenic atoms in the total sample become more substitutional in the <110> and <111> directions.

The results for the tail-only samples are quite different from the total samples. First note that the tail is less substitutional than the total. This suggests that damage annealing is not as complete for the tail samples as compared to the total samples. Secondly, the tail samples become less substitutional in the <110> and <111> directions with increasing annealing temperature. Note the dramatic decrease in substitution fraction between 950°C and 1100°C.

Strain and/or precipitation may play a role in the damage annealing and arsenic diffusion of the total and tail samples. As was noted in an earlier section, Servidori et al. [21] have observed two strained layers in above amorphization dose implanted silicon. In their work a negatively strained surface layer was observed with a positively strained layer in the end-of-range region. A 900°C, 30 minute anneal was found to remove the negatively strained surface region. This anneal did not significantly change the strain in the end-of-range region. This may be an explanation for the tail-only results, but precipitation cannot be ruled out.

Table 3-4. Fraction of arsenic atoms that are substitutional along different channeling directions for the 1 X10^{16} cm^{-2}, furnace annealed samples.

Anneal Temperature (°C)	<100>	<110>	<111>
TOTAL			
800	0.84 ± 0.04	0.91 ± 0.04	0.82 ± 0.04
950	0.93 ± 0.04	0.96 ± 0.04	0.94 ± 0.04
1100	0.93 ± 0.04	0.95 ± 0.04	0.99 ± 0.04
TAIL			
800	0.72 ± 0.04	0.87 ± 0.04	0.86 ± 0.04
950	0.79 ± 0.04	0.84 ± 0.04	0.81 ± 0.04
1100	0.72 ± 0.04	0.63 ± 0.04	0.65 ± 0.04

These results are also consistent with the difference noted between the SIMS and differential Hall effect data in Section 3.4.1.1. In that section it was found that the profiles in Figs. 3-29a and 3-42a could be suspect to different interpretations. From the data in Table 3-4 we see that the arsenic in the tail-only sample at 950°C is only 80% substitutional. Therefore only a fraction of the arsenic is electrically active, which could lead to differences in the profiles determined by SIMS and the Hall effect.

3.4.3 Angular Yield

Additional information about the location of impurity atoms may be obtained by performing angular yield experiments. In this measurement a low-index crystallographic axis is found (see Chu et al. [37] for details on this procedure). Then

the sample is rotated so that the incident beam is a few degrees from this axis. A spectrum is then obtained. The sample is then rotated a small fraction of a degree decreasing the angle between the beam direction and the axis. Another spectrum is obtained. This process is repeated through the channeled direction (tilt angle=0 in Fig. 3-48) until an equal amount of points are taken on the other side of the channel. The normalized yield is then plotted as a function of tilt angle. This is depicted in Fig. 3-48.

From this profile a parameter called the half-angle $\psi_{1/2}$ may be determined. The half-angle is measured at the yield corresponding to $\frac{1}{2}(1 + \chi_{min})$. This is just the angular width at the half minimum. The half-angle is also known as the critical angle [38], thus it is the maximum angle the ion beam can make with the channel direction and still have the ion steered by the rows of atoms in the channel. From theory this is given by [38,39]

$$\psi_{1/2} = 0.8\, F_{RS}(\xi) \left(\frac{2\, Z_i Z_T q^2}{Ed} \right)^{\frac{1}{2}} \tag{3.41}$$

where $F_{RS}(\xi)$ is the square root of the string potential using Moliere's screening function [39]. $F_{RS}(\xi)$ is tabulated in reference [39]. $Z_i Z_T$ are the atomic numbers of the ion and target, respectively; q is the elemental charge; E is the incident ion energy (in MeV), and d is the atomic spacing (in Å) along the axial direction. The normalized distance of closest approach ξ is given by [37,39]

$$\xi = 1.2 \frac{u_1}{a} \tag{3.42}$$

where u_1 is the one-dimensional rms thermal vibrational amplitude and a is the Thomas-Fermi radius.

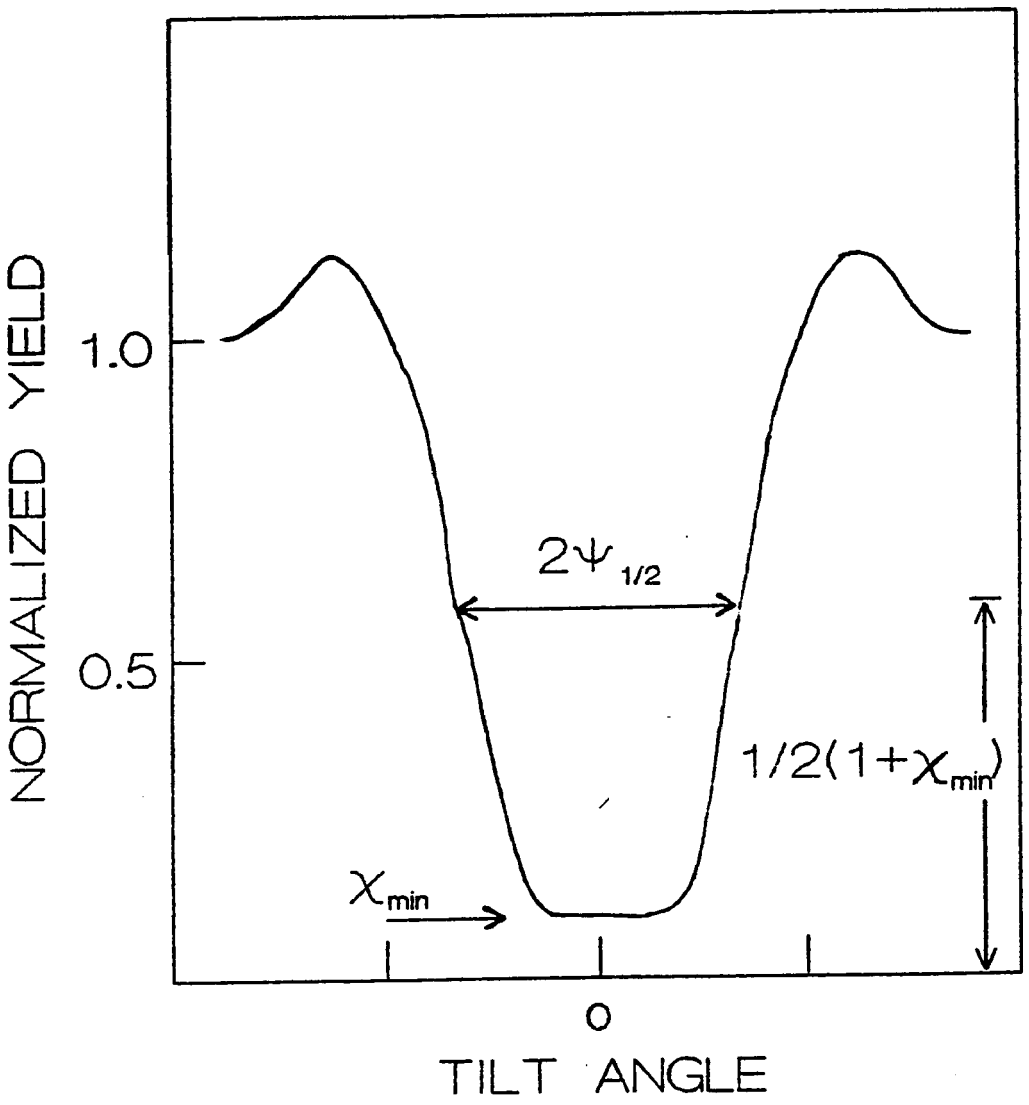

Figure 3-48. A schematic of an angular yield profile.

3.4.3.1 Experimental Results

To gain more insight as to what caused the substitutional fraction of the 1100°C tail-only sample to decrease an angular yield study was performed. This work was done at AT&T Bell Laboratories in Murray Hill, NJ. A van de Graaff accelerator supplied the 1.8 MeV He^+ beam. A two-axis goniometer controlled the sample angle.

Figure 3-49 shows the results of this experiment. Note that the arsenic minimum yield for both axial directions is greater than the silicon minimum yield. The angular half-widths determined from these data are recorded in Table 3-5. For the <111> direction, the experimental arsenic and silicon half-widths are the same within experimental error. In the <110> case the arsenic half-width is slightly less than the silicon half-width. These results suggest that the arsenic atoms may be randomly distributed in the silicon lattice. A similar result was observed by Haskell et al. [40] after bombardment with a high current beam of MeV helium ions.

Silicon half-widths have been estimated by the method described above. Results of these calculations are listed in Table 3-5. Note that the calculated and measured silicon half-width values for the <111> axis are equivalent. Contrary to this, the calculated value along the <110> direction is much larger than the experimental value. This suggests that there is a narrowing of the <110> channel which could be due to stress in the end-of-range region. It should be noted that the formation of a precipitate cannot be ruled out from these data.

3.5 Structural Characterization

Transmission electron microscopy (TEM) was employed to complement the RBS studies presented in Sections 3.4.2 and 3.4.3. This technique allows examination of the microstructure of defects after implantation and annealing. Therefore, the annealing of implantation damage can be examined.

Table 3-5. Angular half-widths for the 1100°C, 1 X 10^{16} cm^{-2} tail sample.

	$\psi_{1/2}$ <111>	<110>
Silicon		
Experimental	0.38° ± .02°	0.44° ± .01°
Theoretical	0.39°	0.61°
Arsenic		
Experimental	0.38° ± .03°	0.41° ± .01°

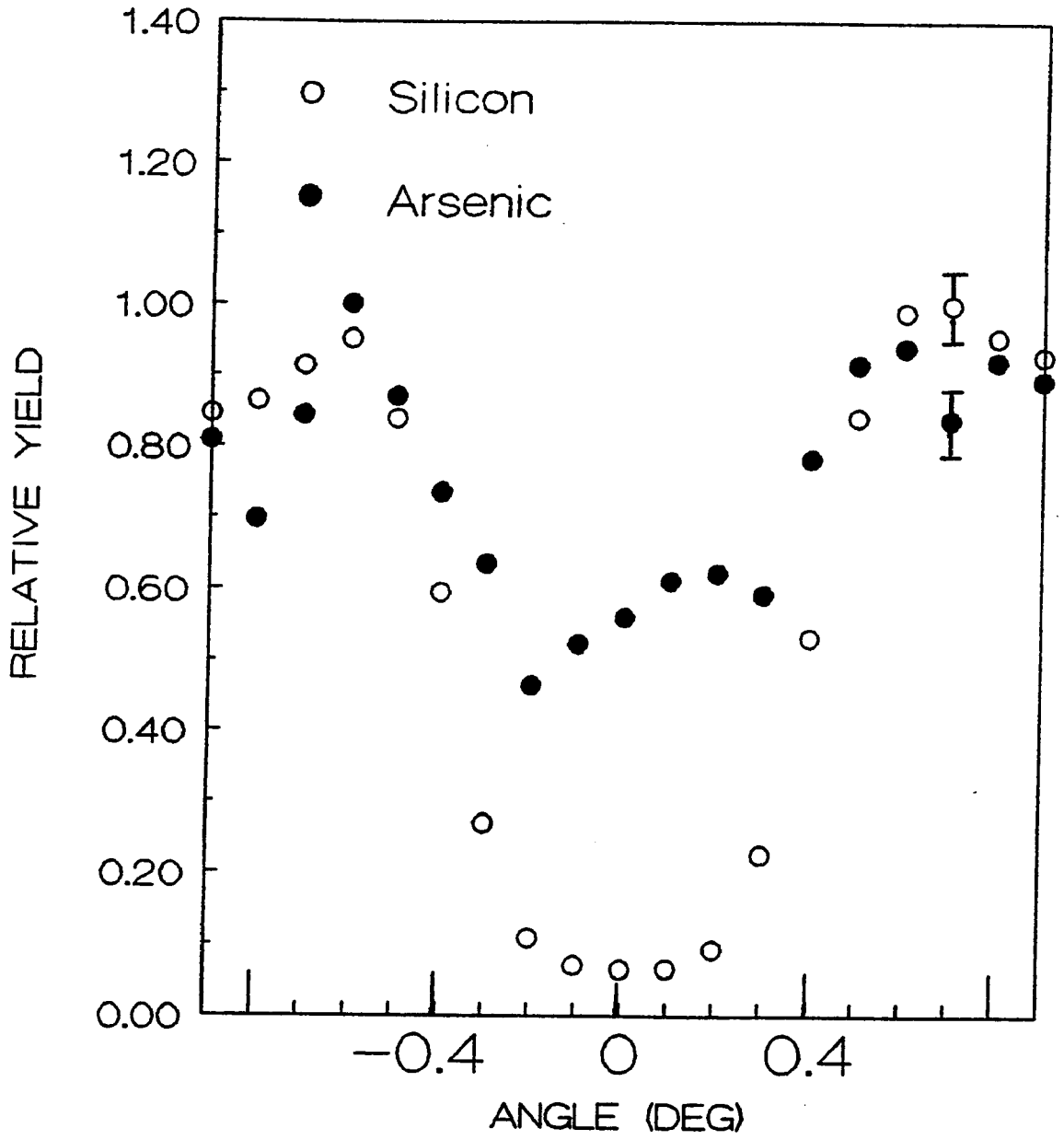

Figure 3-49. Angular yield profiles for the 1100°C, 1 X 10^{16} cm^{-2} tail only sample. Results from analysis about the (a) <111> axis.

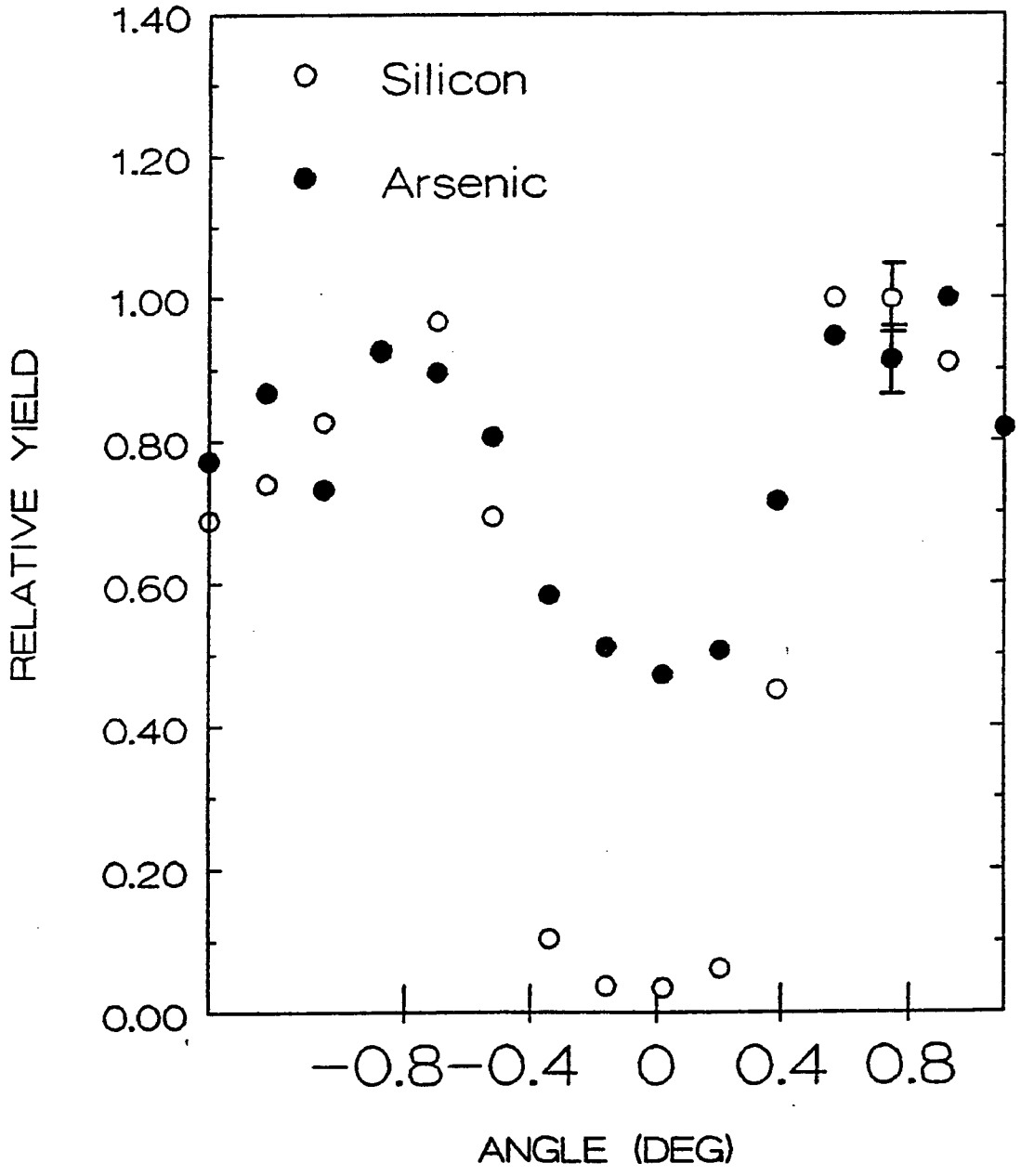

Figure 3-49. Angular yield profiles for the 1100°C, 1 X 10^{16} cm^{-2} tail only sample. Results from analysis about the (b) <110> axis.

3.5.1 Cross-Sectional Transmission Electron Microscopy

A TEM microscope uses a series of magnetic lenses to focus an electron beam on a sample. The electrons usually have an energy between 20 and 100 keV [41] and are focussed by a double condenser lens system onto the specimen. The transmitted electrons form either an image or a diffraction pattern on a fluorescent screen. This image can be magnified by a set of lenses between the sample and the viewing screen.

As discussed in Section 1.2.3, the morphologies of implantation defects have been characterized with respect to their distance from the silicon surface and/or the amorphous/crystalline (a/c) interface. Therefore, this study has utilized the electron microscope to perform cross-sectional TEM (XTEM) studies. Since we wish to examine the samples in cross-section special specimen preparation must be performed before putting the sample into the microscope.

To prepare cross-section specimens for TEM study the technique suggested by Bravman and Sinclair [42] has been utilized with a few modifications. After a sample was annealed it was scribed and diced into small rectangular pieces (approximately 10mm X 3mm in size). Six of these pieces were epoxy bonded so that every two slices had the implanted surfaces face to face (see Fig. 3-50). Hardman epoxy (manufactured by Hardman, Inc., Belleville, NJ) was used in this process. After curing the epoxy for 2 hours at room temperature , the composite is sliced to a thickness of approximately 650 μm using a diamond wafer saw. From this slice a 3 mm diameter disc is cut out using an ultrasonic disc cutter. The specimen is now ready for thinning.

To begin the thinning process the disc is glued onto a glass microscope slide with a low melting point wax (Crystal-Bond) and mechanically polished using 600 grit SiC paper. This is followed by polishing using successively smaller grits (8 μm, 3 μm, and

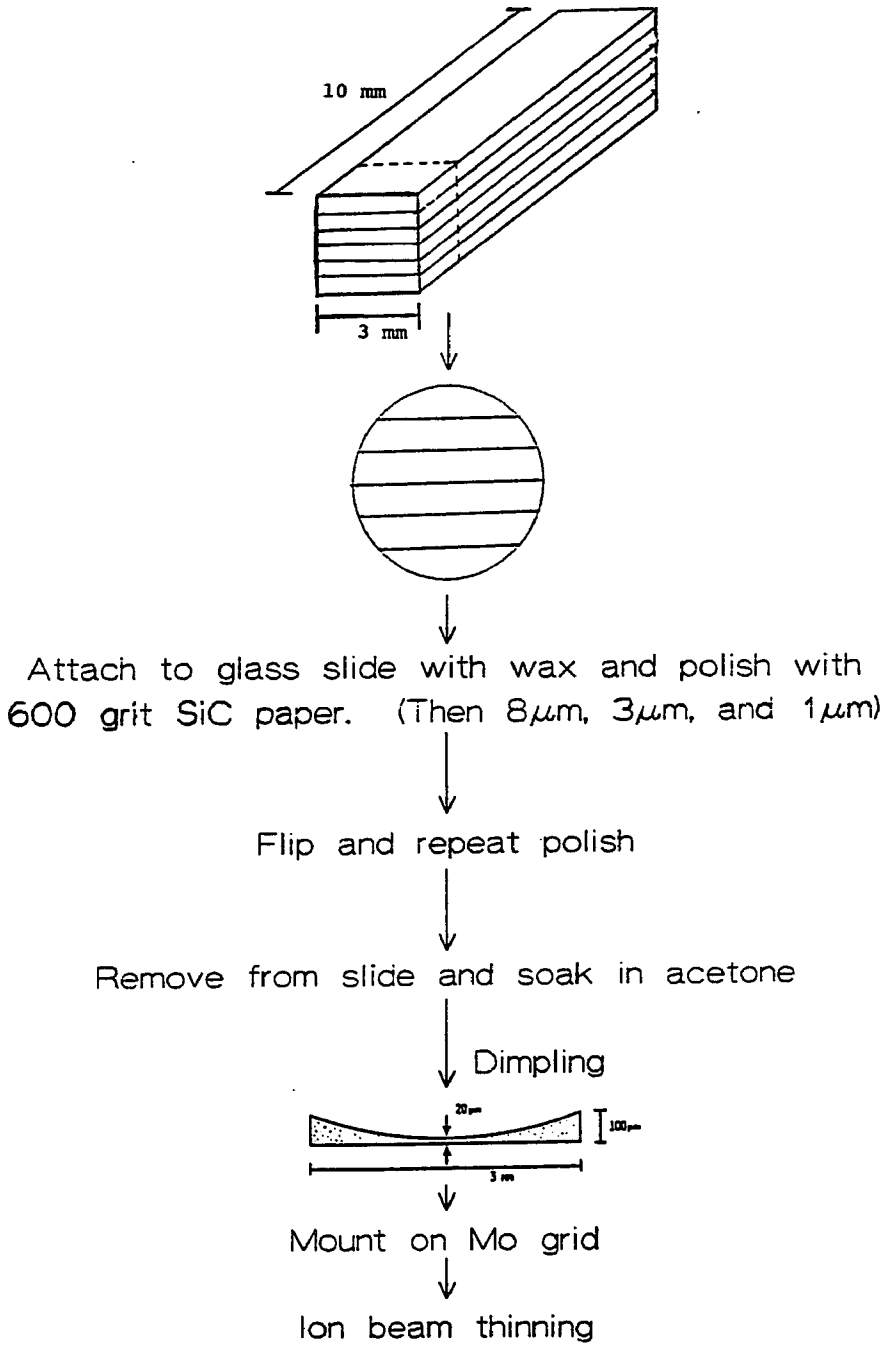

Figure 3.50. **A flow chart describing the fabrication of the XTEM specimens.**

finally 1 μm) to obtain a smooth surface. At this stage the specimen is approximately 250 to 300 μm thick. The specimen is removed from the glass slide, flipped over, and mechanically polished to a 1 μm finish. Now the sample is approximately 75 μm thick. The specimen is removed from the glass slide and washed in acetone to remove the residual wax. At this point the sample is dimpled using a Gatan dimpler until its thickness is about 15 μm or the silicon becomes transparent. The specimen removed is from the dimpler stage and washed in acetone. After mounting the sample on a Mo grid it is ion milled with a 4.5 keV Ar ion beam set at 15° from the sample surface. During milling the sample is cooled to liquid nitrogen temperature. After a small perforation is formed, the argon beam energy is reduced to 3.5 keV and the angle of incidence is reduced to 13°. The sample is then subjected to another 5 to 10 minutes of additional milling.

3.5.1.1 Experimental Results

The 1 X 10^{16} cm^{-2}, furnace annealed samples were examined by XTEM to determine the role the amorphous layer and the end-of-range region play in the annealing of implantation damage. This technique will also allow us to determine whether precipitation in the tail-only samples can account for the decrease in substitutional fraction with increasing annealing temperature as seen in Table 3-4. A Philips 400T analytical electron microscope operated at 120 keV was used in this study. A magnification of 130,000X was used.

Results of the XTEM study of the 800°C total sample are shown in Fig. 3-51. In this micrograph note that two layers of defects are observed. This structure has also been observed by several other groups [43-46]. The defects closest to the surface are located near the projected range of the implant. Jones et al. [45] have suggested that these dislocation loops form due to exceeding the solid solubility of arsenic in silicon in

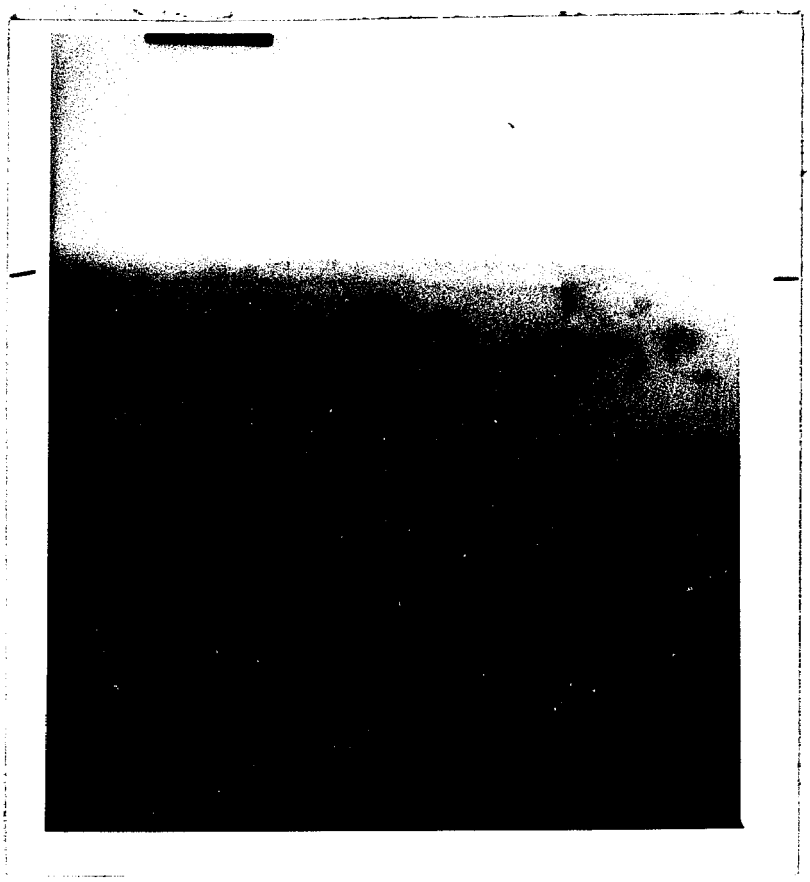

Figure 3-51. XTEM micrograph of the 1 X 10^{16} cm^{-2}, 800°C total sample.

this region. Hsu and Chen [46] have attributed the formation of these loops to the agglomeration of self-interstitials mediated by a high concentration of electrically inactive arsenic in the region.

The lower layer of loops occurs beyond the original a/c interface, in the tail region of the implant. These defects are known to form whenever an amorphous layer has been created during implantation [45]. A recent model for the formation of these loops suggests that two sources contribute to the formation [45]. First there is an excess of ions coming to rest beyond the a/c interface which increase the density of the crystal and the loops should be extrinsic. It is also suggested that these dislocation loops should be composed primarily of silicon interstitials since there are more Frankel pairs than implanted ions beyond the a/c interface.

Jones et al. [45] also proposed that at higher doses of the heavier ions used as dopants in silicon (such as arsenic) a second factor will dominate the formation of end-of-range loops. Here the energy deposited into nuclear collisions in the amorphous layer is important. They suggest that elastic collisions within this region create free atoms which either recoil or diffuse through the a/c interface to the end-of-range region, and thus contribute to the total concentration of atoms in the loops. This description seems reasonable since calculations (see Figs. 1-7 and 1-8) of the damage recoil energy distributions show that a significant amount of silicon is displaced from the surface region of the implant. Typically, a silicon atom that has been displaced within 400 Å of the surface will displace another 20 silicon lattice atoms. Therefore, the end-of-range region will have an excess of silicon atoms.

A band of dislocation loops were also observed in the 800°C, tail-only sample (see Fig. 3-52). Recall that the fabrication of this sample required the removal of the amorphous layer before annealing. Approximately 1200 Å of silicon was removed

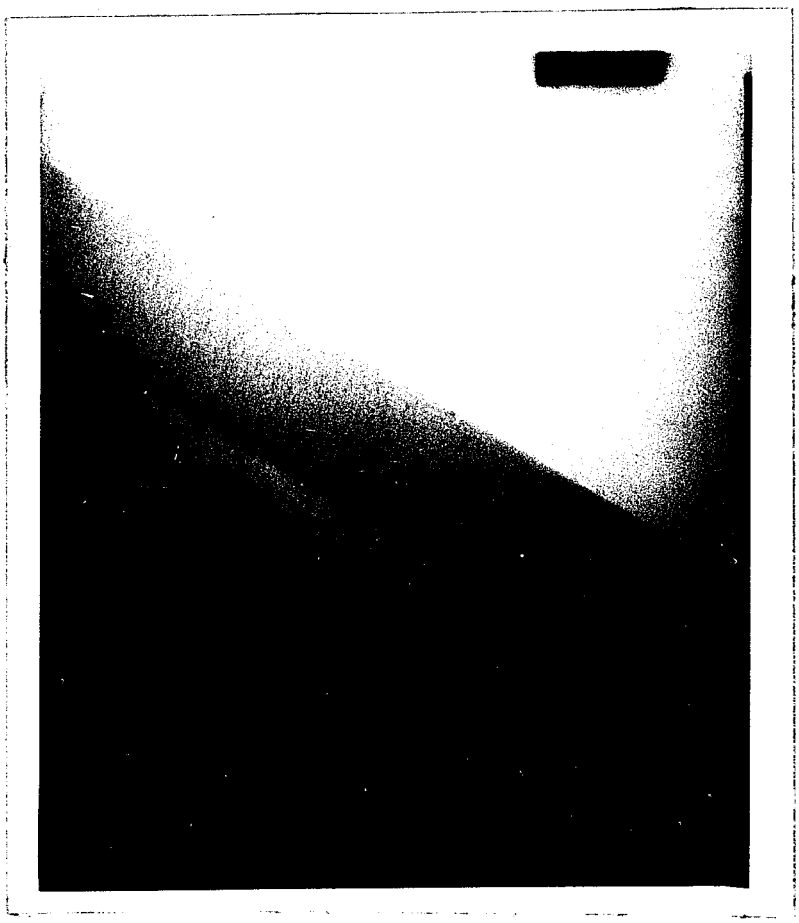

Figure 3-52. XTEM micrograph of the 1 X 10^{16} cm^{-2}, 800° tail-only sample.

from this sample. The fact that loops were found in this sample correlates well with the substitutional fraction determined by RBS (see Table 3-4).

At 950°C and above no defects were observed in the total samples. The elimination of dislocation loops for these higher temperature annealing conditions has also been noted by other authors [47-49]. Thus one would expect that the 950°C tail-only sample would not have any dislocation loops. As can be seen in Fig. 3-53 this is not true. Here we see that dislocation loops are still present but their density has decreased. Since no defects were observed in the 950°C total sample, these results suggest that the annealing of the end-of-range damage is assisted by point defects generated in the amorphous region during annealing. The results in Fig. 3-52 also suggest that point defect generation in the amorphous region (during annealing) is not required for the formation of end-of-range loops as proposed by Kim et al. [49].

No loops were observed in the 1100°C tail-only sample. It is therefore suggested that the dramatic decrease in substitutional fraction (Table 3-4) for this sample is not due to precipitation but is probably related to strain.

A contrast technique was also used to determine whether the dislocation loops were interstitial or vacancy in nature [41]. In each use where loops existed, both vacancy and interstitial loops were found.

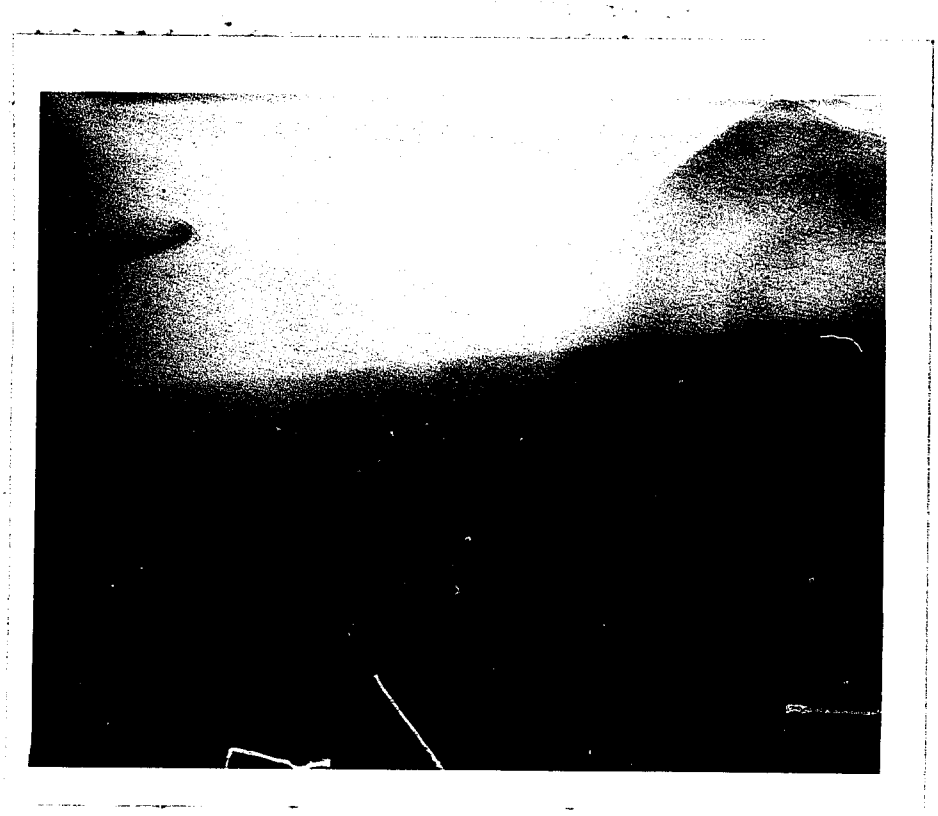

Figure 3-53. XTEM micrograph of the 1 X 10^{16} cm^{-2}, 950° tail-only sample.

CHAPTER 3

References

1. S.A. Ghandi, VLSI Fabrication Principles, (John Wiley & Sons, New York, 1983) Chapter 7.

2. S.R. Morrison, The Chemical Physics of Surfaces, (Plenum, New York, 1977).

3. D.R. Turner, in The Electrochemistry of Semiconductors, P.J. Holmes, eds., (Academic, New York, 1962).

4. K.M. Busen and R. Linzey, *Trans. Met. Soc.* AIME, 236, 306, (1966).

5. W. Przyborski and J. Roed, J. Lippert, and L. Sarholt-Kristensen, *Rad. Eff.*, 1, 33 (1969).

6. S. Prussin, D.I. Margolese, and R.N. Tauber, *J. Appl. Phys.* 51, 180 (1985).

7. R.G. Mazur and G.A. Gruber, *Solid State Technology* 24 69 (1981).

8. D.C. D'Avanso, R.D. Rung, and R.W. Dutton, Spreading Resistance for Impurity Profiles, Technical Report No. 5013-2, (Integrated Circuits Laboratory, Stanford University, Stanford, CA, 1977).

9. P.A. Schumann and E.E. Gardner, *Solid State Electron.* 12, 371 (1969).

10. H.L. Berkowitz and R.A. Lux, *J. Electrochem. Soc.* 128, 1137 (1981).

11. E.H. Putley, The Hall Effect and Related Phenomena, (Butterworths & Co., Ltd. London, 1960).

12. A.C. Beer, Galvanomagnetic Effects in Semiconductors, (Academic Press, Inc., New York, N.Y., 1963).

13. B.G. Streetman, Solid State Electronic Devices, (Prentice-Hall, Inc., Englewood Cliffs, N.J., 1980).

14. L.J. van der Pauw, *Philips Res. Rep.*, 13, 1 (1958).

15. N.G.E. Johansson, J.W. Mayer, O.J. Marsh, *Solid-State Electronics*, 13, 317 (1970).

16. R. Baron, G.A. Shifrin, O.J. Marsh, and J.W. Mayer, *J. Appl. Phys.*, 40, 3702 (1969).

17. 1985 Annual Book of ASTM Standards, vol. 10.05, Standard F76-84, p. 155.

18. S. M. Hu, *J. Appl. Phys.* 53, 1499 (1982).

19. H. Jorke and H.-J. Herzog, *J. Appl. Phys.* 60, 1735 (1986).
20. G. Masetti, M. Severi, and S. Solmi, *IEEE Trans. Electron Devices* ED-30, 764 (1983).

21. M. Servidori, R. Angelucci, F. Cembali, P. Negrini, S. Solmi, P. Zaumseil, and U. Winter, *J. Appl. Phys.* 61, 1834 (1987).

22. D.V. Lang, *J. Appl. Phys.* 45, 3014 (1974).

23. G.L. Miller, D.V. Lang, and L.C. Kimerling, *Ann. Rev. Mater. Sci.*, 377 (1977).

24. D.V. Lang, in Thermally Stimulated Relaxation in Solids, P. Braunlich, ed., (Springer Verlag, New York, 1979), Chapter 3.

25. J.R. Troxell, Ph.D. Dissertation, Department of Physics, Lehigh University, Bethlehem, PA, 1979.

26. T.E. Seidel, C.S. Pai, D.J. Lischner, D.M. Maher, R.V. Knoell, J.S. Williams, B.R. Penumalli, and D.C. Jacobson, in Energy-Beam Solid Interactions and Transient Thermal Processing, D.K Biegelsen, G.A. Rozgonyi, C.V. Shank, eds., (Mater. Res. Soc. Proc. Vol. 35, Pittsburgh, PA 1985) p. 329.

27. K.L. Wang, Y.H. Lee, and J.W. Corbett, *Appl. Phys. Lett.* 33, 547 (1978).

28. R.D. Harris, Ph.D. Dissertation, Department of Physics, Lehigh University, Bethlehem, PA, 1981.

29. L.W. Song, Ph.D. Dissertation, Department of Physics, Lehigh University, Bethlehem, PA, 1988.

30. C. Clark, private communication.

31. J.L. Hoyt and J.F. Gibbons, in Rapid Thermal Processing, T.O. Sedgwick, T.E. Seidel, and B.-Y. Tsaur, eds., (Mater. Res. Soc. Proc. Vol. 52, Pittsburgh, PA, 1986) p. 15.

32. J.A. McHugh, in Methods of Surface Analysis, A.W. Czanderna, ed., (Elsevier, Amsterdam, 1975) Chapter 6.

33. C.W. Magee, *Nucl. Inst. and Methods* 191, 297 (1981).

34. C.G. Pantano, in Metals Handbook Ninth Edition: Volume 10 Materials Characterization (Am. Soc. for Metals, Metals Park, Ohio, 1986) p. 610.

35. F. Degreve, N.A. Thorne, and J.M Lang, *J. Mater. Sci.* 23, 4181 (1988).

36. F.A. Stevie, P.M. Kahora, S. Singh, and L. Kroko, in Secondary Ion Mass Spectrometry: SIMS VI, A. Benninghoven, A.M. Huber, and H.W. Werner, eds., (J. Wiley & Sons, New York, 1988) p. 319.

37. W.-K. Chu, J.W. Mayer, and M.-A. Nicolet, Backscattering Spectrometry (Academic Press, New York, 1978).

38. L.C. Feldman, J.W. Mayer, and S.T. Picraux, Materials Analysis by Ion Channeling: Submicron Crystallography (Academic Press, New York, 1982).

39. B.R. Appleton and G. Foti, in Ion Beam Handbook for Material Analysis, J.W. Mayer, and E. Rimini, eds., (Academic Press, New York, 1977) Chapter 3.

40. J. Haskell, E. Rimini, and J.W. Mayer, *J. Appl. Phys.* 43, 3425 (1972).

41. J.W. Edington, Practical Electron Microscopy in Materials Science, (Van Nostrand Reinhold Co., New York, 1976).

42. J.C. Bravman and R. Sinclair, *J. Electron Micros. Tech.* 1, 53 (1984).

43. N.R. Wu, D.K Sadana, and J. Washburn, *Appl. Phys. Lett.* 44, 782 (1984).

44. S.J. Pennycook, R.J. Culbertson, and J. Narayan, *J. Mater. Res.* 1, 476 (1986).

45. K.S. Jones, S. Prussin, and E.R. Weber, *Appl. Phys. Lett.* 27, 2304 (1989).

46. S.N. Hsu and L.J. Chen, *Appl. Phys. Lett.* 27, 2304 (1989).

47. T.E. Seidel, D. J. Lischner, C.S. Pai, R.V. Knoell, D.M. Maher, and D.C. Jacobson, *Nucl. Inst. Methods Phys. Res. B* 7/8, 251 (1985).

48. K.S. Jones, S. Prussin, and E.R. Weber, *J. Appl. Phys.* 62, 4114 (1987).

49. Y. Kim, H.Z. Massoud, and R.B. Fair, *J. Elec. Mat.* 18, 143 (1989).

Chapter 4
Discussion

4.1 Arsenic Tail Diffusion

In Chapter 2 the diffusion and electrical activation of arsenic was discussed. Most of the models presented relied upon vacancy controlled diffusion and a concentration dependent diffusivity. In this study a concentration dependence has also been observed. Figure 4-1 shows the difference in carrier concentration profiles for two different implantation doses (1 X 10^{14} cm^{-2} and 1 X 10^{15} cm^{-2}) annealed for 10 seconds in a rapid thermal annealer. Note that in the lower dose case very little diffusion and electrical activation has occurred when the anneal temperature was increased from 800°C to 1080°C. Thus, as would be expected for this low dose, diffusion is independent of arsenic concentration. Increasing the dose by a factor of 10 we begin to see the affect of a higher arsenic concentration on electrical activation and diffusion. Therefore the results presented in Chapter 3 and Fig. 4-1 are consistent with the models in Chapter 2.

One way to validate a model is to compare it to actual data. This has been done for 1 X 10^{15} cm^{-2} and 1 X 10^{16} cm^{-2}, 100 keV implants of arsenic which were subsequently furnace annealed. The results of this study are shown in Fig. 4-2 where SIMS data and the PREDICT simulation [1] are compared. Note in the two cases shown the tail region of the simulation is deeper than the actual data. This was observed for all of the conditions studied. Also note the kink in the tail region of the 800°C simulation (Fig. 4-2a). This is due to enhanced tail diffusion as discussed in Section 2.5. Although this kink is not observed in the SIMS data of Fig. 4-2a it is

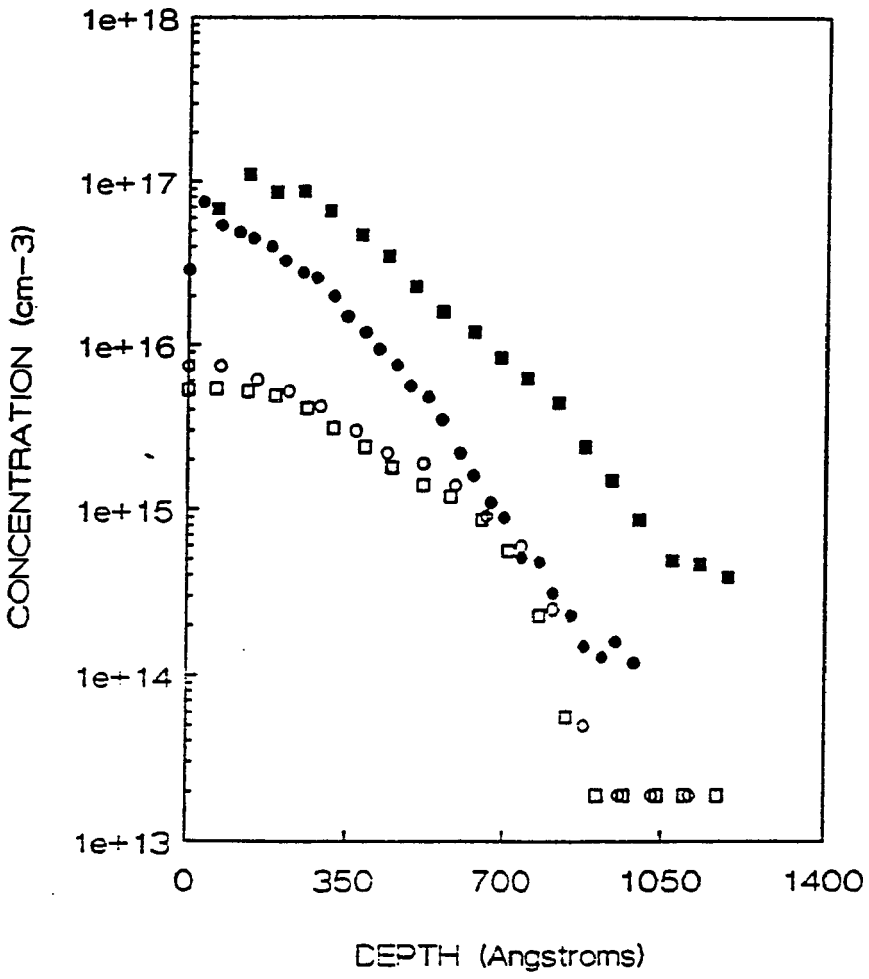

Figure 4-1. Profiles determined by spreading resistance for 1 X 10^{14} cm^{-2}, 50 keV (open symbols) and 1 X 10^{15} cm^{-2}, 50 keV (filled symbols) implanted samples. These samples were rapid thermal annealed for 10 seconds at 800°C (circles) and 1080°C (boxes).

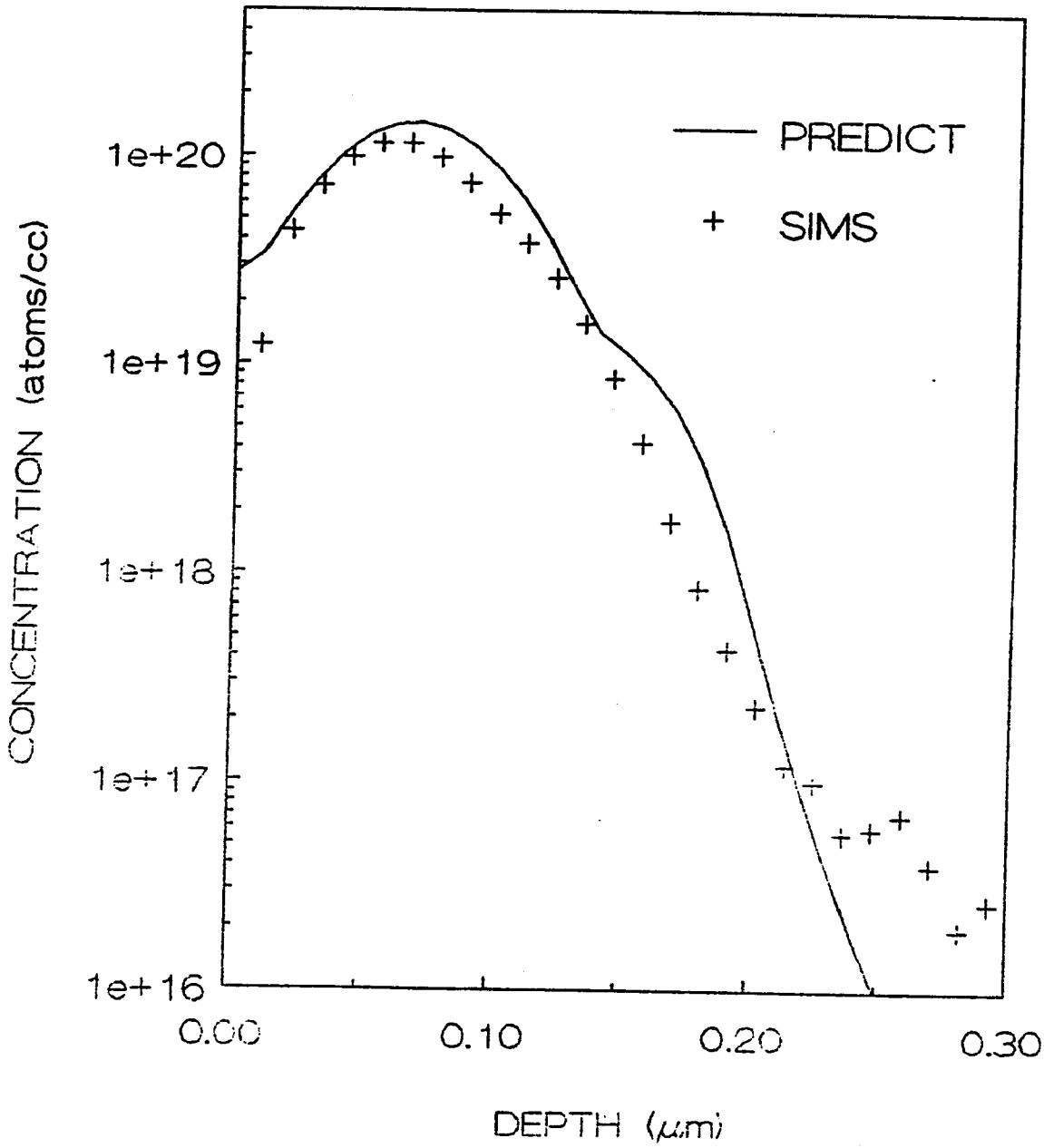

Figure 4-2. Comparison of SIMS total chemical concentration data to a simulation by PREDICT for a 1 X 10^{15} cm^{-2} implant annealed for 30 minutes at (a) 800°C.

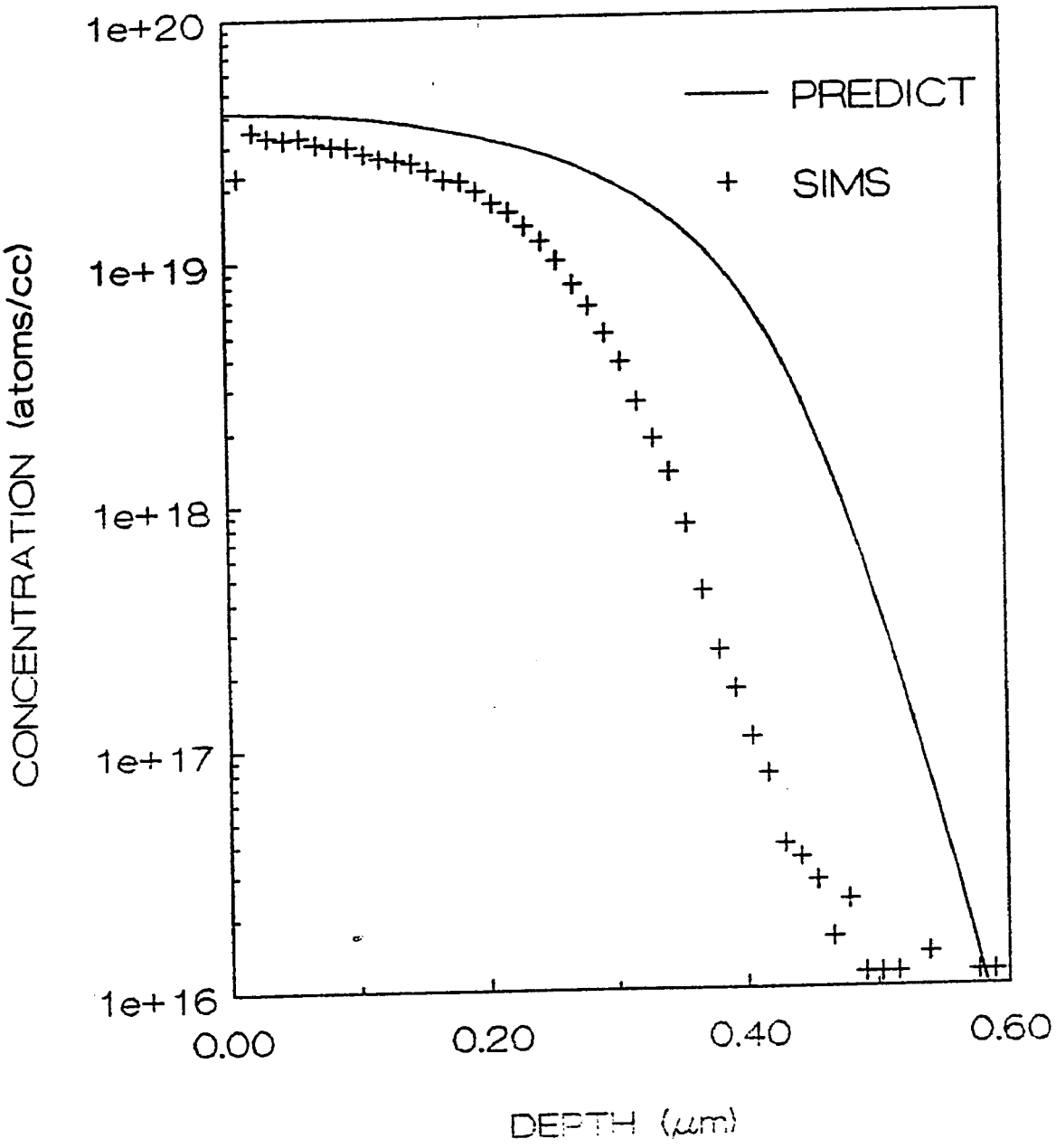

Figure 4-2. (b) 1100°C.

observed in the 1 X 10^{16} cm^{-2} data of Fig. 3-41. The simulation of this profile also shows a kink, but it is deeper (along with its junction) than the SIMS profile. Since there are some discrepancies between the SIMS data and the simulation, this suggests that the model used in PREDICT (see Section 2.4) does not fully characterize the mechanisms related to the arsenic diffusion.

What has not been considered in these models is the effect ion implantation damage has on the diffusion of high concentrations of arsenic in silicon. For a majority of the work presented here above amorphization doses of arsenic ($\gtrsim$ 3 X 10^{14} cm^{-2}) were used. This allowed the study of two distinct regions in the implanted profile: the amorphous region and the end-of-range (or tail) region. The tail region was of particular interest since is has an excess of silicon atoms (due to recoil implantation from the near surface amorphous region) and it can be isolated by removing the amorphous layer.

As was seen in Chapter 3 the tail-only samples appeared to diffuse deeper into the original sample than the total samples at room temperatures below 950°C (see for example Figs. 3-10, 3-12, 3-16, and 3-41). This was especially true for the electrically active profiles and the lower dose (1 X 10^{15} cm^{-2}) total chemical concentration profiles (Figs. 3-41b and 3-42b). For the total chemical concentration profiles of the high dose (1 X 10^{16} cm^{-2}) implant, the tail diffused as much as the total profiles up to 950°C (Figs. 3-41a and 3-42a). This suggests that there is a relationship between the concentration, temperature, and damage that is related to the tail diffusion and electrical activation (carrier concentration) in this region. It is also suggested that the high concentration of the 1 X 10^{16} cm^{-2} total sample has a greater effect on the diffusion of this profile than the 1 X 10^{15} cm^{-2} case. In this lower dose case, it is suggested that the excess silicon atoms in the tail-only sample have a greater effect

than the concentration magnitude on the arsenic diffusion. Therefore, a higher percentage of the arsenic atoms in the tail region (than the total sample) diffuse by an interstitial(cy) mechanism.

As has been previously stated, these data suggest an effect on the electrical activation. Figure 4-3a is a comparison of the total and carrier concentration profiles for the 1 X 10^{16} cm^{-2}, 800°C total sample. This data is consistent with the RBS data (Table 3-4). The decrease in electrical activation between 0.04 μm and 0.08 μm is consistent with the precipitation observed in this region (Fig. 3-51). These results are in qualitative agreement with the PREDICT simulation (Fig. 4-3b). It should be noted that the simulation results show equal total and carrier concentrations in the tail region. This is not observed in the data (Fig. 4-3a).

Similar results were found for the 1 X 10^{16} cm^{-2}, 950°C total sample except the total and carrier concentrations in the tail region are equivalent experimentally. At 1100°C, the total and carrier concentration profiles were the same for the experimental data (within errors) and the simulation (Fig. 4-4).

When the dose was decreased to 1 X 10^{15} cm^{-2} different results were obtained. As shown in Fig. 4-5 the carrier concentration profile matches the total concentration profile at 800°C. This is true for both the data and the simulation. Similar results were obtained for the higher temperature anneals (carrier and total concentration profiles were equivalent from both experimental data and simulation).

From this discussion it can be asked whether the tail-only samples behave similar to their respective total samples. In Fig. 4-6 are shown the total and electrically active concentration profiles for the 1 X 10^{16} cm^{-2} tail-only samples. At 800°C the carrier concentration is lower than the total concentration. By 950°C the profiles are essentially the same. Annealing at 1100°C results in the electrically active

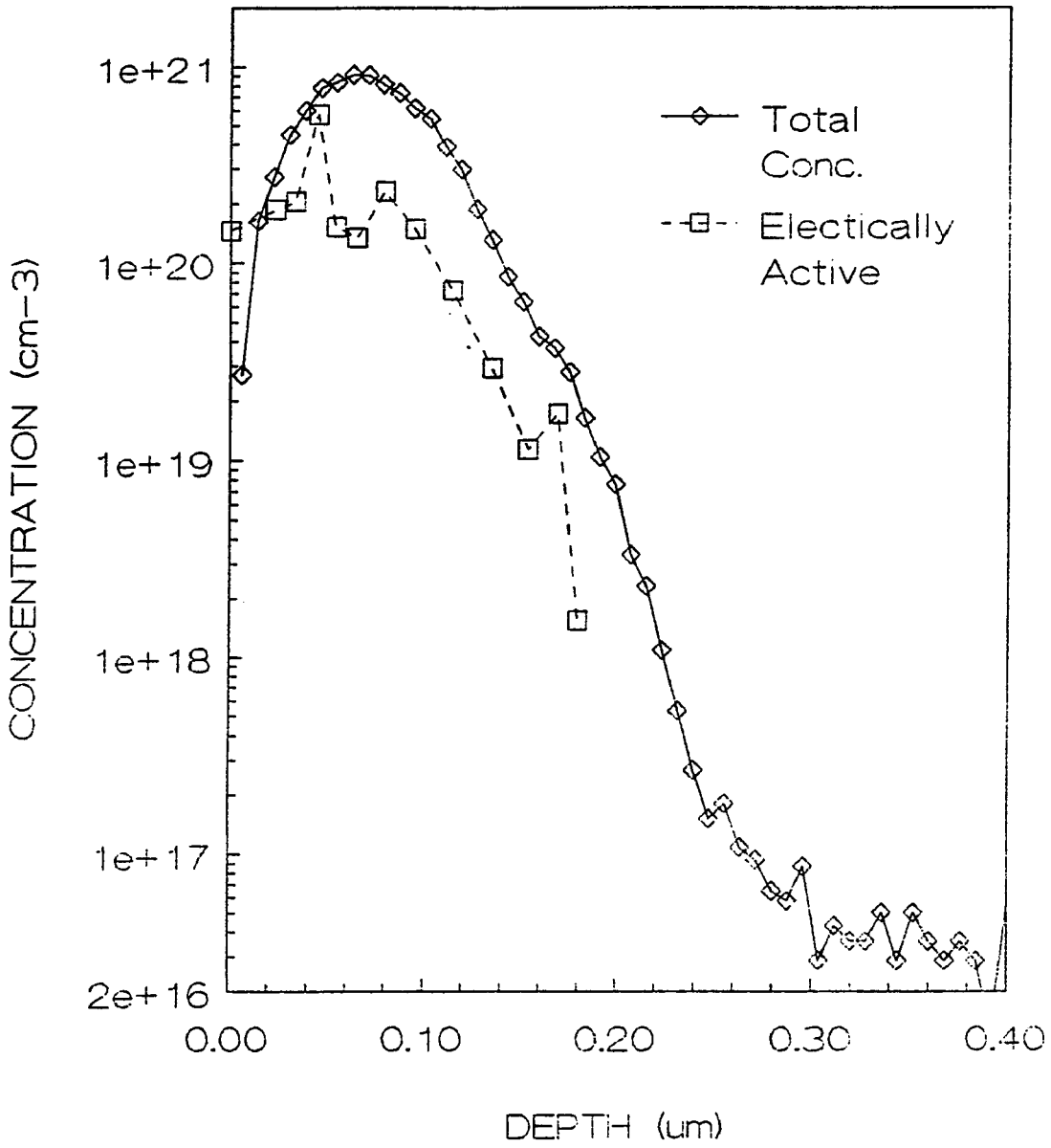

Figure 4-3. Comparison of the total chemical concentration to the electrically active concentration for the 1 X 10^{16} cm^{-2}, 800°C total sample (a) SIMS and Hall effect data.

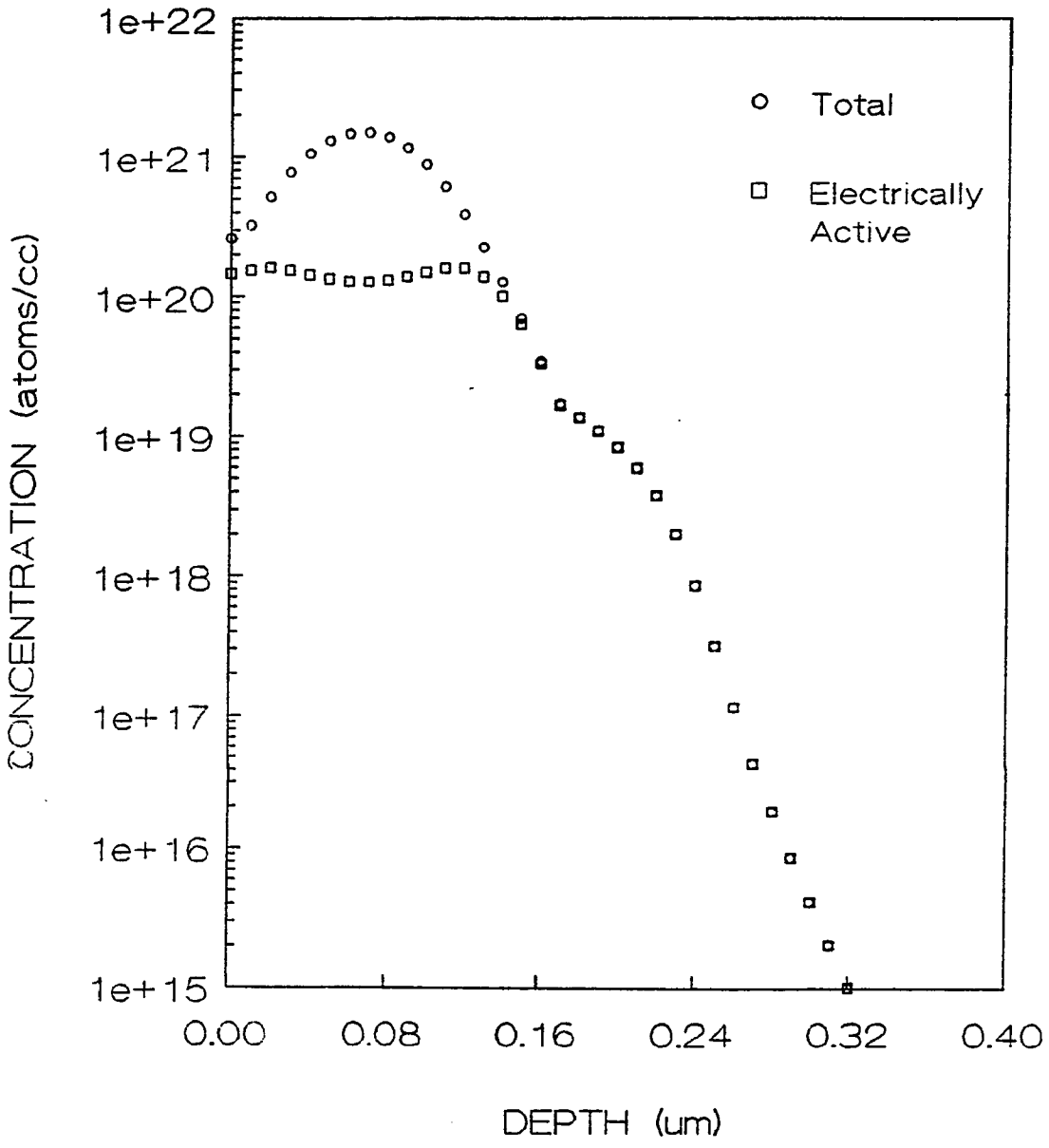

Figure 4-3. (b) PREDICT Simulation.

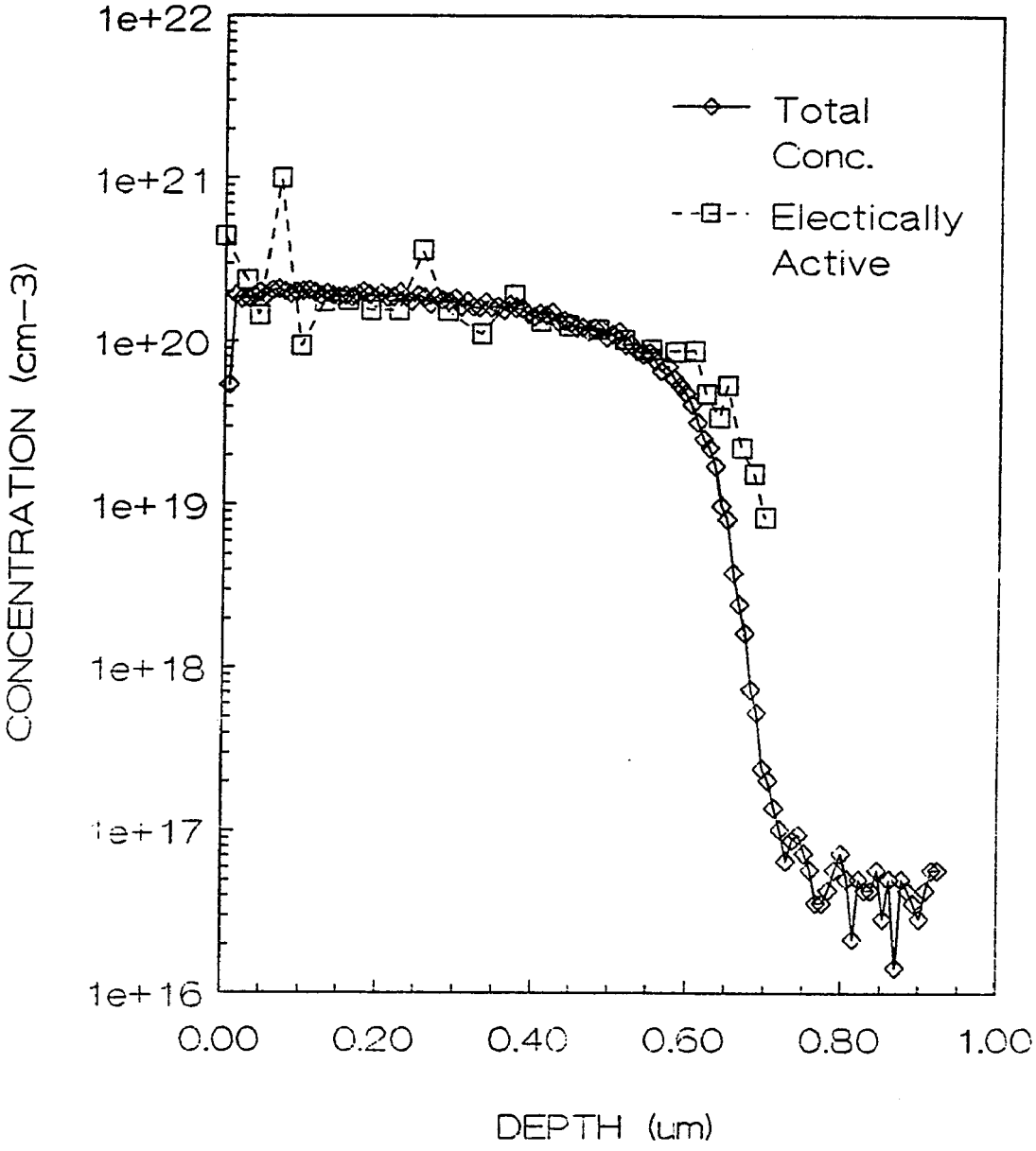

Figure 4-4. **Comparison of the total chemical concentration to the electrically active concentration for the 1 X 10^{16} cm^{-2}, 1100°C total sample (a) SIMS and Hall effect data.**

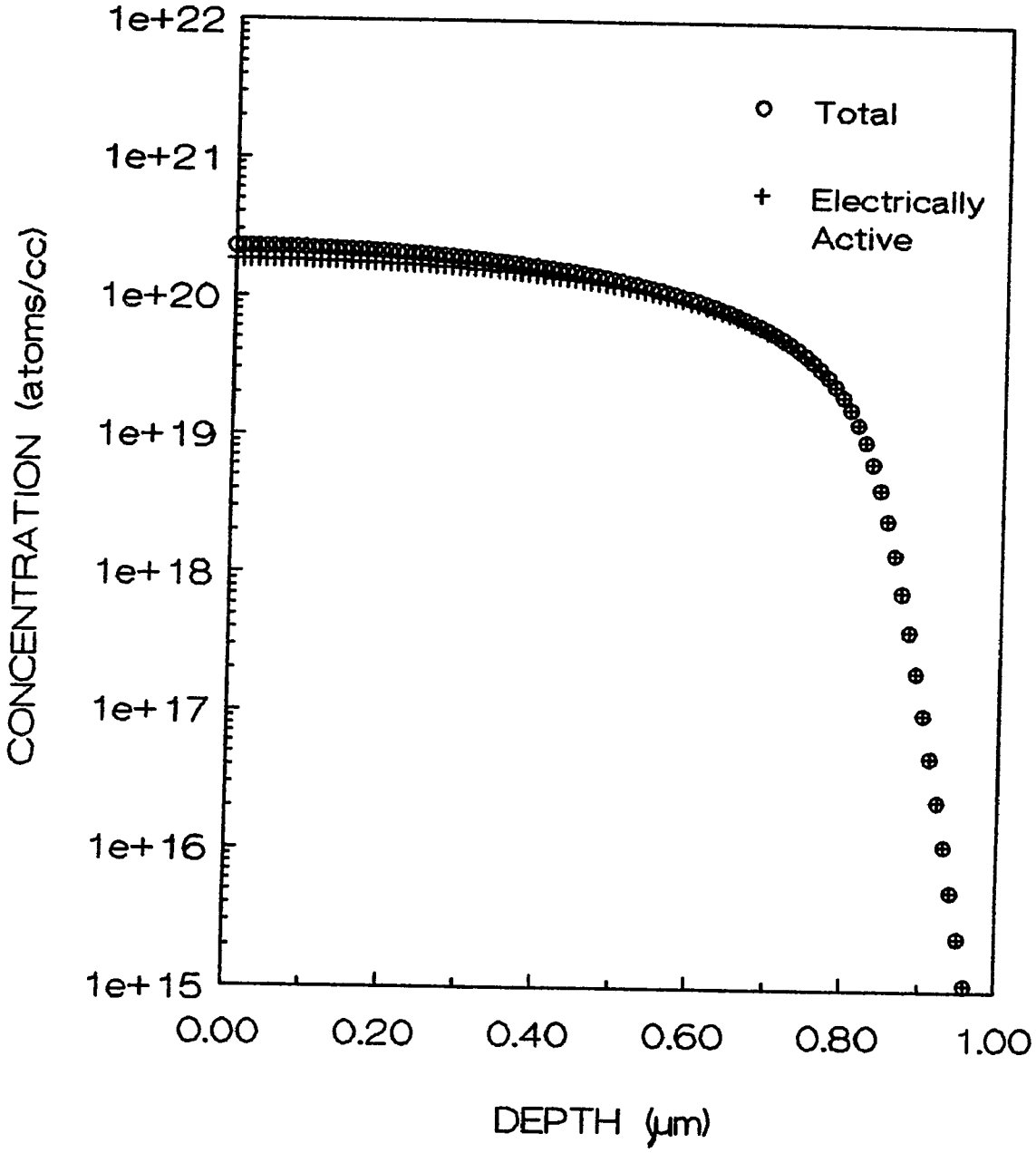

Figure 4-4. (b) PREDICT Simulation.

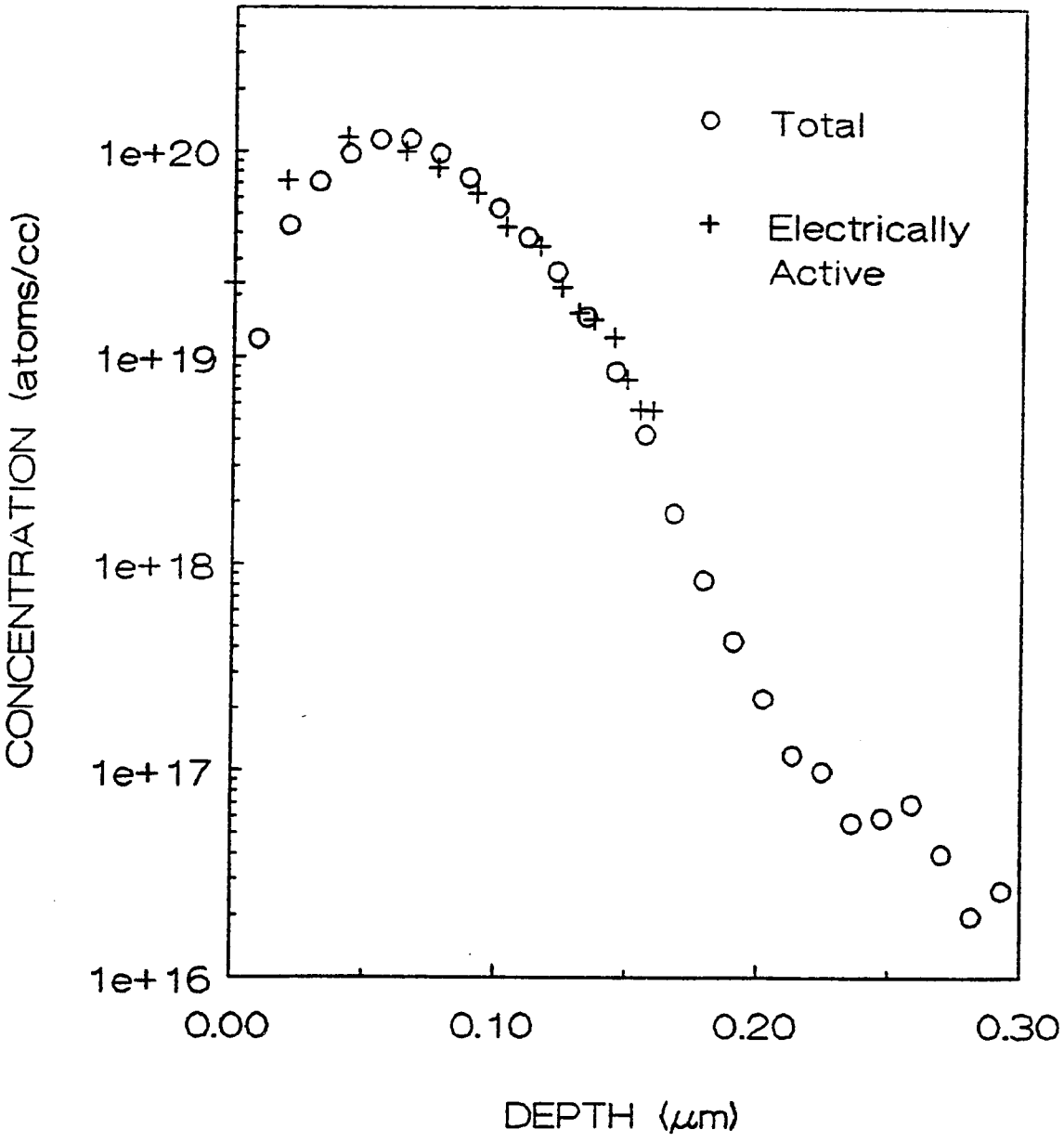

Figure 4-5. Comparison of the total chemical concentration to the electrically active concentration for the 1 X 10^{15} cm^{-2}, 800°C total sample (a) SIMS and Hall effect data.

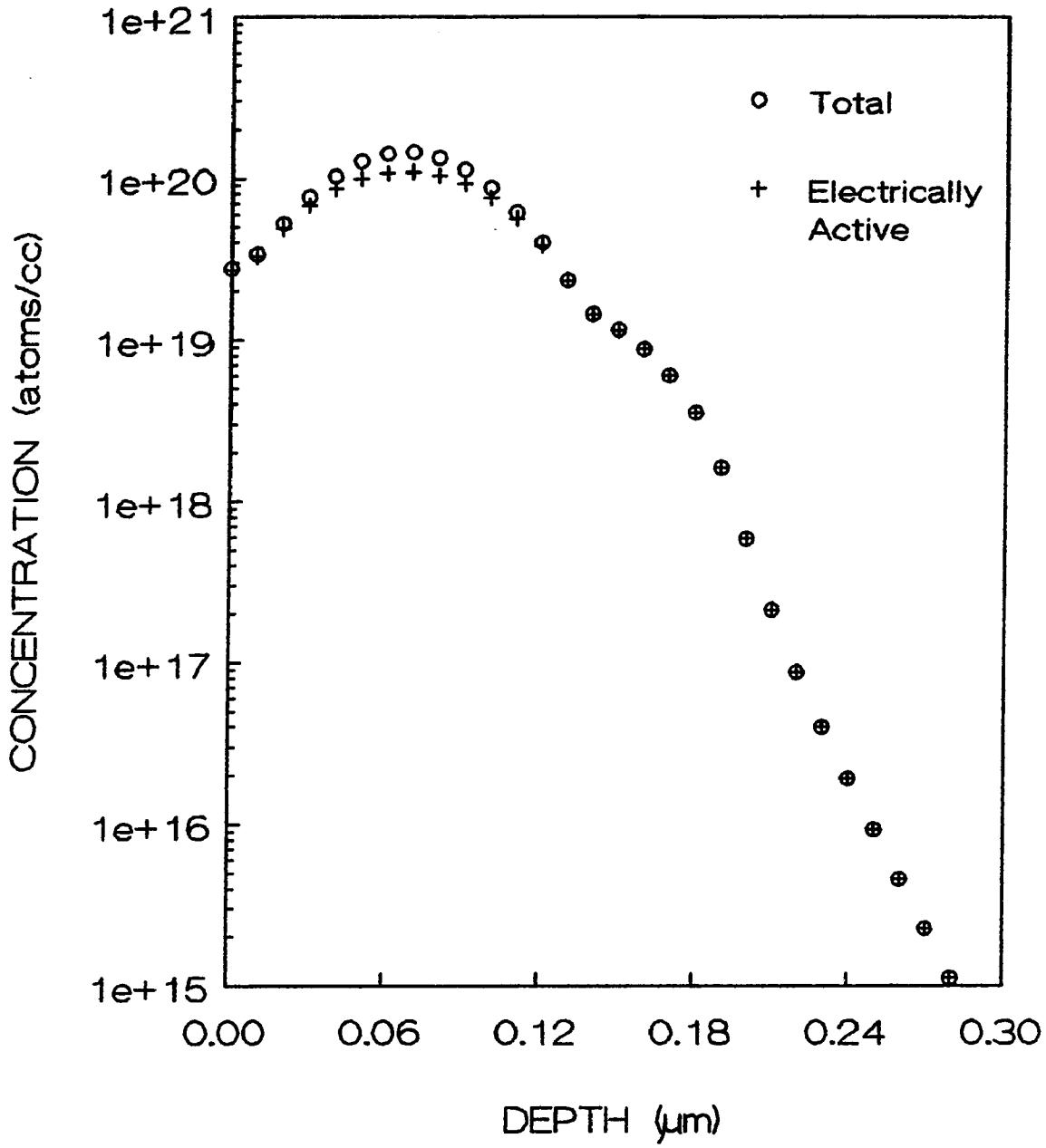

Figure 4-5. (b) PREDICT Simulation.

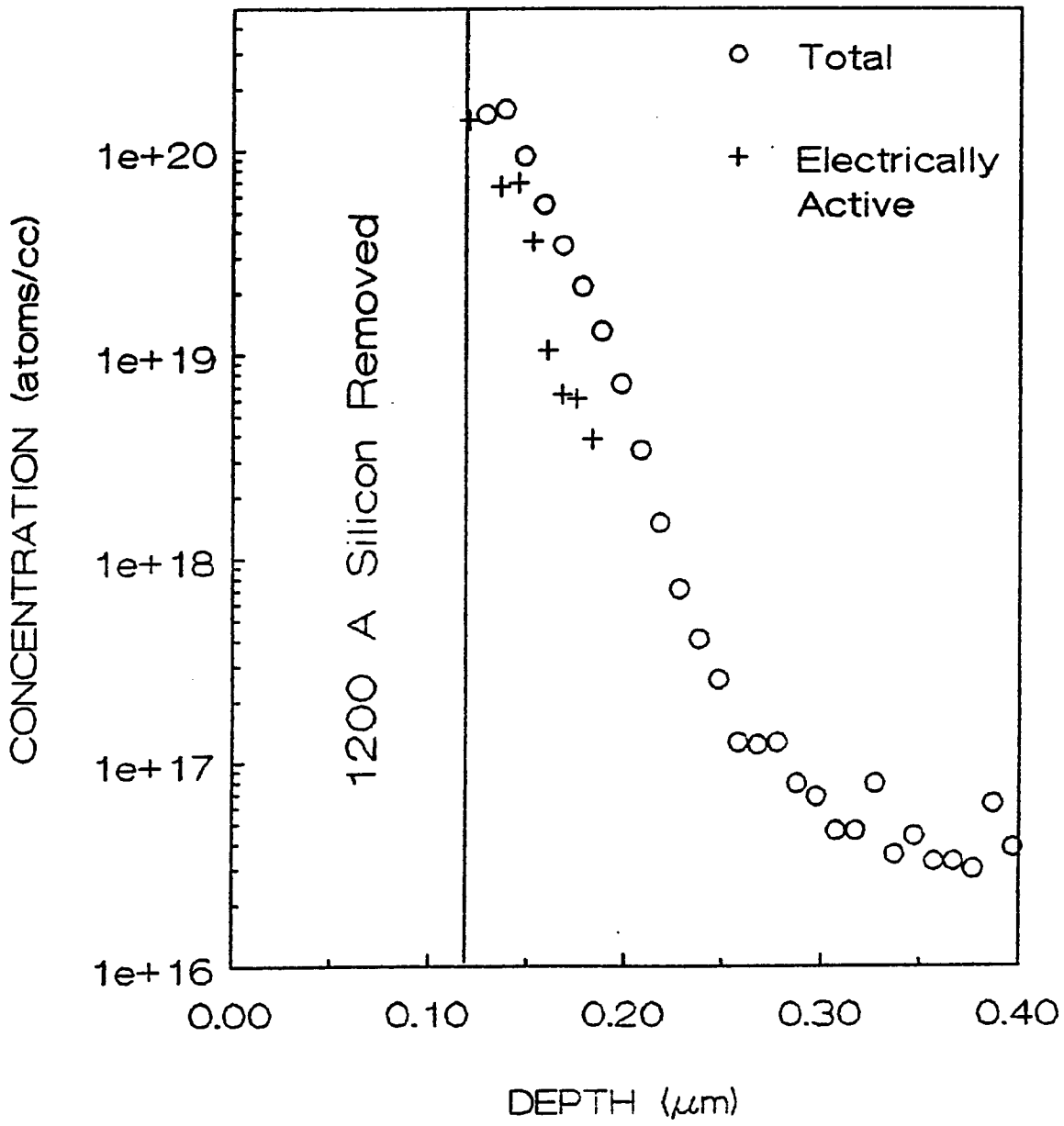

Figure 4-6. Comparison of the total chemical concentration to the electrically active concentration for the 1 X 10^{16} cm^{-2} tail-only samples (a) 800°C.

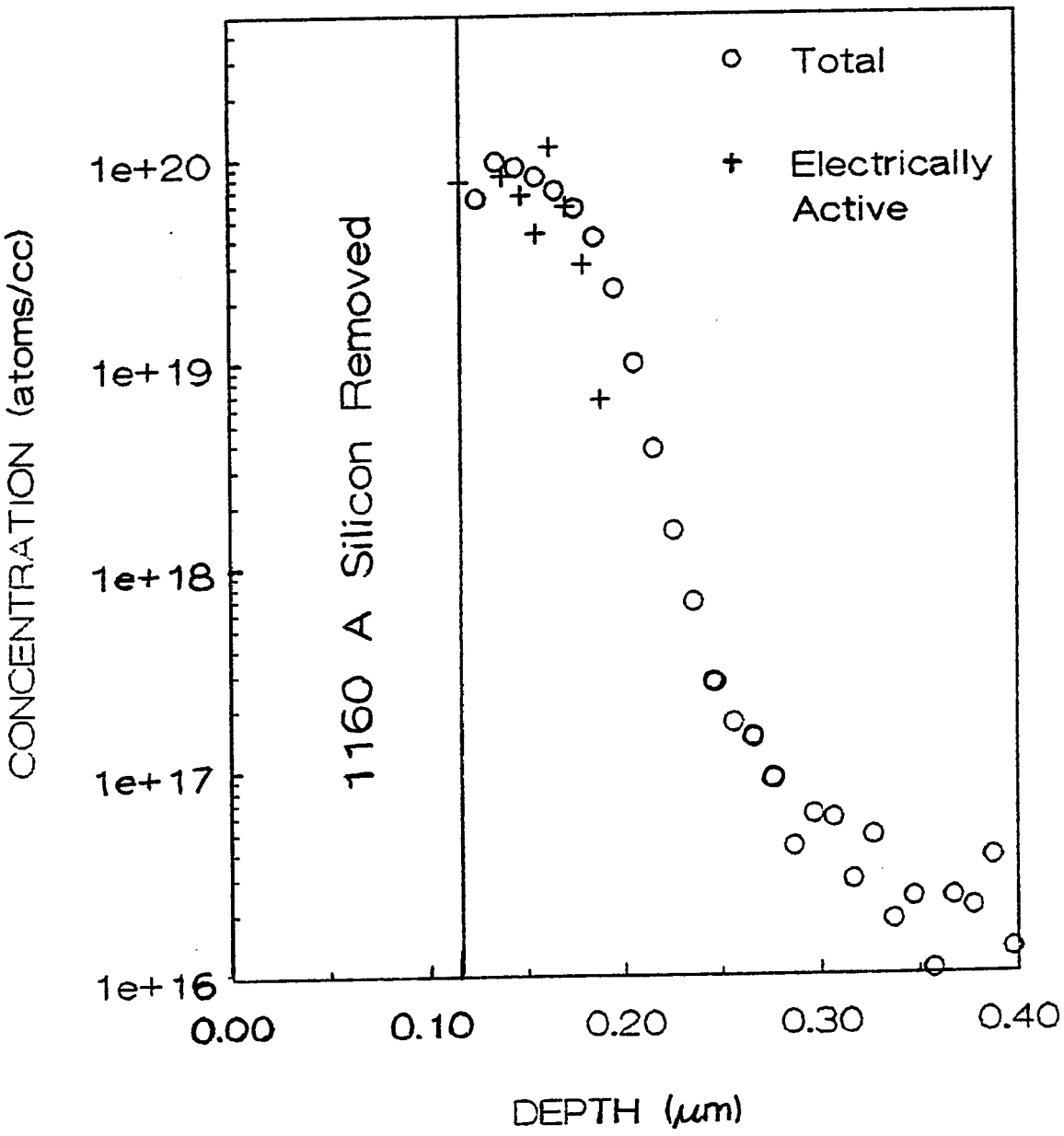

Figure 4-6. (b) 950°C.

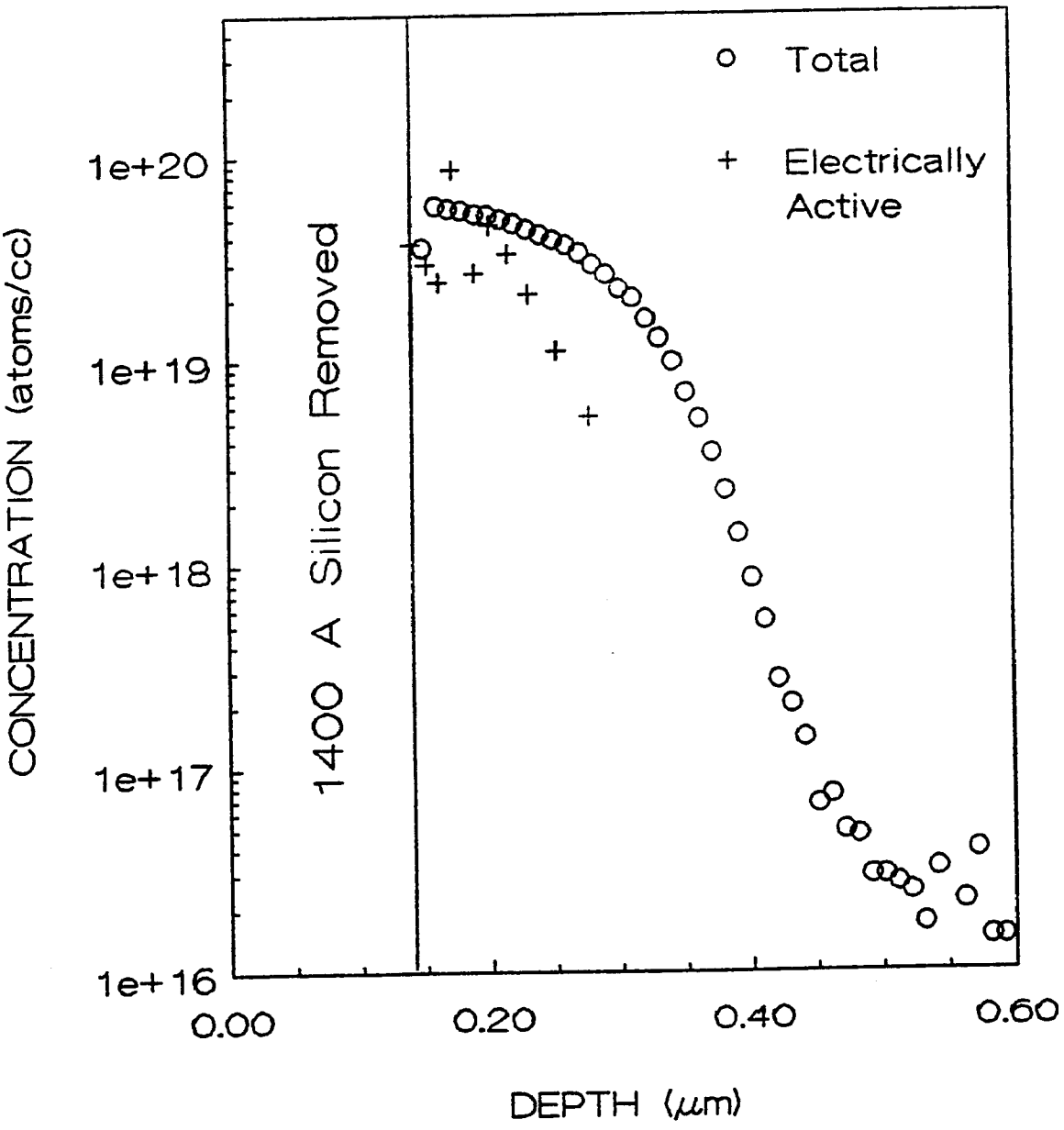

Figure 4-6. (c) 1100°C.

concentration being lower than the total chemical concentration. This is consistent with the RBS results (Tables 3-4 and 3-5) where the arsenic substitutional fraction decreased dramatically at 1100°C. Similar results were obtained for the 1 X 10^{15} cm^{-2} tail-only samples (Fig. 4-7).

These results are not consistent with the finding for the total samples (Figs. 4-3 through 4-5). Especially note that the tail regions of the 1 X 10^{16} cm^{-2} total samples annealed above 950°C and all of the 1 X 10^{15} cm^{-2} total sample tail regions had comparable total and electrically active concentrations. Since this behavior is not seen in the tail-only samples, diffusion and electrical activation occur by a different mechanism(s) than the total samples. It is suggested that this difference is a result of the excess silicon that has been recoil implanted from the surface region into the end-of-range region. Since the surface amorphous layer has been removed the excess silicon in the tail region cannot diffuse back into the surface region and therefore affects the arsenic diffusion and electrical activation.

4.2 The Annealing of Above Amorphization Dose Arsenic Implanted into Silicon

Several models have been proposed for the formation of the dislocation loops found below the amorphous/crystalline (a/c) interface (see Fig. 3-51) [2,3]. Kim et al. [2] have proposed that these dislocations initially form from point defects that diffuse from the amorphous layer to the bulk of the crystal during annealing. Jones et al. [3] propose that both the implanted ions in the tail region and atoms knocked out of the amorphous layer during implantation play a role in the formation of these loops.

The XTEM results of Figs. 3-51 to 3-53 (and the results of Section 4.1) suggest that both of these models may play a role in the loop formation and damage annealing. Since loops form in the 800°C tail-only sample (Fig. 3-52) the point defects

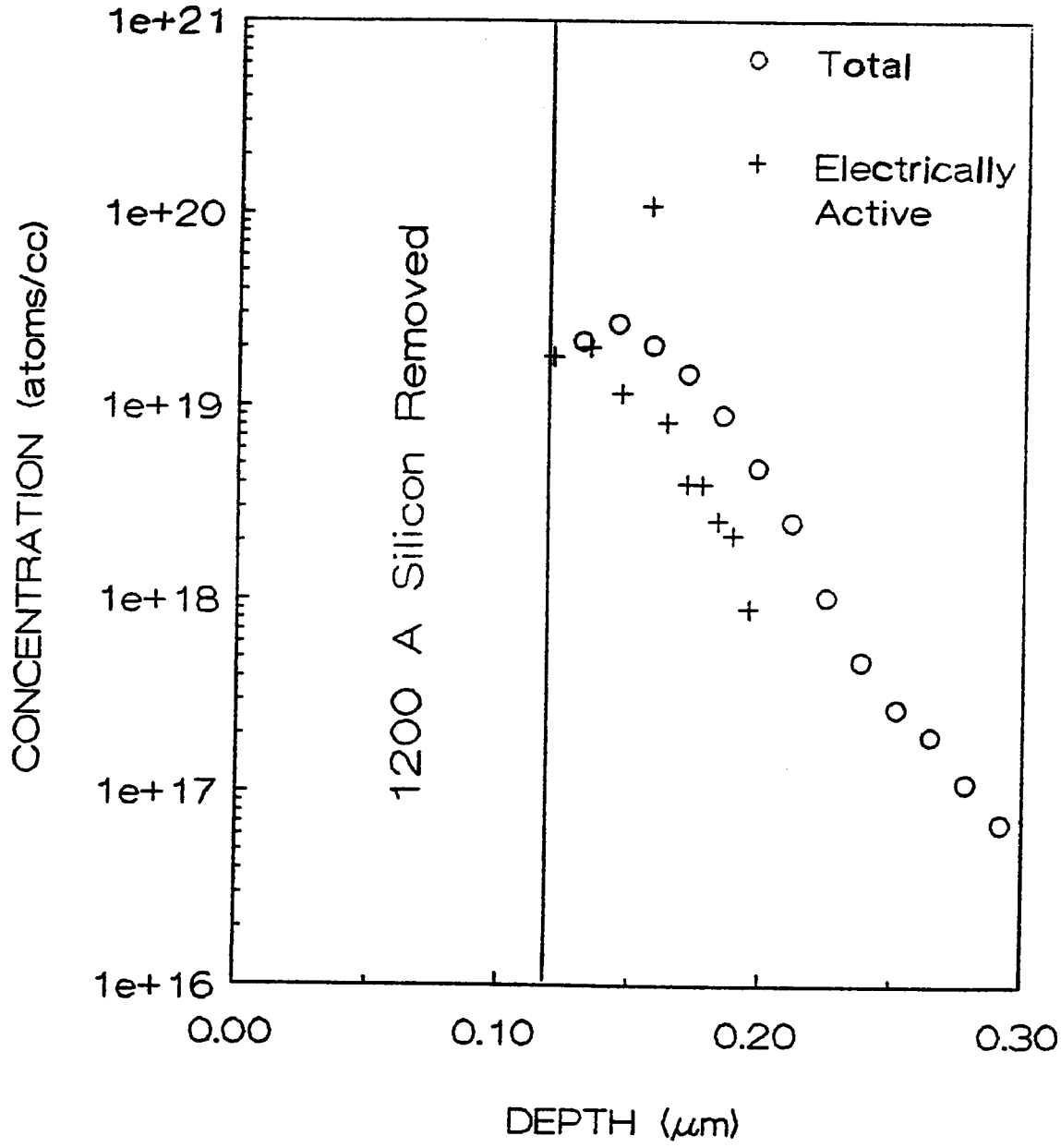

Figure 4-7. Comparison of the total chemical concentration to the electrically active concentration for the 1 X 10^{15} cm^{-2} tail-only samples (a) 800°C.

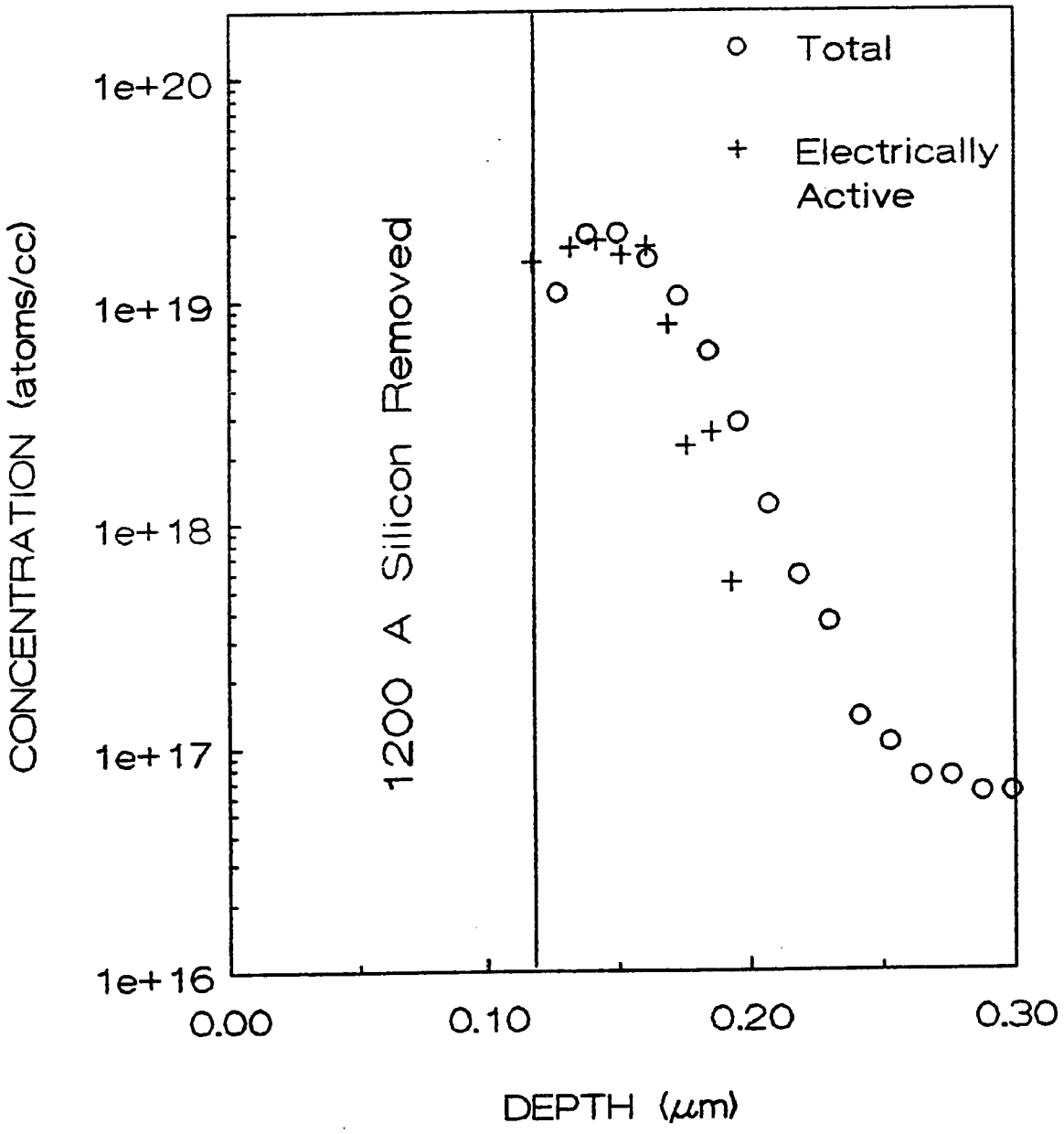

Figure 4-7. (b) 950°C.

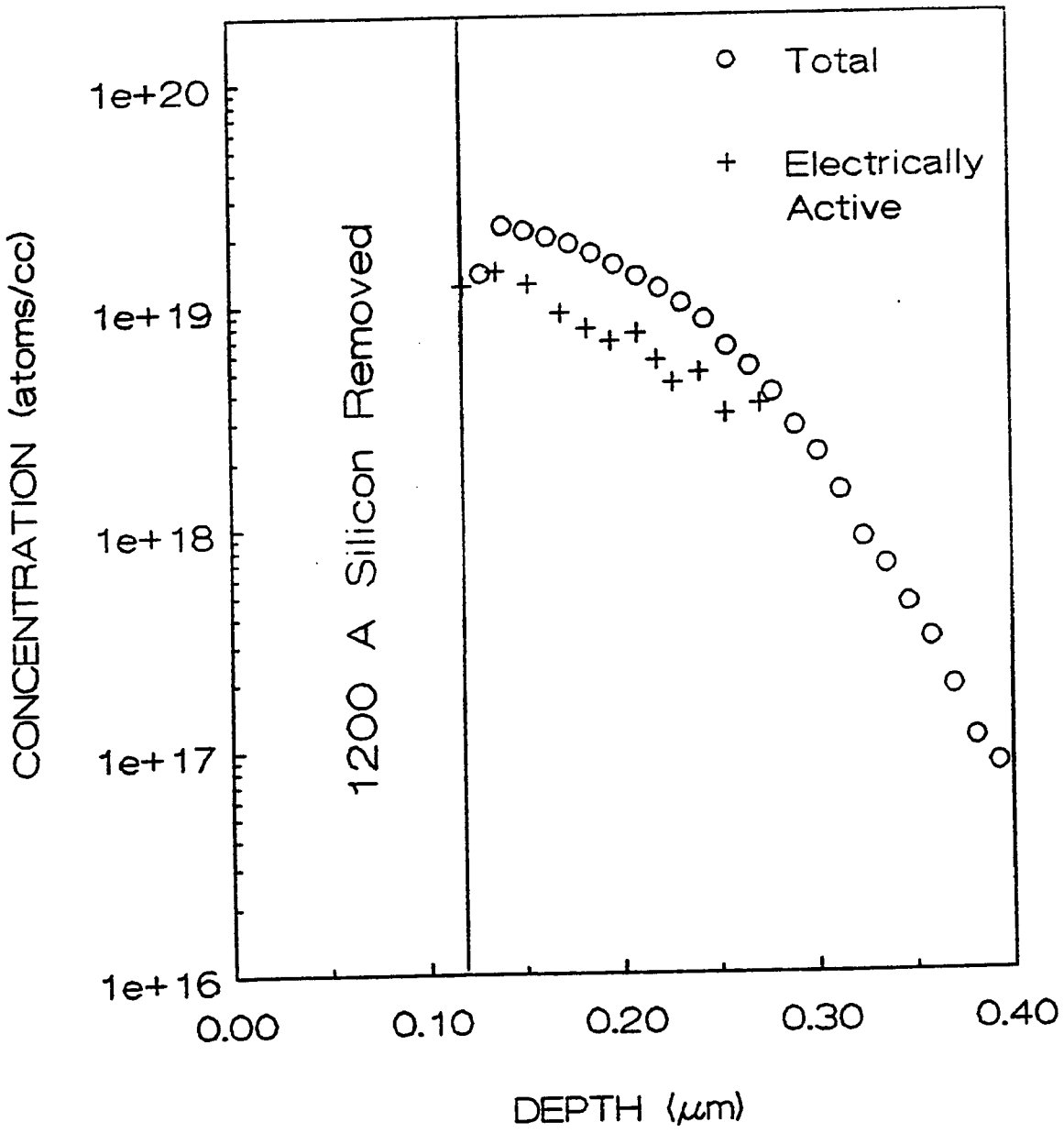

Figure 4-7. (c) 1100°C.

that are created by the annealing amorphous layer are not required to form these end-of-range (or category II; see Section 1.2.3) defects. Thus, the proposal of Jones et al. [3] would seem correct. Kim et al. [2] have also suggested that these end-of-range loops coalesce to form layer loops through dislocation—dislocation reactions and nonconservative climb. The results for the 950°C tail-only sample (Fig. 3-53) show an increase in loop size and decrease in density. The results in Figs. 4-6b and 4-7b and in Table 3-4 are also consistent with this change in defect morphology.

By 1100°C no dislocation loops were observed in the XTEM samples. This would suggest that the damage was annealed, but other techniques reveal that this may not be true. The Hall mobility profiles (Fig. 3-35), the comparison of total chemical concentration with carrier concentration (Figs. 4-6c and 4-7c), and the RBS results (Tables 3-4 and 3-5) suggest that something other than dislocation loop removal must be considered in the tail region diffusion and electrical activation.

From these data a model is proposed to explain the annealing of damage created by above amorphization doses of arsenic in silicon. Initially the damage in each region (amorphous and end-of-range) plays a vital role in the annealing of its own region. As the projected range and end-of-range loops grow in size, excess vacancies and interstitials are able to diffuse into the bulk or toward the surface. These excess points defects aid in the annealing process until regrowth of the damaged region is complete. Since the amorphous layer cannot contribute point defects to assist in the dissolution of loops in the tail-only samples, these loops take longer to anneal (see Fig. 3-53). In other words, the tail-only sample must be heated above 950°C to remove these defects.

At 1100°C the excess silicon interstitials (created during implantation) below the original a/c interface produce a strained layer in the end-of-range region. This

strained layer may also be present in the total sample case since a "kink" in the mobility profiles is seen for both of the total samples in Fig. 3-35. The RBS data for the 1100°C, total sample may not show this effect, since the χ_{min}^{Si} χ_{min}^{As} values used for the determination of the substitutional fraction (equation 3.40) are averaged over a majority of the implanted and diffused region.

4.3 The Effects of Implant Damage on Arsenic Diffusion

This work has primarily concentrated on the diffusion of above amorphization doses of arsenic in silicon. By removing the amorphous layer and studying the annealing and diffusion in the tail region of the implant we have gained insight into how the damage layer affects the total implant diffusion.

For the 800°C anneals the results reported in Chapter 3 and Section 4.1 show that the total sample diffuses quite differently than the tail-only sample. In Section 4.2 a model was presented for how the implantation damage anneals. It was suggested that initially the damage in each region (amorphous and end-of-range) played an important role in the annealing of its own particular region. Therefore the 800°C results should not be illogical with respect to this model. The annealing of the amorphous layer (which is rich in vacancies and deficient in silicon interstitials) would require some of the implanted arsenic in this region to complete solid phase epitaxial (SPE) regrowth. Thus a majority of this arsenic would not diffuse until SPE regrowth was complete (as in Fig. 3-41). The reason the tail-only and total sample profiles in Fig. 3-41a are coincident is due to the peak concentration of the 1 X 10^{16} cm^{-2} implant exceeding the solid solubility limit. Therefore the diffusivity for this dose is more concentration dependent than the 1 X 10^{15} cm^{-2} sample.

Since a nonequilibrium concentration of interstitials exists in the tail region this affects the diffusivity of the tail-only samples. Some theoretical work on an

interstitial component of the arsenic diffusivity can be found in the literature [4-6]. All of these models include a contribution from vacancies. The DLTS results presented in Table 3-3 show the existence of vacancy related defects. Therefore it is suggested that the tail-only samples have a greater interstitial related component to the diffusivity than the total samples. But vacancies still play a role in the diffusion. Once the damage observable by XTEM has been annealed there is still an excess of interstitials in both types of samples (tail-only and total). In the tail-only samples the excess interstitials encounter the oxide-silicon interface and a majority are probably reflected back into the silicon bulk, thus affected the arsenic diffusion in these samples. For the total samples, the excess interstitials in the end-of-range region can also diffuse toward the surface. Before they reach the oxide-silicon interface these interstitials encounter the annealing amorphous region and assist in the annealing and arsenic diffusion there. Therefore, once the implant damage has annealed there is an excess of interstitials available to assist in arsenic diffusion throughout the arsenic distribution. This is consistent with theoretical work that suggests a dominant interstitial component to the arsenic diffusivity [4-6].

4.4 A Discussion of Arsenic Clustering/Declustering

As was discussed in Section 2.1 the incomplete activation of arsenic in silicon was attributed to arsenic clustering. The results in this dissertation for high doses (1 X 10^{16} cm^{-2}, Fig. 4-3) also show incomplete activation. But the XTEM results for this sample also show a layer of loops attributed to arsenic precipitation (Fig. 3-51). It should also be noted that the tail-only samples (which have maximum concentration values in the range of 10^{19} cm^{-3} to 10^{20} cm^{-3}) are much lower in concentration than the total samples and also experience incomplete electrical activation (see Figs. 4-6 and 4-7). The question can be raised as to whether clustering is a viable mechanism

in arsenic diffusion.

Recall that Pandey et al. [7] have suggested a cluster which is the first step in the growth of larger complexes and eventually precipitation (Section 2.1). This would suggest that both clustering and precipitation could be coexistent. The results presented in this dissertation are in agreement with this view.

In this work evidence for extended point defects (Section 3.3.3.2), precipitation (Section 3.5.1.1), and incomplete electrical activation at the lower anneal temperatures (Figs. 3-27, 4-3, 4-6, and 4-7) has been presented. It is suggested that the implantation damage and arsenic concentration play a role in these mechanisms. These results also imply that extend point defects (clusters) coexist with precipitates until the damage annealing is complete. Then the excess interstitials begin to affect the defect complexes and the arsenic diffusion. Therefore new energy levels are observed in the DLTS spectra (see Table 3-3, for example) and diffusion is enhanced. Since the tail-only samples have a much higher interstitial concentration, in a smaller volume than the total samples, different defects are possibly formed than in the corresponding total sample. This would explain the differences in the spectra of high temperature annealed total and tail-only samples.

The DLTS results in Section 3.3.3.2 also show support for a declustering mechanism [8] with diffusion including a doubly charged vacancy mechanism [8,9] at the highest temperature of this study ($\sim$ 1100°C). The 1 X 10^{14} cm^{-2} total samples also exhibited this change in defect level at 1080°C. Recall that this dose creates a buried amorphous layer (Section 1.1.2). Although this dose is well below that required to form arsenic precipitates, implant damage is still present. Therefore, as seen above, the amorphous layer regrowth and the excess interstitials remaining after annealing are the most probable contributors to the defects observed by DLTS.

Since defects are observed over the entire range of doses, up to the highest dose where precipitates were found, this suggests that extended point defects and precipitates may coexist. It should be pointed out that the role of precipitates on deep levels has not, to this author's knowledge, been examined. Thus, if the precipitates do produce deep levels, the analysis of the high temperature data would not be affected since precipitation is not observed in these samples. Therefore the change in spectra as the anneal temperature is increased above 1050°C must be related to the excess interstitials that remain after annealing.

4.5 The Effect of Recoil Implanted Oxygen on Arsenic Diffusion and Electrical Activation

A preliminary study of through-oxide-implanted arsenic was performed. There were several reasons for doing this type of study. First the implants were done so as to keep most of the damage in the oxide. This also produced a layer of recoil implanted oxygen in the silicon substrate. Thus the effects of oxygen diffusion and activation can be studied. Also an arsenic tail was therefore studied.

It should be noted that most of the studies presented in Chapter 2 were actually performed on arsenic that was implanted through a surface oxide layer. This has not been taken into account in those models. The electrical activation of arsenic has been known to be affected by the presence of recoil implanted oxygen [10,11]. From a technological standpoint, a surface oxide is usually present before implantation to reduce surface contamination. Oxides are also commonly used as implantation masks and are tapered to modify the lateral profile of a well.

Arsenic was implanted through an 800 Å layer of silicon dioxide into n-type <100> silicon at 140 keV to fluences of 1 X 10^{15} cm^{-2} and 5 X 10^{15} cm^{-2}. This implant condition placed the peak of the arsenic implant at the oxide-silicon interface.

SIMS profiles of the as-implanted wafers are shown in Fig. 4-8. Also shown in this figure are oxygen profiles calculated by the method of Gibbons and Christel [12,13]. They note that the oxygen concentration near the interface will be higher than that calculated. The implant condition was selected so as to recoil the greatest amount of oxygen into the silicon substrate.

4.5.1 Furnace Anneal Study

Anneals of the implanted samples were performed over the same temperature range as the bare implant studies (800°C to 1100°C, 30 minutes). The results of this preliminary study are shown in Fig. 4-9. In both implant cases there is an apparent outdiffusion of arsenic for the 800°C case. For the 1 X 10^{15} cm^{-2} implant a 1025°C anneal is required for the arsenic to diffuse deeper than its original junction depth. This occurs at 950°C for the 5 X 10^{15} cm^{-2} case, thus showing the effects of a higher concentration of arsenic.

Both 800°C and 950°C profiles are non-Gaussian in shape. This would suggest that the recoil implanted oxygen plays a role in the arsenic diffusion at the lower temperatures of this study. At 1025°C and above the oxygen probably diffuses rapidly into the silicon and therefore has little chance to interact with the slower moving arsenic.

4.5.2 Rapid Thermal Anneal Study

Rapid thermal anneals were also performed on the implanted samples described above. In this case short time annealing effects on the electrical activation can be studied. The results of this study are shown in Fig. 4-10.

For the 1 X 10^{15} cm^{-2} samples a decrease in the carrier concentration is observed for anneals above 800°C (Fig. 4-10a). In the case of the 5 X 10^{15} cm^{-2} implant (Fig.

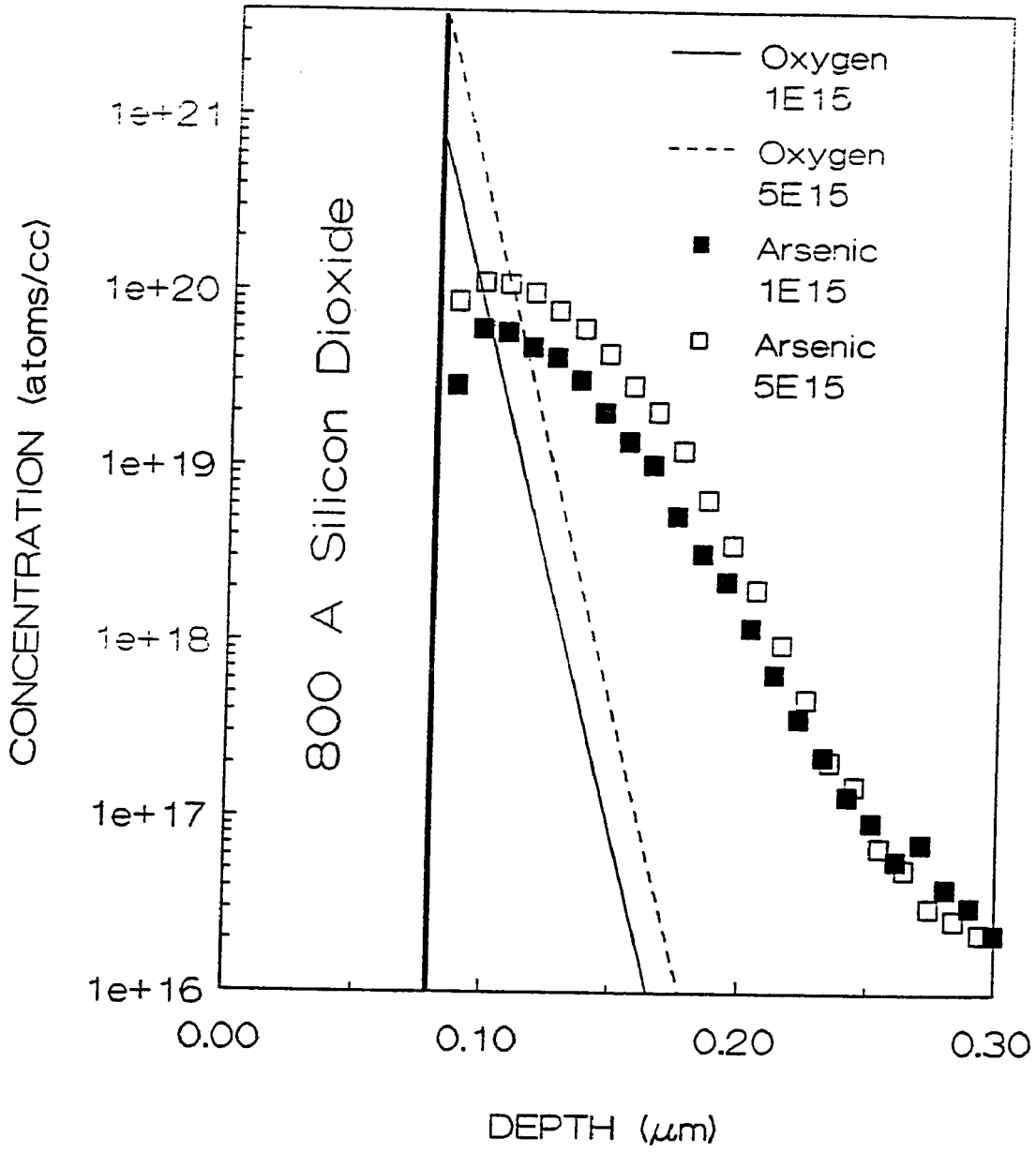

Figure 4-8. SIMS profiles for 140 keV arsenic implanted through 800 Å of silicon dioxide. Also shown are the recoil implanted oxygen profiles calculated by the method of Gibbons and Christel [12,13].

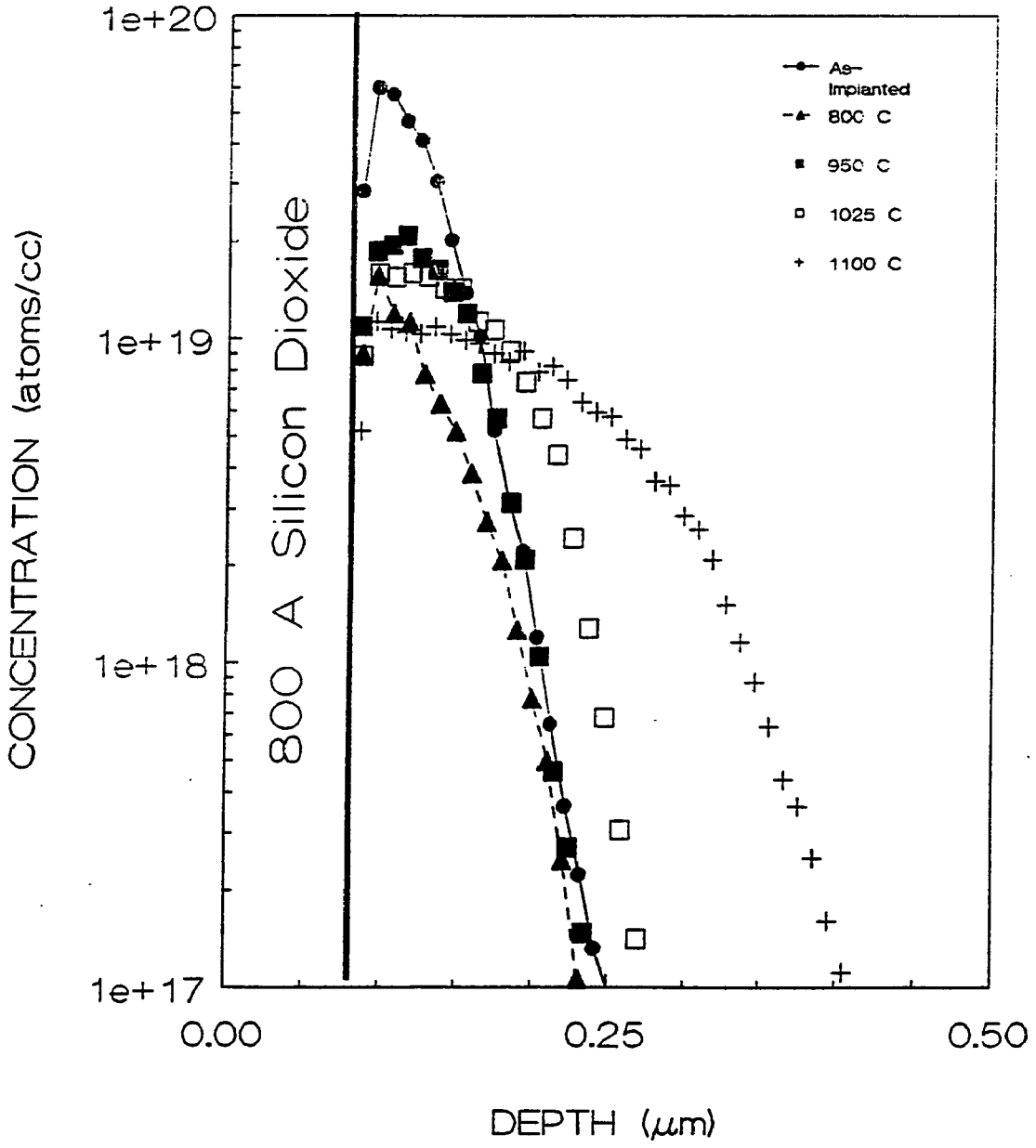

Figure 4-9. SIMS profiles of furnace annealed through oxide arsenic implanted silicon (a) 1 X 10^{15} cm^{-2}.

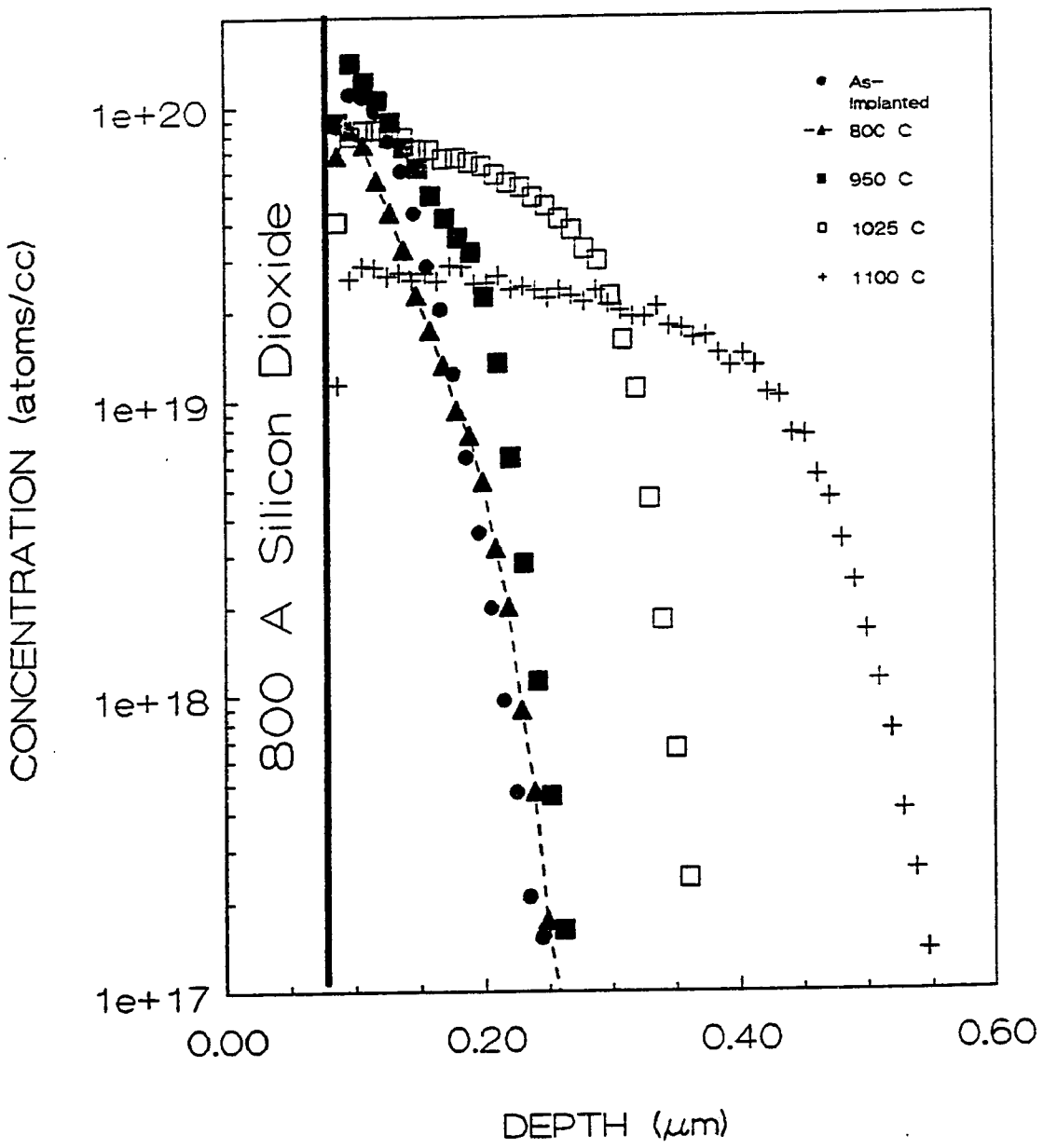

Figure 4-9. (b) 5 X 10^{15} cm^{-2}.

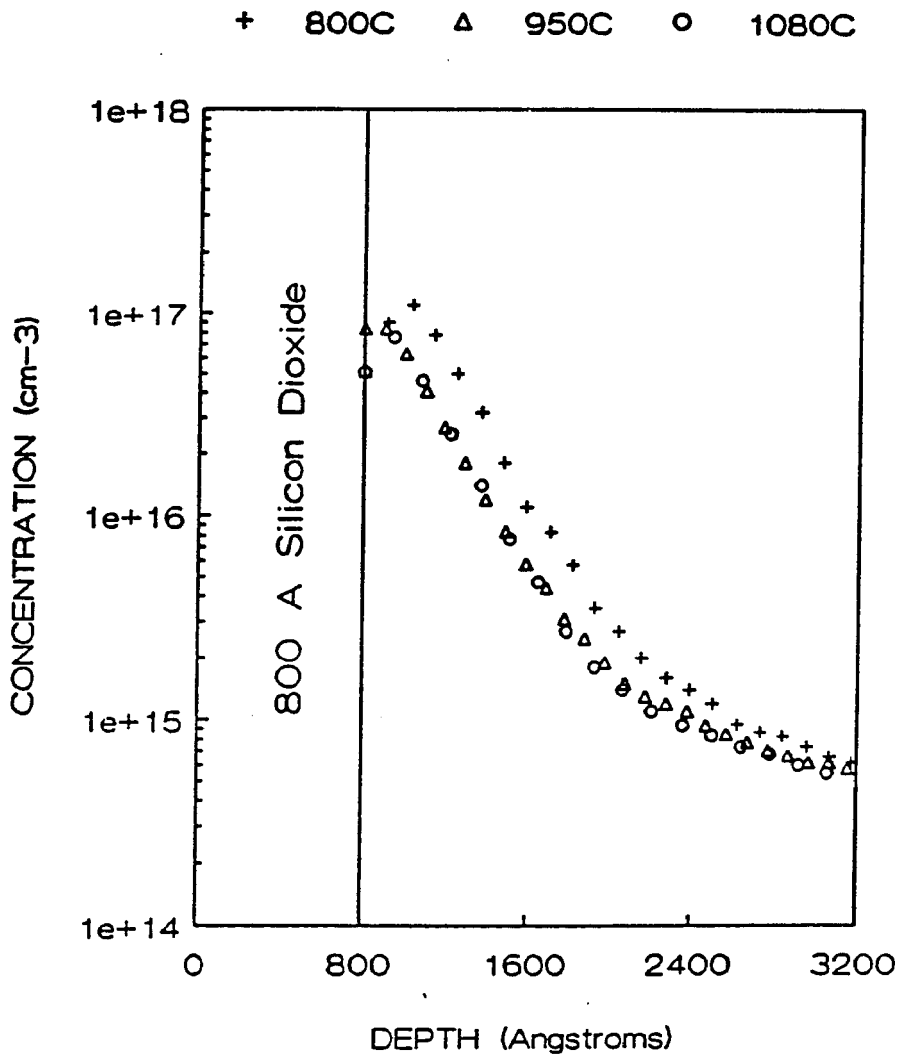

Figure 4-10. Carrier concentration profiles of rapid thermal annealed arsenic annealed implanted silicon (a) 1 X 10^{15} cm^{-2}.

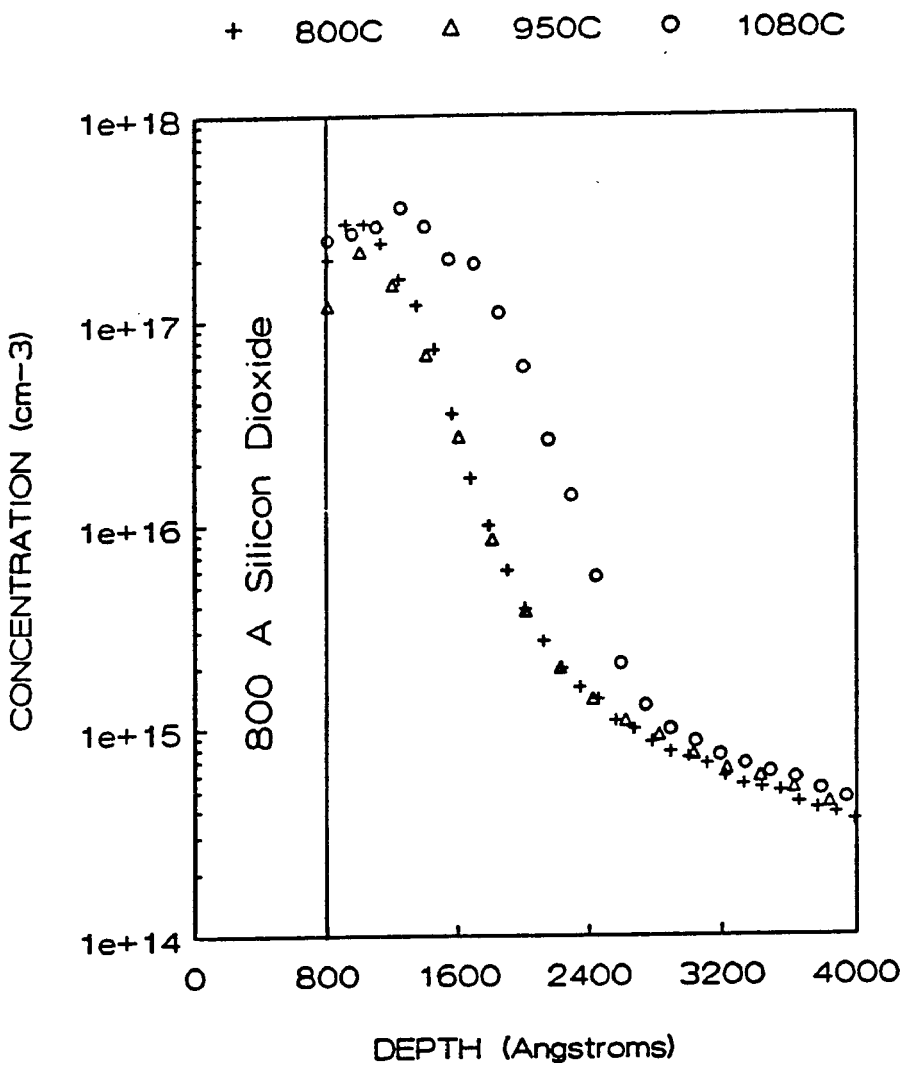

Figure 4-10. (b) 5×10^{15} cm^{-2}.

4-10b), the electrical activation is about the same for the 800°C and 950°C anneals, and increases after a 1080°C anneal. Here again oxygen plays a role in the arsenic diffusion and electrical activation.

It has been suggested that arsenic-oxygen complexes form through a reaction of oxygen with interstitial arsenic [14], and thus the arsenic becomes electrically inactive. By comparing the results from the two doses this complexing is not initially evident. The maximum arsenic concentration in the silicon substrate of the 5 X 10^{15} cm^{-2} is above the reported solid solubility limit [15], whereas the 1 X 10^{15} cm^{-2} is below. Therefore, for the higher dose implant the high arsenic concentration drives the diffusion. For this low dose case the recoil implanted oxygen plays a greater role.

4.6 The Role of the Capping Spin-on-Glass

Using the methods described in Section 1.2.4.4 attempts were made to determine the diffusivity of the arsenic profiles analyzed by SIMS. Good fits were obtained for the as-implanted profiles. But after many attempts an accurate fit to the diffused profiles was not possible. Attention was then turned to the spin-on-glass.

It is known that arsenic tends to diffuse out of silicon with increasing implant fluence and decreasing implant energy [16,17]. To prevent this outdiffusion an oxide cap is commonly used. Spin-on-glass was chosen as a cap since it could be applied at room temperature and cured below 100°C. Other capping methods (such as chemical vapor deposition) were ruled out due to the elevated temperatures required for these processes.

After carefully performed SIMS analysis, measured fluences were determined. Figure 4-11 shows the results of this experiment for the 1 X 10^{16} cm^{-2}, 100 keV furnace annealed samples. It is evident from the total sample data that the arsenic outdiffuses into the spin-on-glass up to 950°C. This is determined by the decrease in

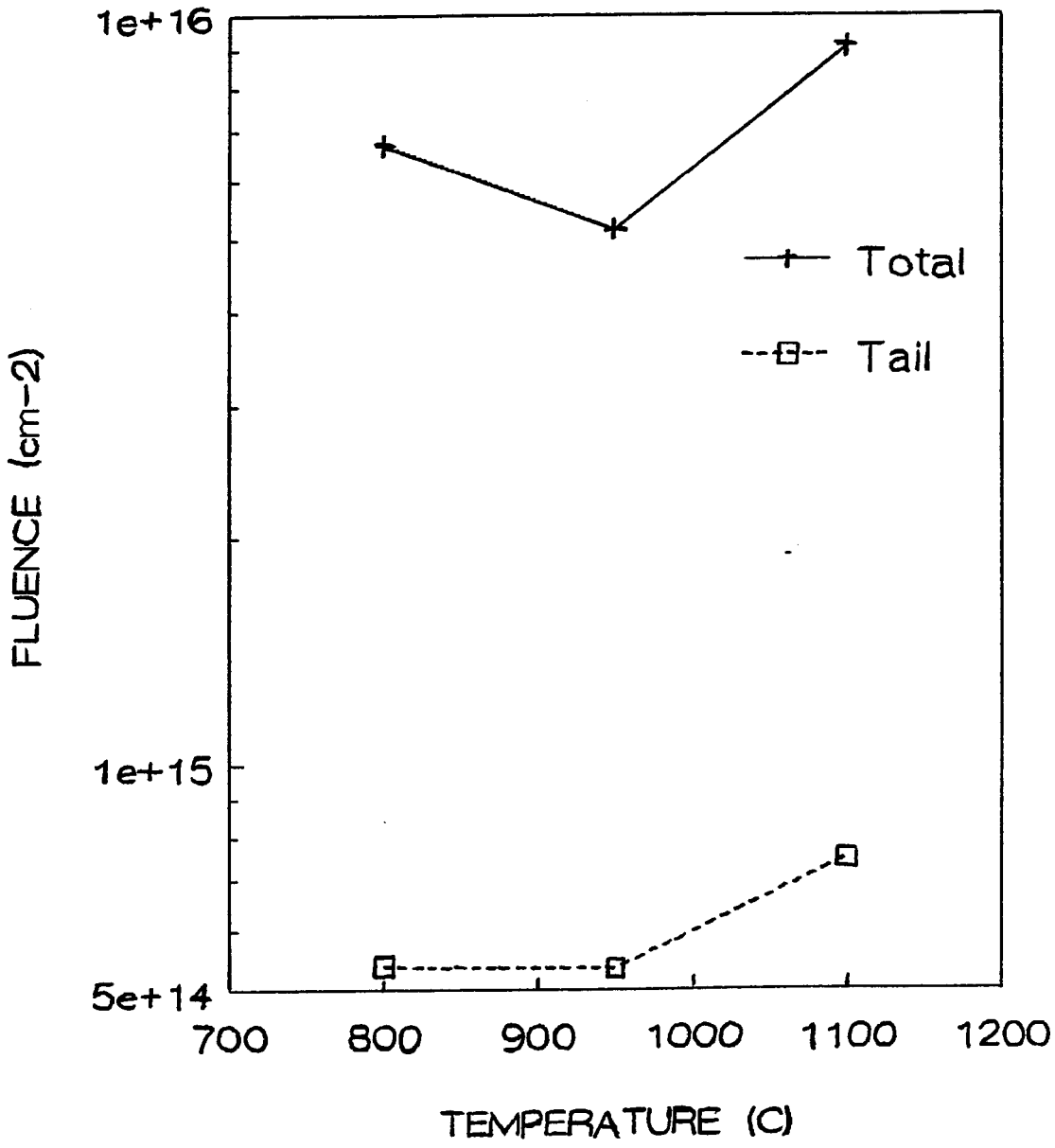

Figure 4-11. Fluences measured by SIMS for the 1 X 10^{16} cm^{-2}, 100 keV implanted and diffused profiles.

measured fluence. Above 950°C the measured fluence increased. Therefore, the capping spin-on-glass acts as a trap for outdiffusing arsenic up to 950°C. At the higher temperatures it begins to act as an additional arsenic source. To actually determine the arsenic diffusivity would then require the incorporation of arsenic diffusing into and out of the spin-on-glass.

CHAPTER 4

References

1. R.B. Fair, *IEEE Trans. Electron Dev.* 35, 285 (1988).

2. Y. Kim, H.Z. Massoud, and R.B. Fair, *J. Elec. Mat.* 18, 143 (1989).

3. K.S. Jones, S. Prussin, and E.R. Weber, *Appl. Phys. A* 45, 1 (1988).

4. D. Mathiot and J.C. Pfister, *J. Appl. Phys.* 55, 3518 (1984).

5. N.E.B. Cowern, *J. Appl. Phys.* 64, 4484 (1988).

6. C.S. Nichols, C.G. Van de Walle, and S.T. Pantelides, *Phys. Rev. Lett.* 62, 1049 (1989).

7. K.C. Pandey, A. Erbil, G.S. Cargill, R.F. Boehme, and D. Vanderbilt, *Phys. Rev. Lett.* 61, 1282 (1988).

8. T.E. Seidel, C.S. Pai, D.J. Lischner, D.M. Maher, R.V. Knoell, J.S. Williams, B.R. Penumalli, and D.C. Jacobson, in Energy-Beam Solid Interactions and Transient Thermal Processing, D.K. Biegelsen, G.A. Rozgonyi, and C.V. Shank, eds., (Mater. Res. Soc. Proc. Vol. 35, Pittsburgh, PA, 1985) p. 329.

9. J.L. Hoyt and J.F. Gibbons, in Rapid Thermal Processing, T.O. Sedgwick, T.E. Seidel, and B.-Y. Tsaur, eds., (Mater. Res. Soc. Proc. Vol. 52, Pittsburgh, PA, 1986) p. 15.

10. T. Hirao, G. Fuse, K. Inoue, S. Takayanagi, Y. Yaegashi, and S. Ichikawa, *J. Appl. Phys.* 50, 5251 (1979).

11. T. Hirao, G. Fuse, K. Inoue, S. Takayanagi, Y. Yaegashi, and S. Ichikawa, T. Izumi, *J. Appl. Phys.* 51, 262 (1980).

12. J.F. Gibbons and L.A. Christel, in Ion Implantation and Beam Processing, J.S. Williams and J.M. Poate, eds., (Academic Press, New York, 1984) Chapter 3.

13. L.A. Christel, J.F. Gibbons, and S. Mylroie, *Nucl. Inst. and Methods,* 182/183, 187 (1981).

14. S. Alexandrova and D.R. Young, *J. Appl. Phys.* 54, 174 (1983).

15. A. Lietola, J.F. Gibbons, and T.W. Sigmon, *Appl. Phys. Lett.* 36, 765 (1980).

16. G. Chaussemy, B. Canut, S.N. Kumar, D. Barbier, and A. Laugier, in Fundamentals of Beam-Solid Interactions and Transient Thermal Processing, M.J. Aziz, L.E. Rehn, and B. Stritzker, eds., (Mater Res. Soc. Proc. Vol. 100, Pittsburgh, PA, 1988) p. 695.

17. S.N. Kumar, G. Chaussemy, B. Canut, D. Barbier, and A. Laugier, *Appl. Surf. Sci.* 36, 545 (1989).

Chapter 5

Summary and Recommendations

5.1 Summary

This dissertation has examined arsenic diffusion and damage annealing of above-amorphization-dose arsenic implanted silicon. Anodic oxidation and stripping was used to separate the high concentration portion of the as-implanted arsenic profile and the amorphous layer from the end-of-range (or tail) region. This led to the production of total samples and tail-only samples before any heat treatment. Thus, the tail-only samples allowed for the study of arsenic in a region with excess silicon which was recoil-implanted into the end-of-range region during the arsenic implantation. Comparison of the tail-only sample with its corresponding total sample (i.e., subjected to the same annealing conditions) allows the determination of the role the original amorphous layer plays in the damage annealing, arsenic diffusion, and arsenic electrical activation.

Figure 5-1 depicts the various mechanisms which contribute to arsenic diffusion in silicon for above-amorphization doses of arsenic. The amorphous layer plays an important role in the arsenic diffusion and electrical activation at the lower temperatures of this study (800°C to 950°C). In this temperature range category V (projected range) and category II (end-of-range) defects form (see Section 1.2.3 and Fig. 3-51). Very little arsenic diffusion is also observed. It is suggested that the arsenic in the original amorphous region (which includes the peak concentration in the arsenic distribution) aids in the annealing of this vacancy rich region (see Fig. 1-7) before any considerable diffusion can occur. Increasing the arsenic dose results in

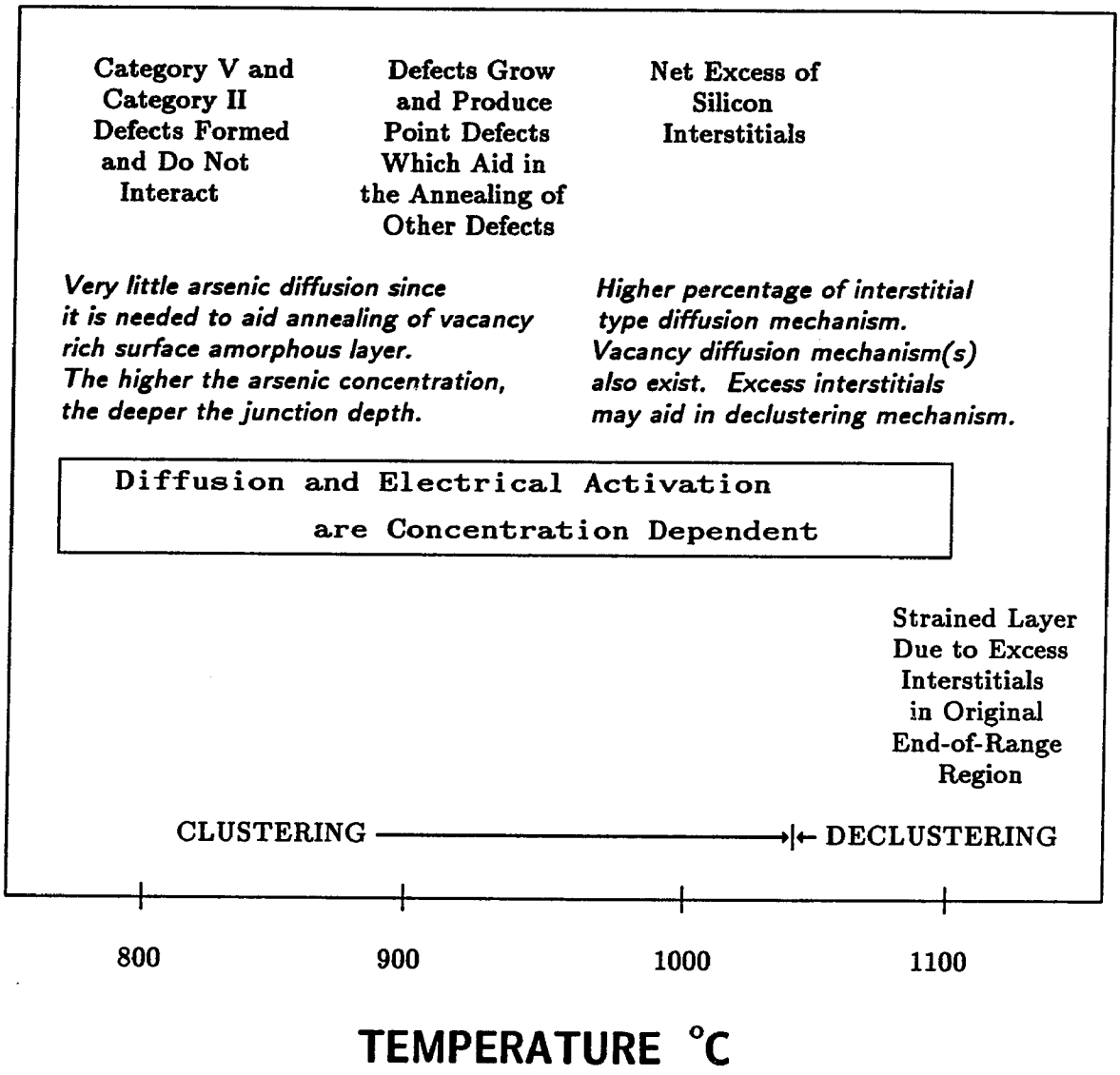

Figure 5-1. Mechanisms involved in damage annealing and arsenic diffusion for above-amorphization doses of arsenic implanted into silicon.

deeper junctions at these low temperatures. Therefore the diffusivity will be dependent upon the damage annealing and the arsenic concentration. At these high doses the carrier concentration will be less than the total chemical concentration of arsenic due to clustering. The clusters formed after the lower temperature anneals are also dependent on the arsenic concentration.

By increasing the annealing temperature the category V and category II defects grow in size and decrease in density. As these defects grow point defects are created which diffuse into the other region (i.e., point defects created in the original amorphous region diffuse into the original end-of-range region, and vice versa) and aid in the annealing and diffusion processes.

By 950°C the damage has annealed and there is a net excess of silicon interstitials. These interstitials are then available to contribute to the arsenic diffusion. Above 1050°C declustering is observed. The original clusters seen at the lower temperatures are affected by the silicon interstitials. Since the excess silicon interstitials are available to contribute to interstitial type diffusion mechanisms, this process also breaks the original clusters and forms new defects. Therefore, for above-amorphization-dose implants of arsenic, a higher percentage of the arsenic will diffuse by interstitial type mechanisms at the higher temperatures of this study (> 1000°C).

This dissertation also shows the results of a preliminary study of high-arsenic-dose implantation through a surface oxide layer before heat treatment. Compared to the above discussion these samples also have a net excess of silicon in the end-of-range region. Also present in this region is oxygen that has been recoil-implanted from the oxide surface layer into the end-of-range region. It was found that this excess oxygen plays a role in both the arsenic diffusion and electrical activation. Therefore, any

model for arsenic diffusion under these conditions would include the above model plus the effects of the oxygen present. To date this has not been done by any research group.

5.2 Recommenations for Future Studies

In this work the role of implantation damage and interstitials on the diffusion of implanted arsenic in silicon was emphasized. Current processing simulators, such as SUPREM and PREDICT (see Section 2.4), include only the role of vacancies in computing arsenic diffusion. Therefore a computational model based on the experimental results presented within this dissertation would be a subsequent step in determining the actual contribution of an interstitial dopant diffusion mechanism.

The role of interstitials could also be determined by studying the effects various fluences of silicon have on intrinsically and extrinsically arsenic doped silicon. DLTS studies could be performed on these samples (before and after annealing) and compared to the present results. This would result in more knowledge of the role the interstitial plays in the deep level defects observed.

The "declustering" mechanism observed as the sample was annealed above 1050°C should be further investigated. Since Kamgar et al. [1] have suggested that this is dependent upon time, it is suggested that an isothermal experiment be conducted at a temperature below 1050°C. DLTS spectra could be taken for various anneal times to see if the spectrum changes. If it does, then the suggestion by Kamgar et al. [1] is correct. RBS and XTEM should be used to determine any structural changes.

The preliminary through-oxide results are a clear indication that oxygen plays a role in the diffusion and electrical activation of arsenic. Results from differential Hall effect measurements and SIMS could be compared to the tail-only profiles of Figs. 4-6 and 4-7 to see if the fraction of arsenic that is electrically active differs in any way.

Also, DLTS measurements would lead to a better understanding of the way the recoil-implanted oxygen affects the defects present after annealing. One would expect to at least see the oxygen-vacancy pair.

CHAPTER 5

References

1. A. Kamgar, F.A. Baiocchi, and T.T. Sheng, *Appl. Phys. Lett.* 48, 1090 (1986).

VITA

Scott Edward Beck was born to Marlin and Miriam Beck on January 21, 1960 in Allentown, Pennsylvania. He attended L.E. Dieruff High School in Allentown, Pennsylvania and graduated in 1977. In September of 1977, he entered Lehigh University. Here he received a Bachelor of Science degree in Electrical Engineering, a Bachelor of Science degree in Engineering Physics, and a Masters of Science degree in Physics. In the fall of 1984 he entered the Ph.D. program in Physics at Lehigh University. From January 1983 through June 1986 he served as a physics teaching assistant. He was the recipient of a Sherman Fairchild Fellowship from September 1986 to September 1989. In September 1988, he was married to Brenda Lee Scheirer. He is a member of the American Physical Society, the American Vacuum Society, the Electrochemical Society, the Institute of Electrical and Electronics Engineers, and the Materials Research Society.